Microporous carbons for gas storage

Chen, Xuesong

Award date:
1997

Awarding institution:
University of Bath

MICROPOROUS CARBONS FOR GAS STORAGE

submitted by **Xuesong Chen**

for the degree of Ph.D. of the University of Bath

1997

Signed ----------

Xuesong Chen

ProQuest LLC
789 East Eisenhower Parkway
P.O. Box 1346
Ann Arbor, MI 48106-1346

ACKNOWLEDGEMENTS

This thesis would not have been accomplished without the Overseas Research Student Awards from the Committee of Vice-Chancellors and Principals of the Universities of the United Kingdom and a Bursary from the School of Materials Science, University of Bath, and I wish to thank both bodies for their financial support.

I would like to take this opportunity to express my sincere appreciation to Professor Brian McEnaney to whom I am deeply indebted for his excellent supervision, consistent encouragement and constant support.

I am also very grateful to Dr. Tim Mays for many stimulating discussions in molecular simulations and constructive suggestions in the course of this research work.

Acknowledgement also goes to the staff and technicians working in the School of Materials Science, University of Bath, for their assistance in the experiments. Collaborations for high pressure methane isotherm measurements from Professors A. Linares-Solano and D. Cazorla-Amoros of the University of Alicante, Spain, as well as for X-ray diffraction measurements from B.F. Chapman in the School of Physics, University of Bath, are highly appreciated.

DEDICATIONS

This PhD thesis is dedicated with my heart and soul to my wife, Chengjuan Liu, and my dear mother, Zhongqing Liu. Their love and support have encouraged me to realise my dream.

ABSTRACT

This thesis reports a study of the development of microporous carbons for storage of natural gas. This work supports the development of adsorbed natural gas as a vehicle fuel. Grand canonical ensemble Monte Carlo molecular simulations of methane adsorption at 298 K were performed in a model pore with variable microstructure and the volumetric methane capacities on model carbon monoliths with different morphologies were estimated from the molecular simulation results. It was found that the adsorbed methane density is sensitive to the variation in carbon atom number density in pore walls and pore width, but not sensitive to the interlayer spacing and the number (greater than 2) of carbon layers within each pore wall. The simulation results have shown that the optimal pore size of activated carbons for adsorbed natural gas at 298 K and 3.4 MPa is around 1.12 nm and that mesopores, macropores and voids play little role in enhancement of methane storage capacity. The maximum delivered methane capacity estimated for model carbon monoliths indicates that the defined industrial target of 150 v/v is theoretically feasible.

Microporous carbons were developed from meso-carbon microbeads, petroleum coke, phenolic resin, lignite and waste paper by either physical activation (using CO_2) or chemical activation (using KOH, K_2CO_3 or H_3PO_4). The mechanism of KOH activation of meso-carbon microbeads was studied by thermogravimetry coupled with a mass spectrometer, and by X-ray diffraction. Microporous carbon monoliths were fabricated from the KOH-activated meso-carbon microbeads and AX-21 carbon powder with phenolic resin as binder.

The excess methane isotherms of the carbon monoliths were gravimetrically measured on a high pressure electronic microbalance. The delivered methane capacities of AX-21 carbon powder packed under high pressures were volumetrically measured using a high pressure methane adsorption-desorption test rig. The delivered methane capacity on the best carbon monolith made from KOH-activated meso-carbon microbeads is 146 v/v, which is very close to the defined target value of 150 v/v.

CONTENTS

SECTION A

INTRODUCTION

CHAPTER 1 GENERAL INTRODUCTION

1.1 OBJECTIVES OF THE RESEARCH

Natural gas is a clean, cheap and readily available natural resource which has been used for many years as an industrial fuel for stationary engines to drive compressors and pumps, as a feedstock in the chemical industry and as a domestic fuel for cooking and heating. However, the low storage density of natural gas has restricted its broad acceptance as an alternative fuel to petrol in transportation. In recent years, the instability of world oil markets and the ever-increasing environmental concerns over pollution caused by the exhaust from petrol or diesel vehicles have again stimulated research into the feasibility of gas-driven vehicles, since natural gas is cheaper and burns more cleanly than petrol, emitting fewer toxic hydrocarbons and less carbon monoxide. But one of the main problems in gas-driven vehicle design, or natural gas storage for other purposes as well, is how to enhance the natural gas storage density at a reasonable cost. Compared to dissolved, compressed or liquefied natural gas, adsorbed natural gas on microporous carbons is a very promising technique to increase natural gas density at an ambient temperature and a moderate pressure (3.4 MPa). So the investigation and the development of such a suitable microporous material is currently an active research area.

The objective of this research project was to develop, to characterise and to evaluate microporous carbons and carbon monoliths for the purpose of natural gas storage.

In this study, methane was used as a model gas to represent natural gas since the major constituent (about 90% in volume) of natural gas is methane (Medici and Mime, 1974). The higher the methane adsorption on the carbon is, the greater the storage capacity of natural gas on the carbon should be, even though other minor components in natural gas might have some influences on methane adsorption. Methane is the first member of alkane series and has a low critical temperature of 191 K, which means that methane will remain in the gaseous state at ambient temperatures no matter how high the applied pressure is. The spherical symmetric structure of methane molecules makes the adsorption of methane on carbons depend mainly on London dispersion forces. Therefore, it is the physical size of the

pores within the carbon material, rather than the chemical property of the carbon surface that mainly determines methane adsorption.

Basically the over-lapped potential energy from the opposite pore walls makes the adsorbed methane density in pores greater than the bulk methane density. Based upon molecular simulation results of the methane adsorption in a slit between two single graphite planes, Matranga, *et al* (1992) concluded that the optimal pore size for methane storage at 298 K and 3.4 MPa is 1.14 nm. This conclusion was verified by Cracknell, *et al* (1993) using a similar method but in a slit between two graphite slabs. The results from Cracknell, *et al* also showed that the adsorbed methane density on model carbon adsorbents decreased with the increase of pore width for a given temperature (298 K) and pressure (3.4 MPa), and that only micropores could significantly enhance the average methane density in pores while mesopores and macropores play little role.

On the other hand, the packing density of carbon adsorbents is also very important because it is the volumetric rather than gravimetric methane capacity that decides the driving range of the vehicles using adsorbed natural gas as a fuel. These fundamental researches have elucidated that carbon adsorbents for the application of natural gas storage should have the following properties:

- large micropore volume, especially around the pore size of 1.0 nm which is an optimal pore size for methane storage at 298 K and 3.4 MPa;
- small mesopore and macropore volumes so that both large porosity and high piece density of the carbon adsorbent can be achieved;
- the carbons should be in monolithic forms so as to reduce the interparticle voids in the storage vessels.

The adsorbed natural gas for vehicles requires the carbon adsorbent to have both a high porosity and a high bulk density. But these two factors oppose each other since a higher porosity means a lower bulk density. A compromise has to be found between these two effects. One way to approach this balance is to control the pore structure of activated carbon by increasing the ratio of micropores to mesopores and macropores. Another way is to produce monolithic carbons so as to minimise interparticle voids. An effort in both directions has been made in this study.

Parkyns and Quinn (1995) evaluated various commercially-available activated carbons for adsorbed natural gas storage in terms of stored methane capacity. These carbons are in various forms, including powders, fibres, granules and pellets, and they represent a variety of carbon precursors and processing techniques. The surface areas (BET, N_2, 77K) of these carbons range from 81 m^2 g^{-1} to 3410 m^2 g^{-1}. But none of them give a delivered methane capacity greater than 100 v/v (the volume of methane discharged at 0.1 MPa per volume of carbon after being equilibrated with methane at 3.4 MPa and 298 K). This value is only two thirds of the target delivered methane capacity 150 v/v, which is defined by Atlanta Gas Light Adsorbent Research Group (1995). This target is believed to be necessary for a broad acceptance of adsorbed natural gas in vehicles. The unsatisfactory performance of the commercial activated carbons for natural gas storage may be because either these activated carbons have inadequate micropores and too many mesopores and macropores or they have low bulk densities. Most of the commercial carbons are activated by steam. By this processing technique (usually called physical activation), the development of mesopores and macropores in the carbons is inevitable while the micropores are developed due to the way pore structure is created. By chemical activation, for instance, the heat-treatment of petroleum cokes (Wennerberg, 1971) or meso-phases (Otawa, *et al*, 1992) with excess KOH, highly microporous carbons can be produced but they are usually very fluffy powders which have a low bulk density, ~0.27 g/ml.

Now the question is whether or not activated carbons can be prepared to have a delivered methane capacity greater than or close to the defined target. In this study, molecular simulations using a grand canonical ensemble Monte Carlo method have been carried out, using a model carbon that is more realistic than those used previously by Matranga, *et al* (1992) and Cracknell, *et al* (1993). The simulation results prove that the defined target of the delivered methane capacity on carbon adsorbents is theoretically possible and methane storage capacity on activated carbons can be improved by tailoring the pore structure from well-selected precursors by a suitable processing technique. Also in this study attempts are made to develop highly microporous carbon powders from meso-carbon microbeads by KOH activation and to produce carbon monoliths from KOH-activated meso-carbon microbeads and from AX-21 carbon powders (a commercial activated carbon) with phenolic resin binder.

1.2 LAYOUT OF THE THESIS

The thesis consists of three sections: section A — introduction, section B — experimental work, and section C — results and discussions, also including conclusions and future work.

In section A, a general introduction to natural gas and activated carbons is given. The significance, the feasibility, the advantages and disadvantages of using natural gas as an alternative automobile fuel to petrol or diesel are addressed in Chapter 2. Chapter 3 reviews activated carbon manufacture, the pore structure and the morphology of carbon adsorbents required for natural gas storage.

In section B, there are three chapters on material design (Chapter 4), development of materials (Chapter 5) and characterisation of materials (Chapter 6). In Chapter 4 the grand canonical ensemble Monte Carlo molecular simulation method is reviewed. A pore model and carbon models used in the molecular simulations of methane adsorption are described. The volumetric methane capacities on model carbon monoliths are also defined in Chapter 4. Chapter 5 presents the properties of the raw materials used in this study, i.e. meso-carbon microbeads, petroleum coke, lignite, phenolic resin, coconut shells, wastepaper and AX-21 carbon powder. The preparation techniques of activated carbons are also described in Chapter 5. Chapter 6 includes the characterisation methods and instruments used to evaluate the activated carbons prepared in this study.

In section C, Chapter 7 presents the molecular simulation results. Effects of carbon microstructure on the adsorbed methane density in a slit-shaped carbon pore and the volumetric methane capacities on model monoliths are discussed in this chapter. The optimal pore size of activated carbon for adsorbed natural gas and the maximum methane capacity for a given adsorption pressure (3.4 MPa), desorption pressure (0.1 MPa) and temperature (298 K) on model carbon monoliths are also discussed in Chapter 7. The characterisation results of activated carbons as well as a study on KOH activation of meso-carbon microbeads are discussed in Chapters 8. Chapter 9 includes the experimental results

of methane adsorption on carbon monoliths produced in this study. The conclusions and proposals for future work are summarised in Chapter 10.

CHAPTER 2 NATURAL GAS

2.1 RESERVES, TRANSPORTATION, STORAGE AND PROPERTY OF NATURAL GAS

2.1.1 Reserves And Consumption

Natural gas is one of the major energy sources with many attractive properties. It is cheap, readily available and, most importantly, clean to burn. Proved world natural gas reserves in 1987 are estimated to be around 107.6 x 10^{12} m^3 (O'Callaghan, 1993), which consists of 11 % of the total world recoverable fossil reserves (about 40 peta Joules of energy, including oil, coal and gas). Natural gas reserves are roughly equivalent to the oil reserves in terms of heat value. There are still extensive potential natural gas reserves to be discovered in the future since its exploration is not so well developed as it is for oil. Natural gas supplies about 20 % of world primary energy consumption and the share of natural gas in the energy market is as high as 34 % in USSR and 45 % in Netherlands (Khan, 1986). Both the production and the consumption of natural gas are forecast to increase world-wide for economic, environmental, strategic and political reasons. For Western Europe as a whole, gas consumption was anticipated to increase to 290 billion cubic meters by the year 2000.

Today natural gas is primarily used as a fuel in both domestic and industrial fields. There are no toxic hydrocarbons, sulphur compounds and carbon monoxide in the products of complete combustion of natural gas, which makes it an ideal fuel in domestic heating and cooking applications. Natural gas has been used as an stationary engine fuel in electricity generation and in driving pumps, refrigerators and compressors because compared with petrol, natural gas has the advantages of higher octane rating, higher power/weight ratio and greater compression ratio (Weaver, 1989). Natural gas is also an important feedstock in the chemical industry to synthesise a wide range of chemical products such as hydrogen, methanol, formaldehyde, *etc.* In recent years the ever-increasing concern over environmental pollution caused by the exhausts from petrol and diesel vehicles makes natural gas an attractive alternative to the conventional fuels, since natural gas produces

much less pollutants than petrol or diesel. There are already more than one million natural gas fuelled road vehicles world-wide and this figure increases steadily as the emission standards become more and more difficult to meet by the conventional transportation fuels. The conversion of a large number of vehicles from petrol or diesel to natural gas will play a significant role in boosting natural gas consumption as well as related technologies.

2.1.2 Transportation And Storage

Natural gas resources like oil resources are often located in remote areas and the gas needs to be transported from production sites to domestic or industrial consumers either by long distance pipelines (compressed natural gas) or by thermally insulated tankers (liquefied natural gas). The pipeline is the most common form of natural gas transport. The first natural gas pipeline was made of wooden tubes in 1821 and the first relatively long distance and high pressure pipeline was a 20 cm wrought iron pipe which operated at a pressure of 3.6 MPa (Tiratsoo, 1967). From the 1920s onwards, steel pipe was widely used because it could withstand higher pressure and could be joined by welding on site so that the pipeline could be extended to wherever it was needed with the help of "booster" pumping stations. The trend has always been towards a longer distance of transmission, a greater diameter of pipe and a higher operating pressure, which makes natural gas more economic to transport and to consume. With stronger materials available, for example a special alloy with a yield strength of 414 MPa, a one meter diameter gas pipe is possible (Tiratsoo, 1967). In the United States, pipes of diameter 76 ~91 cm are commonly used under the operating pressure of ca. 7.0 MPa. This operating pressure is high enough for the adsorbed natural gas application (3.4 MPa) but not for the compressed natural gas application (20 MPa).

Another way of natural gas transport is to deliver it in liquid form in special thermally-insulated tanks. This kind of transmission is suitable for batch use or where it is too expensive to lay down pipelines. For instance, each year a large amount of liquefied natural gas is shipped to Japan from Russia and Indonesia and to Western Europe from Algeria, Libya and Nigeria (International Energy Agency, 1982). On a large scale natural gas can be stored in huge gas tanks under a high pressure or in thermally insulated containers at a low temperature (-162 °C). The natural gas tanks are usually connected to distribution pipelines for regular domestic and industrial users. Liquid natural gas is often

stored to meet peak demands in extreme circumstances like very cold weather. On a widely distributed, small scale natural gas is stored in cylinders which can be transported to the consumers. In future it might be possible to transport adsorbed natural gas at an ambient temperature in activated carbon filled tanks so that the storage pressure can be significantly reduced.

2.1.3 Property Of Natural Gas

Natural gas is a mixture of hydrocarbon gases and non-hydrocarbon gases as shown in Table 2.1.

Table 2.1 Typical average composition of natural gas in different world areas

(From Medici and Mime, 1974)

	North Sea British area	Alberta Canada	Spilimbergo Italy	Crosfield USA	Horizon M1 USSR
methane	90.43	95.62	96.73	80.93	93.00
ethane	3.76	0.24	1.51	6.45	4.00
propane	0.94	0.05	0.63	2.33	1.40
butane	0.30	0.05	0.31	1.26	
pentane	0.14	0.03	0.14	0.88	
C_6H_{14} and higher	0.24		0.03	0.39	
nitrogen	3.86		0.65		
carbon dioxide	0.26			6.13	
helium	0.05			0.96	
hydrogen sulphide				1.06	
benzene	0.02				

Note: The data are in units of percentages by volume.

All hydrocarbon gases in natural gas are members of the alkane series. The most abundant component is methane which does not condense to liquid under the temperature and pressure conditions of reserves. There are small proportions of other hydrocarbons with carbon numbers ranging from two to seven. Non-hydrocarbon gases include hydrogen,

carbon dioxide, helium, hydrogen sulphide, nitrogen and moisture, *etc.* The composition of natural gas varies with the different reserves and productions. Usually it is classified into three categories: (i) "dry" gas which has less than 0.1 gallon of extractable liquid hydrocarbons (ELH) per cubic foot of gas at standard temperature and pressure; (ii) "lean" gas which has 0.1 to 0.3 gallon of ELH per cubic foot and (iii) "wet" gas whose ELH is greater than 0.3 gallon/cubic foot.

Commercial natural gas (which has a calorific value of about 35 ~ 45 MJ m^{-3}) usually contains 85 ~ 95 per cent of methane by volume. Therefore, in this study methane was used as a model gas representing natural gas in evaluating activated carbons for natural gas storage. Quinn (1990), Lewis, *et al* (1991), Mullhaupt, *et al* (1992) and many other researchers also used methane as a model gas in order to compare the results with each other.

2.2 NATURAL GAS VEHICLES

Alternatives to conventional motor fuels (petrol and diesel) are currently being studied for the reasons of energy security and environmental protection in developed countries. The alternative fuels under investigation include hydrogen, natural gas, methanol, propane, solar energy, electricity, *etc.* Among these alternatives, natural gas is an attractive candidate in particular and appears most likely to be able to displace a significant portion of the conventional transport fuels over the next 10 to 15 years (Margaret, 1989). The US Department of Energy (DOE) has sponsored a number of studies estimating the capital cost of developing a natural gas supply infrastructure and vehicles to displace one million barrels of petroleum per day in the transport sector in the period of 1995-2005. This means that 32.8 million natural gas driven vehicles will be required to consume 147 million cubic meters of natural gas per day. If this plan can be put into practice, the environmental pollution caused by the transportation sector will be significantly reduced, especially in big cities.

2.2.1 Advantages And Disadvantages Of Natural Gas Vehicles

Advantage Of Natural Gas Vehicles

Natural gas vehicles offer a number of technical and economic advantages. The technical advantages of natural gas vehicles include extremely low photochemical reactivity, zero evaporation leak, reduced cold-start and low temperature emissions due to elimination of cold enrichment, and compatibility with fuel-efficient lean-burn technology. Natural gas vehicles are safer than petrol vehicles because natural gas has a higher ignition temperature, which means it is resistant to self-ignition. In addition the high pressure gas cylinder is stronger than a petrol tank. Therefore, natural gas vehicles do not explode in the case of road accidents. The economic advantages of natural gas vehicles come from the reduced fuel cost, engine wear and maintenance costs. Natural gas is available at low cost from abundant domestic supplies through existing transmission and distribution system which have been well established for more than a century in most developed countries. For example, in the United States of America there is more than one million miles of natural gas pipelines that can supply 650 billion cubic meters of natural gas per year, while the annual demand is 570 billion cubic meters. The excess 13 % capacity (80 billion cubic meters per year) would be enough to supply about 20 % of the entire fleet of highway vehicles if they were all converted into natural gas vehicles (Knowles, 1984). The compressed natural gas in USA costs just 30 % to 50 % the price of petrol, based on one gallon of petrol being equivalent to 100 cubic feet of natural gas (Knowles, 1984). If a vehicle is driven 15,000 miles and the fuel consumption is 15 miles per gallon, the fuel bill will be $1250 if petrol is used as a fuel at the price of $1.25 per gallon. A natural gas vehicle running the same distance will save $870 at the price of $0.38 per 100 cubic feet of natural gas. A natural gas vehicle costs about $800 more than a petrol vehicle, therefore, the pay-back period for a natural gas vehicle will be less than one and a half years, supposing that the average annual mileage of the natural gas vehicle is 10,000 miles.

Disadvantages Of Natural Gas Vehicles

Compared with petrol and diesel, natural gas has a lower energy density (combustion heat per unit volume of fuel). The volumetric energy content of compressed

natural gas at 20 MPa is about one fifth that of diesel or one fourth that of petrol. Due to the low density of natural gas , a stoichiometric mixture of natural gas and air occupies about 10 % more volume than that of petrol/air mixture with the same energy content. Therefore, for a fixed engine displacement, the amount of natural gas/air mixture in each stroke is about 10 % less in engine power output. But this problem can be overcome by increasing the compression ratio. As natural gas has a higher equivalent octane number (pure methane has 130 octane number), the compression ratio of natural gas/air mixture can go up to 15:1 while the compression ratio for petrol/air is only 8-10:1 assuming the octane number of petrol is 91 (Margaret, 1989).

Another drawback of natural gas vehicles is the weight and the volume of the storage cylinder. The compressed natural gas at 20 MPa and 298 K occupies about five times the volume of diesel and four times the volume of petrol for the same amount of energy. This poses a problem for family cars since they do not have enough space to hold the large heavy gas cylinders. Probably that is one of the reasons why natural gas vehicles have not been widely accepted by the public and why natural gas vehicles are normally trucks, buses, and heavy-duty vehicles because they have adequate space for compressed natural gas cylinders. The weight of the gas cylinder can be reduced by using new materials as shown in Table 2.2.

Table 2.2 Comparison of the weight of the fuel tank for compressed natural gas (20 MPa) and petrol (From Weaver, 1989)

compressed natural gas (kg/gallon) (a)				petrol (kg/gallon)
plain steel	fibre reinforced steel	fibre wrapped aluminium	all composite	
21	16	12	11	4

Note: (a) kg/gallon is the weight of the cylinder required to contain one gallon of diesel equivalent.

Another solution to this problem is to reduce the natural gas storage pressure from 20 MPa to 3.4 MPa so that the gas tank can be made lighter and formed into a body-fitting shape. This is the major objective for the research to investigate the potential of adsorbed

natural gas on microporous carbons (at 3.4 MPa and 298 K) in order to overcome the drawback of compressed natural gas (20 MPa) in this respect.

2.2.2 Environmental Benefits From Natural Gas Vehicles

It becomes increasingly obvious that the environmental pollution has a great impact on our society. The global warming which results from the 'greenhouse effect' has caused more floods and droughts each year; large areas of rain forest disappear due to acid rain; and the decreasing ozone level threatens the existence of all living creatures on earth. These problems are certainly not solely caused by conventional vehicle fuel but according to a report to the US Environmental Protection Agency (EPA) (Greene, 1989) transportation accounts for 70 % of carbon monoxide, 33 % of ozone producing hydrocarbons and 21 % of suspended particulates in air pollution. Despite that the emission rates of new petrol or diesel vehicles have been improved by adopting expensive and complicated modern technologies such as 'lean burn' engines and catalyst converters, it is still difficult for the vehicles burning conventional fuels to meet the stringent emission standards.

The main pollution from vehicle exhausts are carbon monoxide (CO), carbon dioxide (CO_2), non methane hydrocarbons (C_mH_n) , particulate matter (PM) and oxides of nitrogen (NO_x) and sulphur (SO_x). All these pollutants can be significantly reduced when natural gas is used as a fuel for a converted or specially designed engine as shown in Table 2.3.

Table 2.3 Full fuel cycle emissions for the 1995 Chrysler Mini Van operating on petrol and compressed natural gas (From Ingersoll, 1996)

	NO_x (g/mile)	C_mH_n (g/mile)	CO (g/mile)	PM (g/mile)	SO_x (g/mile)	CO_2 (g/mile)
compressed natural gas	0.093	0.085	0.420	0.002	0.004	371
petrol	0.626	0.698	3.462	0.013	0.044	468
emission standards [a]	0.400	0.125	3.400	0.080		

Note: a — the emission standards for passenger cars and light trucks in the United States, 1996.

Natural gas possesses a number of advantages as a clean fuel for motor vehicles:

(1) Natural gas is comprised of about 90 % methane while methane is considered as non-reactive photochemical in ozone formation, therefore, natural gas vehicles release very low ozone active hydrocarbons;

(2) The low sulphur content of natural gas, compared with petrol or diesel, will help to reduce sulphur dioxide and sulphate particle levels. The reduction in NO_x and SO_x emission due to natural gas vehicles will reduce acid deposition by reducing the supply of acid precursors in air. In addition, the inherent low CO emission will decelerate the rate of conversion of SO_2 to sulphuric acid;

(3) Carbon dioxide (CO_2) emission from natural gas vehicles is also lower since natural gas contains less carbon than any other fossil fuel per unit of energy. The global CO_2 level has increased from 270 ppm to 350 ppm over the last 150 years and is currently increasing annually by 1.5 ppm (Alson, *et al*, 1989). The reduction in CO_2 emission will help to slow down the "greenhouse" effect;

(4) Compared with petrol or diesel engines, natural gas engines produce much less particulates so that the air quality in big cities will be dramatically improved if all passenger vehicles were converted to burn natural gas.

2.2.3 Engineering And Technical Development Of Natural Gas Vehicles

Natural gas is rather hard to ignite and requires a high-energy spark, especially if a high air/fuel ratio (lean combustion) is used or if exhaust gas recycling is adopted. Ignition timing has an important effect on fuel economy and emissions. As the mixture becomes leaner, flame speed is lower, and the optimal spark timing must be advanced. Earlier ignition results in higher NO_x emissions and a loss of efficiency. This problem can be solved by a special design of ignition and combustion systems. Using a separate pre-chamber where ignition occurs with a richer mixture, the burning gases in the pre-chamber shoot into the main chamber through turbulent jets and provide excellent mixing and rapid combustion through the main chamber (Alson, *et al*, 1989). The combustion chamber is designed to generate very high turbulence to enhance flame speed and minimise the distance the flame has to travel. By using the "lean burn and fast burn" engines, 15~20 % advantage in fuel consumption compared to stoichometric engines can be achieved and also substantial lower CO and NO_x emissions.

There are no big problems in engineering since natural gas has been used for more than a century and a lot of infrastructure and technical achievement can be directly used in the natural gas vehicles sector.

2.3 ADSORBED NATURAL GAS

The low storage density of natural gas is one of the key problems in natural gas applications, especially in natural gas vehicles. There are several ways to increase the storage capacity of natural gas: the liquefied, the compressed, the adsorbed and the dissolved natural gas. Table 2.4 shows that energy density of the natural gas in different states, compared with that of petrol.

Table 2.4 The energy density of natural gas and petrol

(From Parkyns and Quinn, 1995).

Fuels	State	Energy density ($MJ\ dm^{-3}$)
petrol	liquid at 298K and 0.1 MPa	32
natural gas	gas at 298 K and 0.1 MPa	0.04
liquefied natural gas	liquid at 113 K and 0.1 MPa	23
compressed natural gas	gas at 298 K and 20 MPa	9.7
adsorbed natural gas [a]	adsorbate at 298 K and 3.4 MPa	6.2
dissolved natural gas [b]	clathrate at 298 K and 35 MPa	~6.0

Note: a — based upon the defined target methane capacity of 150 v/v on carbon;

b — dissolved into decane.

Liquid natural gas is suitable for the storage of natural gas on a large scale but it is not realistic as an on-board vehicle fuel because it is difficult for a vehicle to carry a cryogenic tank. Compressed natural gas needs expensive multi-stage compressing facilities to fill up the heavy high pressure cylinders, which requires a large amount of capital to built high pressure gas filling stations and so is not economically competitive. Dissolved natural gas still requires a high pressure and it is no better than simple compression. Adsorbed

natural gas on microporous carbons at a relative low pressure (3.4 MPa) and at an ambient temperature (298 K) is a very promising technique to increase natural gas energy density within a reasonable cost.

The reduction of the storage pressure from 20 MPa in compressed natural gas to 3.4 MPa in adsorbed natural gas can result in two benefits: firstly, the premier investment on the natural gas filling stations, which is the major cost in converting conventional fuel supply system to natural gas filling system, will be significantly reduced since the filling pressure of adsorbed natural gas can be reached by a single stage compressor; secondly, the on board adsorbed natural gas container can be made lighter due to the reduced storage pressure and also the adsorbed natural gas container can be shaped to a "body-fit" form so that more space will be available for storing the adsorbed natural gas . In addition a wider range of materials can be considered for building the fuel container, which will make it possible to make the container lighter and bigger as well as cheaper.

The negative factors of using adsorbed natural gas to replace compressed natural gas are that the gas filling time is longer and the driving range is shorter. The temperature of the adsorbed natural gas container will rise during the natural gas filling due to the heat released from the gas adsorption in the micropores of the adsorbents. It takes time to equilibrate to the ambient temperature. Fast filling (say 5 minutes) will reduce the storage capacity.

On the other hand, using only one fifth of the compressed natural gas pressure, adsorbed natural gas, provided that the delivered methane capacity is 150 v/v at 298K and 3.4 MPa, can deliver about 65 % (theoretically 91 %) of compressed natural gas at 20 MPa in a similar storage space (Matranga, 1992). The storage capacity of adsorbed natural gas has been improved by developing new microporous carbons. Up to date the highest adsorbed natural gas storage capacity (methane used as a model gas) is reported to be 181 v/v on carbons developed from polyvinylidene chloride (PVDC), which is equivalent to about 80 % of compressed natural gas (Atlanta Gas Light Adsorbent Research Group, 1995).

2.4 SUMMARY

Natural gas is a very promising alternative to conventional automobile fuels because it is abundant, readily available, cheap and more importantly clean to burn. Comparing with petrol or diesel, natural gas emits much lower levels of toxic hydrocarbons, less carbon monoxide and fewer particulates. The infrastructure of natural gas transmission and distribution system has been well established after its application as the fuel in both domestic and industrial markets for more than a century. Technically and economically it is feasible to replace a significant portion of conventional fuel vehicles by natural gas.

Natural gas is normally stored in liquefied or compressed forms. Adsorbed natural gas on microporous carbons is a very attractive technology to store natural gas at a low pressure (ca. 3.4 MPa), relative to the pressure of the compressed natural gas. The reduction of the storage pressure in adsorbed natural gas can provide two advantages over the compressed natural gas: first, the investment on gas filling systems for natural gas fuelled vehicles will be significantly reduced; second, the on-board natural gas container can be made lighter, bigger and cheaper due to the decrease of the storing pressure of the adsorbed natural gas.

CHAPTER 3 ACTIVATED CARBONS

3.1 GENERAL INTRODUCTION TO ACTIVATED CARBONS

3.1.1 Applications Of Activated Carbons

The term "activated carbon" was not defined as a single chemical entity but as a general name for a class of material with a highly developed internal pore structure and hence having a large capacity to adsorb chemicals from gas or liquid phase. Long before the term "activated" was coined, the use of carbon (called char or charcoal) for the manufacture of bronze and medicines had been known to ancient Egyptians though the function of the carbon was not clear at that time (3750 BC to 460 BC). The adsorptive phenomena on porous carbons were first discovered by Scheele in 1773 (Hassler, 1963) who measured the adsorption of various gases on different carbons. In the 19th century porous carbons were mainly used for decolorising syrups in sugar refining industry. The research, the production and the application of activated carbons were vigorously pursued and boosted during the First and the Second World Wars in the early 20th century due to the need for carbon adsorbents in military respirators to combat chemical warfare gases. It was during this period that a wide range of precursors were investigated to produce activated carbons with different properties and different shapes, and also that the activation step was introduced into the activated carbon manufacture (Derbyshire, *et al*, 1995). The post-war applications of activated carbons were extended to water treatment, solvent recovery, gas purification, catalysis and gold production, *etc*. The application of activated carbon in natural gas storage is a relatively new subject in the carbon industry and in the research field as well, although methane adsorption on solids has been studied for a long time for pore structure characterisation (Gregg and Stock, 1957) (Dollimore and Shingles, 1969). The researches specialised on methane or natural gas storage on activated carbons only became active in the last ten years when natural gas was considered as an alternative clean fuel.

3.1.2 Production Of Activated Carbons

Activated carbons can be made from a variety of carbonaceous materials but considering the cost and availability of feedstocks and the quality of the final products, commercial raw materials are normally of natural botanical origins (wood, coconut shells, walnut shells, nut kernels) or geologically transformed plant residues such as lignite, bituminous coal, anthracite. Sometimes synthetic materials like phenolic resins, polyvinyl chloride (PVC) or polyvinylidene chloride (PVDC), polyfurfuryl alcohol, coal tar pitch or petroleum pitch are selected to produce activated carbons with special properties. The production processes of activated carbons are normally classified into two categories: thermal gasification (also called physical activation) and chemical activation. The thermal gasification process, as shown in Figure 3.1, includes two main steps, i.e. carbonisation and activation. The purpose of carbonisation is to drive off the volatiles in precursors and to create some pores which are mainly voids left behind by the volatiles. The porosity created in the carbonisation step is normally not sufficient for practical usage. Therefore it is necessary to create new pores, to expand the existing pores and to open closed pores in the activation step by partially oxidising the carbonised materials at high temperatures, using gaseous oxidants like steam, carbon dioxide, air or their mixtures. The adsorptive properties of the final products or, in other words, the pore structures of activated carbons can be tailored to some extent by adjusting the processing parameters such as carbonisation and activation temperatures, carbon burn-off and the oxidising atmosphere. The production of regularly-shaped activated carbons requires reformulating the mixture of ground precursor and binder (coal tar, pitch, resin, and water, *etc.*) into cylinders or pellets by extruding or compressing. Some raw materials, for instance anthracite and coconut shells, do not need the reformation as their original hardness values are high enough to give a good mechanical strength after a heat treatment.

In chemical activation processes as shown in Figure 3.2, reagents such as $ZnCl_2$ or H_3PO_4 are used to digest the cellulose structures in the precursors (usually wood and other lignocellulosics). The functions of the chemical reagents are mainly to promote the water elimination, to increase cross linking and aromatisation and to inhibit shrinking during heat treatment (Derbyshire, *et al*, 1995). Sometimes reagents like KOH and NaOH are adopted to attack the ordered carbon structure in some graphitizible precursors such as coke, pitch

and meso-phases. Table 3.1 shows the typical properties of some activated carbons. It can be noticed from Table 3.1 that the surface areas and micropore volumes of activated carbons are inversely proportional to their bulk densities.

Table 3.1 The properties of several typical commercial activated carbons

(from Sircar, *et al*, 1996)

Carbons	Raw materials	Surface area ($m^2\ g^{-1}$)	Micropore volume ($cm^{-3}\ g^{-1}$)	Bulk density ($g\ cm^{-3}$)
BPL [a]	Bituminous coal	1100	0.70	0.48
PCB [b]	coconut shell	1200	0.72	0.44
PX21 [c]	petroleum coke	3150	1.80	0.30

Notes: a — Calgon's coal-based carbon for water-treatment; b — Calgon's coconut-shell-based carbon for gas adsorption; c — Anderson's microporous carbon made by KOH activation.

3.2 DEVELOPMENT OF ACTIVATED CARBONS FOR ADSORBED NATURAL GAS

The activated carbons for natural gas storage were well reviewed by Parkyns and Quinn (1995) and Mullhaupt, *et al* (1992) in terms of volumetric methane storage capacity or methane uptake based upon the experimental results on most commercially available activated carbons. These commercial activated carbons are made from various precursors by different processing technologies. Unfortunately, none of them gave a volumetric methane storage capacity higher than 100 v/v at 298 K and 3.4 MPa as shown in Figure 3.3. The reasons for this unsatisfactory performance of commercial activated carbons for methane storage are either they do not have enough pores and suitable pore size distribution or their packing densities are too low.

The research on how to improve the methane capacity on the existing activated carbons and how to develop carbons with well tailored pore structure from well selected precursors has been vigorously pursued by several groups. Chahine and Bose (1991) reported that the pellets they solidified from AX-21 with 2 % thermoplastic binder could store 144 volume of methane per volume of carbon at 3.5 MPa and 298 K. Lewis *et al*

(1991) prepared a series of activated carbons from isotropic, mesophase pitch and rayon fibres, phenolic resin, cotton and newsprint by steam or NaOH/KOH activation for natural gas storage. The highest stored methane capacity they achieved is 196 v/v on rayon fibres but this capacity is calculated based upon the piece density of a single fibre. When the fibres are packed into a container as required in real applications, the stored volumetric methane capacity per volume of storage space will be much lower than 196 v/v because the packing density of the fibres is much smaller than the piece density due to the high interparticle voids. Quinn and MacDonald (1992) reported methane storage capacity on the PVDC derived carbons and CO_2 activated coconut shell carbons. Capacities of ~170 v/v and ~120 v/v were obtained on the PVDC series and the coconut shell series, respectively. A comprehensive program which embraces both laboratory research on carbon adsorbents and field tests with adsorbed natural gas powered vehicles has been carried out by the Atlanta Gas Light Adsorbent Research Group (AGLARG, 1995). An industrial target of the delivered methane capacity on activated carbon was defined by AGLARG as 150 v/v at 298 K, 3.4 MPa for gas loading and 0.1 MPa for gas unloading. The AGLARG group fabricated monolithic PVDC carbons which can store around 180 cubic meters of methane at 298 K and 3.4 MPa per cubic meter of carbon monolith. But a large portion (ca. 30 %) of adsorbed methane on the PVDC carbons can not be desorbed at ambient pressure (0.1 MPa) and 298 K, which means their delivered methane capacities (about 120 v/v) are much lower than their stored methane capacities (AGLARG, 1994). The delivered methane capacity on the PVDC carbon can be improved to some extent by a new patent technique called air cycled activation but only can reach 130 v/v. Moreover the PVDC carbons are too expensive due to the high cost of the raw material, the low carbon yield and the time consuming processing route.

Other materials like AX-21 and Maxsorb (carbon powders with very high surface areas made from petroleum pitch by potassium hydroxide activation) can store and deliver much more methane per unit mass of carbon than most other carbons but their volumetric methane capacities are low because the packing density of these carbon powders is very low (0.27 g cm^{-3}). Attempts have been made to consolidate these highly porous powders to improve their volumetric storage capacity (Quinn, 1990). Some new carbons synthesised from cellulose precursors like cotton and fibres also shows very promising capacities (Lewis, *et al*, 1991) if they can be successfully made into monoliths. So far there are no

reports on monolithic carbons which can deliver 150 m^3 of methane at 298 K and 0.1 MPa per cubic meter of carbon adsorbent after equilibrated with methane at 3.4 MPa and 298K.

3.3 PORE STRUCTURE OF ACTIVATED CARBONS REQUIRED FOR ADSORBED NATURAL GAS

The pores in carbon adsorbents are highly irregular and variable, which poses a problem for the precise definition of the pore size. For this reason the description of pore structure in porous carbons are often based on model pores. Slits are commonly used as model pores and the pore width is defined as the space between the carbon nuclei in the opposite walls. The total porosity of a porous material is classified into three groups by International Union of Pure and Applied Chemistry (IUPAC) as follows (Sing, *et al,* 1985):

Micropores	width less than 2 nm
Mesopores	width between 2 and 50 nm
Macropores	width greater than 50 nm

These definitions are not based on direct measurement, so they should not be treated as rigid sizes but rather as being more meaningful in description of adsorption and desorption processes. For instance, mesopores are characterised by hysteresis loops during desorption due to capillary condensation; micropores are considered to have a dimension of one to three times of the adsorptive molecule size and are characterised by a sharp rise in adsorption isotherms at a low relative pressures, associated with micropore-filling. Micropores are further divided into ultra-micropores (less than 0.5 nm in width) and super-micropores (1.0 ~ 2.0 nm) (Byrne and Marsh, 1995) to address the molecular sieving effect on microporous carbons. Of course, the adsorption process depends both on the pore geometry and the size of adsorptives. The primary process which is completed in a very low relative pressure region occurs in ultra-micropores where the pore width is less than two times that of adsorbate molecules. The secondary process happens in super-micropores where pore width is between 2 and 5 times that of adsorbate molecules.

As the principal component (~ 90 % in volume) of natural gas is methane whose critical temperature is 190.6 K, the storage of natural gas on carbons at an ambient

temperature (298 K) is a matter of the adsorption of gases at a supercritical temperature. The molecular simulation results of methane adsorption in model pores by Gubbins (1993), Matranga, *et al* (1992) and Aukett, *et al* (1992) suggests that only micropores play an important role in the enhancement of adsorbed methane density and mesopores and macropores have little contribution to adsorbed natural gas storage. Based on these conclusions, the unsuitability of most commercial activated carbons for adsorbed natural gas storage can be attributed to the following three factors: first, they have a wide range of pore size distribution; second, their micropore volumes are too low; and third, the packing densities of commercial activated carbons are too low because they are normally in granular or powder form. Therefore, new activated carbons need to be developed, which should have more micropores and less mesopores and macropores, and also they should be in monolithic forms in order to increase their packing densities.

3.4 SUITABLE MORPHOLOGY OF ACTIVATED CARBON FOR ADSORBED NATURAL GAS VEHICLES

Adsorbed natural gas as on-board fuel for vehicles imposes another challenge, i.e. the space limitation. This limitation requires that the carbon adsorbents should possess both high micropore volume and high packing density. But as noted before a high microporosity implies a low bulk density. One route to improve the carbon properties is to reduce the fraction of mesopores and macropores by well controlled processing techniques and to minimise the interparticle voids by making carbons into monoliths.

Commercial adsorbents are normally granules, pellets or powders. Their packing densities (including pores and voids) are much lower than their particle densities. The interparticle voids make the volumetric methane capacity of most commercial carbons less than 100 v/v even though some highly microporous carbons such as AX-21 carbon powder have very high methane uptakes per unit mass. Therefore it is necessary to produce activated carbon monoliths.

3.5 POTENTIAL OF ACTIVATED CARBON FOR ADSORBED NATURAL GAS

Molecular simulations of adsorption of methane in a slit model pore between single perfect graphite layer plane show that the maximum delivered methane capacity on carbons at 298 K and 3.4 MPa is ~195 v/v (based on desorption at 298 K and 0.1013 MPa) (Matranga, *et al*, 1992). But it is not possible to manufacture such a carbon adsorbent whose pore walls are entirely composed of single graphite sheets. In this study a more realistic pore model and carbon monolith models (see Chapter 4) is proposed to find out whether the defined target value, 150 v/v, of delivered methane capacity by activated carbon is theoretically feasible and on which aspect activated carbons can be improved in order to increase their volumetric methane storage capacity.

3.6 SUMMARY

The objective of this research is to develop, to characterise and to evaluate activated carbons for applications in natural gas storage, especially for vehicles powered by adsorbed natural gas. Most commercial carbon adsorbents have delivered volumetric methane capacities less than 100 v/v, which is far below the defined target value of 150 v/v. So the development and characterisation of carbon adsorbents with suitable pore structure and morphology for adsorbed natural gas storage at an ambient temperature (298 K) and a moderate pressure (3.4 MPa) is the main objective of this study.

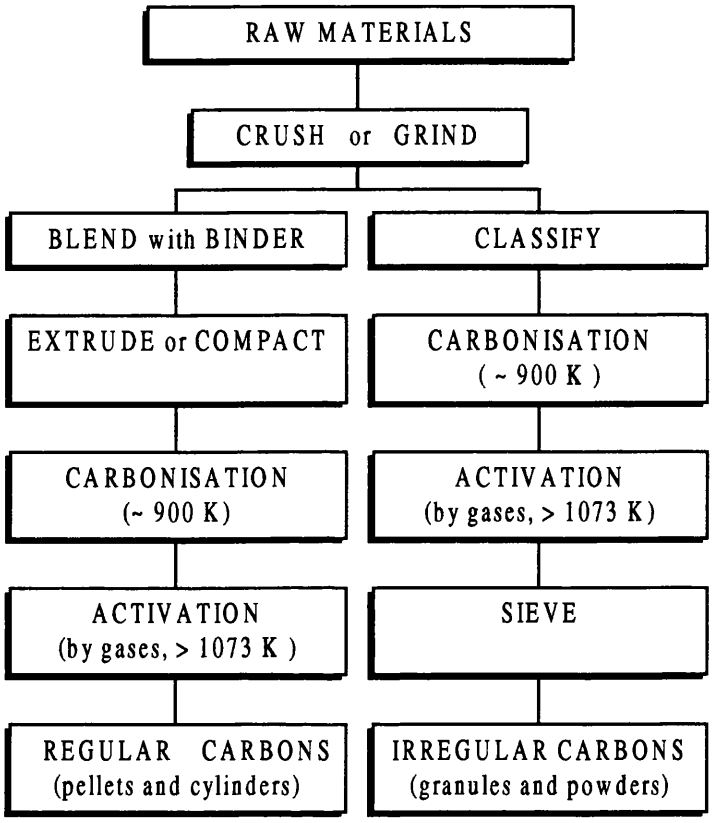

Figure 3.1 A typical flow diagram of activated carbon production by physical activation routes.

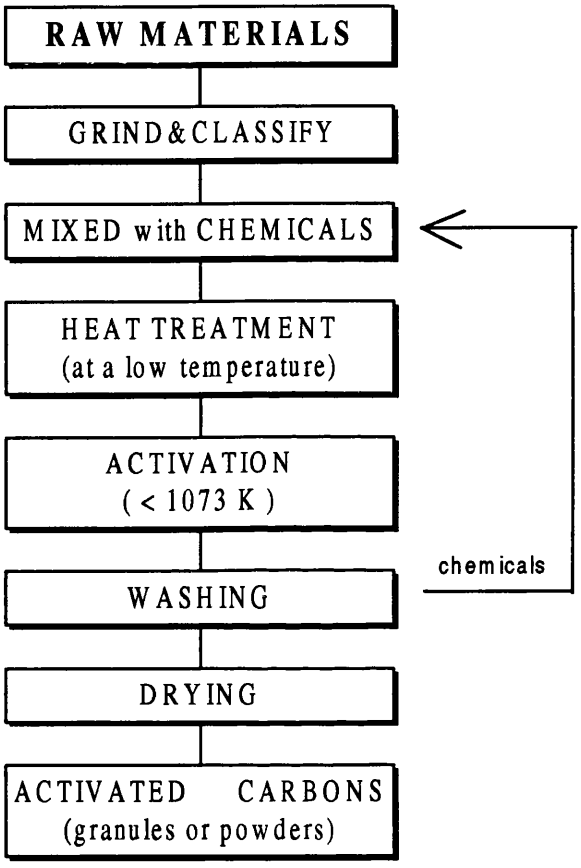

Figure 3.2 A typical flow diagram of activated carbon product by chemical activation routes

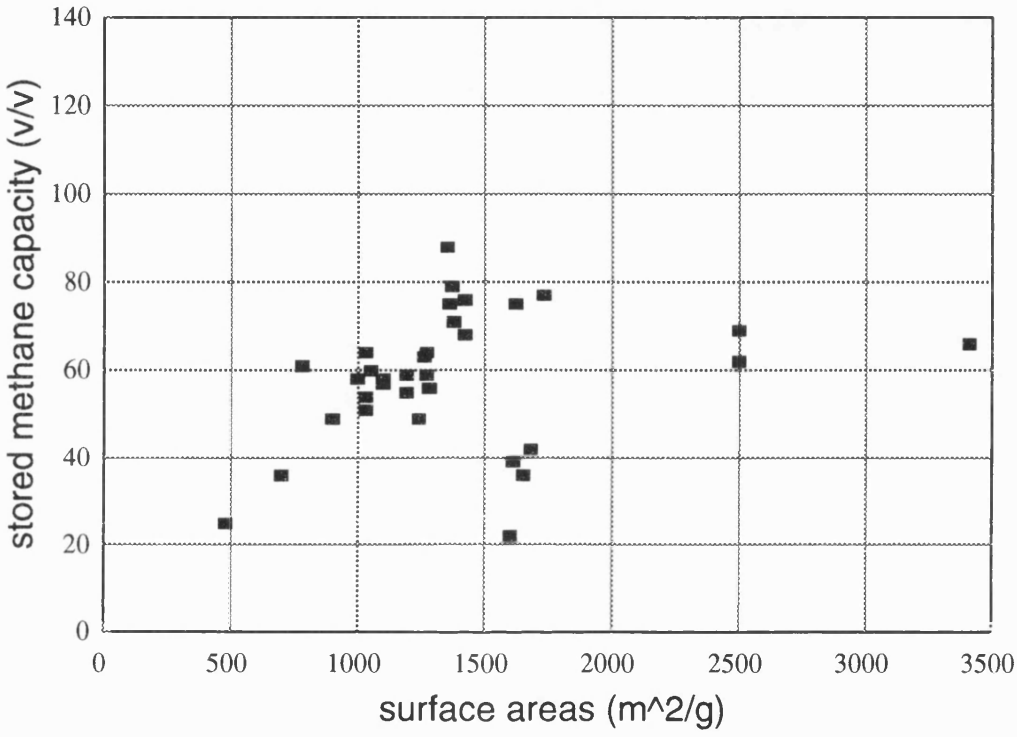

Figure 3.3 The stored volumetric methane capacities of commercial activated carbons at 298 K and 3.4 MPa (from Parkyns and Quinn, 1995)

SECTION B

EXPERIMENTAL WORK

CHAPTER 4 MATERIAL DESIGN

4.1 MOLECULAR SIMULATION

Based on idealised pore models and independently-determined interacting parameters for gases and solids, nowadays it is possible with the help of computers to calculate the adsorbate density in the model pore and to predict the adsorption isotherm. This kind of simulation is still limited to a simple gas-solid system and the estimated isotherms do not quite fit with the measured isotherms. But the technique can provide valuable insights into the adsorption processes by elucidating the influence of factors involved, optimising the pore structure for a particular application, and predicting the maximum adsorption capacity for a given adsorptive and adsorbent based on the idealised models.

In this study, the grand canonical ensemble Monte Carlo method was used to simulate the methane adsorption in a slit at a supercritical temperature of 298 K. The influences of pore wall thickness, pore width, inter-layer spacing and carbon atom density on the adsorbed methane density were investigated. Based on the generated numbers of methane molecules in a model pore, the volumetric methane capacities of carbon monoliths with the configuration of hexagonal close-packed spheres (HCPS), to model monolithic carbons derived from powders, and close-packed parallel cylinders (CPPC) to model monoliths made from carbon fibres were estimated.

4.1.1 Pore Model

High resolution transmission electron microscope lattice images of activated carbons, especially KOH activated mesophase spherules (Yoshizawa, *et al*, 1994) (Fei, *et al*, 1994) and cokes (Marsh, *et al*, 1982) (Wennerberg, 1978) have shown that microporous activated carbons have a kind of pore network consisting of cage-like voids which are separated by a random skeleton of 1~3 graphite sheets. Therefore, the pore model used in this study for microporous carbons was expressed as a slit between a number of carbon layer planes as shown in Figure 4.1. The pore models used before were usually a slit

between single graphite sheets (Matranga, *et al*, 1992) or between two graphite slabs (Aukett, *et al*, 1992). The influences of pore microstructure have been little studied in the past. In this study the effects of pore wall thickness (number of carbon layers in pore wall and inter-layer spacing) and skeletal carbon density as well as pore width on the adsorbed methane density were studied by the grand canonical Monte Carlo molecular simulations.

4.1.2 Potential Energy

Methane molecules in a pore interact with each other and with the carbon atoms in pore walls. There is no electrostatic force in the methane-carbon system. The force which brings about methane adsorption on carbon surface mainly comes from London "dispersion" force, together with short range repulsive force. Therefore, the Lennard-Jones (Steele, 1974) pair potential function, $\varepsilon_{LJ}(r)$, was adopted to represent the methane-methane molecule interaction, while the overall interaction energy between a methane molecule and a pore wall may be represented by summing up all the individual pair potentials.

Methane-Methane Interaction

The Lennard-Jones 12-6 pair potential between two methane molecules with a separated distance r, $\varepsilon_{LJ}(r)$, was expressed as

$$\varepsilon_{LJ}(r) = 4\varepsilon_{ff}\left[\left(\frac{\sigma_{ff}}{r}\right)^{12} - \left(\frac{\sigma_{ff}}{r}\right)^{6}\right] \text{---------- (4.1)}$$

where σ_{ff} is the collision diameter of methane molecule and ε_{ff} is the depth of potential well of a pair of methane molecules. The intermolecular potential energy, $\Phi_{LJ}(r)$, of a particular configuration will be the sum of the pair potentials in equation 4.1 over all the methane molecules in the simulation system:

$$\Phi_{LJ}(r) = \sum \varepsilon_{LJ}(r_{ij}) \text{ ---------- (4.2)}$$

Here r_{ij} is the distance between methane molecules i and j. This calculation of $\Phi_{LJ}(r)$ without a cut and shifted boundary condition would be enormous. Therefore, the intermolecular potential energy was truncated by a cut and shifted distance r_c in the simulation:

$$\Phi_{LJ}(r) = \sum(\varepsilon_{LJ}(r) - \varepsilon_{LJ}(r_c)) \qquad r < r_c$$
$$= 0 \qquad r > r_c \text{ ---------- (4.3)}$$

This approximation will reduce the number of neighbour simulation boxes and save computing time considerably.

Methane-Pore Wall Interaction

The potential energy between a methane molecule and one of the pore walls, $\Phi_{sf}(z)$, was given by summing up all the individual pair potentials between methane molecules and carbon atoms in the pore walls (Mays, *et al*, 1994) (Mays, 1996):

$$\Phi_{sf}(z) = 2\pi A_c \varepsilon_{sf} \sigma_{sf}^2 \left\{ \sum_{i=0}^{n-1} \left[\frac{2}{5} \left(\frac{\sigma_{sf}}{z + i\Delta} \right)^{10} - \left(\frac{\sigma_{sf}}{z + i\Delta} \right)^{4} \right] \right\} \text{ --------- (4.4)}$$

where n (n > 1) is the number of carbon layers in each pore wall; z (z > 0) is the inter-nuclear separation between a methane molecule and carbon atoms in the nearest carbon layer as shown in Figure 4.1; H is the pore width; A_c is the number density of carbon atoms in carbon layer plane; Δ is the inter-layer spacing; ε_{sf} and σ_{sf} are the pair potential parameters for methane-carbon interaction which were calculated by the Lorentz-Berthelot combining rules from σ_{ff} (methane molecule collision diameter), ε_{ff} (methane-methane pair potential well), σ_s (collision diameter of carbon atoms) and ε_s (potential well for a pair of carbon atoms):

$$\sigma_{sf} = \frac{1}{2}(\sigma_s + \sigma_{ff}) \text{ ---------- (4.5a)}$$

$$\varepsilon_{sf} = \sqrt{\varepsilon_s \varepsilon_{ff}} \text{ ---------- (4.5b)}$$

The interaction of a methane molecule with the second pore wall can be expressed as

$$\Phi_{sf}(H-z) = 2\pi A_c \varepsilon_{sf} \sigma_{sf}^2 \left\{ \sum_{i=0}^{n-1} \left[\frac{2}{5} \left(\frac{\sigma_{sf}}{(H-z)+i\Delta} \right)^{10} - \left(\frac{\sigma_{sf}}{(H-z)+i\Delta} \right)^{4} \right] \right\} \quad \text{--------- (4.6)}$$

So the total external potential experienced by a methane molecule within the model pore is

$$\Phi_{sf} = \Phi_{sf}(z) + \Phi_{sf}(H-z) \quad 0 < z < H \quad \text{---------- (4.7)}$$

4.1.3 Parameters For The Simulation

Lennard-Jones Parameters

Literature values of Lennard-Jones parameters used in this simulation were summarised as in Table 4.1.

Table 4.1 Lennard-Jones parameters for grand canonical ensemble Monte Carlo molecular simulation

	σ(nm)			ε/k_B(K)		
	C-C	CH_4-CH_4	C-CH_4	C-C	CH_4-CH_4	C-CH_4
Aukett, *et al* (1992)	0.339	0.381	0.3605		148.1	64.4
Tan&Gubbins (1993)	0.34	0.381	0.3605	28	148.12	64.4
this study	0.34	0.381	0.3605	28	148.12	64.4

Note: k_B is the Boltzmann constant

The sensitivity of the adsorbed methane density to the variations of the number of carbon layers, n, from 1 to 10, of the carbon atom density, A_c, from 38.18 to 31.90 atom nm^{-2}, of the inter-layer spacing, Δ, from 0.3354 to 0.352 nm and of the pore width, H, from 0.7415 to 3.4085 nm were investigated. The inputs of pore parameters for the each simulation are listed in Table 4.2.

Table 4.2 Inputs of pore parameters for grand canonical ensemble Monte Carlo molecular simulation at 298 K

code	n	Δ (nm)	A_c (atoms nm^{-2})	H (nm)
H1	2	0.3354	38.18	0.7415
H2	2	0.3354	38.18	1.1225
H3	2	0.3354	38.18	1.5035
H4	2	0.3354	38.18	1.8845
H5	2	0.3354	38.18	2.6465
H6	2	0.3354	38.18	3.4085
N1	1	0.3354	38.18	1.1225
N2	2	0.3354	38.18	1.1225
N3	3	0.3354	38.18	1.1225
N4	4	0.3354	38.18	1.1225
N5	5	0.3354	38.18	1.1225
N10	10	0.3354	38.18	1.1225
Δ1	2	0.3354	38.18	1.1225
Δ2	2	0.3450	38.18	1.1225
Δ3	2	0.3520	38.18	1.1225
Δ4	2	0.3820	38.18	1.1225
Δ5	2	0.3980	38.18	1.1225
ρ1	2	0.3354	31.90	1.1225
ρ2	2	0.3354	33.67	1.1225
ρ3	2	0.3354	37.04	1.1225
ρ4	2	0.3354	38.18	1.1225

Note: n is the number of the carbon layers in each pore wall; H is the slit width; A_c is the carbon number density of the pore wall and Δ is the interlayer spacing between the carbon layers.

The carbon number density A_c was calculated from the skeletal carbon density ρ_c by the following expression:

$$A_c = N_A \rho_c \Delta M_c^{-1} \quad \text{---------- (4.8)}$$

where M_c is the carbon atomic weight and N_A is the Avogadro's number. The interlayer spacing of pure graphite, $\Delta = 0.3354$ nm, is fixed in the calculation of A_c while the skeletal carbon density ρ_c (g cm^{-3}) varies. The ρ_c values used in the simulation are referred to graphite density, 2.268 g cm^{-3}, which is calculated from the hexagonal model structure, an arbitrary value of 1.89 g cm^{-3} , which assumes one carbon atom is removed away from each carbon hexagon ring, and the values of 2.0 g cm^{-3} and 2.20 g cm^{-3} which are typical values for activated carbons measured by helium pycnometry.

Methane Fugacity

The simulation of methane adsorption was performed at high pressures, so the fugacity instead of pressure should be used for calculation of the chemical potential of the bulk fluid. The Peng-Robinson equation of state was used to calculate the fugacity (Peng and Robinson, 1976). The fugacity and compressibility values for methane at 298 K in a range of pressures from 0.1 to 50 MPa were calculated and the results are illustrated in Figure 4.2.

4.1.4 Grand Canonical Ensemble Monte Carlo Simulation

Methane adsorption in a slit was simulated by the grand canonical ensemble Monte Carlo method at a constant chemical potential (μ), temperature (T) and pore volume of simulation cell ($V = HL^2$, where L is the simulation cell dimension parallel to pore walls). The simulation started with an initial configuration of methane molecules in the pore that was generated from the methane bulk density for the corresponding temperature and pressure. A new configuration was generated by making small trial displacements of methane molecules as well as by adding and subtracting according to the statistical mechanics principles (Aukett, *et al* 1992). The new configuration was compared with the previous ones and only those that reduced significantly the chemical potential of the system

were chosen. By monitoring the mean number of methane molecules in the pore, the total interaction potential within the pore was compared with the chemical potential in the bulk phase to judge whether an equilibrium was reached or not. During the calculation of the configuration energy, a periodic boundary condition was used to overcome the surface effect of the pore wall in x-y plane. For the Lennard-Jones pair function, it should be large enough for $L = 6\sigma_{ff}$ to perform a simulation without a disturbance from the periodic lattice (Allen and Tildesley, 1987). $L = 10\sigma_{ff}$ was used in this simulation. The intermolecular potentials were truncated by a cut and shift distance $r_c = 5\sigma_{ff}$ in order to reduce the simulation time. The simulation was performed by a Pascal program (Mays, *et al*, 1994) in a Sun SPARC station using an operating system Solaris 2.3 — UNIX version 4.

4.2 ADSORBED METHANE DENSITY

The output from the molecular simulation was the reduced methane number density ρ^*_{CH4} which was given by

$$\rho^*_{CH4} = \frac{N\sigma_{ff}^3}{HL^2} \qquad (4.9)$$

where N is the equilibrium number of methane molecules in the simulation cell of volume HL^2. Therefore, the volumetric density ρ_{CH4} of the adsorbed methane in the model pore was converted from the reduced number density ρ^*_{CH4} by the expression:

$$\rho_{CH4} = \frac{10^{21} M_m \rho^*_{CH4}}{N_A \sigma_{ff}^3} \quad (g\ cm^{-3}) \qquad (4.10)$$

where N_A (molecules per mole) is Avogadro's number, M_m (grams per mole) is the molecular weight of methane, and σ_{ff} (nm) is methane molecule diameter.

It should be pointed out that the methane density ρ_{CH4} was calculated based upon the pore width expressed as H. But the real space available to methane molecules is smaller than H. The reduced local density values of methane in the range of z from 0 to $0.75\sigma_{sf}$ and from

H - $0.75\sigma_{sf}$ to H, as shown in Figure 7.1 (refer to Chapter 7), are zero, which means that methane molecules can not reach the regions occupied by the carbon atoms. The mean adsorbed methane density in the model pore was under-estimated by equation 4.10 based upon the pore width of H. The real available space is difficult to define because the interface between the adsorbate and the pore wall is ambiguous and it varies with pressure. Aukett, *et al* (1992) used the H_{snap} referring to the available space defined as:

$$H_{snap} = H - \sigma_s \quad \text{---------- (4.11)}$$

where σ_s is the diameter of a carbon atom "hard sphere". Another definition on the effective pore width was given by Quirke and Tennison (1996) as followings:

$$H_{chem} = H - 2Z_o - \sigma_{ff} \quad \text{---------- (4.12)}$$

where Z_o , as illustrated in Figure 4.3, is the distance at which the interaction potential between a methane molecule and a carbon wall is zero.

In this study the available pore width, H_a , was defined as:

$$H_a = H - \sigma_{sf} \quad \text{---------- (4.13)}$$

in which σ_{sf} = 0.3605 nm is the distance between a methane molecule and a carbon atom calculated by Lorents-Berthelot rules from the equation 4.5a. The adsorbed methane density corrected by H_a was given by

$$\rho_a = (H/H_a)\rho_{CH4} \quad \text{---------- (4.14)}$$

Replacing H_a with H_{snap} and H_{chem} into equation 4.14, the corrected average methane density ρ_{snap} and ρ_{chem} can be obtained similarly. The difference between ρ_a, ρ_{snap}, ρ_{chem} and ρ_{CH4} becomes smaller with increasing of pore width H (see Figure 7.2 in Chapter 7).

4.3 METHANE CAPACITY

Normally the adsorptive capacity of a gas on an adsorbent is expressed based on a mass unit. But in the application of adsorbed natural gas for natural gas vehicles where the storage space is limited, it is the volumetric capacity that is critical in deciding the vehicle driving range. In what follows in this thesis, all methane capacities refer to volumetric bases unless specially annotated. Assuming that carbons consist of assemblies of non-interacting slit pores, the simulation results (ρ^*_{CH4}) of methane adsorption in a single slit can be converted into volumetric methane capacity, V, by the following expression:

$$V = \frac{24.465\times10^{24}\rho^*_{CH4}}{N_A\sigma^3_{ff}}\frac{H}{(H + (n - 1)\Delta)} \quad \text{----- (4.15)}$$

where all the symbols have the same meanings as before. V is in the unit of the volume of methane at 298 K and 0.1MPa per volume of adsorbent. σ_{ff} (methane molecule diameter) is in the units of nanometer.

In a real application of natural gas storage by adsorption on porous carbons, the adsorbents need to be packed into a container in which interparticle voids are inevitable even if the adsorbents are in monolithic forms. Therefore, the methane storage capacity per volume of the space in a container, V_s, was given by

$$V_s = (1 - \theta)V + \frac{PZ_o\theta}{P_oZ} \quad \text{---------- (4.16)}$$

where θ is the void fraction; Z and Z_o is the compressibility of methane at pressure P and P_o (a reference pressure, 0.1 MPa). The first term in equation 4.16 accounts for adsorbed methane in pores and the second term accounts for stored methane in interparticle voids.

The configurations of hexagonal close-packed spheres (HCPS) and close-packed parallel cylinders (CPPC) were proposed to model the carbon monoliths made from

powders and fibres, respectively as shown in Figure 4.4 and 4.5. The void fractions in HCPS and CPPC configurations were calculated using well know geometrical relationships:

$$\theta_{HCPS} = \frac{\cos 30^\circ \bullet \cos 35^\circ - \pi/6}{\cos 30^\circ \bullet \cos 35^\circ} = 0.26 \quad \text{---------- (4.17)}$$

$$\theta_{CPPC} = \frac{\cos 30^\circ - \pi/4}{\cos 30^\circ} = 0.094 \quad \text{---------- (4.18)}$$

The methane capacities on model carbon monoliths (including void-free monolith, the HCPS and the CPPC) at 298 K and 3.4 MPa were estimated from the simulation results for a given pore width while skeletal carbon density and pore wall thickness were varied.

4.4 SUMMARY

The main objectives of the molecular simulation in this study are to find out what is the optimal pore size for methane adsorption at a given temperature (298 K) and pressure (3.4 MPa), to investigate the influences of the carbon pore structure on the adsorbed methane density, and to estimate the methane storage capacity based upon model carbons. Simulations based upon the idealised models can not precisely predict methane adsorption isotherms but they can provide very useful guides on tailoring the carbon pore structure to be suitable for adsorbed natural gas storage. The molecular simulations are also used to study the feasibility of the industrial target which is 150 v/v of delivered methane capacity for adsorbed natural gas application as a clean fuel for vehicles.

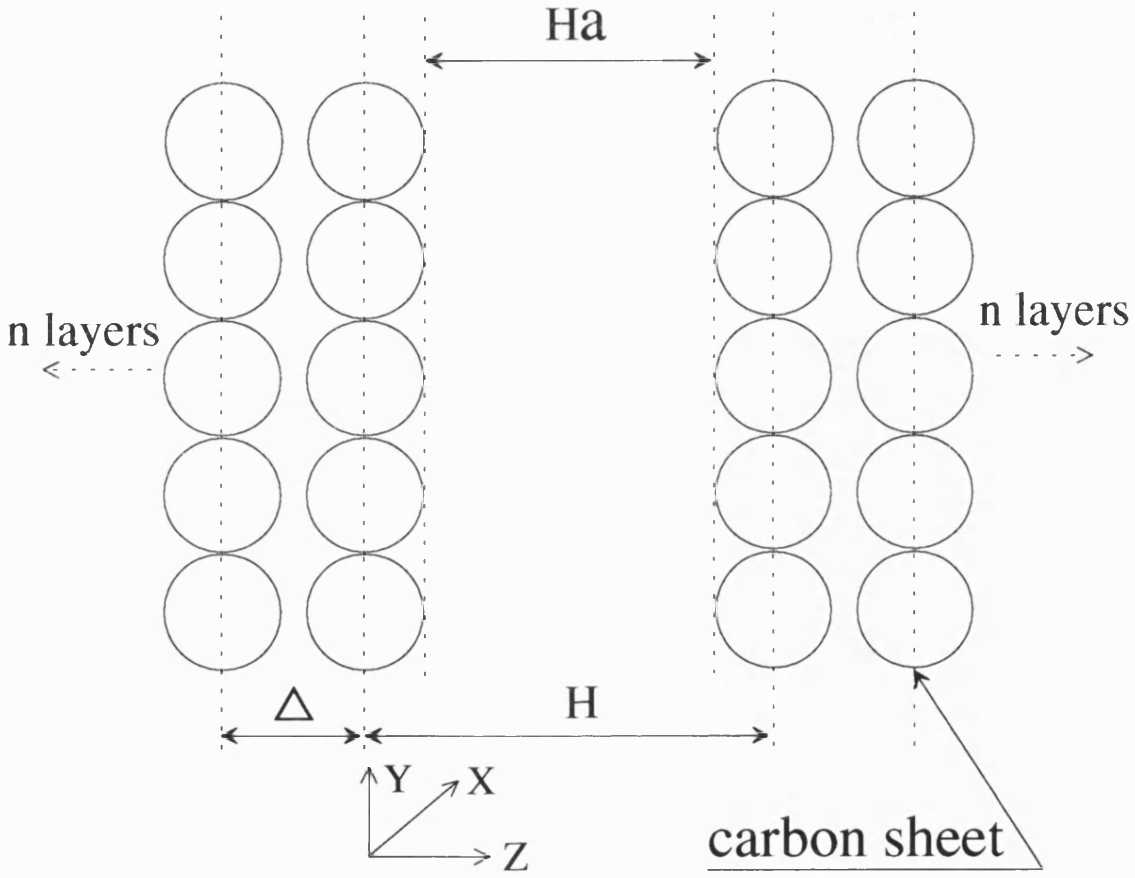

Figure 4.1 The slit model pore for molecular simulation of methane adsorption at 298 K. H is defined as a physical pore width; H_a is defined as an effective pore width; Δ is an interlayer spacing and n is the number of carbon layers within each pore wall.

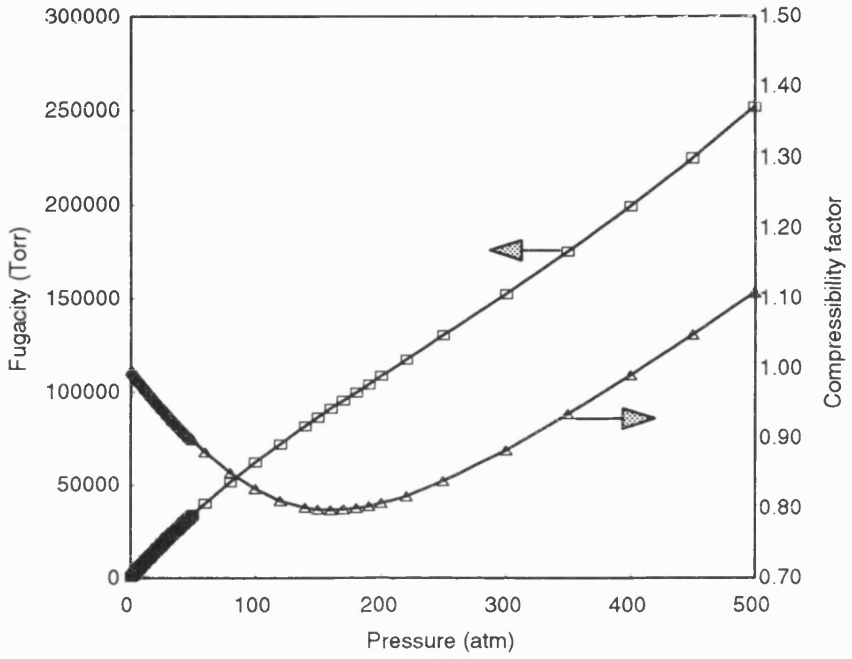

Figure 4.2 The fugacity and the compressibility of methane at 298 K calculated by the Peng-Robinson equation (Peng and Robinson, 1976).

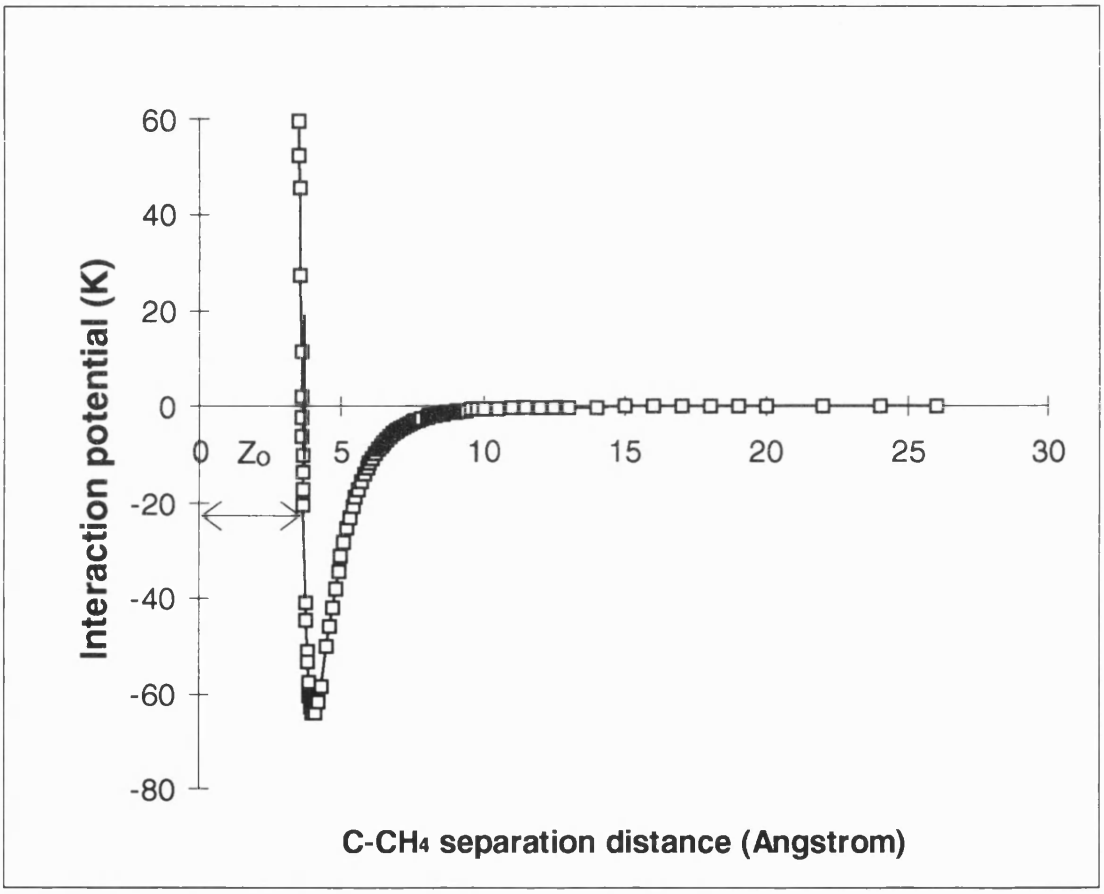

Figure 4.3 Lennard-Jones potential between a methane molecule and a carbon atom at 298 K.

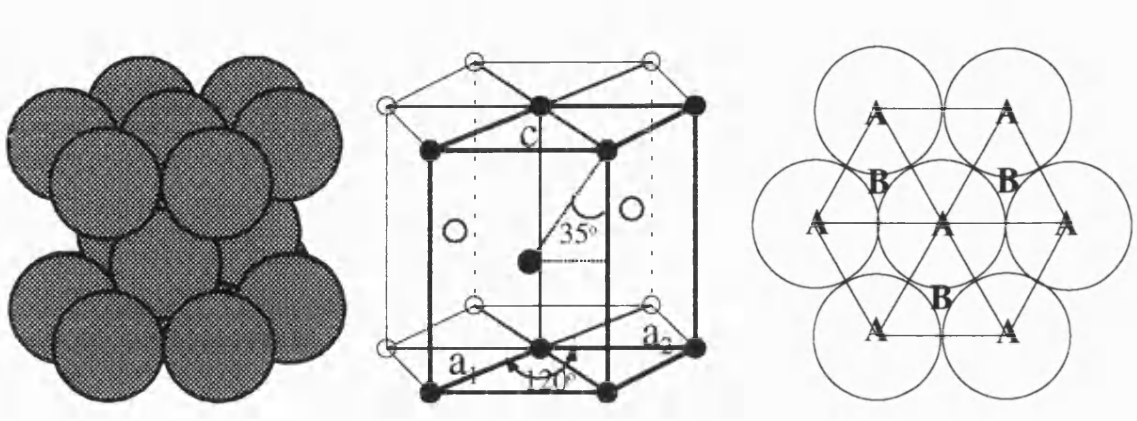

Figure 4.4 The hexagonal close-packed spheres (HCPS) configuration to model monolithic carbon made from activated carbon powders

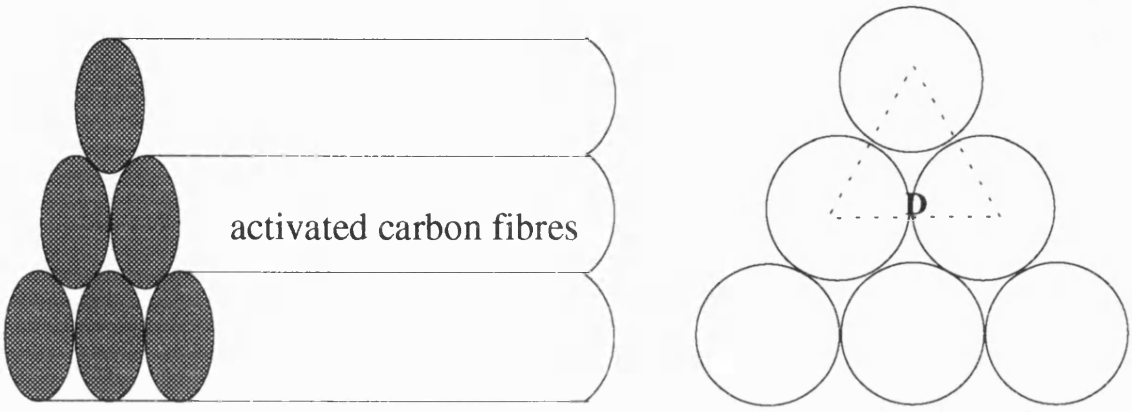

Figure 4.5 The close-packed parallel cylinders (CPPC) configuration to model the monolithic carbon made from activated carbon fibres.

CHAPTER 5 DEVELOPMENT OF MATERIALS

5.1 SELECTION OF RAW MATERIALS

The pore structure and pore size distribution in carbon adsorbents are essentially dependent on the carbon precursors, although they may, to some extent, be tailored by adjusting processing parameters such as heat treatment temperature, heating rate, reaction time, reactants and carbon burn-off. Therefore, it is very important to select appropriate raw materials for producing a special activated carbon such as a highly microporous monolith with less volumes of mesopores and macropores and interparticle voids.

The basic structural unit within carbon materials is layer planes or lamella based on the graphite lattice which contains both σ- and π- bonded atoms in hexagonal two-dimensional networks. However, the variations in the degree of hexagonal unit cell imperfection are considerable. These imperfections include dislocations, vacancies and heteroatoms such as hydrogen, oxygen, nitrogen and sulphur. The variation in extent and the stacking arrangement of these lamellae result in a multitude of carbon forms.

Generally, carbon materials can be classified into two groups: non-graphitizable carbons and graphitizable carbons. However, the majority of carbon materials are classified as being near to one or the other of the extremes. Non-graphitizable carbons are formed from parent materials such as the cellulose or lignin components of wood, nuts and nutshells, or the specific cross-linked structures (C-O-C bonding) of low rank coals (peat, lignite and brown coal). Synthetic polymers such as phenol formaldehyde resin, polyfurfuryl alcohol and polyvinylidene chloride also yield non-graphitizible carbons. These parent materials are composed of macromolecules in nature and do not fuse or melt during the pyrolysis/heat treatment/carbonisation process. The resultant pore structure retains much of the original random arrangement of packed lamellae. This irregular stacking, together with a high degree of cross-linkage, creates a large microporosity which has a specific surface area in the range of 500 to 1500 $m^2 g^{-1}$ (Marsh and Kue, 1989). Graphitizable carbons are usually derived from raw materials such as petroleum pitch, coal tar pitch, coking bituminous coals, polynuclear aromatic compounds and polyvinyl chloride. These materials pass through a

fluid phase stage during high temperature treatment. The degree of parallel stacking may be improved and the layers can be made less defective at this stage. Non-graphitizable parent materials can be easily developed into porous adsorbents simply by carbonisation and activation by steam or carbon dioxide, but the pore size distributions of these carbons are often wide because of the inherent cellular structure in the case of wood or nutshell raw materials and the relics of the original plant structure in the case of low rank coals. The presence of mesopores and macropores is undesirable in highly microporous monoliths. So it is difficult to produce carbon adsorbents with both high density and high micropore volumes from such parent materials. On the other hand, graphitizable raw materials are not readily developed into porous adsorbents since they go through a fluid stage.

Considering the requirement of a high micropore volume and the relationship between pore structure in final carbons and raw material, meso-carbon microbeads were selected as a precursor to develop activated carbons for natural gas storage while other raw materials like lignite, petroleum coke, phenolic resin, waste paper and coconut shell were also investigated in general. The preparation of activated carbons from various precursors by different techniques are detailed in the following sections. A summary is presented in Table 5.1

Table 5.1 Summary of activated carbons produced in this work

precursors	activating agents	physical forms	section
meso-carbon microbeads	CO_2	disc	5.2.4
meso-carbon microbeads	KOH	powder	5.2.5
		monolith	5.6.3
meso-carbon microbeads	K_2CO_3	powder	5.2.6
petroleum coke	KOH	powder	5.3
lignite	KOH	powder	5.4
waste paper	H_3PO_4	disc	5.5
coconut shell	air	monolith	5.6.4
phenolic resin	CO_2	monolith	5.6.1
AX-21 carbon powder	KOH	monolith	5.6.2

5.2 ACTIVATED CARBONS MADE FROM MESO-CARBON MICROBEADS

5.2.1 Meso-carbon Microbeads

The technical term "meso-carbon microbeads" was introduced by Honda, *et al* (1973) to describe the meso-phase spheres generated from heat-treated pitch. The work by Auguie *et al* (1980) has shown that meso-carbon microbeads have the classical Brooks and Taylor (1968) structure which consists of polyaromatic hydrocarbon molecules oriented parallel to the equatorial axis of the sphere.

The meso-carbon microbeads used in this research were supplied by Kawasaki Steel Corporation in Japan. The properties of the meso-carbon microbeads determined by the supplier are as follows:

TI (toluene insoluble matter):	97.5 %
QI (quinoline insoluble matter):	91 %
VM (volatile matter):	9.3 %
Ash:	0.21 %
Mean particle size:	15.9 μm
Maximum particle size:	40 μm
Ratio by weight of C/H:	27.4

Further characterisation of the meso-carbon microbeads is presented in Chapter 8. The pre-oxidation, carbonisation and activation of meso-carbon microbeads are detailed in the following sections 5.2.2 – 5.2.6.

5.2.2 Pre-oxidation Of Meso-carbon Microbeads

As mentioned earlier meso-carbon microbeads have a spherical shape and lamellar structure of polyaromatic hydrocarbons. During high temperature treatment, the polycondensed aromatic rings may grow in the layer directions and the interlayer spacing between lamellae may shrink (Kodama, *et al*, 1992). Thus, the shape of the meso-carbon

microbeads is likely to be distorted due to this anisotropic growth and shrinkage. The consequence of this structural change makes the pellets made from meso-carbon microbeads deform. Therefore the meso-carbon microbeads were pre-oxidised in air in a muffle furnace in the temperature range 250 ~ 300 °C in order to prevent the deformation. The pre-oxidation temperature was selected following a thermogravimetry study (Chapter 8).

5.2.3 Carbonisation Of Meso-carbon Microbeads

The purpose of the carbonisation is to bring about condensation reactions and to drive off some volatile matter from precursors. Carbonisation creates some voids and defects within the carbonised material. The carbonisation temperature, heating rate, residence time and atmosphere will influence the following activation process as well as the pore structure of the final activated carbons.

The meso-carbon microbeads which have been pre-oxidised in air were carbonised in a horizontal tube furnace under a flow of nitrogen (5 dm^3 h^{-1}) by heating up to 600 °C and 1000 °C at 2 °C min^{-1} and soaking for 60 minutes. The carbonised meso-carbon microbeads were cooled naturally to a room temperature in flowing nitrogen.

5.2.4 Activation Of Meso-Carbon Microbeads By CO_2

Carbonised materials normally have a limited pore volume which is not sufficient for practical applications and therefore they need to be further improved by a process called activation. Activation is basically a process of partial gasification of carbon by oxidising gases (physical activation) or reaction with chemicals (chemical activation). Steam, carbon dioxide, air, or a mixture of them, are the common gases used in commercial physical activation. In this study, only carbon dioxide was used as an activating agent because it is believed (Molina-Sabio, *et al,* 1995) (Wigmans, 1989) (Rodriguez-Reinoso, *et al,* 1995) that carbon dioxide is better than steam in creating micropores, due to the fact that the carbon gasification rate (at 800 °C and 0.1 atm) by CO_2 is only one third of the rate of steam activation (Walker, *et al,* 1959). Faster reaction rate will result in more large pores based on a same carbon burn-off.

The carbonised meso-carbon microbeads were activated by CO_2 (5.5 $dm^3\ h^{-1}$) in a horizontal tube furnace in the temperature range 800 ~ 950 °C. The carbon burn-off was used as an index to express the degree of activation. The carbon burn-off (BO) is calculated by

$$BO = \frac{W_o - W_1}{W_o} \times 100\ \% \quad \text{---------- (5.1)}$$

where W_o is the original sample weight before activation and W_1 is the sample weight after activation.

5.2.5 Activation Of Meso-Carbon Microbeads By KOH

It has been reported by Wennerberg (1971), Marsh, *et al* (1984), Kasuh, *et al* (1988) that graphitizible carbon like petroleum coke could be transformed into highly microporous carbons by activation with potassium hydroxide (KOH). In this research, KOH activation of meso-carbon microbeads (MCB) was extensively explored. The influences of KOH/MCB ratio (from 0.1 to 8), heat treatment temperature (from 750 °C to 900 °C), reaction time (from 1 to 4 h) and reaction atmosphere (carbon dioxide and helium) on pore development were investigated. The results of these experiments are presented in Chapter 8.

The experimental procedure of KOH activation was as follows: KOH flakes (85% purity, containing 15% combined water, supplied by BDH, UK) were first ground into powder less than 0.25 mm in particle size. The KOH powders were uniformly mixed with meso-carbon microbeads in different ratios by weight. The KOH/MCB mixtures were compressed into discs (25 mm diameter x 10 mm) under a pressure of 40 MPa at a room temperature. It was necessary to keep the green discs in a desiccator to prevent them picking up moisture in air. Otherwise, the discs disintegrated. A heating rate of 2 °C min^{-1} and helium flow rate of 1.0 $dm^3\ h^{-1}$ were used. The temperature was first raised to 400 °C and maintained for 2 h to remove water from KOH so as to prevent unnecessary carbon burn-off by the steam generated at high temperatures from KOH. Subsequently, the temperature was elevated to different final temperatures and the samples were soaked for a certain time, depending on the requirement of the sample weight loss. It is crucially important to thoroughly leach the reacted KOH/MCB mixtures with boiling distilled water several times until the pH value of the leaching water was near to 7.0. To help the washing,

an ultrasonic water bath (Decon Ultrasonics Ltd.) was used to shake the flask containing the carbon sample for one hour. The washed samples were separated from the water by a centrifuge (Heraeus Sepatech) spinning at a speed of 5000 rpm for 20 min. Finally the activated carbon powders were dried in an oven (Townson & Mercer Ltd) for 8 h.

The degree of activation is expressed in carbon burn-off (BO) which is given by

$$BO = \frac{\theta W_o - W_1}{\theta W_o} \times 100\% \text{ ---------- (5.2)}$$

where W_o is the original sample weight including KOH and meso-carbon microbeads; W_1 is the sample weight after the sample was washed and θ is the fraction of meso-carbon microbeads in the original KOH/MCB mixture.

5.2.6 Activation Of Meso-Carbon Microbeads By K_2CO_3

K_2CO_3 was also used to activate meso-carbon microbeads in the same way as KOH. The weight ratio of K_2CO_3/MCBs = 5 was used, which was equivalent to KOH/MBC = 4 in terms of the potassium element content in the mixture, i.e. K/MCB = 2.8. The experimental procedures were similar to those using KOH as an activating agent.

5.3 KOH-ACTIVATED PETROLEUM COKE

An Indonesia petroleum coke (Dumai Petroleum Coke) was activated by KOH. The average composition of the green petroleum coke determined by the supplier is as follows:

Moisture (wt.):	0.62
Volatile matter (wt.):	14.54
Ash content (wt.):	0.34
Fixed carbon (wt.):	84.50

The coke was ground into powders with maximum particle size less than 0.125 mm. The coke powder was mixed with KOH powder in the ratio of KOH/coke = 4 by weight.

The KOH-coke mixture was heat-treated in a horizontal tubular furnace. The sample was purged with a high flow rate (29 dm^3 h^{-1}) of argon for 2 h and then the flow rate of argon was adjusted to 13 dm^3 h^{-1}. The heat treatment temperature was raised to 400 °C at 2 °C min^{-1} and maintained for 2 h. Then the temperature was further increased to 850 °C at 2 °C min^{-1} and maintained for 5 h. The reacted mixture was washed three times using distilled water and dried in an oven at 110 °C for 8 h. The sample was weighed on an electronic balance (Sartorius A200S) before and after the water washing. The carbon burn-off was calculated according to equation 5.2.

5.4 KOH-ACTIVATED LIGNITE

An Irish lignite (supplied by The Coal Research Establishment), which produces an non-graphitizing carbon, was used as a precursor for preparing porous carbons by KOH activation in order to compare with the graphitizible carbons derived from meso-carbon microbeads and petroleum coke. The lignite was analysed in the present work according to ASTM (American Society for Testing and Materials) standards for coals:

Moisture (ASTM D3302-91):	21.12 %
Ash content (ASTM D3174-93):	6.24 % (dry base)
Volatile matter (ASTM D3175-89a):	59.27 % (dry base)
Fixed carbon (ASTM D3174):	34.49 % (dry base)

The dried lignite was ground into powder with maximum particle size less than 0.125 mm. The lignite was mixed with KOH powder at the ratio of KOH/lignite = 2. The mixture was heated in helium (42 dm^3 h^{-1}) to 400 °C at 2 °C min^{-1} and maintained at 400 °C for 2 h. The temperature was further increased to 800 °C and maintained for 2 h. The reacted mixture was washed in the same way as the KOH/MCB mixtures. The carbon burn-off was calculated using equation 5.2 (θ represents the fraction of lignite in KOH/ lignite mixture).

5.5 H_3PO_4 ACTIVATED WASTE PAPER

An attempt was made to develop porous materials from office photocopy paper, as a source of cheap raw material, by chemical activation using H_3PO_4 solutions. The waste paper was cut into small pieces. The paper was mixed with 1.4 times H_3PO_4 solution by weight and was shredded in a food processor into a thick paste. The paste was kneaded at 150 °C for 2 h until its moisture content was about 40% by weight. The kneaded paste was compressed into a disc (65 mm diameter x 10 mm) under 40 MPa. The disc was heated up to 500 °C at 25 °C min^{-1} in argon (5.5 dm^3 h^{-1}) and maintained at 500 °C for 2 h. The residue was thoroughly washed by distilled water and dried in an oven. Burn-off values were calculated using equation 5.2. The paste was also directly heat treated without compressing into discs under the same conditions as mentioned above.

5.6 MONOLITHIC CARBONS

As mentioned in section 3.4, a suitable adsorbent for adsorbed natural gas application should be in monolithic form so as to reduce the interparticle voids. There are two strategies which can be considered to produce carbon monoliths as illustrated in Figure 5.1 I and II. The essential difference between the two procedures is whether the reformulating should be before or after the activation. In the procedure I, raw materials such as phenolic resin beads and meso-carbon microbeads can be easily reformulated into monolithic forms such as cylinders or discs without a binder. However, there are some problems in producing an uniform micropores monolith in this way. These problems are discussed in Section 8.5.1 (Chapter 8). In the procedure II, raw material is first transformed into microporous powder and then consolidated into a carbon monolith. Microporous powders lose their binding property after high temperature treatment, therefore, a binder is needed to consolidate the powders into a monolith. The advantage and disadvantage of the procedure II over the procedure I is discussed in Section 8.5.2 (Chapter 8).

The monolithic activated carbons made from phenolic resin, AX-21 carbon powder, KOH-activated meso-carbon microbeads and coconut shell are described in the following section 5.6.1 – 5.6.4

5.6.1 Carbon Monolith Made From Phenolic Resin Carbon

The phenolic resin beads FRD3656 (particle size less than 0.25 mm), supplied by Borden (UK) Ltd, were used as a non-graphitizing raw material to develop porous carbon monoliths by CO_2 activation. As phenolic resin contracts during a high temperature treatment, it is necessary to thermally set the resin at 300 °C in nitrogen for 1.0 h in order to prevent the deformation of the phenolic resin monolith. The pre-heated phenolic resin was ground into fine powder and then compacted into a disc (13 mm diameter x 5 mm) under a pressure of 1847 MPa at a room temperature. The pre-heat treatment temperature should not exceed 350 °C. Otherwise , the phenolic resin particles were not able to be compacted into an integrate monolith again. The resin pellet was carbonised at 800 °C for 1 h in argon and then activated by CO_2 at 950 °C for 12 h.

Alternatively the phenolic resin beads were thermally moulded into a cylinder (30 mm diameter x 20 mm) under a pressure of 40 MPa at the temperature of 150 °C for 30 min. The well-formed cylinder was heat-treated in argon at a very slow heating rate (0.1 °C min^{-1}) to 800 °C in a tube furnace and kept at 800 °C for 1 h. The carbonised cylinder was then activated by CO_2 (29 dm^3 h^{-1}) at 950 °C for 12 h. The piece density (ρ_p), the carbonisation yield (η) and the activation burn-off (BO) of the phenolic resin cylinder were calculated using the following expressions:

$$\rho_p = \frac{W_0}{\pi d^2 h} \quad \text{---------- (5.3)}$$

$$\eta = \frac{W_1}{W_0} \times 100\ \% \quad \text{---------- (5.4)}$$

$$BO = \frac{W_1 - W_2}{W_1} \times 100\ \% \quad \text{---------- (5.5)}$$

where d (cm) is the diameter of the resin cylinder; h (cm) is the thickness of the resin cylinder; W_o (g) is the original sample weight, W_1 (g) is the sample weight after carbonisation and W_2 is the sample weight after activation. The values of d and h were

physically measured using a microcalliper (reading error ± 0.001 mm) and the values of W_o, W_1 and W_2 were measured on an electronic balance (precision ± 0.0001 g).

5.6.2 Carbon Monolith Made From AX-21 Carbon Powder

AX-21 carbon is a highly microporous activated carbon made by reacting petroleum pitch with an excess of potassium hydroxide. The original patents by Wennerberg (1971) for this process was assigned to Amoco who produced the PX and GX series of carbons in the 1970s. The manufacturing right was then licensed to Anderson Development Co in 1985, who branded their product as AX-21 carbon, but the production was suspended at the end of the 1980s. Now a similar product named Maxsorb is commercially available from The Kansai Coke and Chemicals Co. Ltd., Japan (Otawa., *et al*, 1992). AX-21 carbon has a very high surface area (~ 2500 m^2 g^{-1}) and a large micropore volume (~ 1.0 cm^3 g^{-1}) and it can adsorb more methane per unit mass of carbon than most other activated carbons (Parkyns and Quinn, 1995). But the low packing density (~ 0.27 g cm^{-3}) of AX-21 carbon powder makes it less competitive in terms of volumetric methane capacity. In this study an effort was made to improve its volumetric methane capacity by consolidating AX-21 carbon powder into a monolith with phenolic resin as binder.

As shown in diagram in Figure 5.2 (a), the dried AX-21 carbon powder was thoroughly mixed in a mortar with phenolic resin beads FRD3656 (particle size less than 0.25 mm) in the weight ratios of AX-21/FRD3656 from 83%, 69%, 56% and 45%, respectively. The mixtures were compacted into discs (30 mm or 25 mm diameter) under a pressure of 40 MPa at a temperature of ca. 150 °C in a mounting press (Metaserv Model C190 with a heating and cooling mantle). Thermal compression is essential because the phenolic resin becomes soft and its binding property is improved at an elevated temperature. It is also important to maintain the compressing pressure and temperature for a certain time (normally 10 min) to allow the internal parts of the discs become well-cured. The compacted discs were heat-treated in argon at 800 °C (heating rate 2 °C min^{-1}) for 2.0 h. Some carbonised monoliths were activated by CO_2 at 800 °C for 1.0 h in a tubular furnace. The bulk density and carbonisation yield of the monolith were calculated using equation 5.3 and 5.4.

5.6.3 Carbon Monolith Made From KOH-Activated Meso-Carbon Microbeads

The KOH activated meso-carbon microbeads are microporous powders. The tapping bulk density of the activated meso-carbon microbeads is around 0.27 g cm^{-3}. They have a similar problem of a low packing density as AX-21 carbon powder. Therefore, the activated meso-carbon microbeads with different burns-off were also consolidated into monoliths following the procedure in Figure 5.2 (b). The activated meso-carbon microbeads with carbon burn-off of 40 %, 48 % and 66 % were mixed with 30 wt % phenolic resin beads. The mixtures were compacted into discs (25 mm diameter x 5 mm) at 40 MPa and 150 °C for 20 min. The discs were heat-treated in nitrogen at 800 °C for 1.0 h. The bulk density and the carbon yield of the carbon monolith after the heat treatment were calculated using equations 5.3 and 5.4.

5.6.4 Carbon Monoliths Made From Coconut Shells

Coconut shell is a commonly used raw materials in manufacturing granular activated carbons (Laine, *et al*, 1989) for gas adsorption, water treatment and gold recovery, etc. In this study coconut shells are used to produce monolithic carbons for adsorbed natural gas storage. The preparation process is illustrated in the flow diagram in Figure 5.3. Raw coconut shells were dried at 110 °C for 8 hours. The soft layers of the shells were scraped off. Large pieces of coconut shells were crushed down to small granules less than 5 mm in size. The granular coconut shells were ground into powders in a hammer mill to pass through a 300 mesh sieve. The fine powders were compacted into a cylinder (20 mm diameter x 15 mm) under a high pressure of 1275 MPa at an ambient temperature. The green cylinder was carbonised at 750 °C (2.0 °C min^{-1}) for 1.0 h in a horizontal tube furnace in flowing nitrogen (5.5 dm^3 h^{-1}). The carbonised coconut carbon cylinder was activated by air-cycling oxidation, that is, repeated treatment in air (200 °C, 1.0 h) and in nitrogen (750 °C, 0.5 h) for many times. The number of this cycling treatment depends on the final carbon burn-off required. The bulk density of activated carbon monolith and the carbon burn-off of the activation process are calculated using expressions 5.3 and 5.5.

Commercially available coconut activated carbon powder, NV5M325 supplied by Eurocarb Products Ltd, UK, was also used to produce carbon monolith by using thermal compacting method which is similar to the procedure described in Figure 5.2(b); but higher temperature (500 °C) and pressure (170 MPa) were adopted in order to increase the bulk density of carbon monoliths.

5.7 SUMMARY

In this study, graphitizible materials (meso-carbon microbeads, petroleum coke) and non-graphitizible materials (phenolic resin, lignite, wastepaper and coconut shell) were used to produce microporous carbons by either physical (CO_2, air) activation or chemical activation (KOH, K_2CO_3, H_3PO_4). Monolithic carbons were fabricated from AX-21 carbon powder, KOH-activated meso-carbon microbeads and coconut shell carbons. The activated carbons prepared in this study were characterised by nitrogen adsorption, mercury intrusion, helium pycnometry, X-ray diffraction, infrared absorption and scanning electron microscopy techniques. Some carbon monoliths were evaluated by methane adsorption measurement. These analysing methods and instruments are presented in the following Chapter 6.

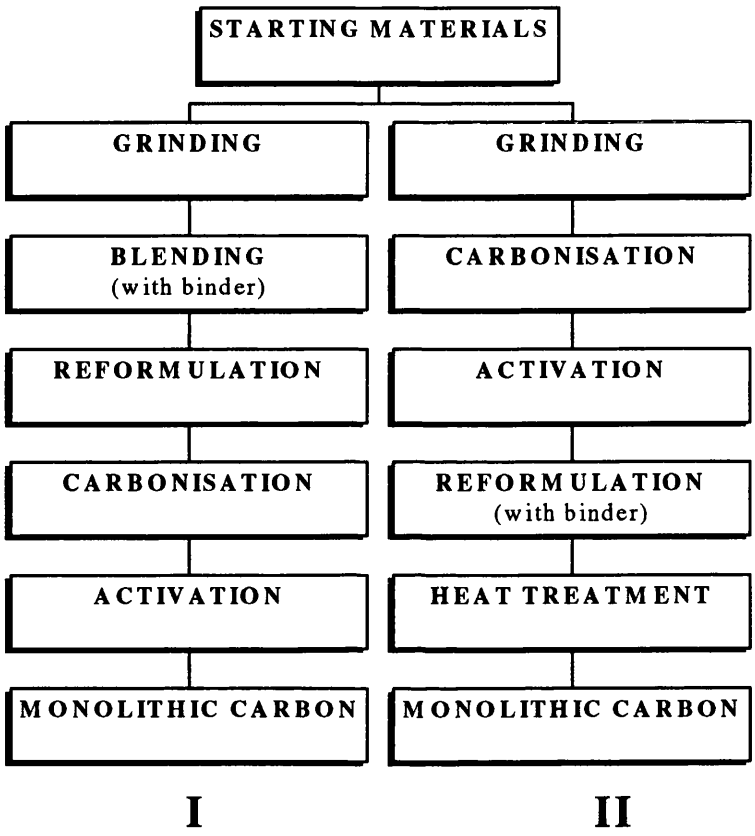

Figure 5.1 The general diagram of monolithic carbon production; I is a procedure to manufacture monolithic carbon by direct carbonisation and activation of pre-formed carbon block; II is a procedure to produce a microporous carbon monolith by consolidating microporous carbon powders.

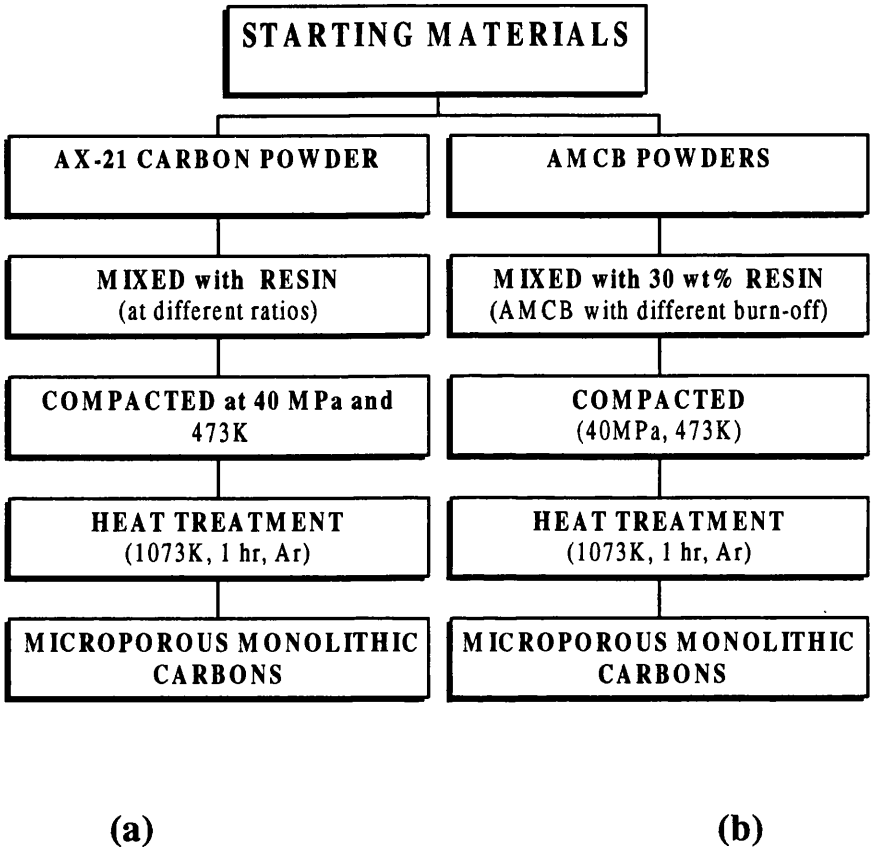

Figure 5.2 Schematic diagrams of the preparation of monolithic carbons from (a) AX-21 carbon powder and (b) KOH-activated meso-carbon microbeads (AMCB).

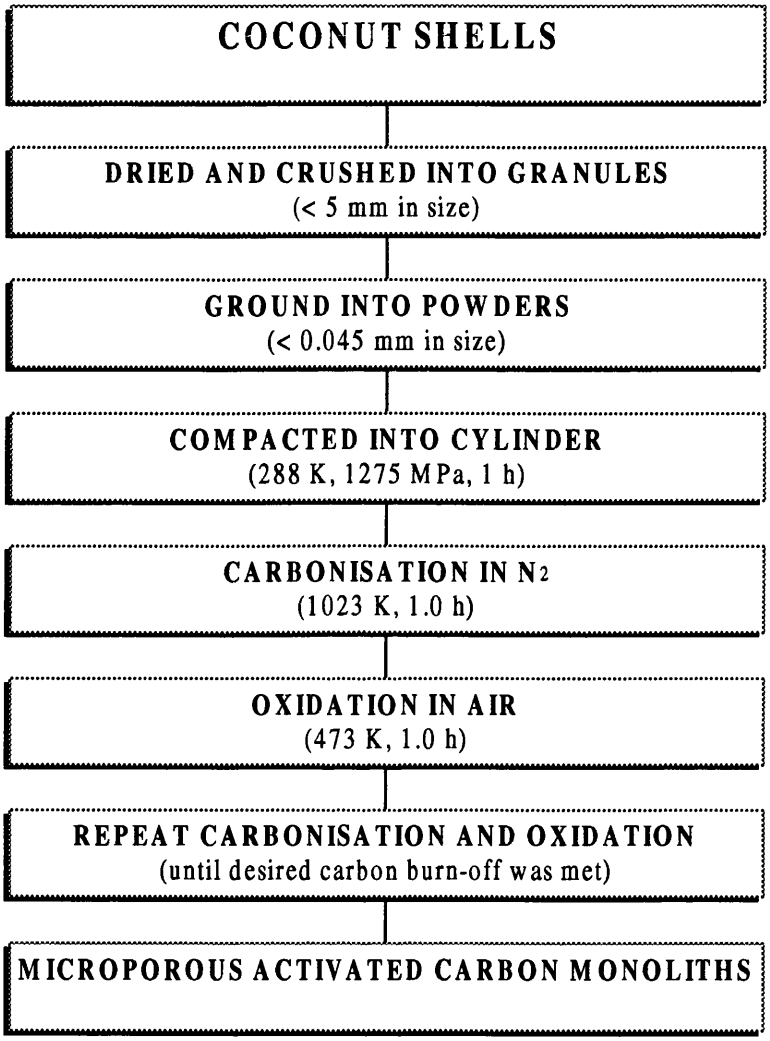

Figure 5.3 Schematic diagram of the preparation of monolithic carbons from coconut shells.

CHAPTER 6 CHARACTERISATION OF MATERIALS

6.1 CHARACTERISATION OF ACTIVATED CARBONS BY GAS ADSORPTION METHODS

Gas adsorption and/or desorption are the most widely used methods to characterise porous carbons. The important applications include physical adsorption for the determination of surface area and pore size distribution and chemisorption followed by temperature-programmed desorption for the estimation of the active sites or reactivity of carbons (Fritz and Hüttinger, 1992). The most extensively-used adsorptive is nitrogen at its normal boiling temperature of 77.2 K, which has been standardised in ASTM (C819)-77, although some other gases such as carbon dioxide, argon and low molecular weight hydrocarbons can also be used as adsorptives for special purposes. For example, when the pore sizes of carbons are similar to the dimensions of nitrogen molecules, activated diffusion effects become prominent, caused by constrictions in the microporous network (McEnaney, 1989) due to the fact that nitrogen molecules at 77.2 K have insufficient kinetic energy to penetrate fully into very small pores. In this case, carbon dioxide is often used as an adsorptive to measure isotherms at 195 K or 298 K (Rodriguez-Reinoso, *et al*, 1989).

Based on thousands of recorded isotherms for a wide range of gas-solid systems, Brunauer, Deming, Deming and Teller (Brunauer, *et al*, 1940) proposed a classification now called the BDDT or Brunauer classification, which embraced nearly all types of known adsorption and/or desorption isotherms. The BDDT classification, as illustrated in Figure 6.1, linked with the IUPAC classification of pore size (see page 21), has played a very important role in analysing isotherms and in understanding adsorption and desorption processes. According to the shapes of the measured isotherms, some preliminary estimation can be made, for instance, the presence of porosity including mesopores and macropores. These preliminary estimates can often indicate which analytical methods are appropriate for analysing specific isotherms.

Gas adsorption can be recorded gravimetrically or volumetrically. With the fast development of computer technologies for both hardware and software, computer

controlled instruments for the measurement of isotherms volumetrically and the following data analysis have become more popular. In this study, nitrogen adsorption and desorption isotherms of all samples were carried out on a Micromeritics ASAP 2000 instrument, which can automatically analyse adsorption isotherms by the most commonly-used methods to calculate parameters such as surface area, pore volume, pore size distribution and average pore width. The general background and the validity of these methods are critically reviewed in the following section.

6.1.1 A Critical Review Of The Methods Used For Isotherm Analysis

The quantity of adsorptive present on a carbon sample at equilibrium depends on the adsorption temperature (T) and pressure (P) and the nature of both the carbon and the adsorptive. The relationship can be expressed as $n = f(P, T, \text{carbon, adsorptive})$, where n represents the moles of adsorptive adsorbed per gram of carbon. For a given gas-carbon system at a constant temperature, the amount of gas adsorbed, i.e. the adsorption isotherm, is only related to the pressure: $n = f(P)_{T,\ \text{carbon,}\ \text{adsorptive}}$. Seeking the expression of various functions f leads to many empirical or semi-empirical equations. Only the most often quoted methods and those used in this thesis are reviewed in the following discussions.

6.1.1.1 The Langmuir Theory

The heterogeneity in both pore structure and pore surface of activated carbons makes any kind of modelling very difficult without a certain degree of simplification. Langmuir assumed: (i) that the surface of a solid is composed of a two-dimensional array of energetically homogenous sites; (ii) that only one molecule can be adsorbed per site and saturation of the surface is reached on completion of the monolayer; (iii) that the adsorbed molecules do not interact with one another. Then, postulating a dynamic equilibrium in which the condensing rate of gas molecules on bare surface sites is equal to the evaporating rate of adsorbed molecules from occupied sites, Langmuir derived the following equation:

$$\frac{n}{n_m} = \frac{BP}{1 + BP} \qquad \text{(6.1)}$$

where n_m is the monolayer capacity and n is the amount of adsorbate at pressure P; B is a constant. Equation 6.1 can be transformed into:

$$\frac{P}{n} = \frac{P}{n_m} + \frac{1}{n_m B} \quad \text{---------- (6.2)}$$

By plotting P/n against P, the monolayer capacity n_m can be estimated from the slope of the straight line. Specific surface areas of carbons can be calculated from the monolayer capacity.

6.1.1.2 The Brunauer-Emmett-Teller (BET) Method

BET Equation

Extending Langmuir's evaporation-condensation mechanism to a multi-layer adsorption process by assuming: (i) that except for first adsorbate layer, the adsorption heats of other layers are equal to the molar condensation heat of the adsorptive; (ii) that except for first adsorbate layer, evaporation and condensation conditions are identical (iii) that when the number of adsorbate layers becomes infinite the adsorption pressure approaches the saturation pressure of the adsorptive, Brunauer, Emmett and Teller reached the well known BET equation:

$$\frac{n}{n_m} = \frac{C(P/P_o)}{(1-P/P_o)[1+(C-1)P/P_o)]} \quad \text{---------- (6.3)}$$

where n, n_m and P have the same meanings as in equation 6.1; P_o is the saturation pressure of adsorptive and C is a constant given by

$$C = \frac{a_1 v_2}{a_2 v_1} \exp[(q_c - q_L)/RT] \quad \text{---------- (6.4)}$$

where a_1 and a_2 are the condensation coefficients of first and second layers of adsorbate; ν_1 and ν_2 are the frequency of oscillation of first and second layer of adsorbate in the direction normal to carbon surface; q_c is the isosteric adsorption heat and q_L is the condensation heat of adsorptive. Assuming $a_1\nu_2/a_2\nu_1 = 1.0$, the net heat of adsorption, i.e. $q_c - q_L$, can be estimated from equation 6.4 which becomes $q_c - q_L = RT \ln C$, but the value of $a_1\nu_2/a_2\nu_1$ can be quite different from 1.0, ranging from 0.2 to 20 (Gregg and Sing, 1982). So the net adsorption heat calculated from the above equation should only be recognised as an approximation. Equation 6.3 is often rewritten as a linearised BET equation:

$$\frac{P}{n(P_o - P)} = \frac{1}{n_m C} + \frac{C-1}{n_m C}\frac{P}{P_o} \quad \text{---------- (6.5)}$$

By plotting $\frac{P}{n(P_o - P)}$ against $\frac{P}{P_o}$ from the measured isotherm in a certain range of relative pressure (usually from 0.02 to 0.2), a straight line should be obtained. The monolayer capacity n_m and the constant C can be calculated from the intercept Y_{int} and the slope S of the straight line by the expressions:

$$n_m = \frac{1}{S + Y_{int}}$$

and

$$C = \frac{S + Y_{int}}{Y_{int}}$$

The specific surface area, A, can be calculated by

$$A = n_m N_A A_m \quad \text{---------- (6.6)}$$

where N_A is the Avogadro number; A_m is the cross sectional area of an adsorbate molecule in the completed monolayer and n_m is the monolayer capacity which can be obtained either from BET equation or from Langmuir equation.

The Validity Of The BET Equation

The BET method is the most commonly-used method to calculate surface areas of porous carbons or non-porous carbons both in the carbon industry and in the academic world of carbon research. Perhaps it is just because of the overwhelming popularity of BET equation that its assumptions, limitations and validity are easily ignored. It must be pointed that the application of BET equation without any discrimination can sometimes lead to a wrong conclusion, especially in the case of highly microporous carbons.

The Implications Of Surface Area

The surface area obtained by the BET method should not be used as a true value to represent geometrical surface area of a carbon no matter if it is porous or non-porous. This conclusion is based on the following considerations. Firstly, the cross section area (A_m) of the adsorbate molecules in a completed monolayer in equation 6.6 is estimated from the bulk liquid density of the adsorptive at its normal boiling point. The configuration of the adsorbate molecules can be quite different from that in bulk liquid state. The adsorbate molecules tend to be localised on preferred lattice sites of the carbon (Ricca, *et al*, 1971), which will make the packing density of the adsorbate less than the bulk liquid density of the adsorptive. Therefore, the proportion of the uncovered geometrical surface is greater than the value expected from the bulk liquid configuration. This argument can be easily justified by using different adsorptives on a same adsorbent. The same surface area should be obtained, but unfortunately, significantly different values were obtained (Davis, *et al*, 1947). Secondly, there is always a problem to separate the completion of monolayer from the building-up of multilayers, which poses questions about what relative pressure range should be used to calculate the monolayer capacity n_m from the BET equation. Especially when the micropore filling process occurs, the BET method may give unrealistically high surface areas (sometimes up to 4000 $m^2 g^{-1}$), that are greater than the maximum theoretical value of 2630 $m^2 g^{-1}$ which is calculated by accounting both sides of a single layer of a graphite plane as surface area (Everett and Powl, 1976). Thirdly, the constriction caused by activated diffusion or molecular sieve effects in ultra-micropores makes the BET surface area more controversial. The above uncertainties and divergence about n_m and A_m should always be borne in mind when making comments on BET surface areas. Other criticisms of the BET

model are: (a) the variation of adsorption heat with surface coverage suggests that the surfaces of most solids are energetically heterogeneous rather than homogeneous; (b) the horizontal interactions between the adsorbed molecules are not negligible at a high surface coverage; (c) the number of adsorbed molecule layers is finite instead of infinite.

Even though the BET method is subject to a lot of criticisms, it is still a very useful method to evaluate the adsorption properties of carbons when applied properly, that is, by treating BET surface area as a relative rather than absolute specific surface of carbons available to adsorptives and regarding it as a parameter reflecting the degree of pore structure development. In many applications, performances of activated carbons are successfully correlated with their BET surface areas. For instance, adsorbed methane capacity of activated carbon is proportional to BET surface area deduced from nitrogen adsorption isotherm at 77.2 K (Mullhaupt, *et al*, 1992) (Parkyns and Quinn, 1995). In this thesis, BET surface area was used as a process control parameter to evaluate properties of the produced activated carbons for adsorbed natural gas applications.

6.1.1.3 The Micropore Filling Theory Of Dubinin

The Dubinin-Radushkevich (D-R) and Dubinin-Astakhov (D-A) Equations

If carbons contain many micropores which have dimensions that are no more than a few molecular diameters, the potential fields from the opposite pore walls will enhance the interaction energy between the carbon pore walls and the adsorptive molecules. This enhancement in interaction energy results in a significant increase in adsorption at very low relative pressures, which cannot be successfully interpreted by multi-layer adsorption mechanisms such as the BET theory.

Dubinin and his colleagues proposed the theory of volume filling of micropores, in which micropores are filled with adsorbate at low relative pressures by a process similar to, but not identical with, capillary condensation, rather than layer-by-layer building up of a film on pore walls as suggested by the BET theory. The extent of micropore filling is defined as $\theta = V/V_o$ where V represents the pore volume which has been filled at the relative pressure

of P/P_o and V_o is the total micropore volume. This definition of θ is analogous to Langmuir's concept of the occupied site fraction, $\theta_l = n/n_m$. The difference between θ and θ_l is that the former is related to degree of volume filling and the latter is defined as the fraction of surface coverage. Dubinin proposed that micropore filling is a function of adsorption potential, u (reflecting the properties of adsorbents) and what he called a similarity constant, β (representing the similarity of adsorptives to an arbitrary standard adsorptive — benzene for which $\beta = 1$). Therefore, the degree of micropore filling is expressed by $\theta = f(u, \beta)$. By adapting Polanyi's adsorption potential expression $u = RT\ln(P_o/P)$ and assuming that the pore size distribution is Gaussian, Dubinin and Radushkevich arrived at the following empirical expression:

$$\theta = \exp[-\delta(u/\beta)^2] \quad \text{---------- (6.7)}$$

Substituting θ and u into the above expression, the familiar form of the well known D-R equation is obtained:

$$V = V_o \exp\{ - \delta\beta^{-2} [RT \ln (P_o/P)]^2 \} \quad \text{---------- (6.8)}$$

where δ is a constant related to the breadth of the assumed Gaussian distribution of micropore volumes. Provided that the density of adsorbate is constant and equal to the density of the bulk liquid, the equation 6.8 can be rewritten as

$$W = W_o \exp\{ - \delta\beta^{-2} [RT \ln (P_o/P)]^2 \} \quad \text{---------- (6.9)}$$

or

$$\ln W = \ln W_o - \delta\beta^{-2}(RT)^2 \ln^2(P_o/P) \quad \text{---------- (6.10)}$$

where $W = V\rho_L$ and $W_o = V_o\rho_L$; W is the amount of adsorbate at pressure P; W_o is the amount of adsorbate when the micropore filling is complete; and ρ_L is bulk liquid density of adsorptive at its normal boiling temperature. Plotting an adsorption isotherm lnW against $\ln^2(P_o/P)$ should give a straight line from which the micropore volume V_o can be calculated from the intercept of the extrapolated straight line.

The D-R equation is applicable to a variety of adsorption systems over a wide range of adsorption pressures. But occasionally a deviation from linearity in a D-R plot is observed, especially in the case of activated carbons which usually have a very wide pore size distribution. Capillary condensation in mesopores may cause the D-R plot to bend upwards in a region near saturation pressure and an activated diffusion effect in ultra-micropores (less than 0.5 nm) may make D-R plot bend downwards in a region of very low relative pressure. In order to extend the scope of D-R equation, Dubinin and Astakhov put forward a more general expression (the D-A equation) by introducing a third variable, m, into the D-R equation, which gives

$$V = V_o \exp\{ - \delta\beta^{-m} [RT \ln (P_o/P)]^m \} \quad \text{---------- (6.11)}$$

By selecting the value of m, D-A equation can give a better linearity than the D-R equation.

There are many other modified equations based on Dubinin's pore volume filling theory. For example, the two-term Dubinin equation is:

$$V = V_{o,1} \exp[- (u/E_1)^2] + V_{o,2} \exp[-(u/E_2)^2] \quad \text{---------- (6.12)}$$

in which the pore structure is composed of two sub-systems with each having its own characteristic free energy of adsorption, E_1 and E_2. Going further in this direction, Stoeckli (1977) proposed that the overall isotherm could be regarded as the summation of many individual pore groups, with each group obeying the D-R equation, that is

$$V = \sum_i V_{o,i} \exp[-(u / E_i)^2] \quad \text{---------- (6.13)}$$

The benefit of dividing a pore system into individual pore groups is that the equation can give a better fitting to experimental data, but the disadvantage is that the equation itself becomes more complicated.

Deviations From D-R And D-A Equations

The deviations from the D-R or D-A equation are often observed in the case of existence of condensation and activated diffusion effect when applied to N_2 (77.2 K) adsorption isotherms of activated carbons with mesopores and ultra-micropores (McEnaney and Mays, 1989). In this study micropore volumes of activated carbons were extracted from the transformed D-A equation curves based on the linear part of the curve which excludes condensation and activation diffusion effects.

Another question on the micropore volume from Dubinin methods is that the density of adsorbate in pores is assumed to be the same as the bulk density of the adsorptive at its normal boiling temperature. This assumption has to some extent over-simplified the real situation since the adsorbate density in micropores varies with pore size according the molecular simulation (Aukett, *et al*, 1992). When the pore sizes are only in the dimension of several adsorptive molecules, the adsorption process will be quantized. The configuration in pores accommodating integral layers of adsorbate molecules would give a higher packing efficiency than those that do not. Additionally the interaction between the adsorbate and the pore wall is quite different from the bulk liquid. Grand canonical ensemble Monte Carlo molecular simulation of nitrogen adsorption in a slit-shaped carbon pore, Aukett, *et al* (1992) concluded that using the simulated average density of the adsorbed nitrogen, that is 0.93 g cm^{-3}, in the pores less than 2 nm gave a better estimation of micropore pore volume than using the bulk density of nitrogen, i.e. 0.808 g cm^{-3}. In this study, the value of 0.93 g cm^{-3} was used to calculate micropore volumes of the fabricated activated carbons from the linearised D-A equation.

6.1.1.4 Horvath - Kawazoe's Pore Size Distribution

Using thermodynamic argument, Horvath and Kawazoe (1983) derived the following simple expression:

$$RT\ln(P/P_o) = U_o + P_a \quad \text{---------- (6.14)}$$

where U_o is the expression of the adsorbent-adsorbate interactions and P_a is an implicit function of the adsorbate-adsorbate-adsorbent interactions. Assuming that the pores in microporous materials can be modelled as slits between graphite layers, the interaction energies of U_o and P_a are given by

$$U_o = \frac{N_A N_s A_s}{2\sigma^4}\left[-\left(\frac{\sigma}{r}\right)^4 + \left(\frac{\sigma}{r}\right)^{10} - \left(\frac{\sigma}{H-r}\right)^4 + \left(\frac{\sigma}{H-r}\right)^{10}\right] \quad (6.15)$$

$$P_a = \frac{N_A N_f A_f}{2\sigma^4}\left[-\left(\frac{\sigma}{r}\right)^4 + \left(\frac{\sigma}{r}\right)^{10} - \left(\frac{\sigma}{H-r}\right)^4 + \left(\frac{\sigma}{H-r}\right)^{10}\right] \quad (6.16)$$

where N_A is the Avogadro number,

N_s is the atom number per unit area of the adsorbent surface,

N_f is the number of molecules per unit area of the adsorbate,

σ is the distance between an adsorptive molecule and the adsorbent surface at zero interaction energy,

H is the distance between the nuclei of the first surface graphite layers,

r is the perpendicular distance to the adsorbent surface, and

A_s and A_f are the Kirkwood-Muller expressions:

$$A_s = \frac{6mc^2\alpha_s\chi_f}{\frac{\alpha_s}{\chi_s} + \frac{\alpha_f}{\chi_f}} \quad \text{---------- (6.17)}$$

$$A_f = \frac{3mc^2\alpha_f\chi_f}{2} \quad \text{---------- (6.18)}$$

in which α_s and α_s are the polarizabilities of the adsorptive molecule and the adsorbent atom; χ_f and χ_s are the magnetic susceptibilities of the adsorptive molecule and the adsorbent atom; m is the mass of an electron and c is the velocity of light.

Therefore, the average potential value between the pore wall, which depends on the absolute value of the distance, r, can be calculated by :

$$RT\ln(P/P_o) = \frac{N_A(N_sA_s + N_fA_f)}{2\sigma^4(H-d)}\int_{d/2}^{H-d/2}\left[-\left(\frac{\sigma}{r}\right)^4 + \left(\frac{\sigma}{r}\right)^{10} - \left(\frac{\sigma}{H-r}\right)^4 + \left(\frac{\sigma}{H-r}\right)^{10}\right]dr$$

---------- (6.19)

where $d = d_f + d_s$ in which d_f and d_s are the diameters of the adsorptive molecule and the adsorbent atom, respectively. The integration of expression 6.19 gives the H-K equation:

$$RT\ln(P/P_o) = \frac{N_A(N_sA_s + N_fA_f)}{\sigma^4(H-d)}\left[\frac{\sigma^4}{3(H-d/2)^3} - \frac{\sigma^{10}}{9(H-d/2)^9} - \frac{\sigma^4}{3(d/2)^3} + \frac{\sigma^{10}}{9(d/2)^9}\right]$$

---------- (6.20)

where H should be greater than d.

H-K equation gives the function of adsorption pressure P with respect to pore width H. In order to extract a pore size distribution from the H-K equation, an experimental adsorption isotherm is needed. The amount, n, adsorbed at a relative pressure, P/P_o, is interpreted as the amount adsorbed in pores with widths less than or equal to H. Thus a plot of V ($V = nV_m$, here V_m is the molar volume of the adsorbate) against H is a cumulative pore volume curve. The differential pore size distribution, dV/dH, can be deduced from the slope of V versus H curve.

6.1.2 Nitrogen Isotherm Measurement On Micromeritics ASAP-2000

ASAP-2000 is one of a series of Micromeritics instruments for volumetrically measuring gas adsorption on solid materials. The ASAP-2000 system has been designed to run isotherm measurement automatically. The principle of the measurement is to fill a manifold (its exact volume is known) by an adsorption gas and then to dose the gas on to the sample. The gas pressures in the manifold before and after the dosing were recorded. The amount of gas adsorbed each time on the sample was then calculated from the pressure difference. In this way, a series of points against relative pressures at a constant temperature were obtained following a pre-set pressure table. The instrument consists of two separate

internal vacuum systems (two rotary pumps and one molecular drag pump) — one for sample degas and the other for sample analysis. The ultimate vacuum can reach ca. 1.0 μm Hg, which enables it to measure an isotherm down to very low relative pressures. In this study nitrogen was used as an adsorptive and helium as a back-filling gas. Both gases used are 99.99 % pure, supplied by British Oxygen Company Limited.

Calibration Of ASAP-2000 By Standard Materials

The instrument ASAP-2000 was regularly calibrated by the certified reference materials M-11-01 (Sterling FT-G2700) and M11-02 (Vulcan 3-G2700). The certified reference materials, supplied by Laboratory of the Government Chemist (LGC), are two of a series of graphitised carbon blacks which are developed and certified under a collaborative project organised by the Society of Chemical Industry (SCI), the International Union of Pure and Applied Chemistry (IUPAC) and the National Physical Laboratory (NPL), intending for the calibration of instruments used for the determination of specific surface area. The certified surface areas of M11-01 and M11-02 are 11.2 $m^2 g^{-1}$ (standard deviation 0.8 $m^2 g^{-1}$) and 71.3 $m^2 g^{-1}$ (standard deviation 2.7 $m^2 g^{-1}$), respectively, calculated by BET equation (taking 0.162 nm^2 as the cross-sectional area of a nitrogen molecule) from the adsorption isotherm in the relative pressure ranging from 0.04 to 0.172.

The sample used for the calibration should be representative to the bulk quantity of material supplied by LGC. So a rotating riffling instrument (Spinning Riffler Microscal Ltd) was used to divide the sub-sample down to about 2 grams for M11-01 and 0.5 gram for M11-02. The sample quantity of each measurement was decided by the minimum surface area (greater than 20 m^2) required by ASAP2000.

It is very important to completely degas a sample under a high vacuum before analysis. The degas condition of the reference materials was set according to the recommended procedure provided along with the samples. The degas temperature was set to 305 °C. The sample was degassed at 305 °C for 8 h. The final pressure inside the sample holder was 4 μm Hg (the ultimate pressure was required to be less than 7.6 μm Hg). The nitrogen adsorption isotherms on the standard samples were volumetrically measured at the

normal boiling temperature of nitrogen. The collected data were automatically recorded onto a connected computer. The measured surface areas of standard materials M11-01 and M11-02 are 10.82 $m^2 g^{-1}$ and 69.32 $m^2 g^{-1}$ which are within the permitted standard deviation from the certified values.

Nitrogen Adsorption On Experimental Samples

According to the researches done by Quinn (1990), Parkyns and Quinn (1995), Heal (1990), and Mullhaupt, *et al* (1992) the methane storage capacity on porous carbons is linearly proportional to the BET surface areas or micropore volumes derived from the nitrogen adsorption isotherms. Therefore, the activated carbon samples used and developed in this study were tested on ASAP2000 as a primary criterion to evaluate their suitability for natural gas storage. As most of the carbons included in this study are microporous, it is necessary to degas the experimental samples at a high temperature for a longer time comparing to the degas conditions for the reference materials. Except the raw meso-carbon microbeads (the degas temperature is 105 °C), all other carbon samples were degassed at 300 °C for 12 h. The final pressures within the sample tubes after the degas processes were less than 4.0 μm Hg.

Special care was taken when powder samples were degassed in order to prevent the powders from being sucked into the pipe system due to a sudden increase of vacuum. Slow degas mode was used first and then switched to fast mode after the vacuum reached 500 μm Hg.

Microporous carbons have very high surface areas. A small error in sample weight would lead to a large error in surface area. All samples were measured on an electronic balance (Sartorius A200S), accurate to 1.0×10^{-4} grams, which would give an error of 0.3 $m^2 g^{-1}$ if the surface area were 3000 $m^2 g^{-1}$. A degassed sample weight was calculated from the difference of the sample tube with and without the sample in it. In order to avoid the influence from the gas phase inside the tube, the empty tube was degassed and back-filled with helium each time in the same way as was done for the tubes containing samples.

The completely cleaned samples were put on to the analysis port. The nitrogen adsorption and/or desorption isotherms at 77.2 K on the samples were automatically measured and analysed by the installed software. Near the end of this study, ASAP2000 was upgraded to ASAP2010 by installing another two small scale pressure transducers (10 mm Hg and 1.0 mm Hg) which can detect the nitrogen relative pressure down to 1.0×10^{-7}. Two carbon samples (AX-21 carbon powder and AX-21 monolith) were re-measured on ASAP2010. The results showed that there were no significant differences between ASAP2000 and ASAP2010 in terms of surface area and pore volume except ASAP2010 provided more data points in a very low relative pressure region.

6.1.3 CH_4 And CO_2 Isotherm Measurements On A High Pressure Electronic Microbalance

Nitrogen adsorption is a very useful method to compare activated carbons in the first place. But methane capacities can still not be precisely predicted from the independent carbon properties such as specific surface areas, pore volumes and bulk densities. Hence methane adsorption isotherms on some promising microporous carbons produced in this research were tested on a high pressure electronic microbalance at the University of Alicante in Spain.

The balance is Sartorius 4406 as shown in Figure 6.2. The precision of the balance is ± 0.3 mg while the full scale is 200 mg. The highest pressure is 4.0 MPa. The pressure transducer error is ± 0.004 bar. A thermocouple was fixed in the sample chamber to monitor the temperature change during the methane adsorption. The temperature reading error is ± 0.1 °C. The temperature of the sample chamber was maintained constant by the circulating water from a thermostatic water tank. The signals of pressure, temperature and weight change were automatically recorded onto a connected computer.

Before the adsorption measurement, a leak test was done by filling the whole system with methane at 40 bar and then monitoring the pressure change after the inlet and outlet valves were closed. After 8 h, the pressure did not drop. The buoyancy effect was minimised by a non-porous counter-weight (ca. 0.05 ml and 100 mg) which has a bulk

density similar to that of activated carbon. A blank run (without a carbon sample) was carried out by following the same procedure as would be used for a specimen.

All experimental samples were dried in an oven at 110 °C for 4 h. The sample was further degassed in the sample chamber under a vacuum (using a rotary vacuum pump) for one hour before the actual sample weight was taken. Then the methane was introduced into the system by a needle valve. The adsorption pressure was increased step by step from 1.0 bar to 40 bar. Each point was taken until the variation of the sample weight was less than the balance precision, i.e. < 0.3 mg. Normally 30 min was long enough for the equilibrium. The temperature in the sample chamber went up about one degree due to the adsorption heat released during the methane adsorption. But the temperature dropped back very quickly to the original level.

CO_2 adsorption isotherms at 298 K on some activated carbon samples were performed on the high pressure microbalance in the same way as methane adsorption measurement was done. The CO_2 isotherms were analysed by the BET and the D-A equations. The results were compared with those obtained from nitrogen adsorption isotherms at 77.2 K.

6.1.4 Delivered Methane Capacity Of Compacted AX-21 Carbon Powder

Purpose Of This Test

The delivered volumetric methane capacity is a key criterion to evaluate the performance of activated carbons for natural gas storage. The adsorbed natural gas for the envisaged application in natural gas fuelled vehicles requires the carbon adsorbent to have both a large micropore volume and a high bulk density. But a high microporosity and a high bulk density of activated carbons are always difficult to achieve. Using a binder to consolidate microporous powders such as AX-21 carbon can increase its bulk density by two fold (Quinn, 1990), but this increment in bulk density can only be achieved in sacrifice of storage space because very little pore volume can be expected from the binder.

In this study an attempt was made to pack highly microporous AX-21 carbon powder into a specially designed cylinder under elevated pressures without adding any binder. The volumetric delivered methane capacity on the packed AX-21 carbon powder was directly measured by recording the volume of methane released at 0.1 MPa from the cylinder after equilibrium with methane at 3.4 MPa and 298 K.

Experimental Description

The methane loading and unloading test equipment is shown in Figure 6.3. The dried AX-21 carbon powder was compressed under pressures of 15 MPa and 20 MPa into the cylinder as shown in Figure 6.4. The cylinder (inside diameter is 80 mm and depth is 60 mm) contains three layers of sieve screen (300 mesh) on the top of the AX-21 carbon powder, a perforated steel disc (∅80 x 9.7 mm) on the top of the sieve screen and a gas sealing lid which has a gas inlet/outlet in the middle. The AX-21 carbon powder was packed under no pressure and with application of 15 MPa and 20 MPa pressure into the cylinder each time. The packed cylinder was dried in a vacuum oven at 150 °C for 8 h in order to drive out the pre-adsorbed moisture and other gases. After cooling down to the room temperature in a desiccator, the cylinder was connected on the test line as shown in Figure 6.3. The cylinder was immersed in a thermostatic water tank. The cylinder was evacuated for 2 h before methane or helium was filled into the system. The pressure transducer (Sensotec 110G0020M) was calibrated by the standard pressure calibration instrument (Budenberg).

Prior to packing AX-21 carbon powder into the cylinder, the volume of the empty system was determined by filling the empty cylinder with methane to a number of pressures and then releasing to atmospheric pressure each time. The methane volume released, V_{off}, was measured by a wet gas meter and V_{off} can be expressed by:

$$V_{off,i} = V_{sys} [(P_i / Z_i) - 1] \quad \text{---------- (6.21)}$$

Where V_{sys} is the volume of the empty system including the inner volume of the cylinder which contains a gas distribution disc and no AX-21 carbon and the volume of the pipeline

between the two needle valves; P_i is the filling pressure in the unit of atmospheres and Z_i, calculated by Peng-Robinson equation, is the methane compressibility at P_i. The volume of the empty system was determined to be 282 cm^3 from the slope of the straight line of the plot $V_{off,i}$ versus $[(P_i / Z_i) - 1]$ as shown in Figure 6.5.

In order to estimate the packing efficiency of the powders, the fraction (θ) of the total available space for methane storage in the AX-21 packed bed was defined as the ratio of the total void (V_t), including both interparticle voids and intraparticle open pores, to the volume of the packed AX-21 carbon powder (V_c). The value of V_c is 252 cm^3 which is calculated from the physical dimension of the cylinder. V_t was determined by

$$V_t = V_t' - (V_{sys} - V_c) \quad \text{---------- (6.22)}$$

where V_t' is obtained from the equation 6.21 by filling the AX-21 packed cylinder with helium to a number of pressures and then discharging to atmosphere.

The AX-21 packed cylinder was filled with methane at the required pressure (3.4 MPa) at a temperature of 298 K until an equilibrium (the pressure became constant) was reached, and then discharged to one atmosphere while the volume released was recorded. The temperature inside the cylinder increased during the adsorption and decreased during the desorption. The temperature inside the cylinder was not monitored but was believed to be reached to a constant level after equilibrating for 30 min. The 5 min filling and discharging cycle were also tried. The delivered volumetric methane capacity (V_d) of the AX-21 packed cylinder under a given pressure was calculated by:

$$V_d = \frac{\Delta V - \Delta V_{empty}}{V_c} \quad \text{---------- (6.23)}$$

where ΔV is the measured methane volume (converted to 298K and 0.1 MPa) released at 0.1 MPa after the AX-21 packed cylinder was saturated with methane at 3.4 MPa; V_c is the volume of packed AX-21 carbon powder; and ΔV_{empty} is the volume of methane stored in

bulk phase in the pipeline between two needle valves and in the holes of gas distribution disc. ΔV_{empty} is given by

$$\Delta V_{empty} = \frac{P_{load}}{P_{unload}} \bullet \frac{V_{sys} - V_c}{Z} \quad \text{---------- (6.24)}$$

where P_{load} and P_{unload} are methane loading pressure and unloading pressure; Z is the methane compressibility at 3.4 MPa and 298 K.

6.2 MERCURY POROSIMETRY

Gas adsorption method can give information on micropores and mesopores. But for macropores and interparticle voids, mercury porosimetry is a very useful technique to measure the volume of voids and macropores. The determination of large pore size by mercury penetration is based on the behaviour of non-wetting property of mercury in capillaries. Mercury cannot spontaneously enter capillaries which have wetting angles more than 90° because of the surface tension. However the resistance can be overcome by exerting an external pressure. The relationship between pore size and pressure is expressed by the following equation (Washburn, 1921):

$$Pr = 2\sigma \cos\theta \quad \text{---------- (6.25)}$$

where r is the pore radius; P is the absolute pressure exerted; σ is the surface tension of mercury; and θ is the wetting angle between carbon and mercury. The wetting angle θ depends on the nature of the samples. For carbon samples it is normally taken as $\theta = 140°$. The surface tension σ is also variable with pore sizes and $\sigma = 0.48$ Nm^{-1} has been taken as an average value at 298 K. Substituting σ and θ value into equation 6.25 gives the following relationship between pore radius and intrusion pressure:

$$r = 7353/P \quad \text{---------- (6.26)}$$

in which r is in units of Angstroms and P is in units of MPa.

A mercury porosimetry — Autopore II 9220 made by Micromeritics Instrument Corporation was used to measure the open pore volumes of the carbon monoliths developed in this study. The maximum external pressure of the instrument can go up to 414 MPa, which means that pore radius down to 35 Å can be detected. Dried carbon samples (110 °C, 2 h) were put into a penetrometer and sealed by a special vacuum grease (Apiezon). The sample weight was obtained by the weight difference of the penetrometer with and without the sample in it. The penetrometer was inserted into a low pressure port which is horizontally placed in order to minimise the mercury gravity influence (about 0.068 bar). The maximum external pressure was 1.690 bar for low pressure intrusion. The penetrometer was then transferred into a high pressure port (vertically placed) and the intrusion pressure was gradually increased to 414 MPa. The measurement was automatically controlled by a computer and collected data were processed by a built-in software.

Although the mercury porosimetry is a very popular technique to characterise the pore texture, there are a number of uncertainties in wetting angle (in a range 130~150°), surface tension, pore network effect and the possibility of pore wall deformation and damage at high pressures, as detailed by McEnaney and Mays (1989). Therefore, the results in small pore region should be considered with caution. It is generally accepted that the mercury porosimetry is confined to the macropore region and not suitable for characterising micropores.

6.3 THERMAL ANALYSIS

Thermogravimetry analysis (Setaram TG-92) was used to monitor the weight change of meso-carbon microbeads during pre-oxidation in air, carbonisation in nitrogen and activation by carbon dioxide or potassium hydroxide. About 100 mg sample was put into an alumina crucible each time. The balance was tarred before the sample was put in. The whole system is purged in argon or nitrogen at a flow rate of 5.6 $dm^3 h^{-1}$ for 4 h. A flow rate of 1.0 $dm^3 h^{-1}$ was used during analysis. The temperature was increased linearly at a rate of 2 °C min^{-1}. The sample weight change was automatically recorded and processed.

By connecting mass spectrometer (Spectramass Visa), the composition in the gas phase of the KOH/MCB mixtures during heat treatment was also analysed to investigate the mechanism of the KOH activation of the meso-carbon microbeads. The thermogravimetric analyser–mass spectrometer system is illustrated in Figure 6.6. Samples were cleaned by vacuum before temperature was raised up. The mass spectrometer system was evacuated to 1.0×10^{-7} mm Hg by a vapour diffusion pump (Speedivac, Edwards High Vacuum Ltd). The operation pressure of the mass spectrometer was controlled by a needle valve to a level of 1.0×10^{-6} mm Hg during the gas analysis. The mass spectrometer was calibrated by a standard gas mixture: 2% oxygen, 20% carbon dioxide, and 78% argon. After 30 min stabilisation, the concentrations of oxygen, carbon dioxide and argon are measured to be 2.07 %, 19.5 % and 78.4%, respectively. The deviation from the standard values are 3.5 %, 2.5 % and 0.5 % for oxygen, carbon dioxide and argon respectively (Table 6.1). In order to prevent condensation of the moisture derived from the dehydration of KOH, the pipe line between the thermogravimetric analyser and the mass spectrometer was maintained at 200 °C by a flexible heating tape.

Table 6.1 The calibration of mass spectrometer by a standard gas mixture

	O_2 (vol. %)	CO_2 (vol. %)	Ar (vol. %)
standard value	2	20	78
calibration at 0 second	4	19.2	76.8
calibration at 60 second	2.48	19.0	78.5
calibration at 1800 seconds	2.07	19.5	78.4

6.4 PYCNOMETRY

The carbon density, excluding open pores, was measured in a helium pycnometry AccuPyc 1330 (Micromeritics Instrument Corporation) which is shown in a schematically in Figure 6.7. The principle of the helium pycnometry is to determine density and volume of solid objects by measuring the pressure change of helium in a calibrated volume. There are two volume-calibrated chambers: a sample chamber and an expansion chamber. The weighed sample was put into a cup and sealed in the sample chamber. After 20 purge cycles by filling and discharging helium, the equilibrium pressures of the filling and the expansion

were recorded. By calculating the mass balance of helium before and after the expansion based on ideal gas equation, the sample's volume V_{samp} is given by

$$V_{samp} = V_{cell} - V_{exp} (P_1/P_2 - 1) \quad \text{---------- (6.27)}$$

where V_{cell} is the calibrated volume of the sample chamber; V_{exp} is the calibrated volume of the expansion chamber; P_1 is the fill pressure and P_2 is the expansion pressure. The volume measured by this method excludes all open pores because it is believed that there is no helium adsorption under the test temperature and pressure. Therefore the skeletal density (ρ_c) of the activated carbon is given by

$$\rho_c = W / V_{samp} \quad \text{---------- (6.28)}$$

where W is the sample weight. The carbon samples were dried in an oven at 110 °C for 12 h and kept in a desiccator. The test sample was put into a cup which was weighed on an electronic balance (accurate to ± 0.0001 g) without and with sample in it. The cup was sealed in the sample chamber and was purged by 20 helium cycles. The operation of fill and expansion of helium was repeated 10 times and the average value was used to calculate the sample volume and density.

6.5 SCANNING ELECTRON MICROSCOPE STUDY ON CARBON MONOLITHS

The topographical images of carbon monoliths made from AX-21 carbon powder were observed on a scanning electron microscope JEOL JSM-T330. The carbon discs were stuck on a conduction pad which was supported by a metal planchette. There is no need to sputter gold deposition as the carbon monoliths are electrically conductive. 250 kV was used and the magnitude goes up to 2000 times which is high enough to distinguish the particle size and particle voids.

6.6 X-RAY DIFFRACTION (XRD) STUDY ON MESO-CARBON MICROBEADS AND ACTIVATED MESO-CARBON MICROBEADS

Purpose of X-Ray Diffraction Test

Meso-carbon microbeads, carbonised meso-carbon microbeads, K_2CO_3 activated meso-carbon microbeads, KOH activated meso-carbon microbeads and CO_2 activated meso-carbon microbeads were analysed by X-ray diffraction in order to investigate the meso-carbon microbeads structure variation under different processes. The structural parameters obtained from X-ray diffraction analysis are used to study the difference in mechanisms of activation by KOH and CO_2.

Sample Preparation

Natural graphite flake, raw meso-carbon microbeads, carbonised meso-carbon microbeads at 600 °C and 1000 °C, CO_2 activated meso-carbon microbeads at 900 °C and KOH activated meso-carbon microbeads at 400 °C, 700 °C and 800 °C samples were tested and their preparation processes are described in Table 6.2.

Table 6.2 Sample preparation for X-ray diffraction test

sample code	preparation
graphite	natural flakes as supplied
MCB	fine powder as supplied
MCB-600	heating at 2 °C min^{-1} to 300 °C in air remaining 10 min. there and then raising to 600 °C in argon and soaking 1 hr.
MCB-1000	heating at 2 °C min^{-1} to 300 °C in air remaining 10 min. there and then raising to 1000 °C in argon and soaking 1 hr.
KOH-MCB-400	KOH:MCB=4:1 mixture was heated in a tube furnace at 2 °C min^{-1}. to 400 °C for 2 hr and then leached by distilled water in a flask and dried in an oven.
KOH-MCB-700	KOH:MCB=4:1 mixture was heated in a tube furnace at 2 °C min^{-1}. to 700 °C for 2 hr and then leached by distilled water in a flask and dried in an oven.
KOH-MCB-800	KOH:MCB=4:1 mixture was heated in a tube furnace at 2 °C min^{-1}. to 400 °C for 2 hr. and then to 800 °C for 2 hr, followed by water-leaching in a flask and dried in an oven.
K_2CO_3-MCB-850	K_2CO_3:MCB=5:1 mixture was heated in a furnace at 2 °C min^{-1}. to 400 °C for 2 hr. and then to 850 °C for 2 hr, followed by water-leaching in a flask and dried in an oven.
CO_2-MCB-900	MCB was heated to 900 °C in argon and then switched to CO_2 and soaked at 900 °C for 3 h.

X-Ray Diffraction Measurement

The X-ray diffraction spectra for above samples were measured using a Philips PW 1820 computer controlled vertical goniometer. The detector was a xenon proportional counter with a graphite monochromator and automatic divergence slit assembly. The radiation was nickel-filtered copper K_α (λ = 0.15418 nm) from a 4 kW generator connected to a long fine focus 2 kW copper target X-ray tube operated at 40 kW and 25 mA.

The powder samples were packed into a rectangular sample holder mounted on a metal slide. The diffraction spectra were achieved by using a program TMZN1 which has an hour duration and counts between 10° and 100°. The data were automatically stored on to a connected computer. The position of the peaks and their width of the X-ray diffraction spectra were analysed using a profile fitting program called PC-APD Philips diffraction software.

Calculation of Structural Parameters

The characteristic peaks can be determined by comparing with standard spectra for pure graphite sample. The position of each peak was correlated with that of the graphite where the peak at $2\theta \approx 25°$ is attributed to the diffraction by the (002) plane and the peak at $2\theta \approx 43°$ contains overlapping reflections from (100) and (101) plane. The structural parameters of these samples were estimated by:

$$n\lambda = 2d\sin\theta \qquad \text{Bragg equation} \text{ ---------- } (6.29)$$

and

$$L = \lambda\kappa / (\beta \cos \theta) \qquad \text{Scherrer equation} \text{ ---------- } (6.30)$$

where n — the difference in path length between the adjacent X-ray beams which is some integral number of radiation wavelength (λ);

λ — the radiation wavelength which is 0.15418 nm in this test;

d — the spacing between crystal planes;

θ — the angle of scattering;

L — the crystallite size;

κ — a constant related to β;

β — an angular width of peak where the intensity is equal to half of the maximum.

In this study, β was estimated by taking half the difference between the two extreme diffraction angles ($2\theta_1$ and $2\theta_2$) at which the bottom of the characteristic peak intersects with tangent line drawn by PC-APD profile fitting software: $\beta = 1/2\ (2\theta_2 - 2\theta_1) = \theta_2 - \theta_1$. Therefore the interlayer spacing, $d_{(002)}$, stack height, L_c, stack width, L_a, and number of planes in a crystallite, m, were calculated by the following equations:

$$d_{(002)} = \lambda / 2\sin\theta_{(002)} \quad \text{---------- (6.31)}$$

$$L_c = 0.89\,\lambda / (\beta_{(002)} \cos\theta_{(002)}) \quad \text{---------- (6.32)}$$

$$L_a = 1.84\lambda / (\beta_{(100)} \cos\theta_{(100)}) \quad \text{---------- (6.33)}$$

$$m = L_c / d_{(002)} \quad \text{---------- (6.34)}$$

where $\kappa = 0.89$ for L_c and $\kappa = 1.84$ for L_a (Klug and Alexander, 1974) and β is expressed in radians.

6.7 INFRARED ABSORPTION SPECTROSCOPY

A Fourier Transform Infrared spectrophotometer (FT-IR 1720) was used to study the influences of oxidation, carbonisation and activation processes on the surface functional groups of meso-carbon microbeads by comparing their infrared spectra before and after various heat-treatment processes.

The test samples of meso-carbon microbeads, carbonised meso-carbon microbeads and KOH activated meso-carbon microbeads were prepared in the same way as for X-ray

diffraction measurement (see Table 6.2). As all samples were powders, a diffuse reflectance accessory chamber was used to hold the sample in the optical compartment of infrared spectrometer. The absorption of scanning infrared radiation by the black carbon powder was so strong that the sample must be mixed with potassium bromide in order to get the energy of the reflected beam higher than 400. The diffuse reflectance cell in the presence of potassium bromide was scanned as a background before the test carbon sample was scattered on it. The spectrum of the background was automatically subtracted from the measured spectrum of the sample. All spectra were recorded with 20 scans at a resolution of 2 cm^{-1}.

6.8 COMPRESSION TEST OF CARBON MONOLITHS

The compressive strengths of the monolithic carbons made from AX-21 carbon powder and KOH activated meso-carbon microbeads were tested on an Instron 1185 mechanical testing machine referring to the ASTM C 695-91 standard. The test specimen was compressed continuously at a constant rate (2 mm min^{-1}) of the cross-head until ultimate failure. The compressive strength σ_c was given by $\sigma_c = P/A$ where P is the final load on the specimen at failure and A is the cross section area of the specimen.

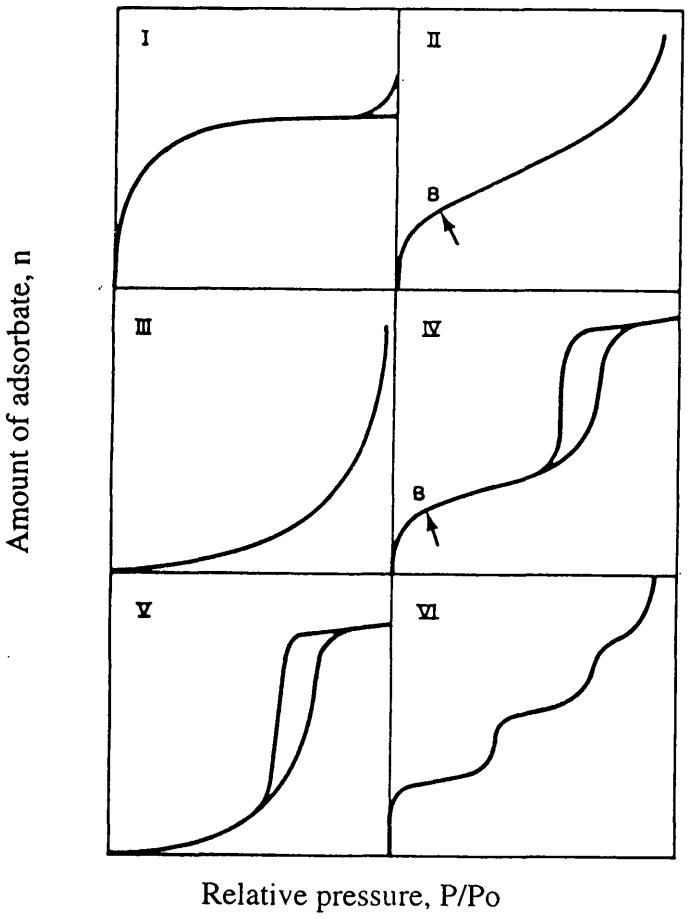

Figure 6.1 The five types of isotherms (I to V) classified by Brunauer, Deming, Deming and Teller (BDDT), together with the step-type isotherm (VI). (From S.J. Gregg and K.S.W. Sing, 1982)

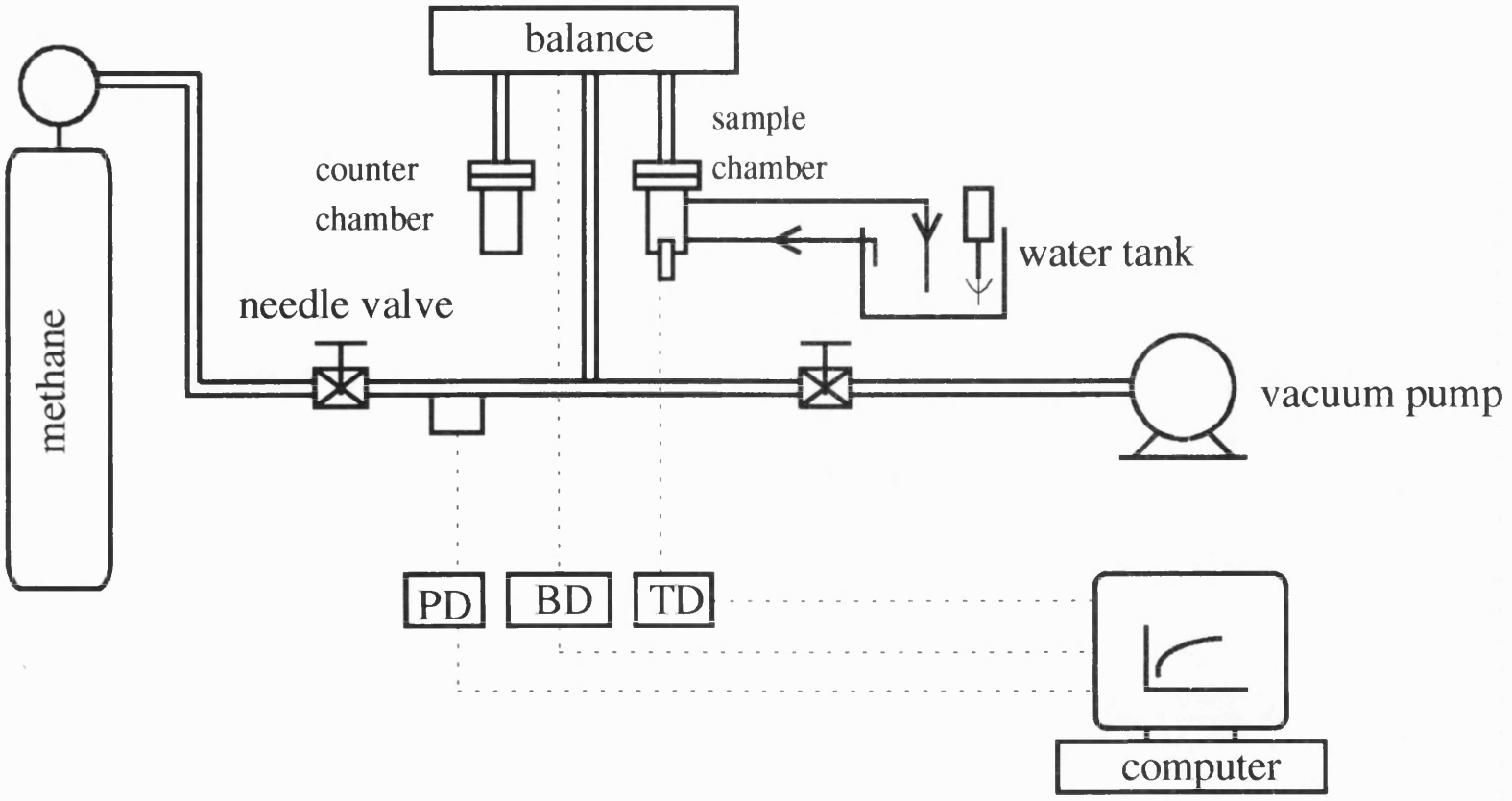

Figure 6.2 The diagram of Sartorius 4406 high pressure microbalance for methane adsorption measurement at 298 K. The system consists of a vacuum pump, two needle valves, a thermostatic water tank, a Sartorius electronic balance, a computer, thermocouples, a pressure transducer as well as methane supply system.

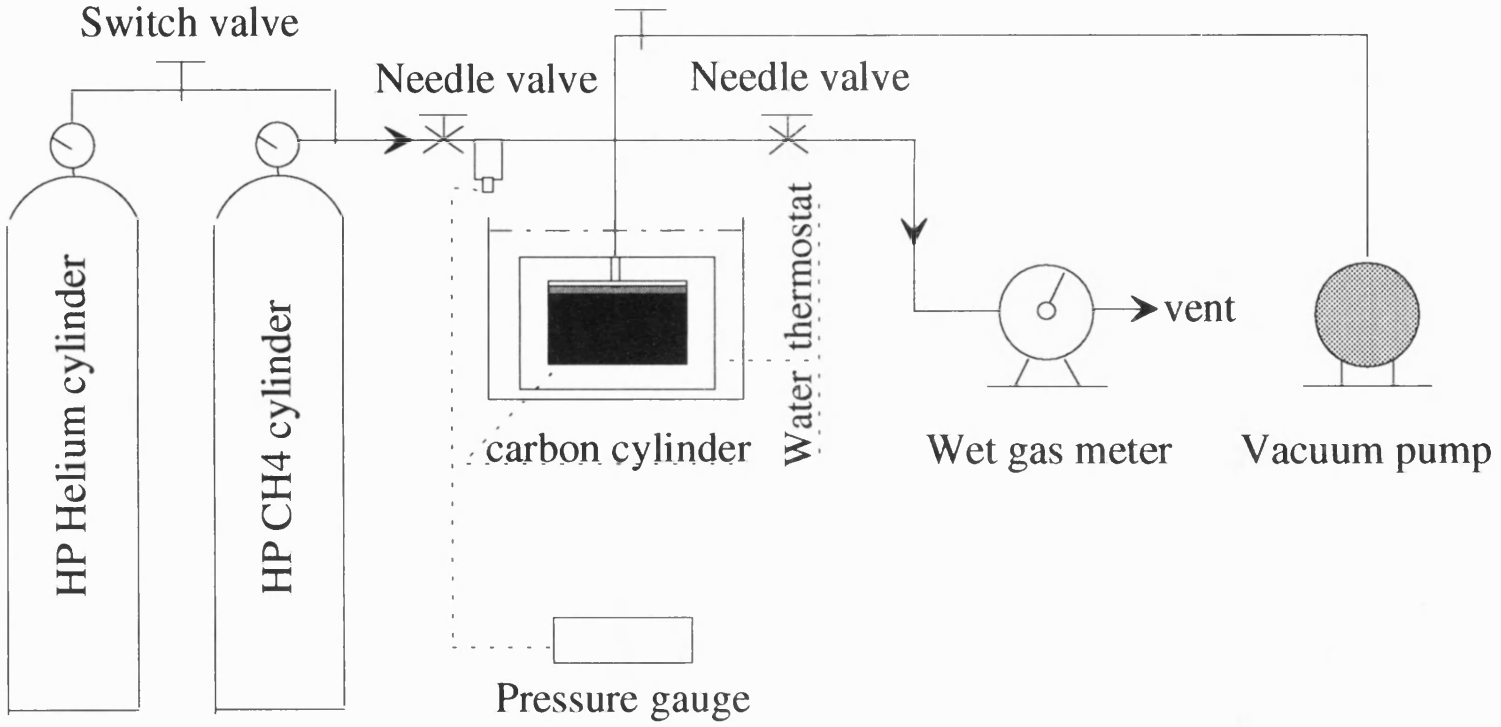

Figure 6.3 The flow diagram of the test rig for the measurement of the delivered methane capacity on packed AX-21 carbon powder. The system consists of a special designed cylinder (to hold the packed AX-21 carbon powder under an elevated pressure), a vacuum pump, a wet gas meter to account the volume of methane released (at 0.1 MPa) from the charged cylinder (at 3.4 MPa), two needle valves, one pressure transducer, a thermostatic water tank as well as a gas supply system.

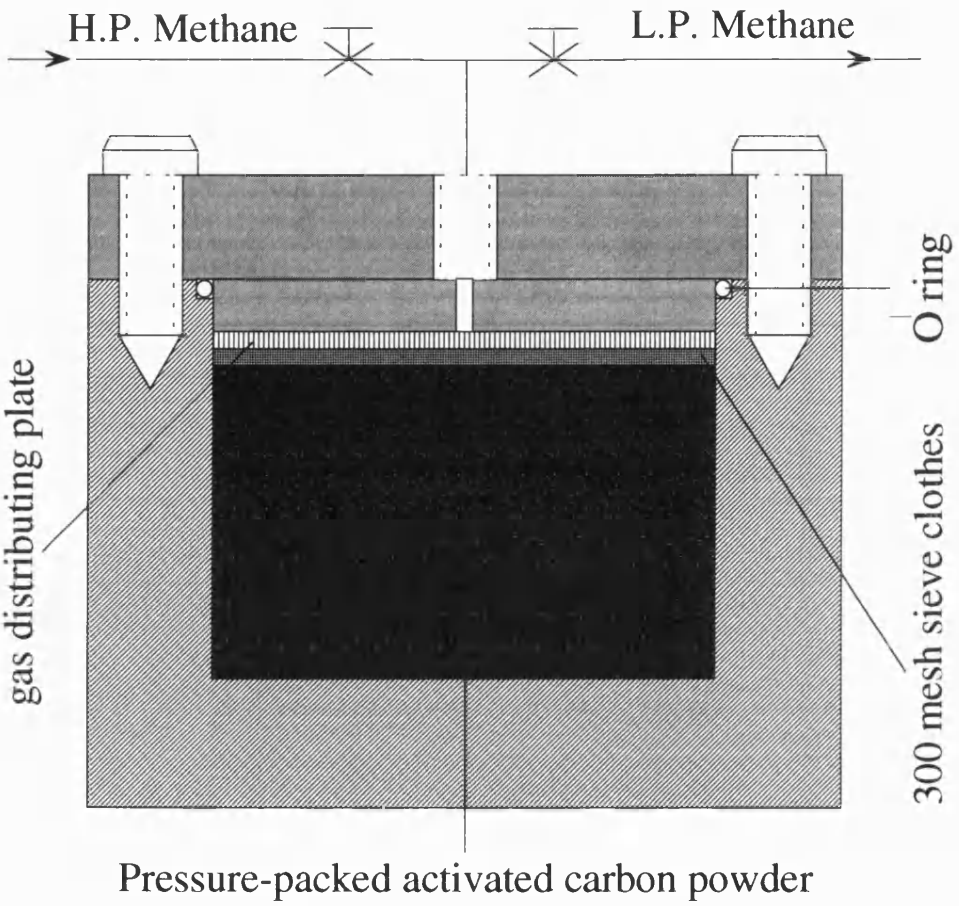

Figure 6.4 The schematic of the cylinder for packing AX-21 carbon powder under an elevated pressure. The cylinder (80 mm in inside diameter × 60 mm in depth) was machined from a block of stainless steel. The cylinder has a special lid which can hold high pressures without gas leakage. On the top of AX-21 carbon powder there are three layers of sieve (300 mesh) and one layer of carbon bonded carbon fibre disc as well as a gas distribution disc.

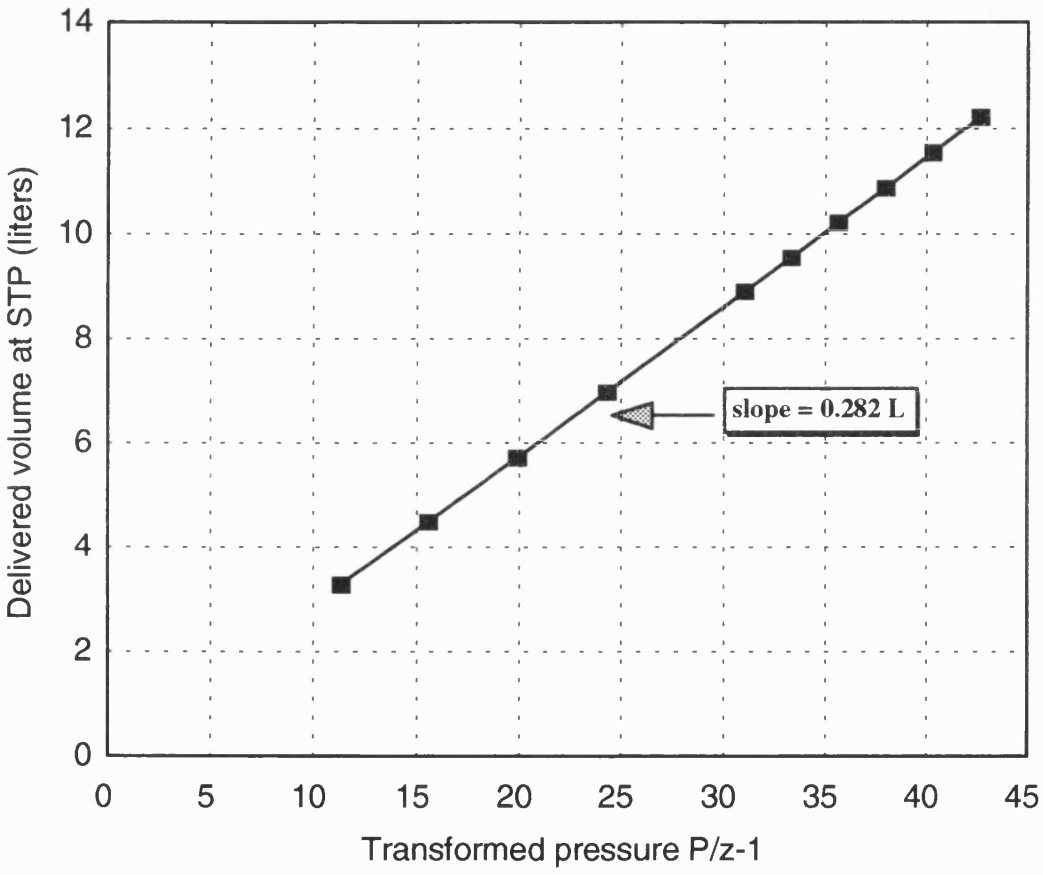

Figure 6.5 The calibration of the empty system volume in the test rig for the delivered methane capacity.

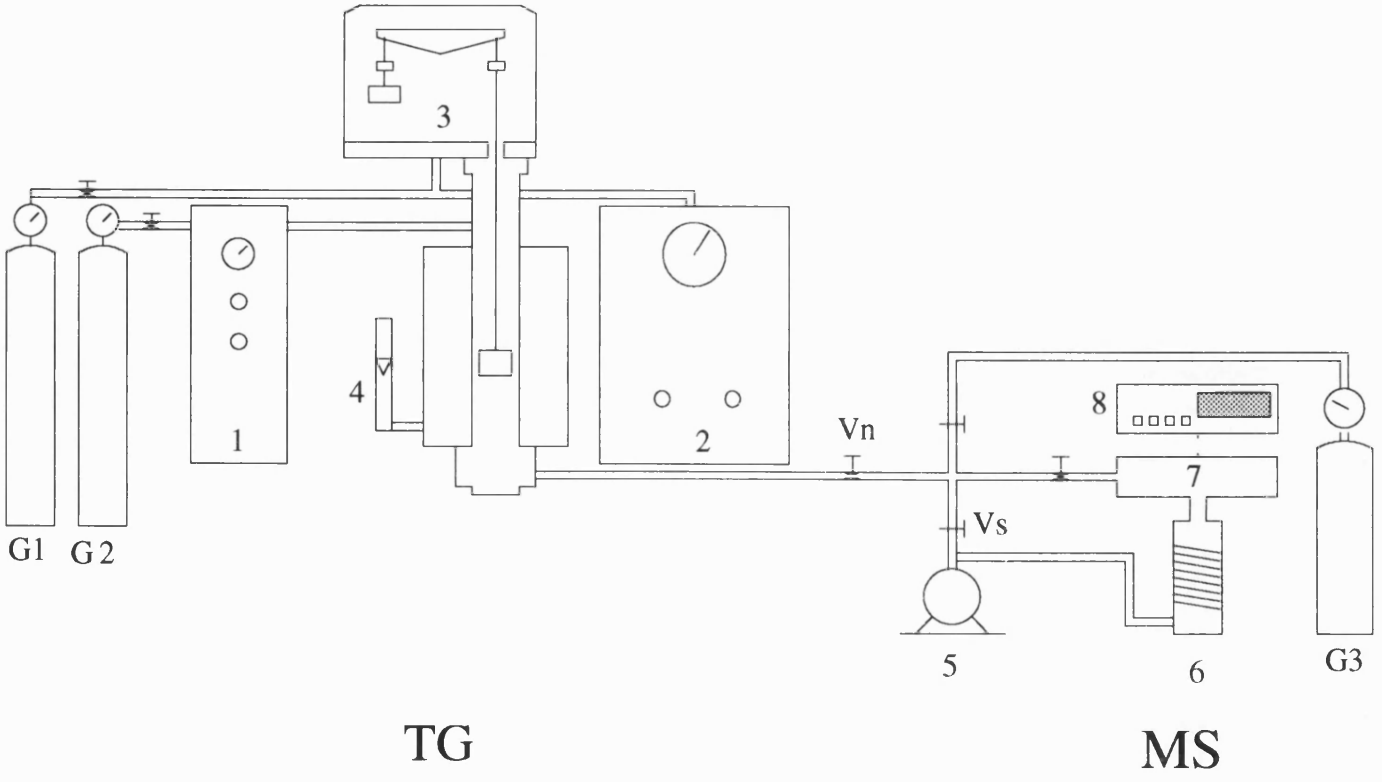

1 - auxiliary gas control pannel; 2 - reactive gas control pannel; 3 - microbalance system; 4 - flow meter; 5 - rotary pump; 6 - diffusion pump; 7 - mass spectrometer; 8 - MS control and output; G1 - reactive gas cylinder; G2 - auxiliary gas cylinder; G3 - standard gas cylinder; Vn - needle valves; Vs - switch valves

Figure 6.6 The diagram of thermogravimetry (TG) - mass spectrometry (MS) system

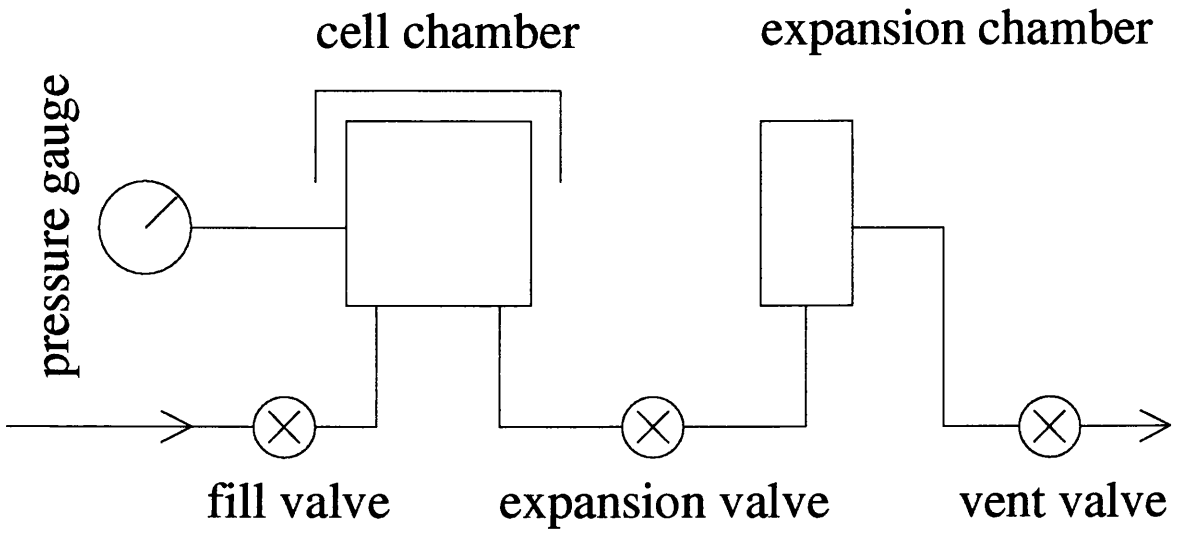

Figure 6.7 The schematic of a Pycnometry, AccuPyc 1330.

SECTION C

RESULTS AND DISCUSSIONS

CHAPTER 7 COMPUTER SIMULATION OF METHANE ADSORPTION

7.1 INFLUENCE OF PORE STRUCTURE ON ADSORBED METHANE DENSITY

The adsorbed natural gas at 3.4 MPa and 298 K on microporous carbons is a very promising alternative to replace compressed natural gas (20 MPa and 298 K) as a clean fuel for natural gas driven vehicles. The characterisation of microporous carbons by methane adsorption is used to evaluate the suitability of carbon adsorbents for this special purpose. Unfortunately, the conventional methods such as the multi-layer adsorption theory (BET equation), the theory of volume filling (D-R or D-A equation) and capillary condensation (Kelvin equation) can not successfully interpret methane adsorption isotherms of carbon adsorbents whose pore structure is dominated by micropores with dimensions similar to adsorptive molecules. The grand canonical ensemble Monte Carlo molecular simulation method provides insights into the impact of micropore structure on the adsorbed methane density. The pore model used before by others was usually a slit formed between two single graphite sheets (Matranga, *et al*, 1992) or between two graphite slabs (Aukett, *et al*, 1992). Rarely reported are the effects of pore structures on methane adsorption at a supercritical temperature. In this study, the influences of carbon atom number density (A_c, carbon atoms per square nanometer), pore wall thickness (n, the number of carbon sheets in a pore wall), inter-layer spacing (Δ) and pore width (H) on the adsorbed methane density in a slit pore were investigated by the grand canonical ensemble Monte Carlo molecular simulation method.

7.1.1 Definition of Adsorbed Methane Density

As addressed in chapter 4, there are different definitions in model pore width: H_{phys}, H_{snap}, H_{chem} and H_a. H_{phys} is a clear concept but it does not represent the space available to adsorbate molecules. H_{snap}, H_{chem} and H_a are ambiguous and variable but they are close to the effective pore width. As the adsorbed methane density in a slit pore depends on the definition of model pore width, a given grand canonical ensemble Monte Carlo output (the

number of methane molecules in a simulation cell) will give different methane density values due to using different definitions of pore width. Figure 7.1 is a typical local methane density in a slit given by grand canonical ensemble Monte Carlo simulation. Figure 7.1 shows that there are no methane molecules within the region of ca. $0.75\sigma_{sf}$ from the nuclear centres of the carbon atom layer, which means the space $2 \times 0.75\sigma_{sf} L^2$ within the simulation cell is not accessible to methane molecules (L is the simulation cell dimension parallel to the pore walls). Therefore, the adsorbed methane density is obviously under-estimated by using L^2H_{phys} as the volume of the simulation cell. The adsorbed methane density values obtained using the corrected pore widths H_{snap}, H_{chem} and H_a are more reasonable than the density obtained using H_{phys}, but the interface between the methane molecules and carbon atoms is ambiguous and it varies with pressure. The differences in mean adsorbed methane density obtained by using H_{phys}, H_{snap}, H_{chem} and H_a are clearly demonstrated in Figure 7.2. The differences in mean adsorbed density for micropores (width less than 2 nm) are quite remarkable while for wider pores the differences become insignificant. In the following discussions, H_a is consistently used for the calculation of the mean adsorbed methane density in pores.

7.1.2 Carbon Density

A carbon atom number density of 38.18 atom/nm^2 corresponds to a conventional density of 2.268 g cm^{-3}, and was calculated from the hexagonal arrangement of carbon atoms in a perfect graphite crystal. This value of carbon atom number density is often used to represent the pore wall carbon density in the grand canonical ensemble Monte Carlo simulation of methane adsorption on microporous carbons. But the real situation is that most porous carbons are often made from non-graphitizable carbon materials such as wood, nutshells and non-fusing coals. Even when graphitizable precursors were used, the heat treatment temperatures (usually less than 1000 °C) in carbonisation and activation processes are not high enough to complete the graphitization (Chahine and Bose, 1991). Therefore, it is reasonable to believe that there must be some defects within the porous carbon structure, for example, stacking faults, dislocations, vacancies and heteroatoms. The presence of these defects makes the skeletal carbon density less than that of pure graphite. The carbon densities measured using a helium pyconometer, as listed in Table 7.1, show that the skeletal

carbon densities (assuming there is no closed pores) of the monoliths made from AX-21 carbon powder, from KOH-activated meso-carbon microbeads and from coconut carbons are lower than for pure graphite.

Table 7.1 The carbon densities of carbon monoliths made from AX-21 carbon powder, from KOH-activated meso-carbon microbeads and from coconut carbon measured on a helium pycnometry

Densities(g cm^{-3})	Run1	Run2	Run3	Run4	Run5	Average	Deviation
AX-70	1.846	1.838	1.841	1.839	1.843	1.841	0.003
AX-56	1.958	1.950	1.945	1.942	1.944	1.948	0.006
AX-45	1.990	2.044	2.035	2.019	2.030	2.024	0.019
BG-5R	2.144	2.137	2.129	2.122	2.116	2.130	0.008
AMCB69	2.205	2.193	2.187	2.180	2.180	2.189	0.009

Note: AX represents the monolith made from AX-21 carbon powder. The number following AX is the AX-21 carbon percentage in the monolith. AMCB69 is the monolith made from KOH-activated meso-carbon microbeads with 69 % burn-off. BG-5R is the monolith made from steam-activated coconut shells.

The effects of varying the carbon atom density in the range 38.18 atoms/nm^2 to 31.90 atom/nm^2 is shown in Figure 7.3. The values of carbon atom density correspond to skeletal carbon densities of 2.26, 2.2 2.0 and 1.89 g cm^{-3}. The density of 2.26 g cm^{-3} corresponds to that of a perfect graphite crystal, while 1.89 g cm^{-3} corresponds to the removal of one carbon atom from each hexagon of the graphite basal plane. The experimental values of helium density in Table 7.1 lie within the range of skeletal densities chosen for the simulations. The simulation result in Figure 7.3 shows that the carbon density has a significant impact on the adsorbed methane density. The results show that for an activated carbon with a skeletal carbon density of 2.0 g cm^{-3} (which is a reasonable value, Table 7.1) the simulated, adsorbed methane density in a pore of 1.12 nm at 3.4 MPa and 298 K is 12 % lower than that obtained using a perfect graphite density of 2.268 gcm^{-3}. This shows that adsorbed methane densities in activated carbons are over-estimated before by Matranga, *et al* (1992) and Aukett, *et al* (1992) using graphite density in their molecular simulations of methane adsorption in pores.

7.1.3 Pore Wall Thickness

Pore wall thickness in the model depends on two factors: the number of carbon layers (n) and the interlayer spacing (Δ). They were investigated independently. The value of n was varied from 1 to 10 while T, Δ, H and A_c were fixed. The influence of varying the value of n on the adsorbed methane density is illustrated in Figure 7.4. The effect of the number of carbon layer on the adsorbed methane density is not significant when n is equal or greater than 2. This is because the interaction potential energy between methane molecules and carbon layers fades away quickly with the increment of their separated distances. So comparing with the potential from the first two carbon layers, the interactions from the other further layers are negligible.

Transmission electron microscope images of microporous carbons reveals that the average pore wall thickness is equivalent to 1 ~ 3 layers of graphite (Yoshizawa, *et al*, 1994) (Fei, *et al*, 1994) (Marsh, *et al*, 1982). The simulation results shows that there is no big difference in the adsorbed methane density when the pore wall is thicker than 2 carbon layers. Consequently, n value was fixed as 2 when other parameter were varied in the simulations.

7.1.4 Interlayer Spacing

From the X-ray diffraction spectra of meso-carbon microbeads, carbonised meso-carbon microbeads and activated meso-carbon microbeads, the interlayer spacing $d_{(002)}$ was calculated by equation 6.31 (section 6.6). The experimental results (see Table 8.2, section 8.3.2) show that the interlayer spacing of all carbon samples tested is higher than 0.3354 nm for pure graphite. This is because the disorder structure in porous carbons. The biggest inter-layer spacing measured is 0.398 nm. Consequently, five interlayer spacing values, Δ, i.e. 0.3354, 0.3450, 0.3520, 0.3820 and 0.3980 nm were used in the molecular simulations to test the sensitivity of the adsorbed methane density to the value of Δ. The simulation results in Figure 7.5 show no remarkable change in adsorbed methane density when the

interlayer spacing varies from 0.3354 nm to 0.3980 nm, which means that the methane density is not very sensitive to changes of interlayer spacing of the carbon wall.

7.1.5 Pore Width

Pore width (H) is the most important parameter which is to be investigated by the molecular simulation because it can provide very useful information on what is the optimal pore size for methane adsorption at a given temperature and pressure, or, in other words, what kind of pore structure should be developed for the carbon adsorbents targeted for natural gas storage at 298 K and 3.4 MPa.

The values of pore width, H, were quantized to widths that can accommodate integral layers of methane molecules by the expression:

$$H = m\sigma_{ff} + \sigma_{sf} \quad \text{---------- (7.1)}$$

where m is an integer, σ_{ff} is the collision diameter of methane molecule and σ_{sf} is the average diameter between methane molecule and carbon atom obtained using the Lorentz-Berthelot combining rule. Substituting m = 1, 2, 3, 4, 6 and 8 respectively, σ_{sf} = 0.3605 nm and σ_{ff} = 0.381 nm into the expression 7.1, six pore widths, i.e. H = 0.7415, 1.1225, 1.5035, 1.8845, 2.6465 and 3.4085 nm, were obtained and were used to simulate the methane adsorption at a given T, n, Δ and A_c.

The local methane density distribution in different pore widths is illustrated in Figure 7.6. Figure 7.6 shows that the maximum local methane density decreases with the increase of pore width. The local methane density profile in the pore with H = 0.7415 nm has only one peak where the potentials from opposite walls completely overlap each other. The pores with H wider than 0.7415 nm have two peaks where the potentials partially overlap. The local density distribution across the pore in Figure 7.6 also shows that methane molecules are concentrated only near the pore walls while in the middle of pores the methane density is near the bulk density in gas phase. The methane density profile in a slit clearly shows that

only micropores can enhance the methane density at a supercritical temperature and that mesopores and macropores play little positive role in the enhancement of methane storage.

Figure 7.7 illustrates the average methane densities in different pore widths against adsorption pressure. The average methane densities are normalised to the liquid methane density (0.42 g cm^{-3} at 112 K). The average methane density in a slit also decreases with the increase of pore width and the highest average methane density is achieved in the pore with H = 0.7415 nm which is just wide enough to accommodate one layer of methane molecules. It is also noticed that the average methane densities at 298K are always lower than the liquid methane density even though the adsorbed methane in the pore with H=0.7415 nm at 20 MPa is quite close to liquid state. This indicates that there is no phase-transition of adsorbed methane molecules from gas to liquid phase at supercritical temperature (298 K), which is about 100 K above methane critical temperature (191 K). The methane molecules cannot reach a liquid state even at a very high pressure.

Figure 7.8 is a plot of the average methane densities in the pores with different widths for a given pressure of 3.4 MPa at 298 K. It is interesting to compare the simulated results of the average methane density in a model pore with those calculated from the measured methane uptakes and the micropore volume (deduced from nitrogen adsorption isotherms) by the following expression:

$$\text{average methane density} = \frac{\text{methane uptake (g / g)}}{\text{micropore volume by D - R equation (ml / g)}} \quad \text{---------- (7.2)}$$

where the methane uptake should include the methane both in adsorbed phase and in bulk phase at 3.4 MPa and 298K. The average methane densities on different carbons obtained from the measured methane uptakes (see Table 9.4, Section 9.3.1) and the micropore volumes (see Table 8.3, Section 8.5.2) are listed in Table 7.2. The results show that the average methane densities in micropores of the carbon monoliths made from AX-21 carbon and KOH activated meso-carbon microbeads are around 0.19 ± 0.01 g cm^{-3} and they do not vary much. The carbon monolith made from coconut carbon has a higher methane density 0.24 g cm^{-3}. The comparison between the measured methane densities on these carbon monoliths (Table 7.2) and the simulated methane densities in model pores (Figure 7.8)

suggests that the average pore size of carbon monoliths made from AX-21 carbon and from KOH activated meso-carbon microbeads is around 1.5 nm and carbon monolith made form coconut carbon is 1.3 nm.

Table 7.2 The average methane density in micropores of different carbons at 298K and 3.4 MPa (methane density in bulk phase is 0.024 g cm^{-3} at 3.4 MPa and 298 K)

carbons	pore volume (cm^3 g^{-1})	methane uptake (g g^{-1})	methane density (g cm^{-3})
AX-83	0.91	0.16	0.20
AX-69	0.86	0.14	0.19
AX-56	0.66	0.11	0.19
AX-45	0.62	0.10	0.19
AMCB-40	0.73	0.11	0.18
AMCB-48	0.96	0.16	0.19
BG-5R	0.41	0.10	0.24

Note: AMCB series are the monoliths made from KOH activated meso-carbon microbeads with 30 wt.% phenolic resin as binder and the number followed the AMCB represents the burn-off value of meso-carbon microbeads after KOH activation. AX series are the monoliths made from AX-21 carbon powder and the number after AX is the AX-21 carbon percentage in the monolith. BG-5R is a carbon monolith made from coconut carbon.

Quinn (1990) also reported that the average methane densities (298 K and 3.4 MPa) of a series of CO_2 activated coconut shell carbons and steam activated Saran (PVC and PVDC copolymer) carbons are ca. 0.23 g cm^{-3} when the carbon burn-off is less than 20 % and ca. 0.18 g cm^{-3} when the burn-off is between 30 % and 50 %. This is in good agreement with the conclusion from the grand canonical ensemble Monte Carlo molecular simulations, that is, the wider the pore, the lower the methane density. Increasing carbon burn-off means widening pores which leads to decrease in the average methane density in pores.

7.2 ESTIMATED METHANE CAPACITIES ON CARBON MONOLITHS

Grand canonical ensemble Monte Carlo molecular simulation gives the number of the methane molecules in a single model pore. It would be very useful to convert the output

into a volumetric methane capacity for a carbon monolith based upon the following three simplified models:

1. void-free model: assuming that the carbon has no interparticle voids and the pore structure is composed of slits with the same width H.
2. hexagonal close-packed sphere (HCPS) model: to describe carbon monoliths made from microporous powders, provided that the powders are equally sized spheres having the same pore width.
3. close-packed parallel cylinder (CPPC) model: to simulate the carbon monolith made from microporous carbon fibres which have the same pore width and the same diameter.

There are two reasons for presenting the simulation results as volumetric methane capacities. First, the models consider not only adsorptive properties but also the packing density of the carbon particles which is equally important in the application of adsorbed natural gas for natural gas vehicles where the storage space is limited. Second, it is easy to compare the measured methane capacity with the estimated value from the simulation. Additionally, it can also be used to judge the feasibility of the defined target.

7.2.1 Void-Free Monolith

Figure 7.9 presents the volumetric stored methane capacities for void-free model monoliths with different pore widths (calculated using Equation 4.15 in Chapter 4). Figure 7.9 leads to a few interesting points. Firstly, at the commonly used adsorption temperature (298K) and pressure (3.4 MPa), the maximum volumetric methane capacity was achieved in the pore width of 1.12 nm as shown in Figure 7.10, even though the highest methane density was in the pore with H = 0.74 nm. This is due to the space utilisation efficiency per volume of carbon. The wider the pore the more space available for methane adsorption while the narrower the pore the higher the methane density. These two opposing factors are optimised at a pore width around 1.12 nm. Secondly, compared with compressed methane gas, the adsorbed methane on the carbon with 1.12 nm pore width at 298K and 3.4 MPa is more than three times higher in storage capacity. In other words, for the same storage capacity, the adsorbed methane pressure on a carbon adsorbent is only one fifth of the compressed methane pressure. This is the essential driving force behind the development of

adsorbed natural gas for the replacement of compressed natural gas because the drop in storage pressure will save a great amount of capital investment in high pressure filling stations as well as operation and maintenance costs. Thirdly, the net enhancement in methane capacity by adsorption over compression becomes small with increasing pressure and finally the enhancement disappears at pressures greater than 20 MPa. This probably explains why ca. 3.4 MPa has been often chosen as an adsorption pressure for adsorbed natural gas at a room temperature, considering that both the net enhancement and the methane capacity are near the optimal point.

7.2.2 Monoliths Made From Powders And Fibres

Unlike other common activated carbons, the carbon for adsorbed natural gas has to be in monolithic form in order to reduce the interparticle voids in the container. On the other hand the carbon should be predominantly microporous. This will pose a big problem in manufacture to meet both requirements fully. Based on works presented in section 8.5, the author believes that the consolidation of previously activated microporous powders or fibres is an appropriate approach to prepare uniform microporous carbon monoliths. Based upon this consideration, two simple configurations are proposed to model the carbon monoliths made from powders (HCPS) and fibres (CPPC). The estimated methane capacities of the monoliths are given by equation 4.16 and the results are plotted in Figure 7.11. The stored methane capacity on the monolith made from fibres is always larger than that on the monolith made from powders for the same pore width as fibres in parallel array have higher packing density. They have the same pattern as the void-free carbon. The maximum stored methane capacities were always found for the carbons with the pore width of 1.12 nm.

Fixing the pore width to the optimal value of 1.12 nm and the interlayer spacing to 0.3354 nm but varying the number (n = 1, 2 and 3) of carbon layers in a pore wall, carbon atom density (A_c = 38.18 nm^{-2}, 33.67 nm^{-2}) and the carbon morphology (void-free, HCPS and CPPC), the stored methane capacities at 298 K and 3.4 MPa obtained from the grand canonical ensemble Monte Carlo simulation results are illustrated in Figure 7.12 and 7.13. Single layer carbon model always gives highest stored methane capacity for all carbon densities and carbon morphologies. But it is not possible to manufacture an activated carbon

with such a pore structure. Perhaps it is more realistic to refer to the case when the number of carbon layers is taken as 2 because the lattice images obtained using the high resolution transmission electron microscopy (Yoshizawa, *et al*, 1994) (Fei, *et al*, 1994) show that the pore structure of real activated carbons resembles stacks of parallel graphite planes of 1 to 3 layers thick at random orientations. Figure 7.12 shows that for the activated carbon with graphite density 2.268 g cm^{-3} (A_c = 38.18 nm^{-2}), 2 layers of graphite sheets in each pore wall and a pore width of 1.12 nm, the stored methane density on the void-free carbon at 298 K and 3.4 MPa is 220 v/v, quite close to the compressed methane capacity (224 v/v) at 20 MPa and 298 K, 203 v/v on CPPC model monolith and 172 v/v on HCPS model monolith. For the activated carbon with a skeletal carbon density of 2.0 g cm^{-3} (33.67 nm^{-2}), the stored methane capacities, shown in Figure 7.13, are 187, 174, and 148 v/v for the model monoliths of void-free, CPPC and HCPS morphologies respectively. The simulation results show that the estimated stored methane capacity on activated carbon monoliths is very sensitive to the carbon atom density used in the model. The stored methane capacity might be over-estimated by 16 to 20 % by using the graphite density to represent the skeletal carbon density of the pore walls in activated carbons.

7.2.3 Delivered Methane Capacity

Delivered methane capacity is more relevant than stored capacity in the application of adsorbed natural gas for natural gas vehicles. For some ultra-microporous carbon the delivered methane capacity can be much lower that the stored methane capacity because there is a lot of adsorbed methane in the very fine pores which cannot be desorbed at the discharging pressure of 0.1 MPa at 298 K. For instance, the delivered methane capacities on the PVDC carbons (Atlanta Gas Light Adsorbent Research Group, 1994) are around 30 % lower than the stored methane densities. This is another problem which needs to be considered for the pore structure design targeted for the natural gas vehicles.

Figure 7.14 illustrates the difference between the stored and the delivered methane capacity in different pore widths. It shows that 75% of the adsorbed methane in the pore of width 0.74 nm at 3.4 MPa and 298 K cannot be desorbed at 0.1 MPa. This indicates that ultra-micropores (like meso- and macro-pores) are not desirable for adsorbed natural gas. For the pore of width 1.12 nm the delivered methane at 0.1 MPa is 91% of the stored

methane at 3.4 MPa. For pores wider than 1.5 nm the difference between the two capacities becomes smaller and remains around 5%.

Figure 7.15 and 7.16 show the delivered methane capacities on carbons with different pore wall thickness, carbon densities and morphologies. It is interesting to compare these delivered methane capacities with the defined value of 150 v/v (298 K and 3.4 MPa) which has been proposed as a target for a broad application of adsorbed natural gas in natural gas vehicles. For the single carbon layer pore model, all delivered methane capacities are higher than the target value. This is also true for the pore models with two layer planes except for the case of HCPS morphology with a true carbon density of 2.0 g cm^{-3}. For the three carbon layer pore model, the carbon has to be void-free in order to meet the target.

7.3 SUMMARY

The grand canonical ensemble Monte Carlo molecular simulation of methane adsorption in a slit at 298K shows that the average adsorbed methane density is sensitive to the carbon density and does not vary considerably with the carbon interlayer spacing and the number of carbon layers when the number is equal or greater than 2. The highest methane density occurred in the pore of width 0.74 nm where the interaction potential wells between the methane molecules and the opposite pore walls completely overlapped. But the largest volumetric methane storage capacity at 298 K and 3.4 MPa was achieved in the pore of width 1.12 nm which could accommodate two layers of methane molecules.

The estimated maximum stored and delivered methane capacities on different models and morphologies provided guidelines for carbon preparations. It was concluded that the optimal pore size for the adsorbed natural gas storage at 3.4 MPa and 298 K should be around 1.12 nm for both stored and delivered methane capacities. In order to meet the defined target 150 v/v of the delivered methane capacity, the carbon has to be void-free if the pore wall is thicker than three layers of graphite, or the skeletal carbon density has to be higher than 2.0 g cm^{-3} if the average pore wall is equivalent to two layers of graphite. It must be pointed out that the estimated methane capacities are based on the idealised pore models and carbon morphology. Some deviations, both positive and negative, have to be considered when comparing with the experimental results. For example, actual pores are of

irregular shapes which will have a lower adsorbed methane density than that in a slit. And also there will be a pore size distribution in real carbons rather than the single pore size assumed in the models. The particles or fibres are not perfect hard spheres or cylinders. The packing density of powders may be higher than that estimated from the HCPS configuration if a right particle size distribution can be obtained. Nevertheless the simulation has provided a lot of useful information on the relationship between adsorbed methane density and pore structure, and between methane capacity and carbon morphology.

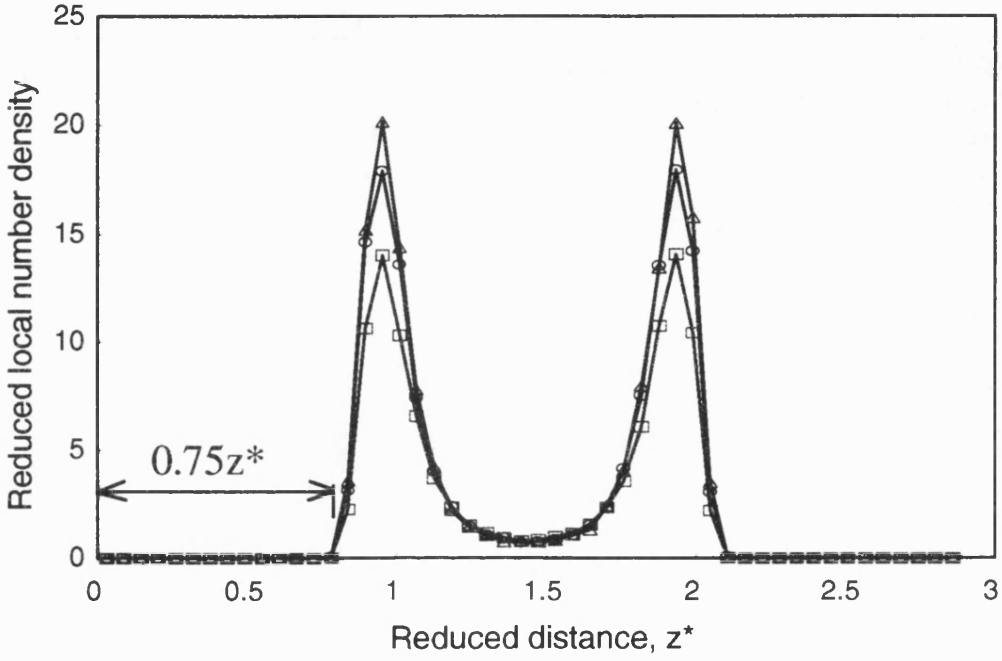

Figure 7.1 A typical reduced local methane density adsorbed in a slit model pore at 298 K and 3.4 MPa. Pore width, H = 1.12 nm, interlayer spacing, Δ = 0.3354 nm, carbon atom density, A_c = 38.18 nm^{-2}. The number of carbon layers, n = 1 (rectangles); n = 2 (circles) and n = 10 (triangles). Here the reduced methane density is defined as the number of methane molecules per reduced volume of simulation cell and the reduced distance z* is defined as $z^* = z\,\sigma_{ff}^{-3}$, refer to section 4.2.

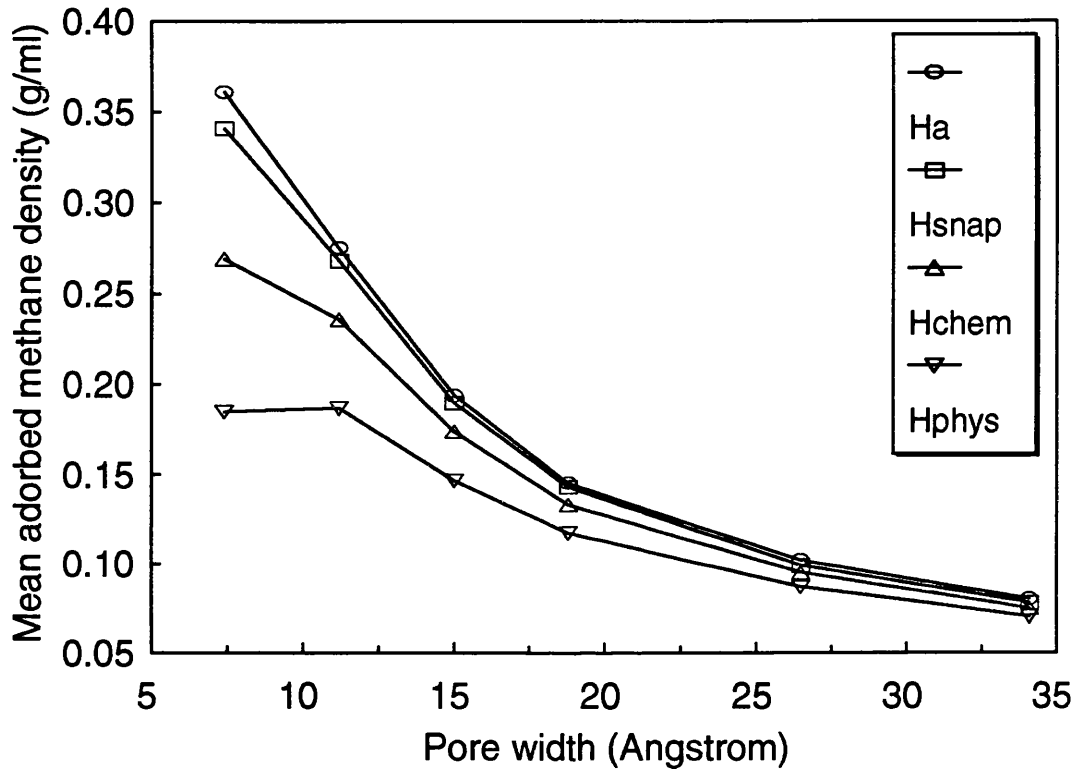

Figure 7.2 The mean adsorbed methane density for different definitions of pore width. Number of carbon layer, n = 2; interlayer spacing, Δ = 0.3354 nm; carbon atom density, A_c = 38.18 nm^{-2} ; pore width, H = 1.12 nm at temperature, T = 298 K and pressure P = 3.4 MPa.

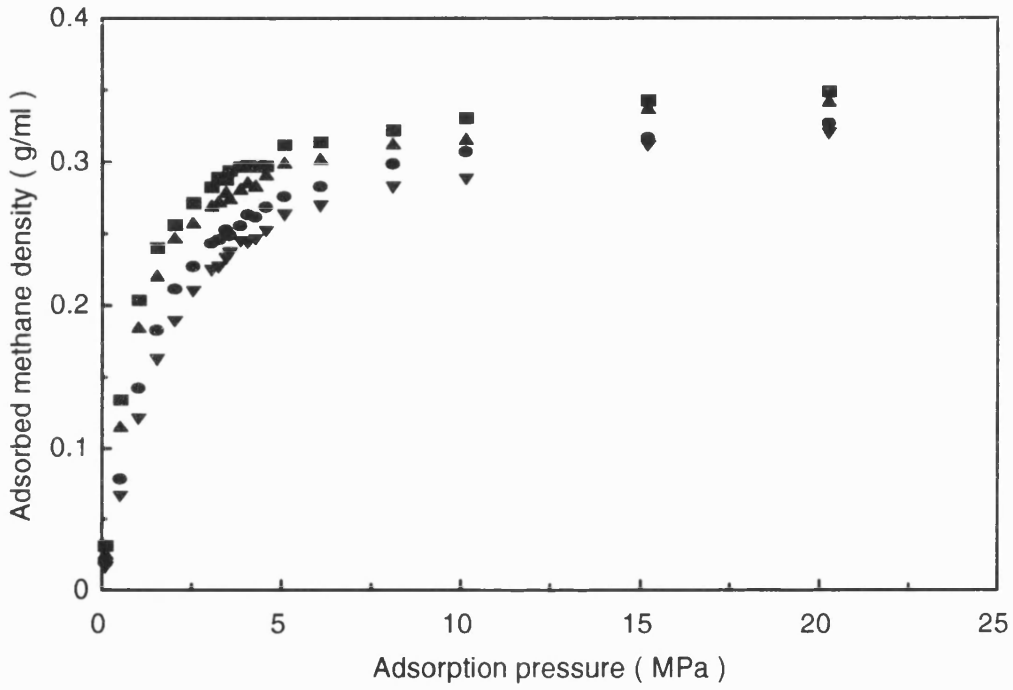

Figure 7.3 Influence of the carbon atoms density (A_c) in the carbon layer plane on adsorbed methane density in a slit model with pore width, H = 1.12 nm, number of carbon layer, n = 2, and interlayer spacing, Δ = 0.3354 nm at temperature, T = 298 K, carbon atom density, A_c = 38.18 /nm^2 (rectangles); A_c = 37.04 /nm^2 (triangles); A_c = 33.67 /nm^2 (circles).and A_c = 31.90/nm^2 (reverse triangles).

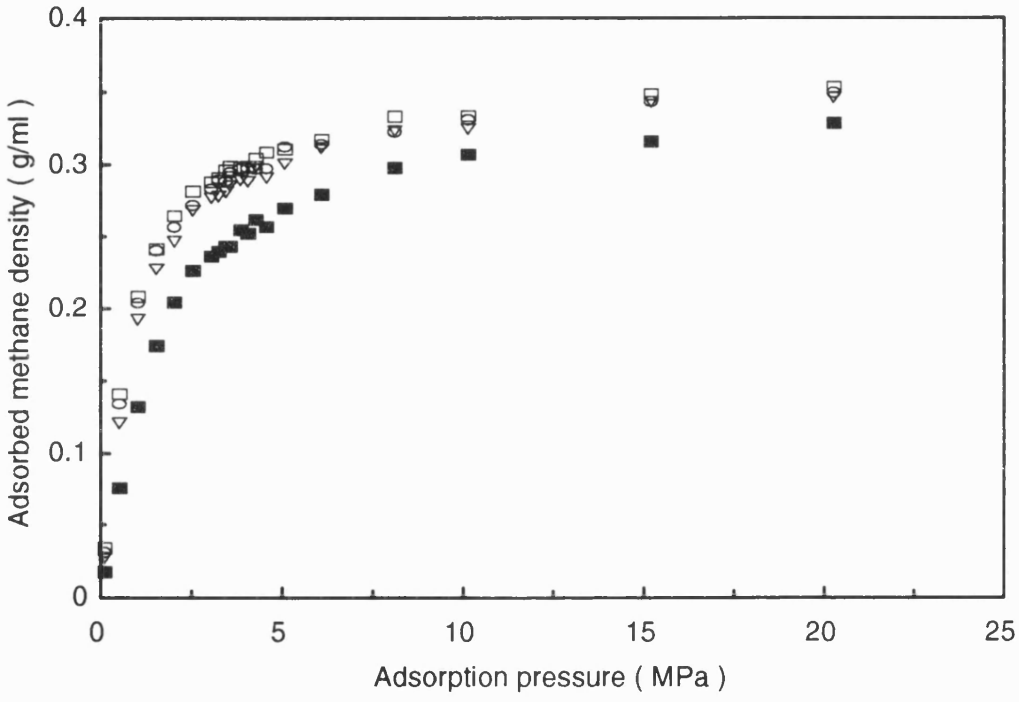

Figure 7.4 Effect of numbers of carbon layers on the adsorbed methane density in a slit model with pore width, H = 1.12 nm, interlayer spacing, Δ = 0.3354 nm, carbon atom density, A_c = 38.18 /nm^2 and temperature, T = 298 K. The number of carbon layers, n = 1 (solid rectangles); n = 2 (triangles); n = 3 (circles); n = 10 (empty rectangles).

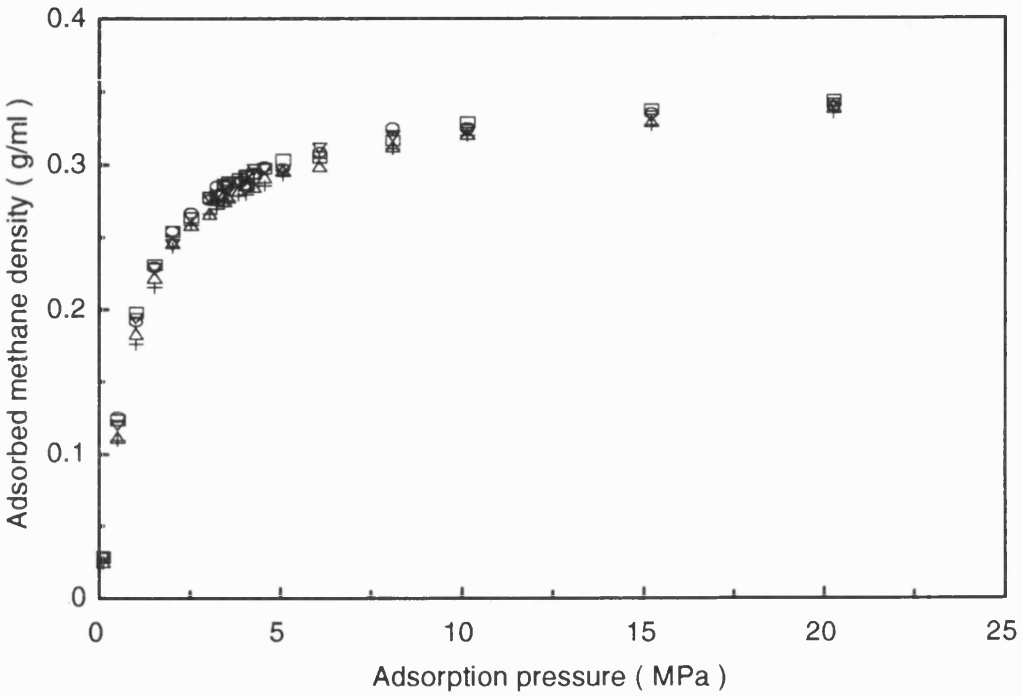

Figure 7.5 Effect of varying interlayer spacing Δ on adsorbed methane density in a slit model with pore width, H = 1.12 nm, carbon atom density, A_c = 38.18 / nm^2 and number of carbon layer, n = 2 at temperature, T = 298 K; Interlayer spacing, Δ = 0.3354 nm (rectangles); Δ = 0.345 nm (circles);. Δ = 0.352 nm (reverse triangles); Δ = 0.382 nm (triangles); Δ = 0.398 nm (cross symbols).

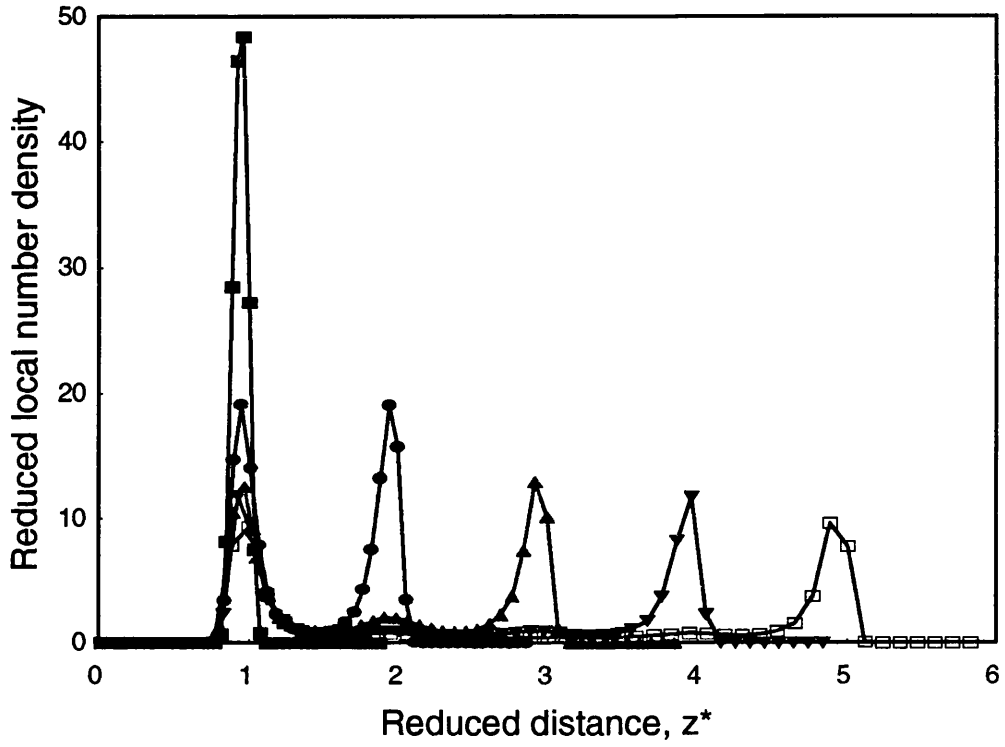

Figure 7.6 The reduced local methane densities in different pore widths: H = 0.74 nm (solid rectangles), H = 1.12 nm (solid circles), H = 1.5 nm (solid triangles), H = 1.88 nm (reverse triangles) and H = 2.65 nm (empty rectangles), at 298 K and 3.4 MPa for constant interlayer spacing (Δ = 0.3354 nm), carbon atom density, (A_c = 38.18 / nm^2) and number of carbon layers (n = 2).

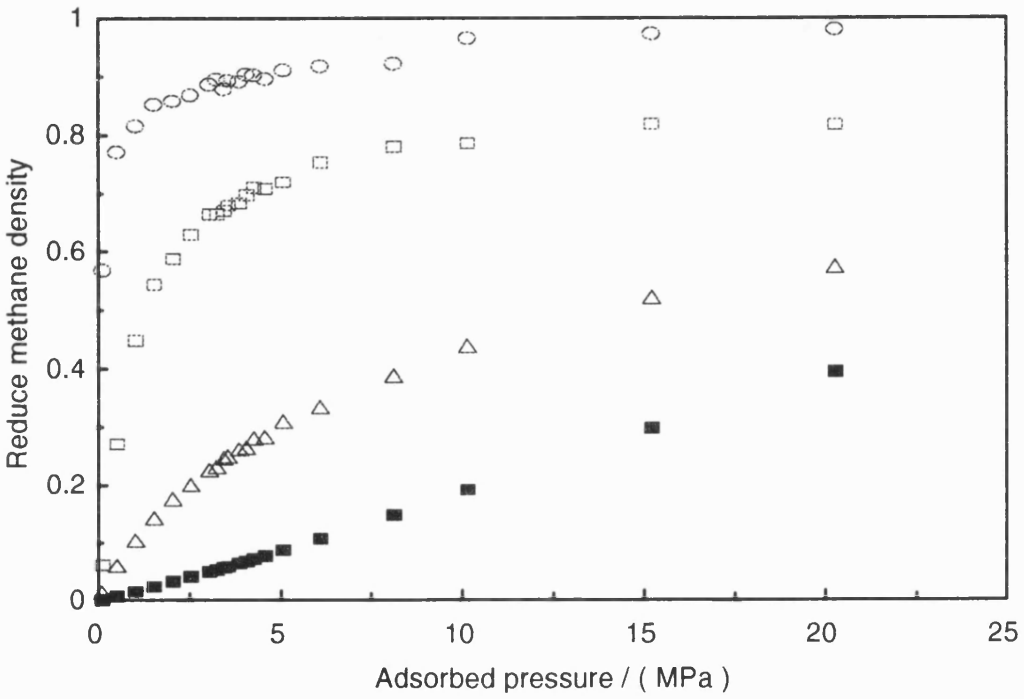

Figure 7.7. Adsorbed methane densities at 298 K in different model pores of different widths normalised to liquid methane (density = 0.41 g cm^{-3} at 112 K). Number of carbon layer planes, n = 2, interlayer spacing, Δ = 0.3354 nm, carbon atom density, A_c = 38.18 nm^{-2}. Pore width, H = 0.74 nm (circles), H = 1.12 nm (rectangles), H = 2.65 nm (triangles) and compressed methane gas (solid rectangles).

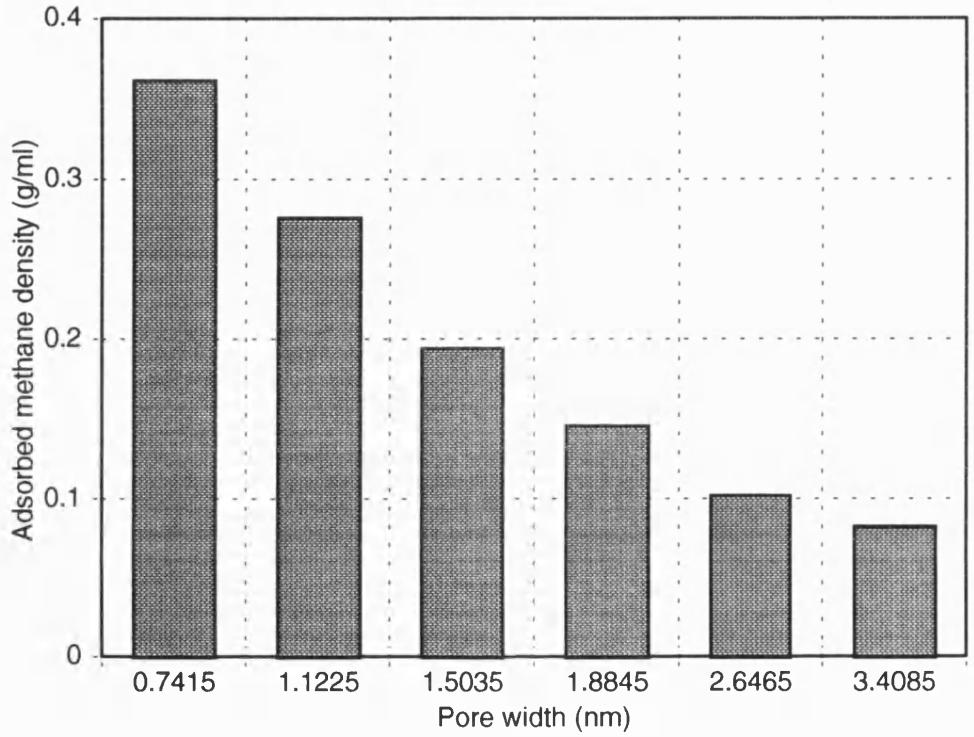

Figure 7.8 The adsorbed methane densities at 3.4 MPa and 298 K in a model pore with different widths. The number of carbon layer planes, n = 2, interlayer spacing, Δ = 0.3354 nm, carbon atom density, A_c = 38.18 nm^{-2}.

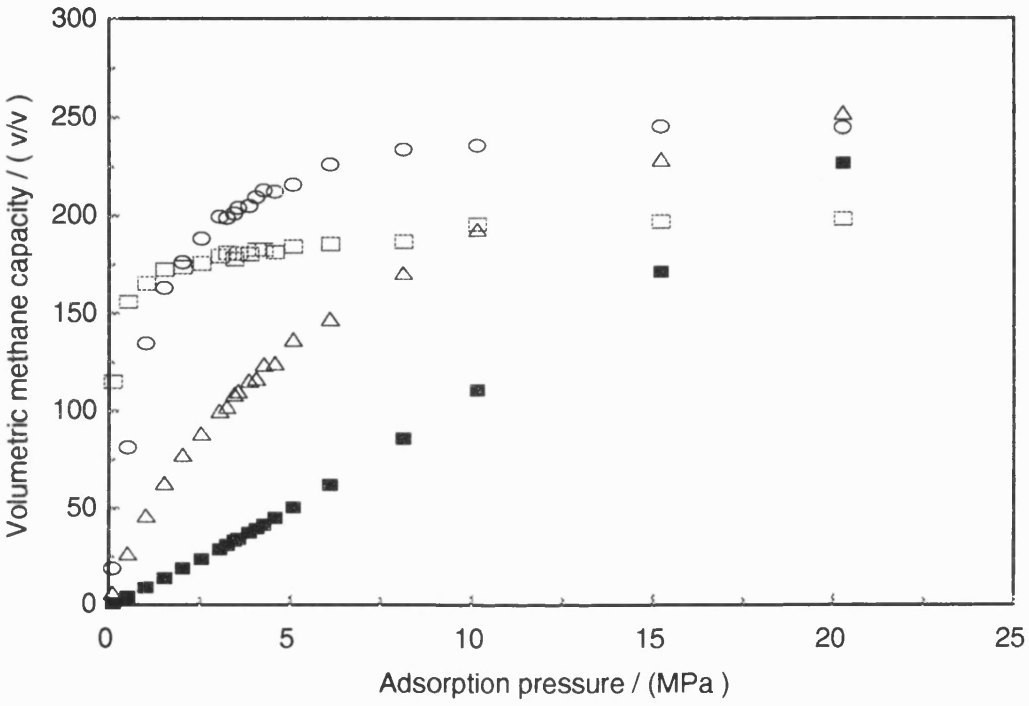

Figure 7.9 The estimated volumetric methane capacity for void free carbons with different pore widths at 298 K for a given number of carbon layer, n = 2, an interlayer spacing, Δ = 0.3354 nm, and a carbon atom density, A_c = 38.18 /nm^2. Pore width, H = 0.74 nm (circles); H = 1.12 nm (rectangles); H = 2.65 nm (triangles) and compressed methane in bulk phase (solid rectangles).

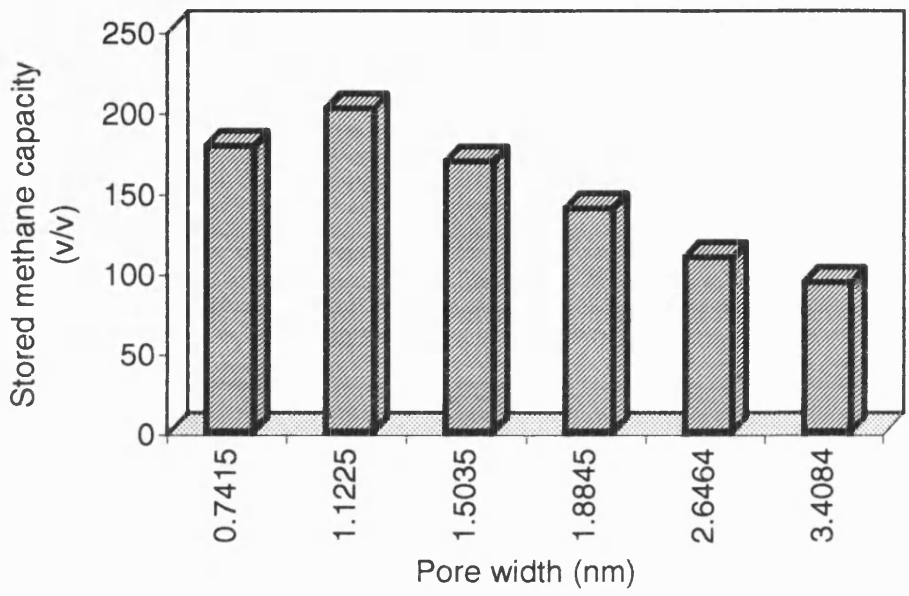

Figure 7.10 The volumetric stored methane capacities at 3.4 MPa and 298 K on void-free model monoliths with different pore widths, estimated from the grand canonical ensemble Monte Carlo molecular simulation results for a given number of carbon layers, n = 2, an interlayer spacing, Δ = 0.3354 nm, and a carbon atom density, A_c = 38.18 /nm^2.

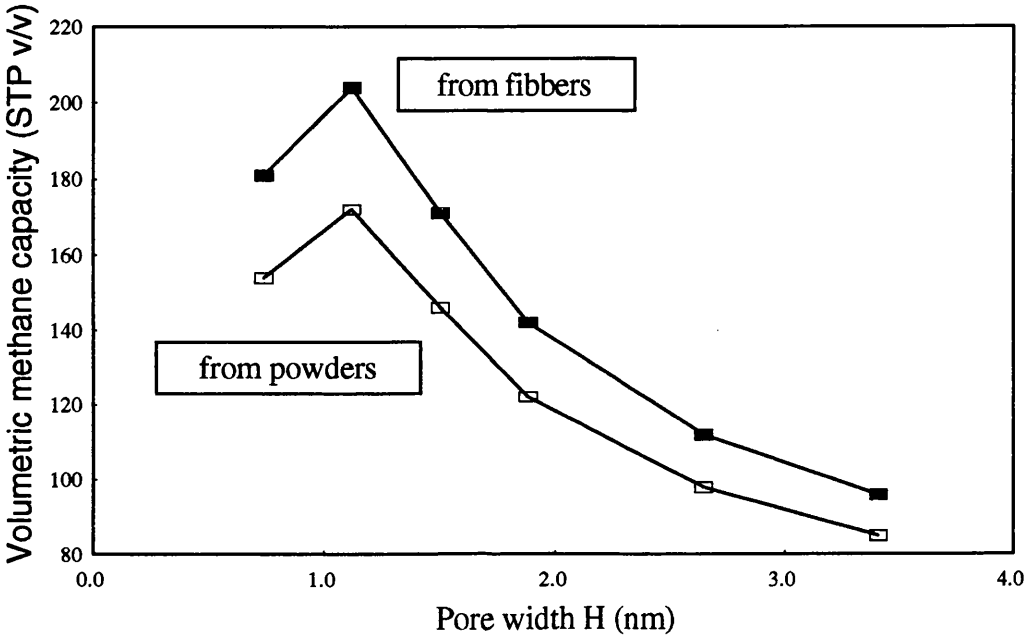

Figure 7.11 The estimated volumetric methane capacities of carbon monoliths made from microporous fibres (CPPC model) and powders (HCPS model) with different pore widths at 298 K and 3.4 MPa, estimated from the Grand canonical ensemble Monte Carlo molecular simulation results for a given number of carbon layers, n = 2, an interlayer spacing, Δ = 0.3354 nm, and a carbon atom density, A_c = 38.18 /nm^2

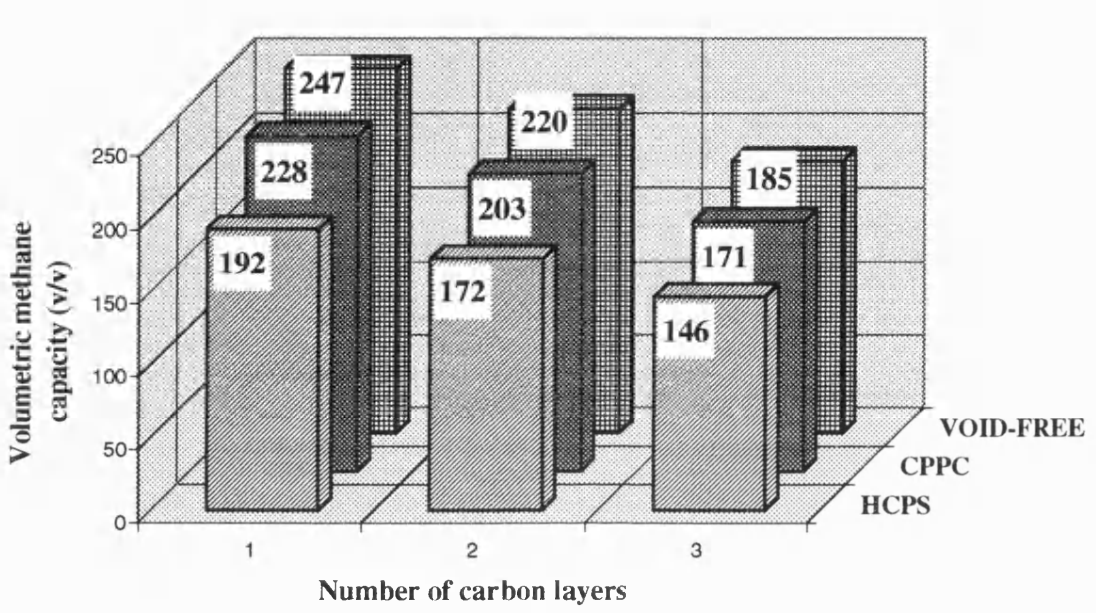

Figure 7.12 The estimated methane storage capacities on model monoliths with different morphology and different pore wall thickness for a given carbon atom density, A_c = 38.18 nm^{-2}, a pore width, H = 1.12 nm and an interlayer spacing, Δ = 0.3354 nm at 298 K and 3.4 MPa

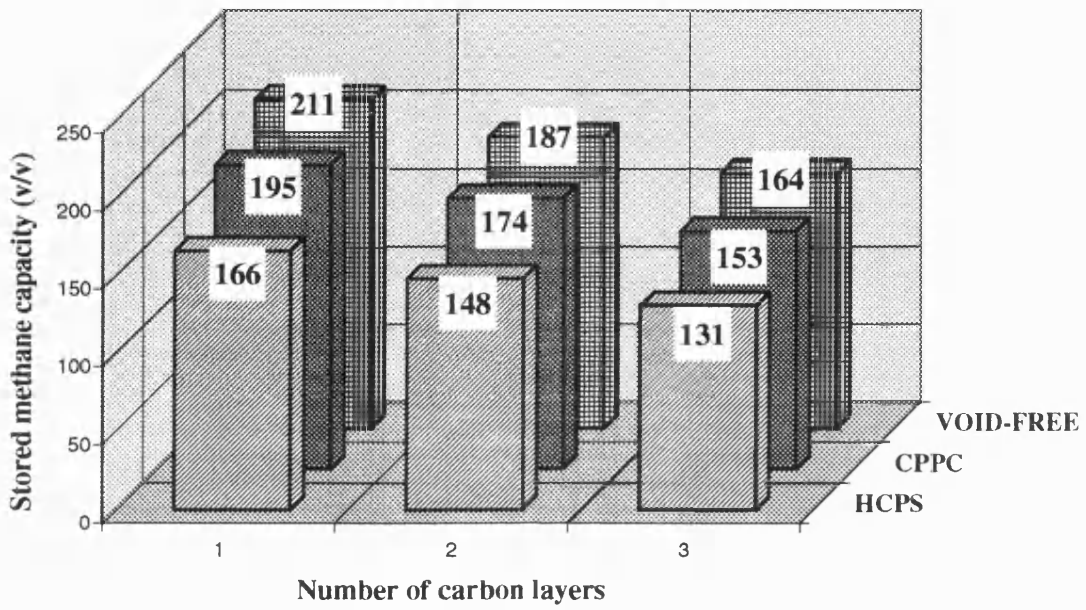

Figure 7.13 The estimated methane storage capacities on model monoliths with different morphology and different pore wall thickness for a given carbon atom density, A_c = 33.67 nm^{-2}, a pore width, H = 1.12 nm and an interlayer spacing, Δ = 0.3354 nm at 298 K and 3.4 MPa.

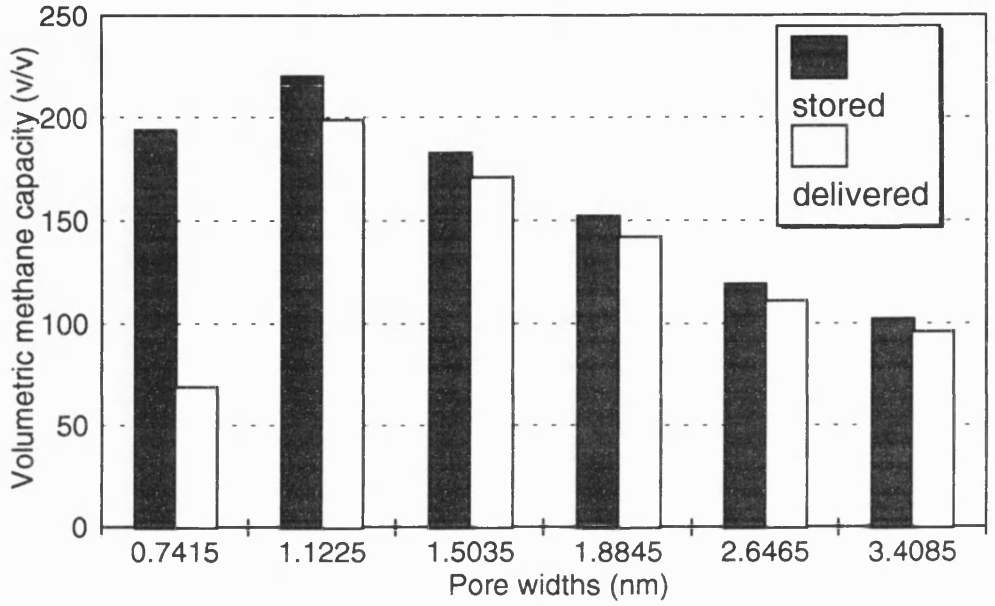

Figure 7.14 The difference between the stored and the delivered methane capacity for void-free monolith with different pore widths for a given carbon atom density, A_c = 38.18 nm^{-2}, the number of carbon layer, n = 2 and an interlayer spacing, Δ = 0.3354 nm at the temperature of 298 K, the adsorption pressure of 3.4 MPa and the desorption pressure of 0.1 MPa.

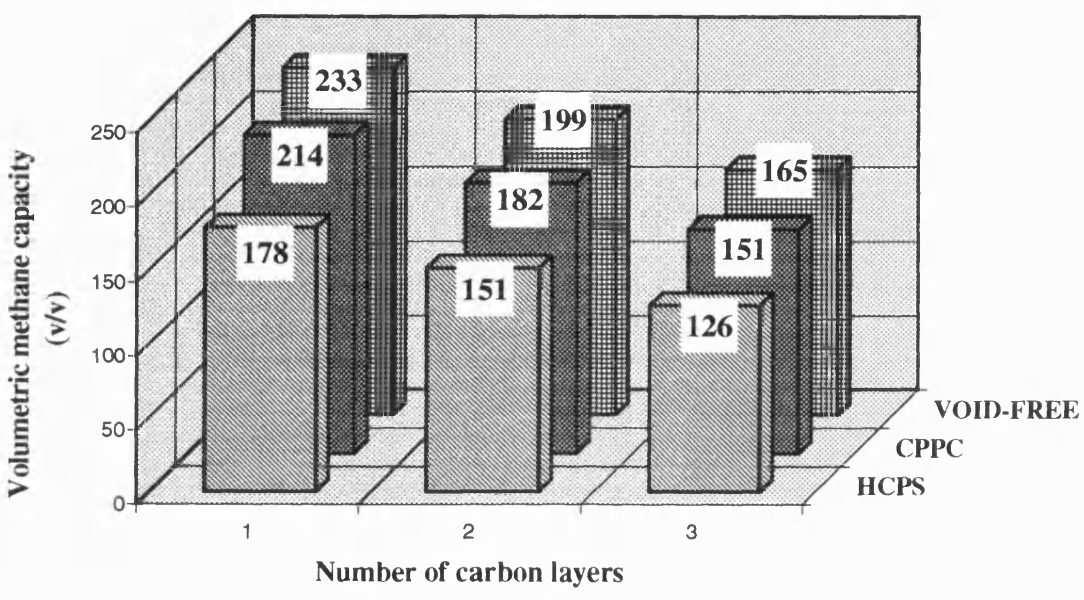

Figure 7.15 The estimated methane delivered capacity on model monoliths with different morphology and different pore wall thickness for a given carbon atom density, A_c = 38.18 nm^{-2}, a pore width, H = 1.12 nm and an interlayer spacing, Δ = 0.3354 nm at 298 K, adsorption pressure of 3.4 MPa and desorption pressure of 0.1 MPa

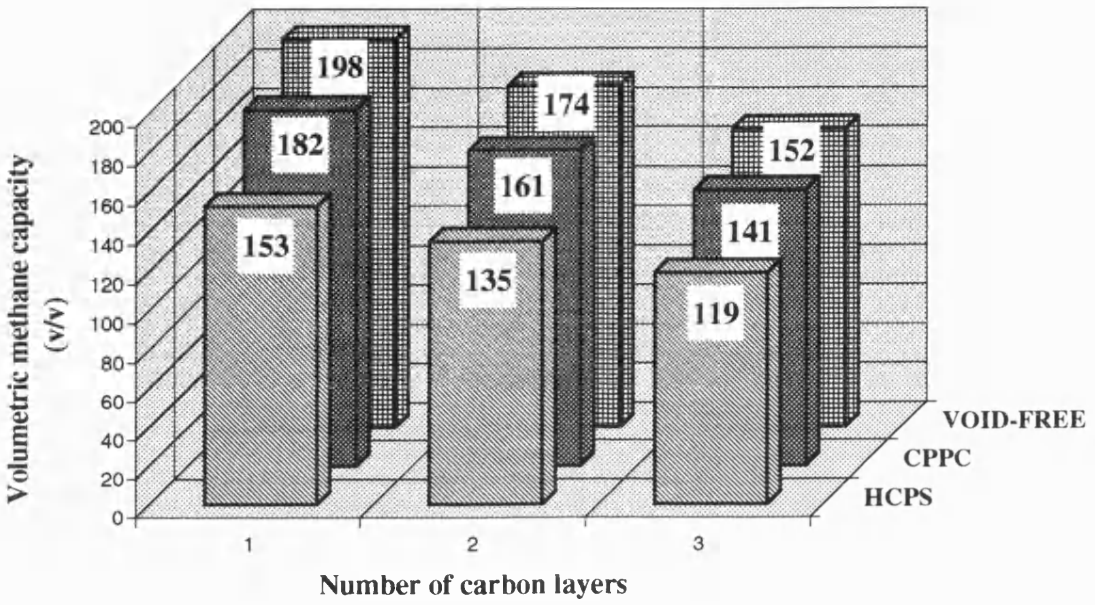

Figure 7.16 The estimated methane delivered capacity on model monoliths with different morphology and different pore wall thickness for a given carbon atom density, A_c = 33.67 nm^{-2}, a pore width, H = 1.12 nm and an interlayer spacing, Δ = 0.3354 nm at 298 K, adsorption pressure of 3.4 MPa and desorption pressure of 0.1 MPa

CHAPTER 8 PORE DEVELOPMENT AND CHARACTERISATION

The basic principle of creating pore structure from carbonaceous materials is partially and selectively to remove carbon atoms or other hetero-atoms from the precursors either by thermal oxidation or by chemical treatment so that the voids or pores left behind can be used as adsorption sites for purification, separation or concentration of other gases or liquids.

In this chapter, the weight changes during pre-oxidation and carbonisation of the raw materials used in this work are reported. The pore development from graphitizible and non-graphitizible carbonaceous materials by either physical or chemical activation process is discussed in terms of surface area, micropore volume and pore size distribution. The results of KOH activation of meso-carbon microbeads at different temperatures, reaction times and ratios by weight of KOH to meso-carbon microbeads are reported. In view of the importance of KOH activation in this work, some studies were made of the mechanisms of KOH activation by using thermal gravimetric analysis coupled with a mass spectrometer, X-ray diffraction and infrared absorption and results from these methods are reported here. Also reported are the results of KOH activation of lignite and petroleum coke, chemical activation of petroleum coke using K_2CO_3 and H_3PO_4 activation of waste paper. Some experimental results of physical activation of meso-carbon microbeads and phenolic resin beads using CO_2 are reported. The chapter concludes with some results on the development of monolithic carbons from KOH-activated meso-carbon microbeads and AX-21 carbon as well as from phenolic resin beads.

8.1 STARTING MATERIALS

The starting materials in this research include meso-carbon microbeads, petroleum coke, lignite, phenolic resin, waste-paper, and AX-21 carbon powder (for making monolithic carbons). All these materials were first studied using thermogravimetry to reveal the extent of weight loss at different temperatures. The results are presented in Sections 8.1.1 to 8.1.4.

8.1.1 Meso-Carbon Microbeads

Meso-carbon microbeads are the main precursors used in this study to develop microporous carbons. Meso-carbon microbeads are formed through a heat treatment (around 350 ~ 450 °C) under pressure of coal tar pitch. After the cracking and condensation reactions meso-carbon microbeads are separated from the pitch matrix by a high temperature centrifuge (Nakagawa, *et al*, 1985) or an emulsion method (Tateishi, *et al*, 1992). Meso-carbon microbeads mainly consist of large polyaromatic molecules and these are characterised by their high insoluble matter in toluene (97.5 %) and in quinoline (91 %) as well as high C/H ratio of 27.4 (refer to Section 5.2.1).

Figure 8.1 (a) shows that the carbonisation yield of raw meso-carbon microbeads in nitrogen at 1000 °C is about 87 %. After pre-oxidation at 300 °C in air for 30 minutes, the carbonisation yield of meso-carbon microbeads is reduced to 83 % as shown in Figure 8.1 (b). The small decrease (~ 4 %) in carbonisation yield is probably due to expulsion of the oxygen as carbon oxides that was incorporated into the structure of meso-carbon microbeads during pre-oxidation. The TGA curves of meso-carbon microbeads during low temperature pre-oxidation and high temperature oxidation in air are shown in Figure 8.2 (a) and (b). Figure 8.2 (a) shows that the weight increase of meso-carbon microbeads after pre-oxidation at 300 °C for 30 min is about 2.5 %. Figure 8.2 (b) shows that meso-carbon microbeads have been completely oxidised in air at 800 °C, which means that there is very little ash content in meso-carbon microbeads. Therefore, the so-called pitting or channelling effect (Marsh ad Kuo, 1989) caused by catalytic impurities can be assumed to be negligible during physical activation.

8.1.2 Petroleum Coke

Petroleum coke is a carbonisation product of high boiling fractions (pitches) from petroleum processing. Pitches are composed of mixtures of mainly polycyclic aromatic hydrocarbons (PAH) and small portions of alkylated PAH, hydrogenated PAH and heterocyclic aromatic hydrocarbons (Mochida *et al,* 1991) (Zander, 1987). The transformation from liquid pitch to solid coke involves complex chemical reactions including devolatization of lower molecular weight components and polymerisation which leads to the

formation of mesophase spherules. These spherules grow and coalesce to form large bulk anisotropic regions as the heat treatment progresses before the entire pitch is converted into a infusible coke (Greinke, 1994). Therefore the petroleum coke contains both isotropic and anisotropic regions. The Dumai petroleum coke used in this study has a low ash content (0.34 %) and a high fixed carbon (84.5 %). The TGA weight loss curve in Figure 8.3 shows that the carbonisation yield of the Indonesia Dumai petroleum coke is about 85 %. Both petroleum coke and meso-carbon microbeads are graphitizible carbons. They are able, as graphite is, to form intercalation compounds with alkali metals (Murdie, *et al*, 1985). The intercalated carbons have a disoriented, random structure which gives very high microporosity after the intercalated metal is washed out.

8.1.3 Lignite

Unlike petroleum coke and meso-carbon microbeads, lignite has a high volatile matter content (59.27 %), a high ash content (6.24 %) and a low fixed carbon content (34.49 %). The carbonisation yield at 1000 °C is only 52 % on dry base as shown in Figure 8.4. The removal of a large amount of volatile matter leaves many voids in the residual carbon. Therefore the lignite carbon has a higher CO_2 reactivity than meso-carbon microbeads and petroleum coke as shown in Figure 8.5. Up to 900 °C nearly all lignite has been gasified while for meso-carbon microbeads and petroleum coke the gasification seems just started.

8.1.4 Phenolic Resin

TGA curve in Figure 8.6 illustrates that phenolic resin FRD3656 has two stages of weight loss during carbonisation. Before 400 °C water vapour and some other low molecular weight substances are evolved. There is a sharp weight loss after 400 °C due to polymerisation and condensation reactions which converted the phenolic resin into a highly cross-linked carbon (Ouchi and Honda, 1959). The CO_2 reactivity of phenolic resin FRD3656 is lower than that of lignite but higher than that of meso-carbon microbeads as shown in Figure 8.5, assuming that the gasification rate of fine powders is controlled by chemical reaction and is not limited by gas diffusion.

8.2 CHEMICAL ACTIVATION

Using chemicals like $ZnCl_2$ or H_3PO_4 to create pore structures from cellulose precursors by dehydration and digestion has been known for a long time (Ostrejko, 1901). But using chemicals like alkali metal compounds to generate a high microporosity from graphitizible carbons is a relatively new technique. Wennerberg (1971) used alkali metal hydroxides to produce highly microporous activated carbons from petroleum coke. Unlike physical activation which generates pores from the outside to the inside of particles by gasifying carbon atoms, chemical activation creates pores by soaking, digesting, or intercalating (Derbyshire, *et al*, 1995) which can generate an uniform pore network with a narrow pore size distribution by selecting appropriate raw materials and chemicals as well as heat-treatment processes. In this study potassium hydroxide (KOH) and potassium carbonate (K_2CO_3) were applied to meso-carbon microbeads, petroleum coke and lignite, while phosphoric acid (H_3PO_4) was applied to waste paper. The experimental results are discussed in the Sections 8.2.1 to 8.2.5.

8.2.1 KOH Activation Of Meso-Carbon Microbeads (MCB)

KOH is a very effective reactant to create micropores from graphitizible carbon materials such as petroleum cokes (Marsh, *et al*, 1984) and meso-carbon microbeads (Nitta, *et al*, 1992). In this research, the KOH activation of meso-carbon microbeads was investigated in detail by changing the ratio of KOH to meso-carbon microbeads, activation temperature, reaction time as well as gas flow rate. The end products were characterised by their surface areas and micropore volumes to monitor the influences of the variations in these processing parameters.

8.2.1.1 KOH/MCB Ratios

KOH/MCB ratios by weight from 1:10, 1:4, 1:2, 1:1, 2:1, 4:1 and 8:1 were tested with a fixed reaction temperature of 800 °C and reaction time of 1.6 hours. The experimental procedure was described in Section 5.2.5. The BET (N_2, 77 K) surface areas and micropore volumes (deduced from D-A equation) are illustrated in Figure 8.7. The

surface areas and micropore volumes of the activated meso-carbon microbeads increased with the KOH/MCB ratio until 4:1. Further increasing KOH/MCB ratio reduced the surface area and the micropore volume. This may be because some micropores are widened by increasing the KOH/MCB ratio to 8:1. The pore size distributions in Figure 8.8 show that the differential pore volume near 2 nm has increased for the KOH/MCB ratio of 8:1, comparing with that for the activated meso-carbon microbeads prepared using a KOH/MCB ratio of 4:1. Other evidence to support this argument is that the carbon burn-off continuously increases with the KOH/MCB ratio for a given activation temperature and time, as shown in Figure 8.9. The meso-carbon microbeads may be over-activated. Therefore, a KOH/MCB of 4:1 by weight seems to be an optimal ratio for the chemical activation of meso-carbon microbeads at 800 °C. The same conclusion was obtained by Otowa, *et al* (1996) and by Marsh and Yan (1984) using petroleum coke as raw material.

The heat-treatment of graphitizible carbons in presence of excess alkali metals or their compounds is a very complicated process which is still not fully understood (Marsh and Walker, 1979) (Murdie, *et al*, 1985). There is general agreement that pore development in the potassium compounds/carbon system involves the intercalation of potassium into polycrystallite carbon structure, the oxidation of cross-linking carbon atoms and formation of functional groups on the edges of the carbon lamellae. All these interactions and intercalation may cause the separation and disorder of the constituent lamellae (Marsh, *et al*, 1984). When potassium or its compounds are removed by water-leaching from the reacted carbons, the lamellae are left as a randomly-oriented, porous structure which gives very high surface areas and micropore volumes.

The intercalated compounds of potassium with graphite have different stages as illustrated in Figure 8.10 (Marsh, *et al*, 1987). These intercalates may convert from one form to the other, depending upon the intercalation temperature and the potassium vapour pressure. It is most likely that there is co-existence of these different stages in the heat-treated KOH/MCB mixture. A higher KOH/MCB means more intercalates with high K/C atom ratios, thereafter a larger porosity can be created after the intercalated potassium was removed. But when the KOH/MCB is up to a certain level (perhaps over 4:1), the carbon oxidation probably starts to plays a negative role in micropore creation as too much carbon is gasified. It was noticed that surface area and micropore volume of KOH activated meso-

carbon microbeads increased with burn-off until around 55 % and then decreased with a further increment in burn-off. This is true no matter what causes the increase in carbon burn-off, by a higher KOH/MCB, or a higher reaction temperature or a longer reaction time.

8.2.1.2 Heat Treatment Temperature

For a given KOH/MCB ratio and a given reaction time, the carbon burn-off increased from 35 % to 62 % with the heat-treatment temperature from 750 °C to 850 °C as shown in Figure 8.11. The KOH-activated meso-carbon microbeads with the highest BET (N_2, 77 K) surface area was achieved at the reaction temperature of 800 °C. Again, the reduction in surface area from 800 °C to 850 °C may be due to the over-activation, because the carbon oxidation would be accelerated at a higher temperature. The investigation on KOH/MCB ratio and reaction temperature indicates that a burn-off between 40 and 60 % is an optimal degree of KOH-activation of meso-carbon microbeads.

8.2.2 K_2CO_3 Activation Of Meso-Carbon Microbeads

K_2CO_3 was also used to activate meso-carbon microbeads. The ratio of K_2CO_3 to meso-carbon microbeads was 5:1, which is equivalent to KOH/MCB = 4:1 in terms of K/C atomic ratio. The experimental conditions were: reaction temperature 850 °C, reaction time 5 h, carbon burn-off 30 %. However the BET surface and micropore volume (N_2, 77 K) obtained (428 $m^2\ g^{-1}$ and 0.1964 $cm^3\ g^{-1}$) were much lower than those obtained for the KOH-activated meso-carbon microbeads (2023 $m^2\ g^{-1}$ and 1.03 $cm^3\ g^{-1}$). Thus it seems that K_2CO_3 is not so effective as activating agent KOH. The same conclusion was reached by Marsh and Yan (1984) in their study of chemical activation of a series of cokes using KOH, NaOH, K_2CO_3 and Na_2CO_3. The reason for this is still not completely understood. A tentative explanation on thermodynamic consideration is that K_2CO_3 is thermodynamically more stable than KOH. Thus, the start temperature at which the interaction and intercalation between carbon and KOH may be lower than the onset temperature for intercalation between carbon and K_2CO_3. This is important because once meso-carbon microbeads are fully carbonised, a significant modification of its constituent lamellae will be hindered, which is not favourable for pore development. In support of this explanation, the

burn-off is only 30 % after 5 hour reaction with K_2CO_3 at 850 °C but with KOH the burn-off is 62 % at the same reaction temperature and 100 min.

8.2.3 KOH Activated Petroleum Coke

Petroleum coke is also graphitizible as are meso-carbon microbeads but coke is much cheaper than meso-carbon microbeads. The Indonesian petroleum coke used in this study is only 90 U.S. dollars per ton while meso-carbon microbeads supplied by Kawasaki Steel Co., Japan cost 20,000 U.S. dollars per ton. The petroleum coke was activated by KOH using a ratio of KOH/coke = 4:1 at 850 °C for 5 hours. Table 8.1 shows the comparison between KOH-activated meso-carbon microbeads and petroleum coke.

Table 8.1 The adsorptive properties of KOH-activated meso-carbon microbeads and petroleum coke.

Raw material	Burn-off (%)	BET surface area ($m^2 g^{-1}$)	Micropore volume ($cm^3 g^{-1}$)
meso-carbon microbeads	62	2313	1.03
Dumai petroleum coke	60	2381	1.07

These results shows that KOH activation of petroleum coke can also produce very high quality activated carbons.

8.2.4 KOH-Activated Lignite

Lignite is a low rank coal with high volatile matter which results in a high physical and chemical reactivity. Lignite has many cross-links within its structure. Therefore, the intercalation of potassium during its heat-treatment with KOH is unlikely according to Platzer (1960) but potassium may be adsorbed within pores left behind by the removal of volatiles. The existence of potassium metal or its compounds will promote the oxidation of lignite as catalysts. Therefore the burn-off of lignite is very high, comparing with meso-carbon microbeads or petroleum coke. 80 % of lignite was gasified after 2 hour reaction at 800 °C with KOH (KOH/lignite ratio by weight was 2:1). The residue has a surface area of

1250 $m^2 g^{-1}$ and a micropore volume of 0.35 $cm^3 g^{-1}$. Comparing the results with those of KOH-activated meso-carbon microbeads or petroleum coke, it is clear that KOH is less effective as an activating agent for lignite than it is for graphitizible carbons such as meso-carbon microbeads and petroleum pitch.

8.2.5 H_3PO_4 Activated Waste Paper

Phosphoric acid is the most commonly used agent in chemical activation of wood, after zinc chloride was abandoned due to the concern over environmental pollution. The function of the activating agent is to promote the dehydration and degradation of the cellulose material and to inhibit the formation of tar, acetic acid, methanol, *etc.* so as to enhance the porosity and the yield of carbon (Bansal, *et al*, 1988). The properties of the final activated carbons depend on the degree of impregnation (the ratio of the activating agent to raw material), the temperature and time of the kneading and the heat-treatment. In this study, the shredded waste paper was impregnated by phosphoric acid solution at the weight ratio of paper/phosphoric acid = 1:1.4. The mixture was kneaded at 150 °C for 2 hours and heat-treated at 500 °C for 2 hours. The surface area and pore volume derived from its nitrogen adsorption isotherm are just 798 $m^2 g^{-1}$ and 0.38 $cm^3 g^{-1}$ respectively, which are far below those of KOH-activated carbons. Therefore, no further investigation was pursued in this direction.

8.3 MECHANISM OF KOH-ACTIVATION OF MESO-CARBON MICROBEADS

After many experiments on different raw materials and processing techniques, it is concluded that KOH activation of meso-carbon microbeads is a most effective process to produce highly microporous carbons. Therefore, KOH activation was studied in more detail by monitoring both gas and solid phases during and after the heat-treatment of meso-carbon microbeads with KOH. Despite a number of reports on developing high-surface-area carbons by co-carbonisation of the mixture of cokes and excess amount of KOH, there is still lack of detailed knowledge concerning the mechanism of KOH activation. This is because the heat-treatment of KOH/MCB mixture is a rather complicated process which involves the interactions between many components such as KOH, K, K_2O, K_2CO_3, CO,

CO_2, H_2, H_2O, C_mH_n and C substrate. The intercalation of potassium, oxidation of cross-linking carbon atoms and formation of functional groups on the edges of the lamellae are considered to be responsible for the creation of pore structure. In this study an attempt was made to elucidate some of the factors which might influence the pore structure development of meso-carbon microbeads, using thermogravimetry analysis, X-ray diffraction and infrared absorption as well as thermodynamic considerations.

8.3.1 Influence Of Reaction Atmosphere

The effect of partial pressure of CO_2 on the reaction between meso-carbon microbeads and KOH was further investigated using TGA by changing the sweeping gas flow rate from 1.0 dm^3 helium per hour to 4.6 dm^3 per hour. The weight loss curves of a KOH/MCB mixture in Figure 8.12 shows that at a low helium flow rate, there is a weight increase between 350 °C and 650 °C. But for a higher helium flow rate, there is no such a weight increase in the whole temperature range. This weight increase at low flow rate of helium is most likely due to the formation of K_2CO_3. Initially, CO_2 is evolved either from pyrolysis of meso-carbon microbeads or from the water-gas shift reaction:

$$CO(g) + H_2O(g) \Leftrightarrow H_2(g) + CO_2(g) \qquad (8.1)$$

The CO_2 in the atmosphere can very quickly convert potassium hydroxide (KOH), potassium oxide (K_2O) or potassium element (K) into potassium carbonate (K_2CO_3) according the following reactions:

$$2KOH(s) + CO_2(g) \Leftrightarrow K_2CO_3(s) + H_2O(g) \qquad \Delta G^\circ = -232 \text{ kJ/mol} \qquad (8.2)$$

$$2K(g) + CO_2(g) \Leftrightarrow K_2O(s) + CO(g) \qquad \Delta G^\circ = -64 \text{ kJ/mol} \qquad (8.3)$$

$$K_2O(s) + CO_2(g) \Leftrightarrow K_2CO_3(s) \qquad \Delta G^\circ = -432 \text{ kJ/mol} \qquad (8.4)$$

since the equilibrium constants of these reactions are very high even at a low temperature. For instance, the equilibrium constants of reactions 8.2, 8.3 and 8.4 at 298 K are 4.63×10^{40}, 1.65×10^{11} and 5.28×10^{75}, respectively.

When a high helium flow was used, the CO_2 was swiftly blown away from the solid sample. Therefore the chance for CO_2 to react with KOH, K_2O or K is minimised. This argument is strengthened by the sharp weight increase when CO_2 is introduced into the KOH/MCB system at 300 °C as shown in Figure 8.13. The rapid increase in sample weight

is most likely due to formation of K_2CO_3 by fast chemical reactions between CO_2 and KOH or K_2O.

H_2, CO_2 and CO contents in the gas phase during the heat-treatment of meso-carbon microbeads with and without KOH were monitored by a mass spectrometer. The effect of KOH on the pyrolysis of meso-carbon microbeads was studied by comparing the difference in gas composition as shown in Figures 8.14 to 8.16.

As shown in Figure 8.14 there are two peaks of hydrogen at 450 °C and 800 °C for KOH/MCB mixture but there is only one peak of hydrogen at ca. 850 °C for meso-carbon microbeads. The temperature at which hydrogen can be detected for KOH/MCB is about 300 °C, much lower than that (~ 500 °C) for meso-carbon microbeads. This indicates (Otowa, *et al*, 1994) that the presence of potassium-containing species in the system probably promotes catalytic gasification ($C + H_2O \rightarrow H_2 + CO$) and may also catalyse the water-gas shift reaction ($CO + H_2O \rightarrow H_2 + CO_2$). Low temperature gasification may be very important in the development of pore structure in the carbon. The evolution of H_2 in the temperature range 400~1000 °C for pure meso-carbon microbeads is attributed to dehydrogenative condensation reactions during carbonisation.

Figure 8.15 shows that carbon dioxide concentration starts to increase significantly after 500 °C for KOH/MCB mixture but for meso-carbon microbeads, CO_2 gradually increases only after 650 °C. The difference in CO_2 concentration between MCB and KOH/MCB systems in the range of 400 ~ 650 °C indicates once again the catalytic promotion of water-gas shift reaction. There might be small contribution from the decomposition of K_2CO_3 ($K_2CO_3 \rightarrow K_2O + CO_2$) but K_2CO_3 is thermodynamically stable before 700 °C. The CO_2 increase for both MCB and KOH/MCB systems in the high temperature region is believed due to the carbonisation process and desorption of oxygen-containing functional groups on carbon surface.

The increasing evolution of CO after 700 °C, as illustrated in Figure 8.16, may be attributed to the reduction and intercalation of K_2CO_3 and K_2O with carbon:

$$K_2CO_3(s) + (4n+2)C(s) \rightarrow 2C_{2n}K(s) + 3CO(g) \qquad (8.5)$$

$$K_2O(s) + C(s) \rightarrow 2K(g) + CO(g) \quad (8.6)$$

$$2K(g) + 4nC(s) \rightarrow 2C_{2n}K(s) \quad (8.7)$$

One piece of visual evidence of the reaction 8.6 is the potassium metal deposited on the furnace tube when the heat treatment temperature is over 800 °C.

To summarise the above discussion, considerable amount of CO_2 exists in the atmosphere of KOH/MCB heat-treatment system. The conversion of KOH, K_2O and K to K_2CO_3 by CO_2 is not favourable for the development of pore structure because as mentioned in Section 8.2.2 K_2CO_3 is not as effective activating agent as KOH. By increasing the sweeping gas flow rate, the negative effect of CO_2 can be minimised but can not be eliminated (Ehrburger, *et al*, 1986).

8.3.2 Structure Changes Of Meso-Carbon Microbeads After Different Heat Treatment

X-ray diffraction was used to analyse natural graphite flake, raw meso-carbon microbeads, carbonised meso-carbon microbeads at 600 °C and 1000 °C, CO_2 activated meso-carbon microbeads at 900 °C, KOH activated meso-carbon microbeads at 400, 700 and 800 °C as well as K_2CO_3 activated meso-carbon microbeads at 850 °C in order to study the lattice structural changes after different processes. The carbon structure parameters were deduced from the X-ray diffraction spectra, illustrated in Figures 8.17 to 8.23, using equations 6.31–6.34 (refer to Section 6.6) and the results are listed in Table 8.2.

Comparing with the X-ray diffraction pattern of natural graphite flake (Fig. 8.17) the characteristic peak of (002) plane diffraction for raw meso-carbon microbeads (Fig. 8.18) and carbonised meso-carbon microbeads (Fig. 8.19) shifts to smaller diffraction angles and becomes broader, which indicates that the interlayer spacings of meso-carbon microbeads both treated and untreated are larger and the L_a and L_c parameters are smaller than the corresponding values for graphite. Following carbonisation of meso-carbon microbeads (Table 8.2) shows that the interlayer spacing decreases from 0.382 to 0.351 nm, the stack height increases from 2.292 to 3.836 nm and the stack width from 3.738 to 7.307 nm. This suggests that during carbonisation, 'hypothetical' crystallites grow bigger and the structure of meso-carbon microbeads becomes more regularly oriented.

Table 8.2 Structure parameters estimated from X-ray diffraction spectra

Samples	$2\theta_{(002)}$	$2\beta_{(002)}$	$2\theta_{(100)}$	$2\beta_{(100)}$	$d_{(002)}$ (nm)	L_c (nm)	L_a (nm)	m
Pure graphite	26.6	0.34	54.7	0.3	0.335	47.55	122.08	142
MCB	23.282	7.008	43.411	9.336	0.382	2.292	3.738	6
MCB-600	24.812	5.071	43.409	7.428	0.359	3.177	4.713	9
MCB-1000	25.410	4.204	43.430	4.791	0.351	3.836	7.307	11
KOH-MCB-400	25.640	3.527	43.218	7.058	0.347	4.575	4.957	13
KOH-MCB-700	no peak		42.329	7.934			4.396	
KOH-MCB-800	no peak		43.480	5.662			6.184	
K_2CO_3-MCB-850	24.143	7.289	43.604	10.55	0.368	2.207	3.321	6
CO_2-MCB-900	22.326	7.064	43.349	4.674	0.398	2.270	7.488	6

Notes: MCB-600 and -1000 are the carbonised meso-carbon microbeads at 600 and 1000 °C; KOH-MCB-400, -700, and -800 are the KOH-treated meso-carbon microbeads at 400, 700 and 800 °C; K_2CO_3-MCB-850 is the K_2CO_3-treated meso-carbon microbeads at 850 °C and CO_2-MCB-900 is the CO_2 activated meso-carbon microbeads at 900 °C.

Comparing the X-ray diffraction spectrum of raw meso-carbon microbeads (Fig. 8.18) with the spectra for KOH-treated meso-carbon microbeads at 400 °C (Fig.8.20) and at 800 °C (Fig. 8.21) shows that the characteristic peak of (002) plane diffraction is retained at 400 °C but is removed at 800 °C. This means that the original regular structure of meso-carbon microbeads was intact after KOH treatment at 400 °C but was completely destroyed after KOH treatment at 800 °C due to the intercalation and interaction, as interpreted before. The regularly oriented 'lamellar constituent molecules' (Marsh, 1989) in meso-carbon microbeads were transformed into a randomly-oriented, irregular configuration. It is this highly-disordered stacking in three dimensions that is responsible for the very high internal surface area and microporosity in KOH-activated meso-carbon microbeads. The X-ray diffraction spectrum (Figure 8.21) for KOH-activated meso-carbon microbeads at 800 °C rises sharply at small angles, which indicates the small angle X-ray scattering from micropores.

For CO_2 activated (Fig. 8.22) and K_2CO_3 treated (Fig. 8.23) meso-carbon microbeads, the $d_{(002)}$ peaks still exist even though the heat treatment temperature goes up to 900 and 850 °C respectively. The formation of the intercalation compounds between K_2CO_3 and solid carbon at temperature less than 1400 K is very small (Marsh, 1995). So the stacking order of lamellar constituent molecules in meso-carbon microbeads has not been interrupted as was the case for the KOH activated meso-carbon microbeads. Unlike the KOH activation process, CO_2 activation does not destroy the basic structure of original meso-carbon microbeads. The pore structure was developed by oxidising the carbon atoms at 'active sites' (edge carbon atoms or defects). Most of the carbon atoms lost during the gasification are on external surfaces instead of from the internal structure.

8.3.3 Surface Functional Groups

The raw meso-carbon microbeads and KOH-activated meso-carbon microbeads at 400 and 800 °C were examined using a Fourier Transform Infrared (FT-IR) to study the variation in their surface properties by comparing their infrared spectra before and after the heat treatment processes. Their infrared absorption spectra are illustrated in Figures 8.24-8.26.

No significant changes (comparing Figures 8.24 and 8.25) in surface properties of meso-carbon microbeads are observed after KOH treatment at 400 °C, but Figure 8.26 shows a radical change after KOH treatment at 800 °C with evidence for surface oxides (Meldrum and Rochester, 1990) at ~1700 cm^{-1} and 1900 cm^{-1} (due to C=O group stretch) and at ~3400 cm^{-1} (due to O-H stretching and vibrations). The strong absorption band between 1600 and 1700 cm^{-1} is probably attributed to the overlap of C=O stretch and skeletal C=C vibrations. The assignment of the peak at 2350 cm^{-1} (anti-symmetrical stretch of O=C=O) is uncertain. It may be due to the carboxyl or lactone functional groups on carbon surface, or, it is caused by imbalance of absorption by atmospheric CO_2 between the sample and background spectral recording.

8.3.4 Pore Development Of Meso-Carbon Microbeads By KOH-Activation

The development of pore structure from meso-carbon microbeads by KOH activation is illustrated in Figure 8.27. The lamellae (Fig. 8.27 a) which are oriented parallel to the equatorial axis of raw meso-carbon microbeads are broken, twisted and puckered up randomly in three dimension (Fig. 8.27 b) because of intercalation and oxidation with potassium and potassium compounds. After the intercalated potassium compounds are washed away by water leaching, the carbon becomes highly porous (Fig. 8.27 c). The results of X-ray diffraction provides the evidence that the regular structure of meso-carbon microbeads is destroyed after KOH activation at a high temperature. The infrared spectroscopic results suggest that there is significant formation of surface groups on the KOH activated meso-carbon microbeads. This may be due, at least in part, to oxidation of the carbon surface by a variation on reaction 8.6:

$$K_2O + 2C \rightarrow 2K + 2C(O)$$

where C(O) represents a surface oxide. Alternatively, the surface of the carbon produced after intercalation by potassium may be more reactive on exposure to air at room temperature than are physically activated carbons (Otowa, *et al*, 1996).

8.4 PHYSICAL ACTIVATION

Physical activation is a most commonly used commercial process to produce activated carbons from coals and coconut shells. It involves the controlled gasification of carbon materials by oxidising gases such as steam, carbon dioxide, oxygen or their mixtures. The pore development by physical activation depends on the difference in reactivity of carbon atoms. The carbon atoms which are located at the edge of aromatic carbon lamellae or at defects and dislocations are more reactive because they have unpaired electrons or residual valences. They form surface compounds more easily by oxidation. These compounds will decompose and remove oxidised carbon atoms from the carbon surface as gaseous oxides, leaving behind new unsaturated carbon atoms for further reaction with the activating gases. Therefore, the porosity and the pore size distribution of the final carbon adsorbent are largely determined by the nature of the raw materials and the extent of carbon burn-off. For a variety of activated carbons produced by physical activation processes, it is

true that micropores are dominant when carbon burn-off is less than 50 %, macropores greater than 75 % and a mixed pore sizes between 50 and 75 % (Bansal, *et al*, 1988). As concluded from the molecular simulation study in Chapter 7, only micropores are useful for methane storage (natural gas storage) at a supercritical temperatures. Based upon this point, the carbon burn-off should be controlled to be lower than 50 %. But there is always a contradiction between micropore volume and total porosity. Low carbon burn-off can generate micropores but the porosity is normally not very high. High carbon burn-off will give a large porosity but at the same time some micropores will be expanded into mesopores and macropores. These problems are inevitable due to the way that pores are created by physical activation. The results of CO_2 activated meso-carbon microbeads and phenolic resin carbon will be presented next to illustrate these points.

8.4.1 CO_2 Activated Meso-Carbon Microbeads

The pre-oxidised meso-carbon microbeads were activated by CO_2 to burn-off values of 10, 27, 36, 60 and 75 %, respectively. The residual carbons were analysed by nitrogen adsorption at 77 K. Their surface areas, micropore volumes and pore size distributions derived from their nitrogen adsorption isotherms are illustrated in Figure 8.28 and 8.29. The results in Figure 8.28 show that the surface areas and micropore volumes of the CO_2 activated meso-carbon microbeads first increase with the carbon burn-off up to 60 % and then decrease. The decline is probably due to the over-activation when the burn-off increases to 75 %. The pore size distribution in Figure 8.29 indicates that the pores are widened as the carbon burn-off increases.

8.4.2 CO_2 Activated Phenolic Resin Carbon

Cured phenolic resin is highly cross-linked and so cannot be re-arranged into pre-graphitic structures during carbonisation as is the case with pitch precursors of meso-carbon microbeads. Consequently phenolic resin carbons have a more disordered structure than meso-carbon microbeads so that they can be readily activated by reaction with CO_2.

In the case of physical activation, carbon atoms are removed by gasification. If all carbon gasification occurs inside the carbon, a high porosity would be created without

changing the particle size. This is more likely to be the case for CO_2 activation of phenolic resin carbons. On the other hand, gasification at the external surface would result in particle shrinkage and no porosity development. This is more likely to be the case for CO_2 activation of meso-carbon microbeads. Based upon the same carbon burn-off value, i.e. 60 %, CO_2 activated phenolic resin carbon has a surface area of about 2000 m^2g^{-1}, while CO_2 activated meso-carbon microbeads only have about 450 m^2g^{-1}. Both internal and external gasification occur during CO_2-activation of phenolic resin carbon and meso-carbon microbeads, but the former has a much higher ratio of internal to external gasification than the latter.

8.5 MONOLITHIC CARBONS

8.5.1 Fabrication Of Large Size Carbon Monoliths

Two procedures are considered for the fabrication of monolithic activated carbons as illustrated in Figure 5.1. The first strategy is that ground raw material is reformed into a monolith with or without binders and then this is followed by carbonisation and activation to develop pore structure from the monolith. The second strategy is that microporous powders are created from precursors first and then the powders are consolidated into a monolith with binders.

For the first route there is a severe gas diffusion problem which will cause a non-uniform pore network within the carbon monolith. This phenomenon was demonstrated by activating a phenolic resin carbon bar (30 mm in diameter and 30 mm in length) by reaction with CO_2. As illustrated in Figure 8.30, the CO_2 activated phenolic resin carbon bar was removed layer by layer using abrasion. The external layer (15 wt.%), middle layer (35 wt.%) and internal core (50 wt.%) of the monolith were analysed by nitrogen adsorption at 77 K. The measured isotherms of the different fractions are illustrated in Figure 8.31. Their BET surface areas derived from these isotherms are given in Figure 8.30 and pore size distributions in Figure 8.32. Figure 8.30 clearly show that the outer layers of the monolith have been well activated while the internal part had an under-developed pore structure. The BET surface area of the external 15 % of CO_2 activated phenolic resin bar is 2056 $m^2\ g^{-1}$ while the internal 50 % core is only 359 $m^2\ g^{-1}$. Further increases in carbon burn-off may improve the internal porosity, but the external regions of the monolith may become over-

activated. The isotherm shapes (Figure 8.31) and the pore size distribution (Figure 8.32) of the different fractions of the monolith indicate that the micropores in external regions have been widened while micropores in the internal portion are being created. The average pore widths of the outer (15 %), middle (35 %) and inner (50 %) layers of CO_2-activated resin bar are 1.2, 0.85 and 0.61 nanometer, respectively. This non-uniform pore network within particles is not a big problem for commonly used activated carbons as their particle sizes are normally less than 5 mm. But in this particular application of activated carbons for adsorbed natural gas as an on-board vehicle fuel, large size microporous carbon monoliths are required in order to reduce interparticle voids. The cylinders used by British Gas plc. to contain activated carbon monoliths for a natural gas vehicle using adsorbed natural gas have a diameter of ca. 300 mm. Despite using regularly shaped monoliths to fill the cylinder, piece by piece, in order to reduce the monolith size, the maximum dimension of individual piece is still much larger than 30 mm. Therefore, this problem of differential pore size within the monolith becomes prominent. Unfortunately, this problem is inevitable in physical activation of large sizes of a carbon monolith as the activation occurs according to the following steps:

1. oxidising gas diffusing from gas phase into the external and the internal surfaces of carbon particles;
2. gas molecules adsorbed to the carbon surface and reacted with carbon atoms;
3. the chemical reaction products desorbed from the carbon surface and diffused out of particles and the carbon monolith.

Reactant gas molecules must diffuse through a long distance in order to reach the internal parts of large size monoliths and also the chemical reaction products have to diffuse out counter-currently which hinders the diffusion of reactive gas molecules into the internal reactive sites. These diffusion limitations result in the concentration gradients of the reactive gas both within monoliths and particles. Therefore, the pore size and the degree of activation in external regions of particles and monoliths are always greater than those in internal regions. This leads to the conclusion that the direct physical activation of a large size carbon monolith is not a suitable process to create uniform microporous carbon monoliths. An effort was made to create micropore structure in coconut carbon monolith using air cycle oxidation technique (See Section 5.6.4), but the measured methane capacity (see Table 9.4, Section 9.3.1) on this carbon is not very encouraging. Considering the unavoidable shortcomings of the procedure I in Figure 5.1, this method was not considered

any further. Instead work was focused on fabricating carbon monoliths from microporous powers with a binder following the procedure II in Figure 5.1.

8.5.2 Binder Percentage

Phenolic resin was selected as a binder to consolidate microporous powders into a monolith. The packing density of the powders can be enhanced by compacting with binder, but the binder will reduce the adsorption capacity because the binder normally does not have a high porosity. A balance between adsorption capacity and packing density as well as mechanical strength of the carbon monolith has to be made in term of the ratio of binder to microporous powders. Using microporous activated carbon powder AX-21, the influences of the binder/filler ratio on the surface area, pore volume and packing density of carbon monolith were investigated. The experimental results of the consolidation of AX-21 carbon powder by phenolic resin beads show that the integrated monolith can only be successfully formulated under an elevated temperature (150 °C) at which the phenolic resin beads become soft. Under an ambient temperature, the compacted powders easily fall apart again, especially in the case of a low binder ratio.

Figure 8.33 shows the nitrogen adsorption isotherms of the monoliths made from AX-21 carbon powder with different phenolic resin ratios. The BET surface areas and bulk densities of these monoliths are illustrated in Figure 8.34. The surface area decreased linearly and the bulk density increased with the addition of phenolic resin binder. The compromise between the decline in surface area) and the enhancement in bulk density on the volumetric methane capacity of the AX-21 carbon monoliths leads to the optimal binder ratio of ca. 30 wt %, estimated by an empirical expression (Mullhaupt, *et al*, 1992) between methane adsorptive capacity and BET surface as shown in Figure 8.35. Therefore, the binder ratio of 30 % by weight was used when the carbon monoliths from KOH activated meso-carbon microbeads powders were made. The properties of the carbon monoliths made from KOH activated meso-carbon microbeads with different burn-off values are listed Table 8.3, along with the monoliths made from AX-21 carbon powder as well as a reference monolith (using for an adsorbed natural gas vehicle road test) made from coconut shells provided by British Gas plc.

Table 8.3 The physical properties of carbon monoliths made from KOH-activated meso-carbon microbeads, AX-21 carbon powder and coconut carbon.

carbon monoliths	surface area (BET, N_2, 77K) ($m^2 g^{-1}$)	pore volume (D-A method) ($cm^3 g^{-1}$)	bulk density ($g\ cm^{-3}$)
AX-83	2432	0.91	0.43
AX-69	2056	0.86	0.59
AX-56	1553	0.66	0.64
AX-45	1357	0.62	0.70
AMCB-40	1687	0.73	0.67
AMCB-48	2145	0.96	0.58
AMCB-66	1775	0.85	0.59
BG-5R	847	0.41	0.77

Note: AMCB series are the monoliths made from KOH activated meso-carbon microbeads with 30 wt.% phenolic resin as binder and the number followed the AMCB represents the burn-off value for the meso-carbon microbeads after KOH activation. AX series are the monoliths made from AX-21 carbon powder and the number after AX is the AX-21 carbon percentage in the monolith. BG-5R is the reference monolith made from coconut shells.

8.5.3 Compressive Strength Of Carbon Monolith

No standard or literature values are available on mechanical strength requirement of carbon monoliths for adsorbed natural gas application. But logically the carbon monolith should have a certain level of compressive strength in order to prevent the generation of dust during gas charge and discharge of monolith-filled cylinders. Some of the monoliths were compressed until total collapse. The compressive strengths of the monoliths are in a region of 10 to 35 MPa as given in Table 8.4. The mechanical properties of AX-21 carbon monolith series were improved by increasing the binder ratio. The compressive strength was enhanced from 10 to 35 MPa when the binder ratio increased from ca. 30 % to 65 %. The AX-21 carbon monolith with 17 % binder is an aggregated but not agglomerated monolith. The monolith with ca. 30 % binder can give a dust free monolith.

Table 8.4 The compressive strengths of carbon monoliths

monoliths	compressive strength MPa
AX-69	10.09
AX-56	10.29
AX-45	28.72
AX-35	35.26
AMCB-40	17
AMCB-66	22

Note: AMCB series are the monoliths made from KOH activated meso-carbon microbeads with 30 wt.% phenolic resin as binder and the number followed the AMCB represents the burn-off of meso-carbon microbeads after KOH activation. AX series are the monoliths made from AX-21 carbon powder and the number after AX is the AX-21 carbon percentage in the monolith.

The monolith with 65 % binder has a mechanical strength comparable to nuclear grade graphite (35 ~ 75 MPa compressive strength). But this high strength is not necessary for the monolith targeted for adsorbed natural gas application because too much binder would significantly reduce adsorption capacity.

8.5.4 Micropore Volume From CO_2 And N_2 Isotherms

The CO_2 adsorption isotherms at 298 K and pressure up to 4.0 MPa on the carbon monoliths AMCB-48 and AX-83 were gravimetrically measured on a high pressure electron microbalance. The gravimetrically measured isotherm is an excess isotherm which must be converted into an absolute isotherm in order to apply Dubinin-Astakhov equation to it. The excess isotherms of CO_2 adsorption on AMCB-48 and AX-83 were corrected into the absolute isotherms according to the following expression (DeGance, 1992):

$$n_{abs} = \frac{n_{exc}}{1 - \frac{v_{ads}}{v_{gas}}} \quad \text{---------- (8.8)}$$

where n_{abs} (mmol g^{-1}) and n_{exc} (mmol g^{-1}) are the absolute and excess amounts of CO_2 at pressure P (MPa) respectively, v_{ads} (cm^3 mol^{-1}) and v_{gas} (cm^3 mol^{-1}) are the molar volumes of CO_2 at 298 K in the adsorbed phase and the gas phase respectively. The density of the adsorbed CO_2 at 298 K is the main problem in above calculation as it can be varying in the range of 0.7 ~ 1.03 g cm^{-3}. The value 0.7 g cm^{-3} corresponds to the density of liquid CO_2 and the value 1.03 g cm^{-3} is the adsorbed CO_2 density according to Dubinin's approach (Dubinin, 1960). In this study a literature value of 0.85 g cm^{-3} , which was obtained from the comparison of CO_2 adsorption at 273 K and 298 K (Cazorla-Amoros, *et al,* 1996), was taken as the adsorbed CO_2 density at 298 K. So the molar volume of the adsorbed CO_2, v_{ads}, is 51.7647 cm^3 mol^{-1}.

The molar volume of CO_2 in gas phase at pressure P, v_{gas}, was calculated by

$$v_{gas} = \frac{RT}{ZP} \quad \text{---------- (8.9)}$$

where Z is the CO_2 compressibility, which was given by Lee and Kesler table (Reid, *et al,* 1977)

$$Z = Z_o(T_r, P_r) + \omega Z_1(T_r, P_r) \quad \text{---------- (8.10)}$$

here Z_o and Z_1 can be found using the reduced temperature T_r ($T_r = T/T_c$) and reduced pressure P_r ($P_r = P/P_c$), where T_c is the critical temperature and P_c is the critical pressure. ω is the acentric factor which is given by

$$\omega = \frac{-\ln P_c - 5.92714 + 6.09648\tau^{-1} + 1.28862\ln\tau - 0.169347\tau^6}{15.2518 - 15.6875\tau^{-1} - 13.4721\ln\tau + 0.43577\tau^6} \quad \text{---- (8.11)}$$

where $\tau = T_b/T_c$. Substituting T_b = 194.7 K, T_c = 304.2 K and P_c = 72.8 atm into equation 8.11, the eccentric factor ω becomes 0.2887. Therefore, the CO_2 compressibility values at 298 K and different pressures were calculated from equation 8.10. The fugacity was given by f = ZP and the calculated results are listed in Table 8.5. The absolute CO_2 adsorption

isotherms on carbon monoliths, i.e. AMCB-48 and AX-83, are calculated by equation 8.8 and the results are also listed in Table 8.5 along with the excess isotherm data.

Table 8.5 The excess and the absolute isotherms of CO_2 adsorption at 298 K on carbon monoliths AMCB-48 and AX-83

Pressure	fugacity	AMCB-48		AX-83	
		excess	absolute	excess	absolute
(bar)	(bar)	(mmol/g)	(mmol/g)	(mmol/g)	(mmol/g)
0.0000	0.0000	0.0000	0.0000	0.0000	0.0000
1.0000	0.9968	1.6560	1.6595	2.1360	2.1434
2.0000	1.9802	2.9680	2.9803	3.5940	3.6165
4.0000	3.9335	4.9060	4.9467	6.2300	6.2951
6.0000	5.8490	6.6370	6.7191	8.3240	8.4425
8.0000	7.7304	7.9620	8.0927	9.8560	10.0256
10.0000	9.4846	9.2080	9.3942	11.2000	11.4243
12.0000	11.3390	10.1950	10.4424	12.4040	12.6807
16.0000	14.8898	11.9450	12.3286	14.3500	14.7295
20.0000	17.8177	13.4490	13.9692	16.0870	16.5707
25.0000	22.1322	15.0730	15.8040	17.7330	18.3387
30.0000	25.5318	16.6290	17.5663	19.0750	19.8019
35.0000	28.5241	17.9850	19.1250	19.9780	20.8097
40.0000	31.2919	19.0130	20.3433	20.5800	21.4938

The absolute isotherms are analysed using the D-A equation using m = 1.0, 1.5 and 2.0 respectively. The D-A transformed isotherms of AMCB-48 and AX-83 are plotted in Figure 8.36 and 8.37. For m equal to 1.0 and 2.0, the isotherm deviated from the D-A equation. m = 1.5 gives a better linearity. But there is little difference in the intercept, which means that the micropore volume reduced from D-A equation using different value of m are similar to each other. The regressed intercepts, i.e. $\log(n_o)$ in Figure 8.8.36 and 8.37 for different m are listed in Table 8.6.

Table 8.6 The regressed intercepts of D-A transformed CO_2 adsorption isotherms

	AMCB-48			AX-83		
	m = 1	m = 1.5	m = 2	m = 1	m = 1.5	m = 2
$\log(n_o)$	1.4114	1.2745	1.2023	1.4579	1.3318	1.2649
std. error	0.018	0.034	0.073	0.03	0.018	0.056

Note: m is the third variable in D-A equation and n_o (mmol g^{-1}) is the molar number of the adsorbed CO_2 when micropore filling is supposed to be completed.

The micropore volume, $V_o(cm^3\ g^{-1})$, is given by

$$V_o = 10^{-3}\, n_o\, v_{ads} \quad \text{---------- (8.12)}$$

Using the average values of n_o obtained from Table 8.6 to calculate V_o by equation 8.12, the micropore volume of AMCB-48 and AX-83 are 1.02 and 1.16 $cm^3\ g^{-1}$, respectively. These values are in reasonable agreement with the micropore volumes, 0.96 and 1.08 $cm^3\ g^{-1}$ obtained from the nitrogen adsorption isotherms on AMCB-48 and AX-83 at 77 K by volumetric measurement. In other words, activated diffusion is not a significant factor for nitrogen adsorption at 77 K on the activated carbon monoliths of AMCB-48 and AX-83.

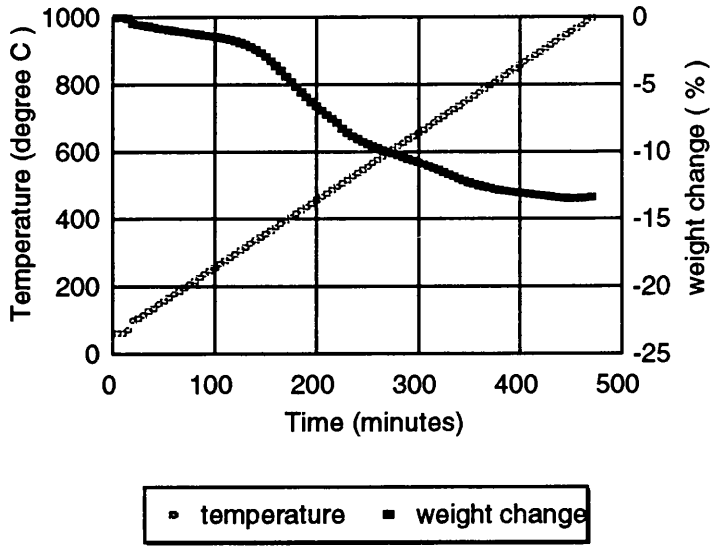

(a)

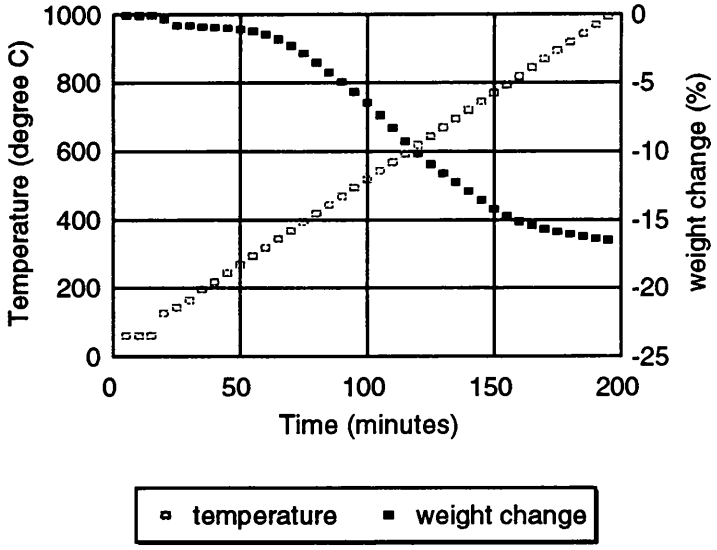

(b)

Figure 8.1 The TGA weight loss curves in nitrogen (1.0 dm^3h^{-1}).

(a) raw meso-carbon microbeads (heating rate 2 °C/min); meso-carbon microbeads (heating rate 5 °C/min) after pre-oxidation at 300 °C in air for 30 minutes.

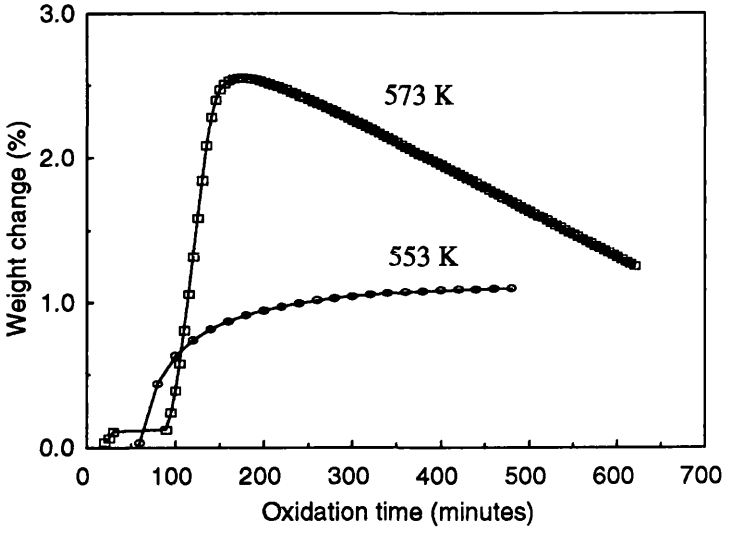

(a)

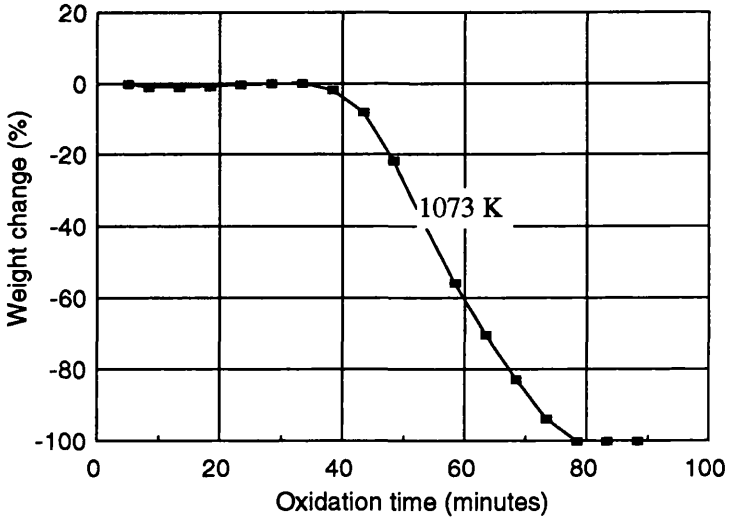

(b)

Figure 8.2 The isothermal oxidation of meso-carbon microbeads in air by TGA. (a) low temperature pre-oxidation; (b) high temperature oxidation.

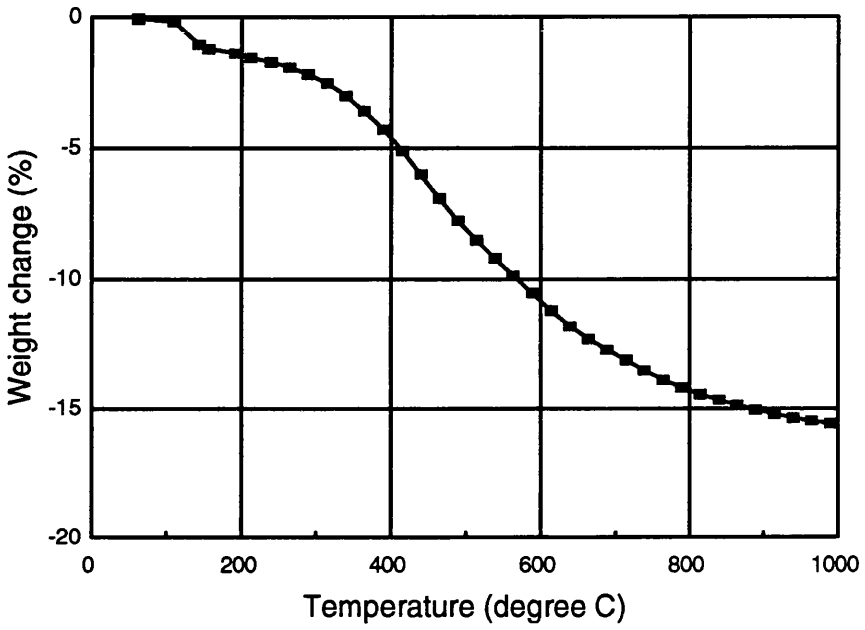

Figure 8.3 The TGA weight loss curve of Indonesian Dumai petroleum coke in nitrogen at a heating rate of 2 °C min^{-1}.

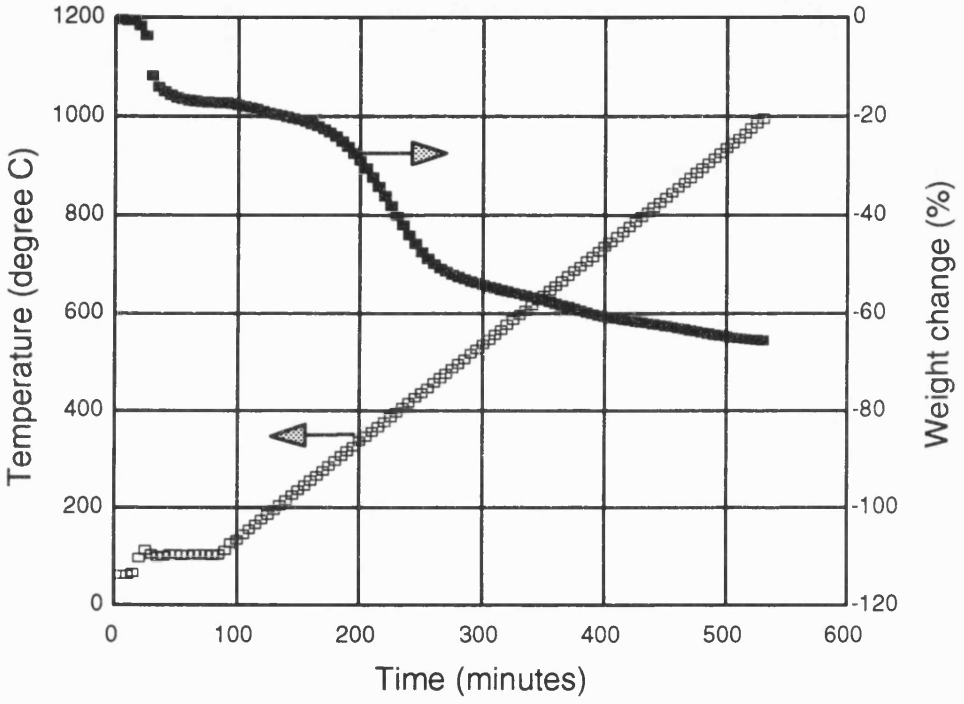

Figure 8.4 The TGA weight loss curve for an Irish lignite in flowing nitrogen (1 dm^3h^{-1}) at a heating rate of 2 $^oC\ min^{-1}$.

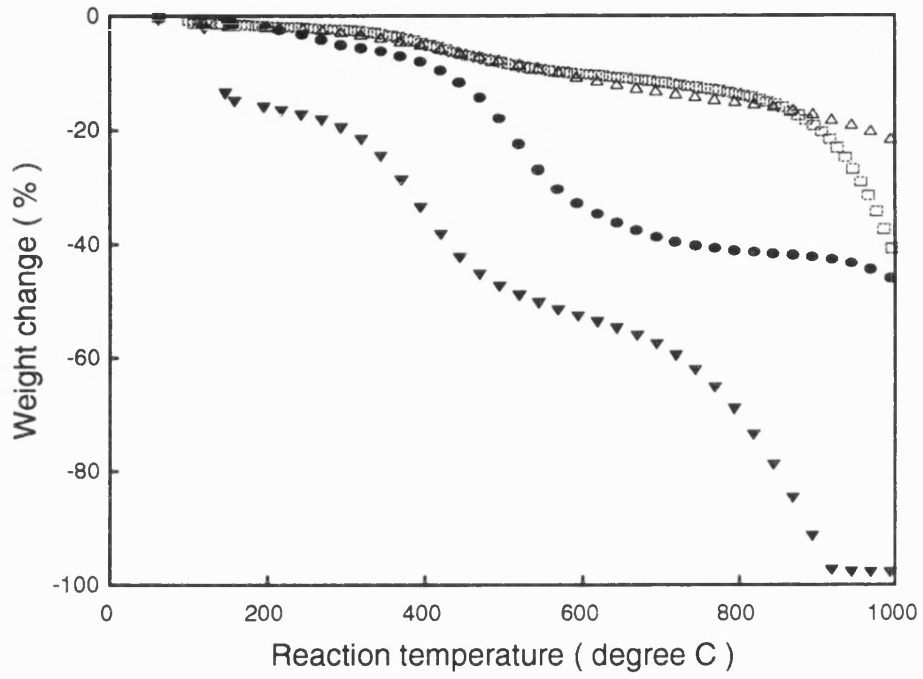

Figure 8.5 The CO_2 reactivity of meso-carbon microbeads (rectangles), petroleum coke powder (empty triangles), phenolic resin beads (circles) and raw lignite powder (solid triangles). The heating rate is 5 $^{o}C\ min^{-1}$ and the CO_2 flow rate is 7.0 dm^3h^{-1}.

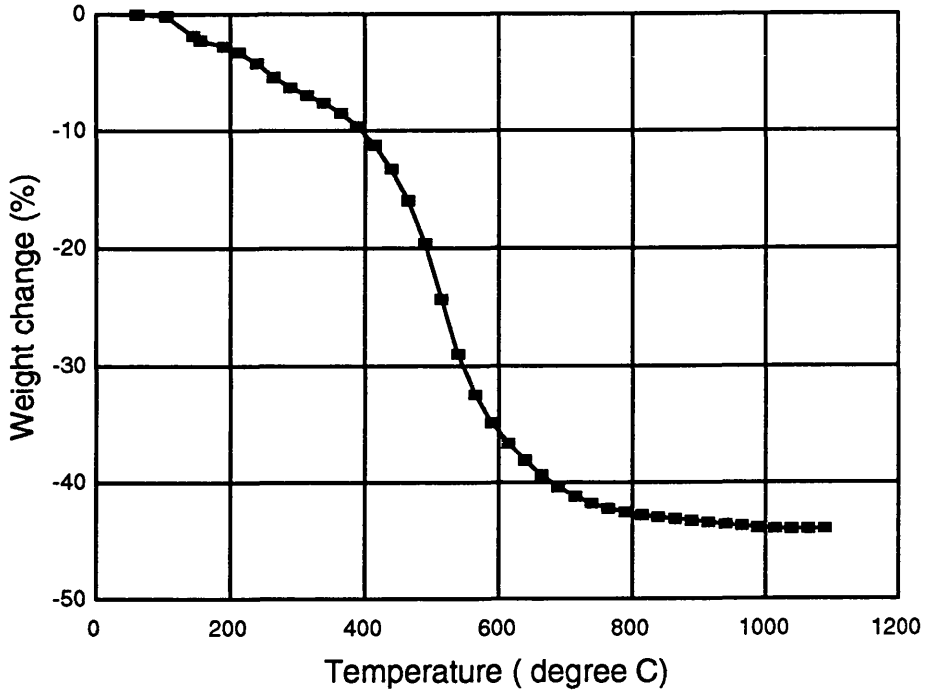

Figure 8.6 The TGA weight loss curve of phenolic resin beads FRD3656 in flowing nitrogen (1 $dm^3 h^{-1}$) at a heating rate of 2 °C min^{-1}.

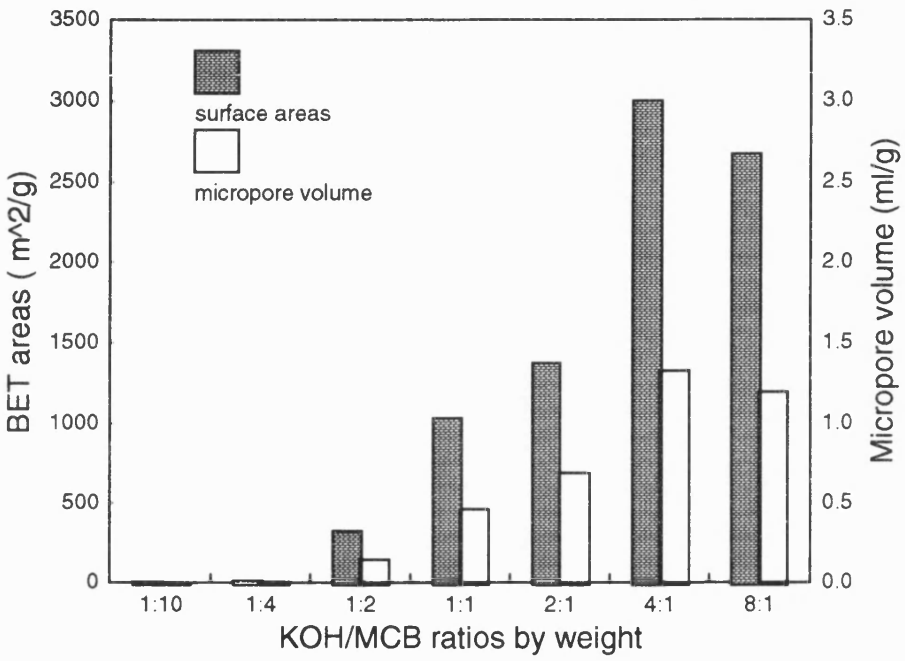

Figure 8.7 The adsorptive properties of KOH-activated meso-carbon microbeads with different ratios of KOH to meso-carbon microbeads. The properties are obtained from nitrogen adsorption at 77 K.

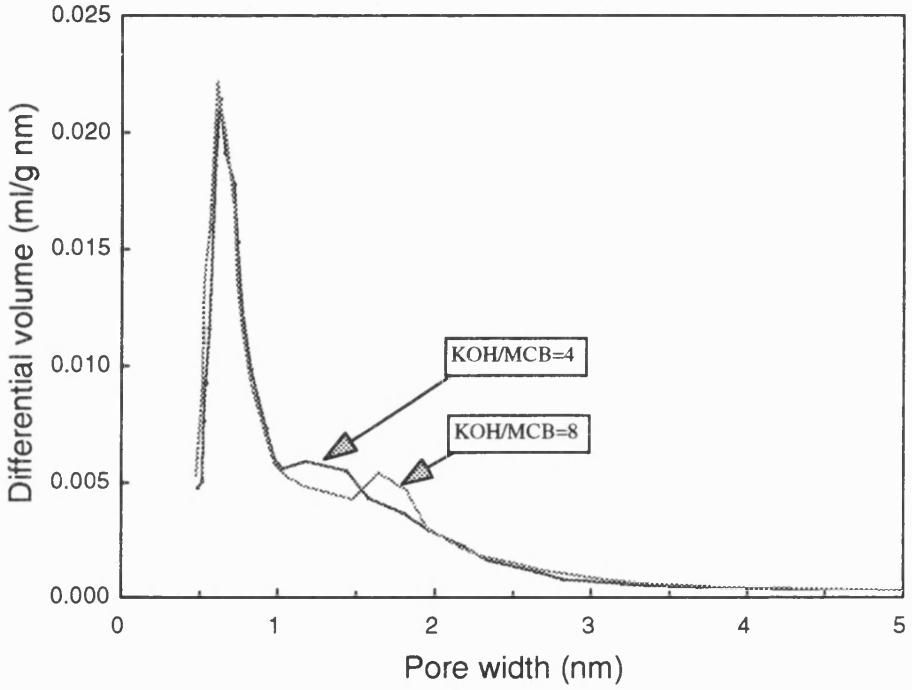

Figure 8.8 The pore size distributions of KOH-activated meso-carbon microbeads with the KOH/MCB ratios of 8:1 and 4:1 at 400 °C for 1.0 hr and 800 °C for 1.6 hr. The pore size distributions are deduced from nitrogen adsorption isotherms by Horvath-Kawazoe method.

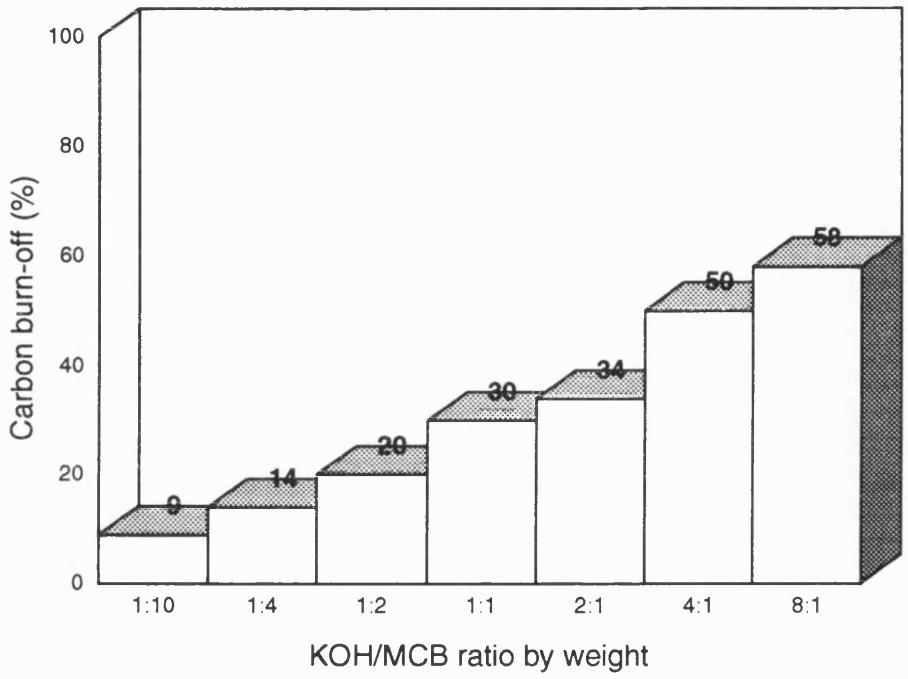

Figure 8.9 The carbon burn-off for activated meso-carbon microbeads using different KOH/MCB ratios at 800 °C.

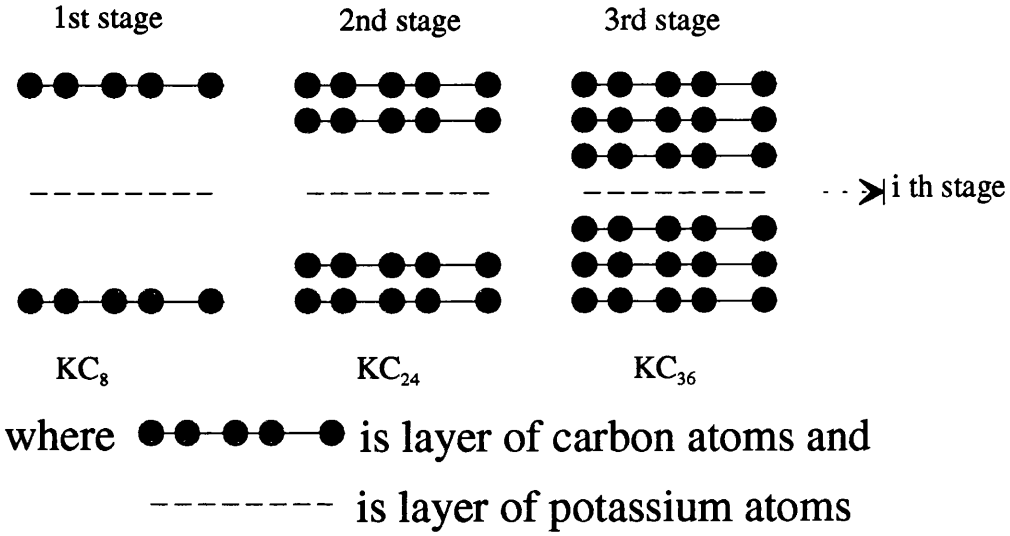

Figure 8.10 Different stages in the intercalation of graphite with potassium (Marsh, *et al*, 1987)

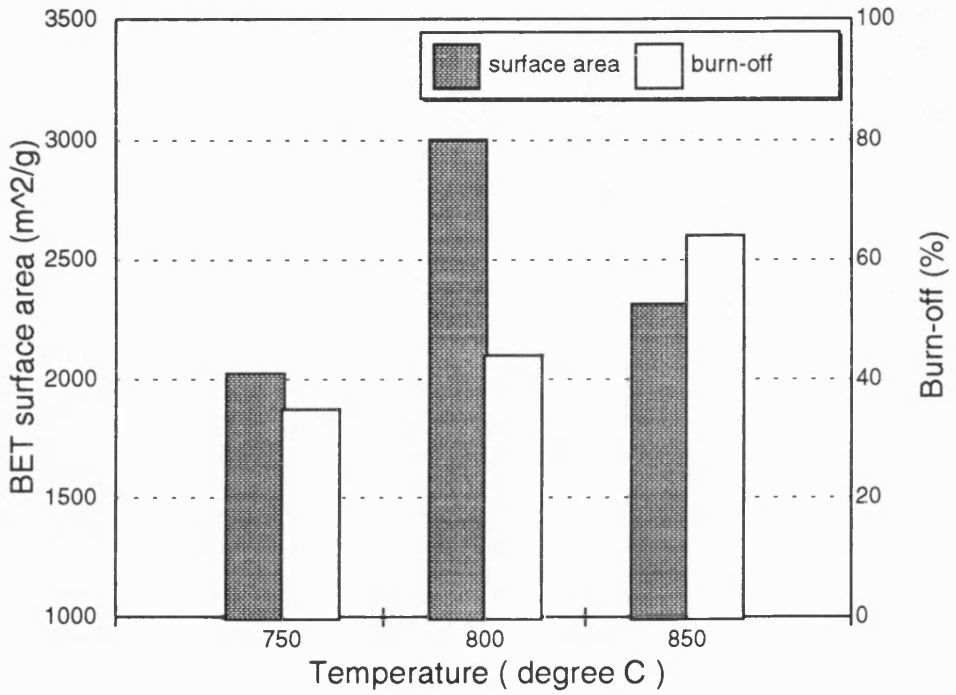

Figure 8.11 The variation of BET surface areas and carbon burn-off with the heat-treatment temperature for the KOH activated meso-carbon microbeads at a ratio of KOH/MCB = 4 and a reaction time of 100 minutes.

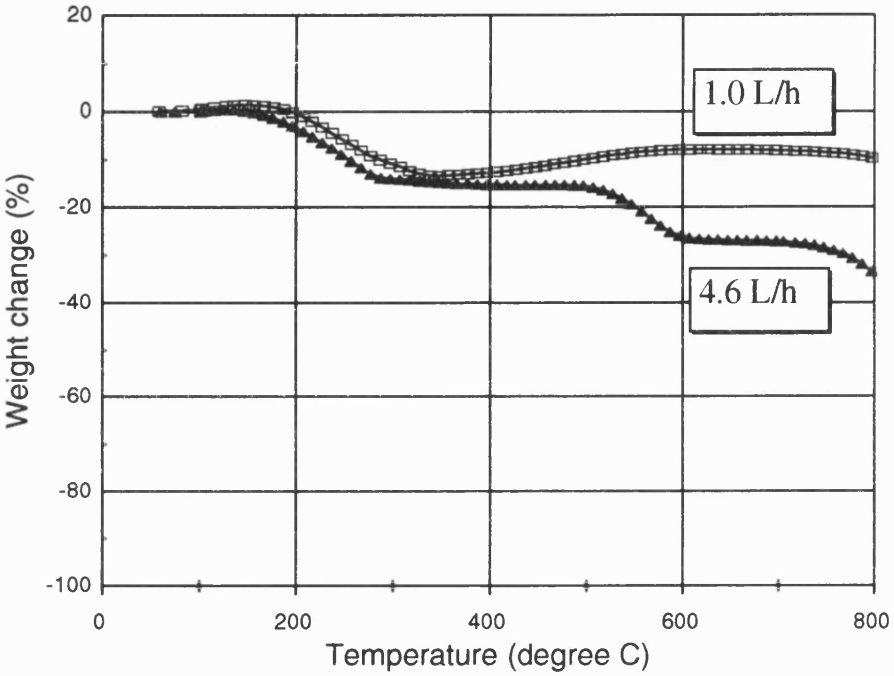

Figure 8.12 The influence of helium flow rate on the weight change of a 4:1 KOH/MCB mixture during heat-treatment (heating rate is 2 ^{o}C min^{-1}).

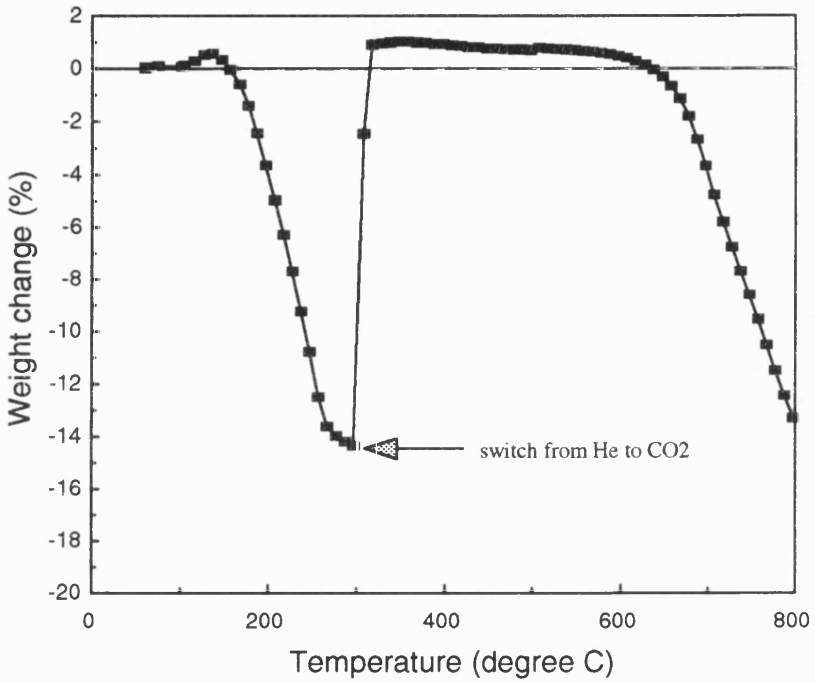

Figure 8.13 The weight change of KOH/MCB mixture after the switch from Helium to CO_2 (heating rate is 2 °C/min).

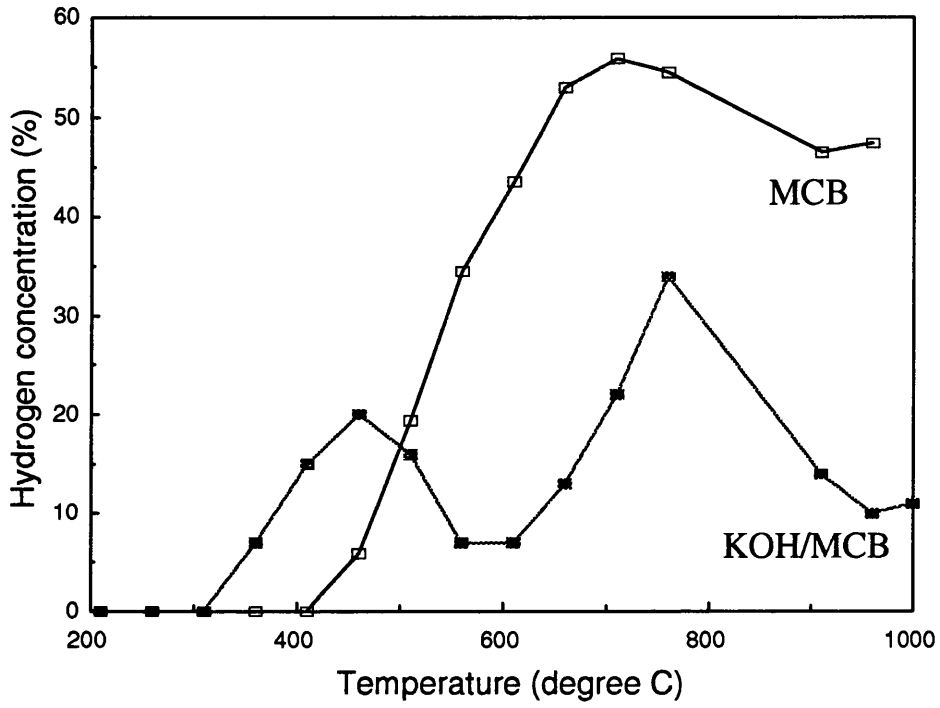

Figure 8.14 The difference of hydrogen content in gas phase during the heat-treatment of meso-carbon microbeads with and without KOH.

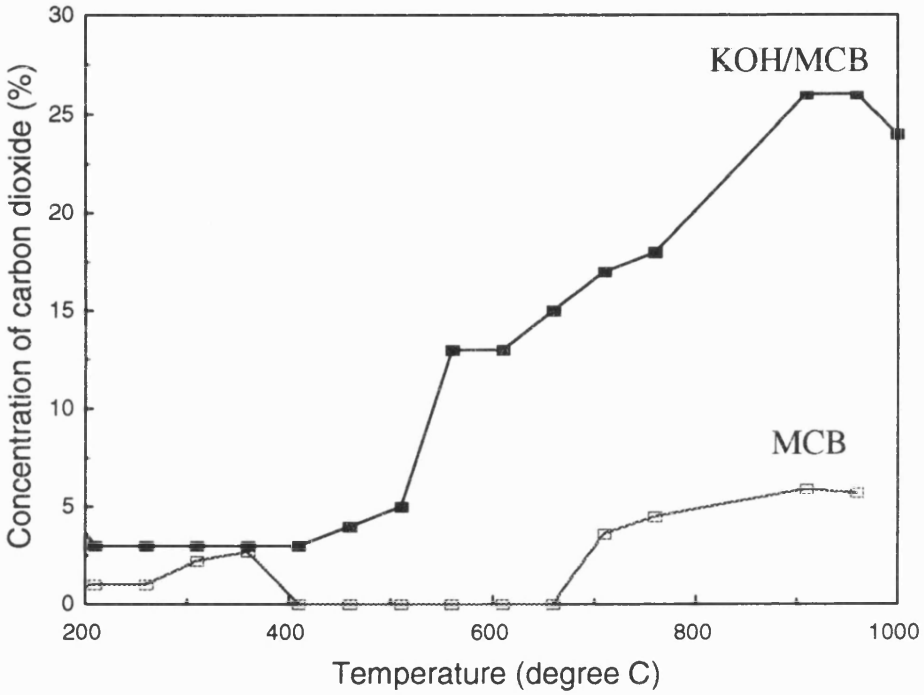

Figure 8.15 The difference of carbon dioxide content in gas phase during the heat-treatment of meso-carbon microbeads with and without KOH.

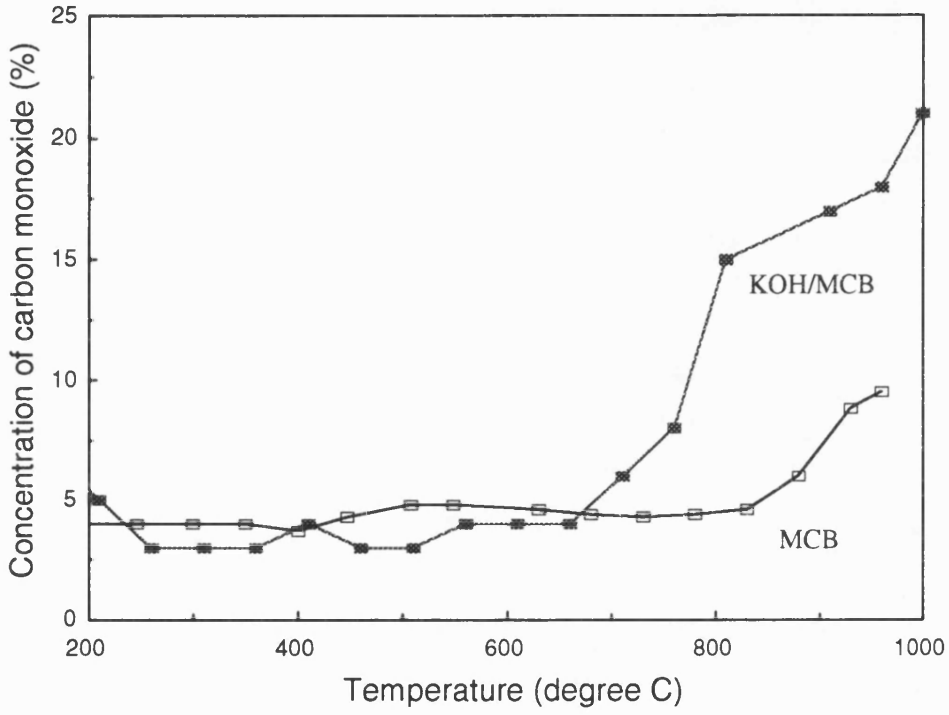

Figure 8.16 The difference of carbon monoxide content in gas phase during the heat-treatment of meso-carbon microbeads with and without KOH.

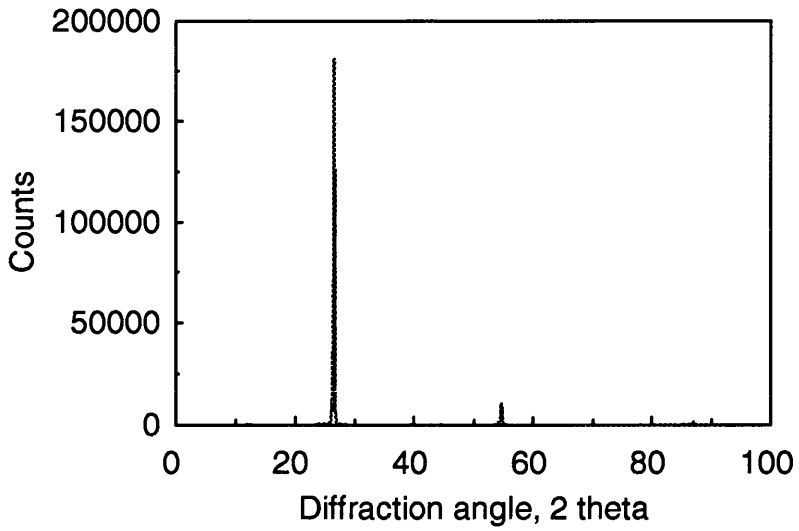

Figure 8.17 The X-ray diffraction spectrum of natural graphite flakes (courtesy of Dr. T Mays).

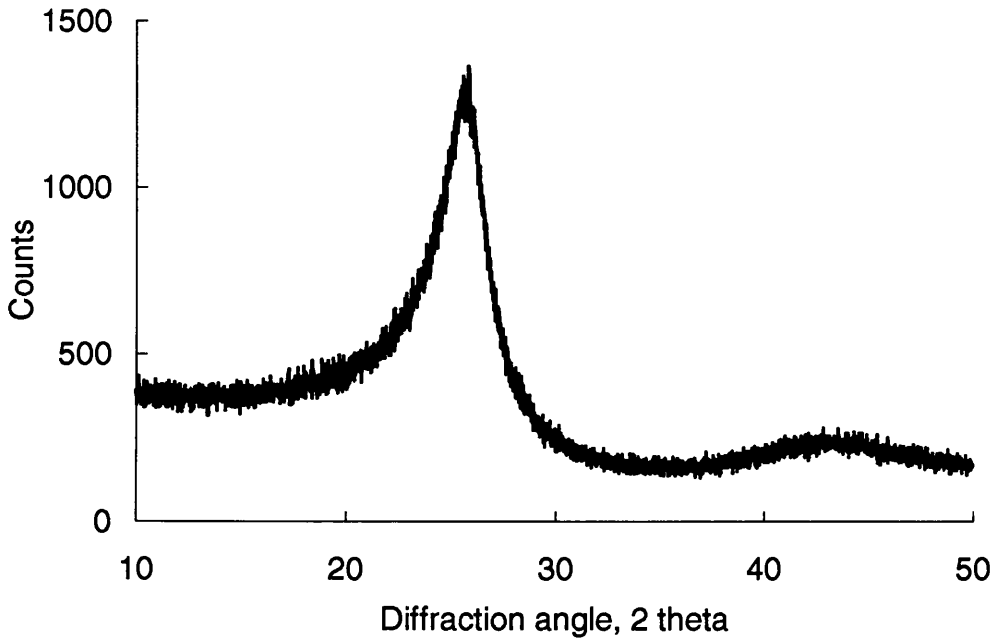

Figure 8.18 The X-ray diffraction spectrum of raw meso-carbon microbeads.

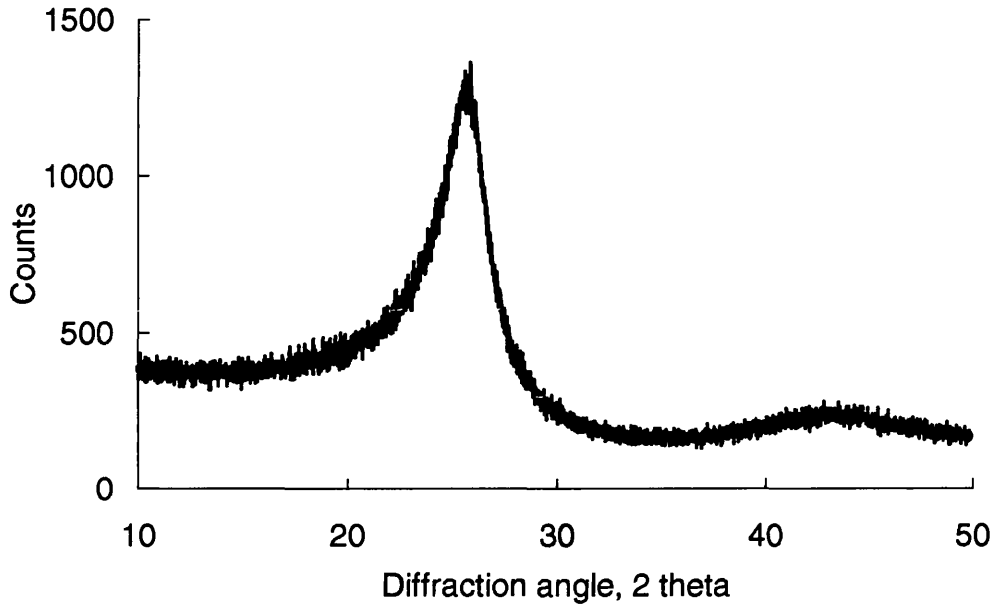

Figure 8.19 The X-ray diffraction spectrum of the carbonised meso-carbon microbeads at 1000 °C.

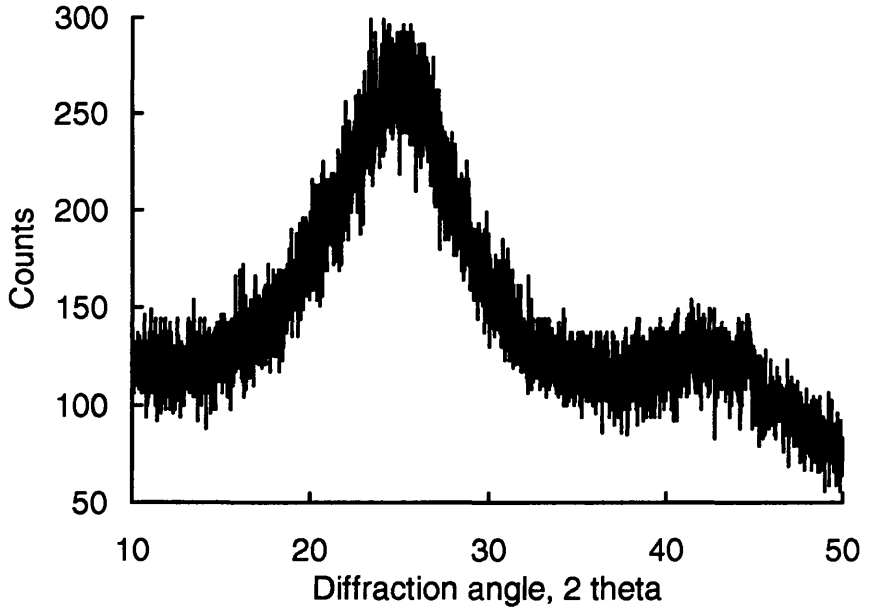

Figure 8.20 The X-ray diffraction spectrum of the KOH activated meso-carbon microbeads at 400 °C

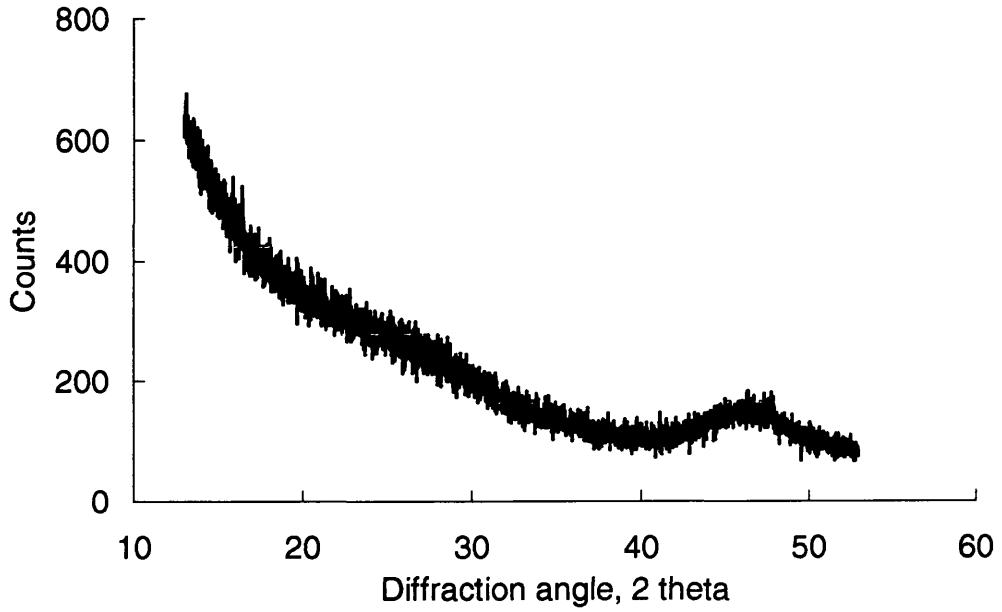

Figure 8.21 The X-ray diffraction spectrum of the KOH activated meso-carbon microbeads at 800 °C with carbon burn-off of 48 %.

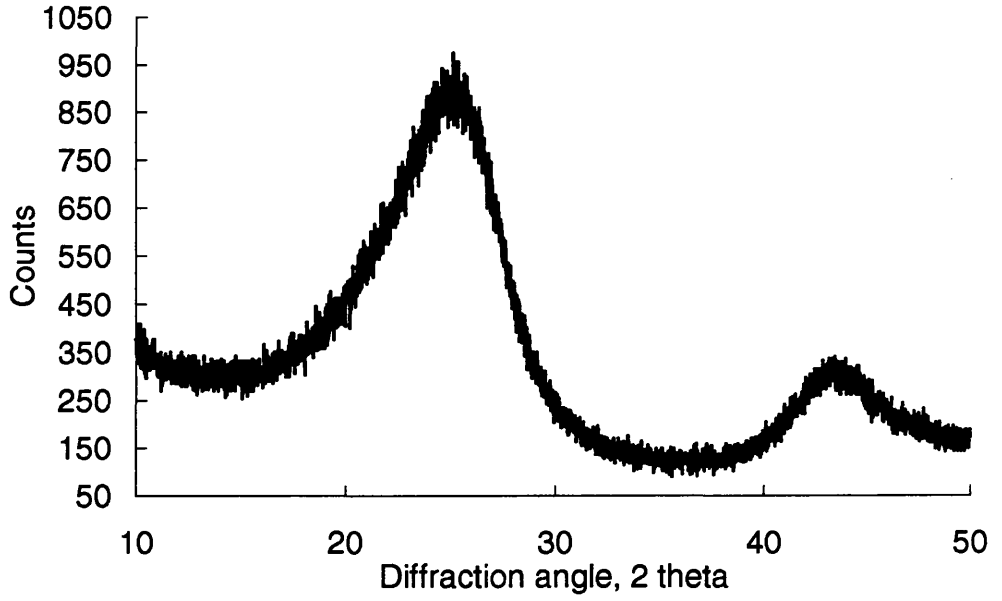

Figure 8.22 The X-ray diffraction spectrum of the CO_2 activated meso-carbon microbeads at 900 °C.

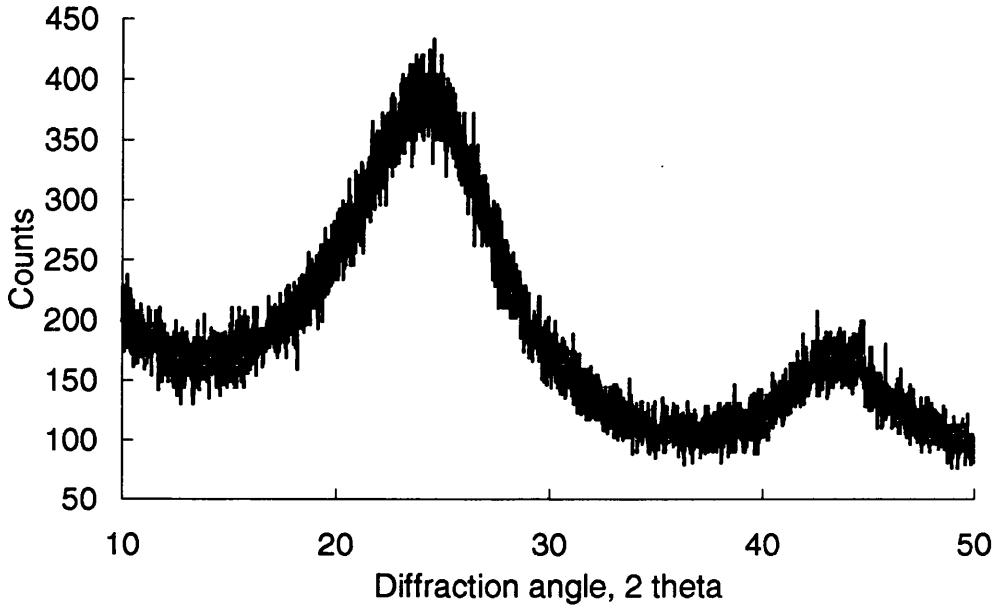

Figure 8.23 The X-ray diffraction spectrum of the K_2CO_3 activated meso-carbon microbeads at 850 °C with carbon burn-off of 60 %.

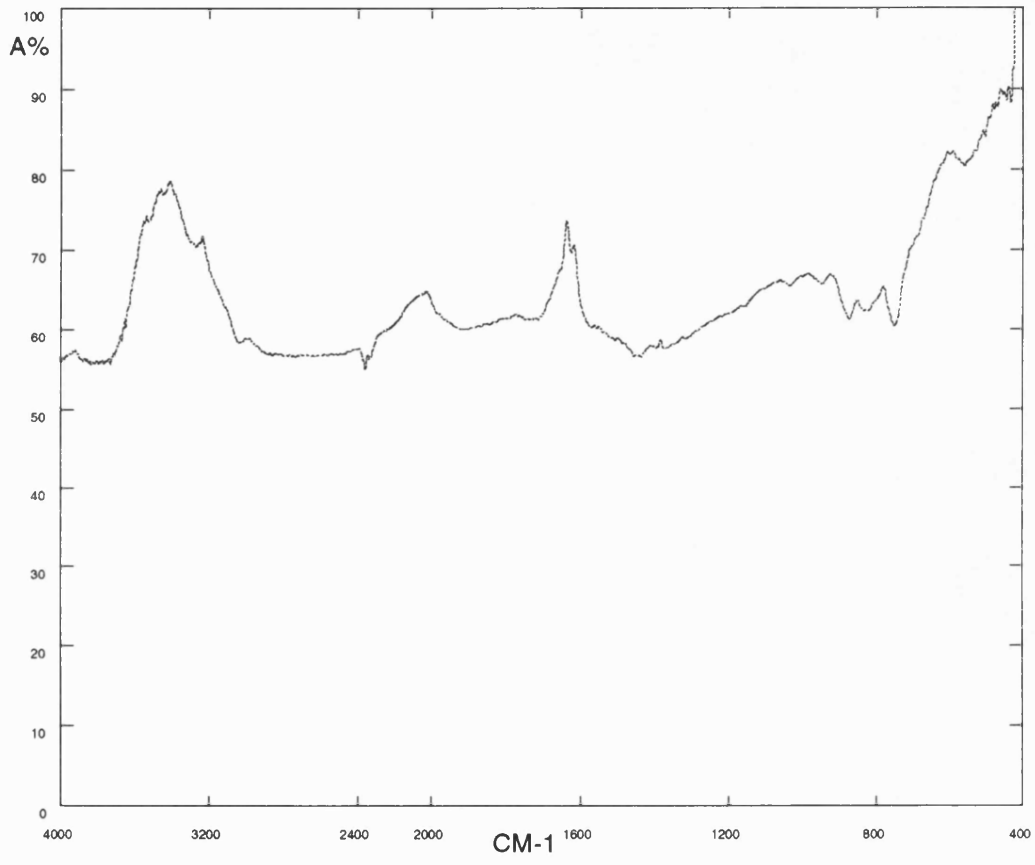

Figure 8.24 The infrared spectrum of original meso-carbon microbeads.

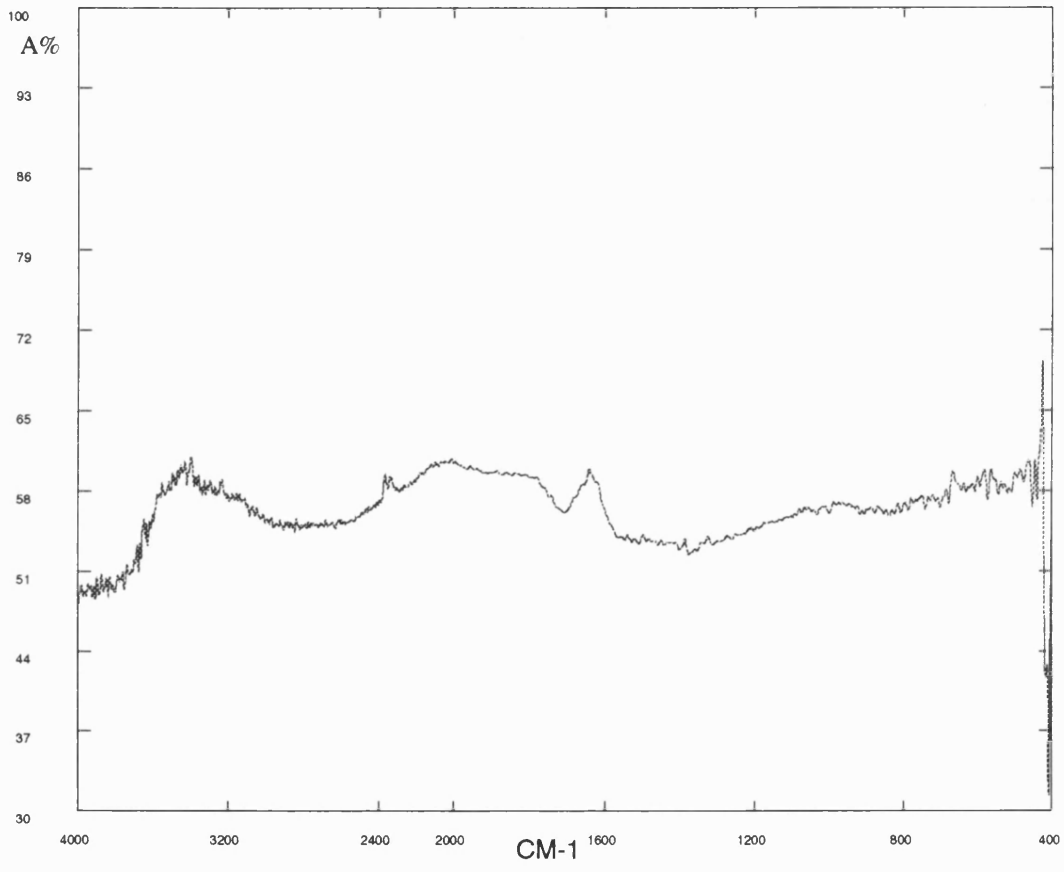

Figure 8.25 The infrared spectrum of the KOH treated meso-carbon microbeads at 400 °C.

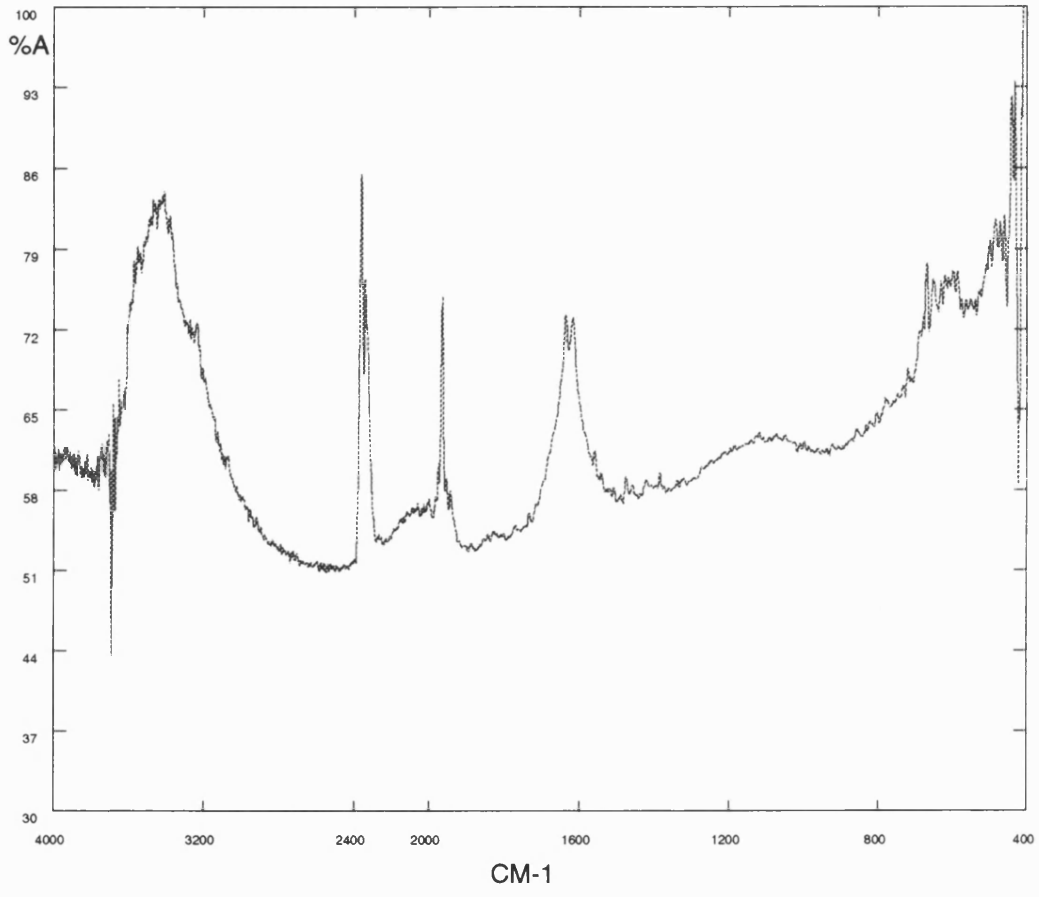

Figure 8.26 The infrared spectrum of the KOH activated meso-carbon microbeads at 800 °C.

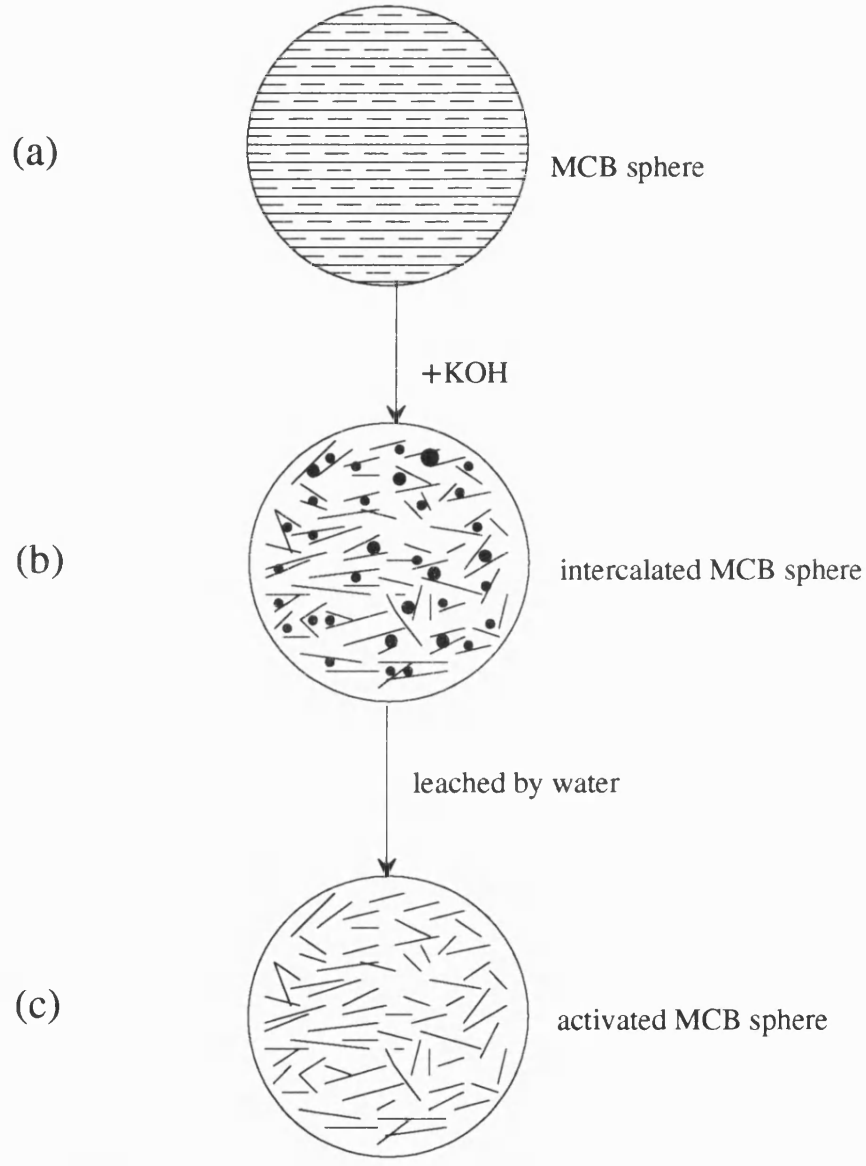

Notes: short lines represent lemellar constituent molecules
and black dots stand for the intercalated potassium

Figure 8.27 The schematic illustration of pore development in KOH-activated meso-carbon microbeads (MCB). The basic pores are the wedge-shapes between "lamellae" puckered up randomly in three dimensions but here only illustrated in two dimensions.

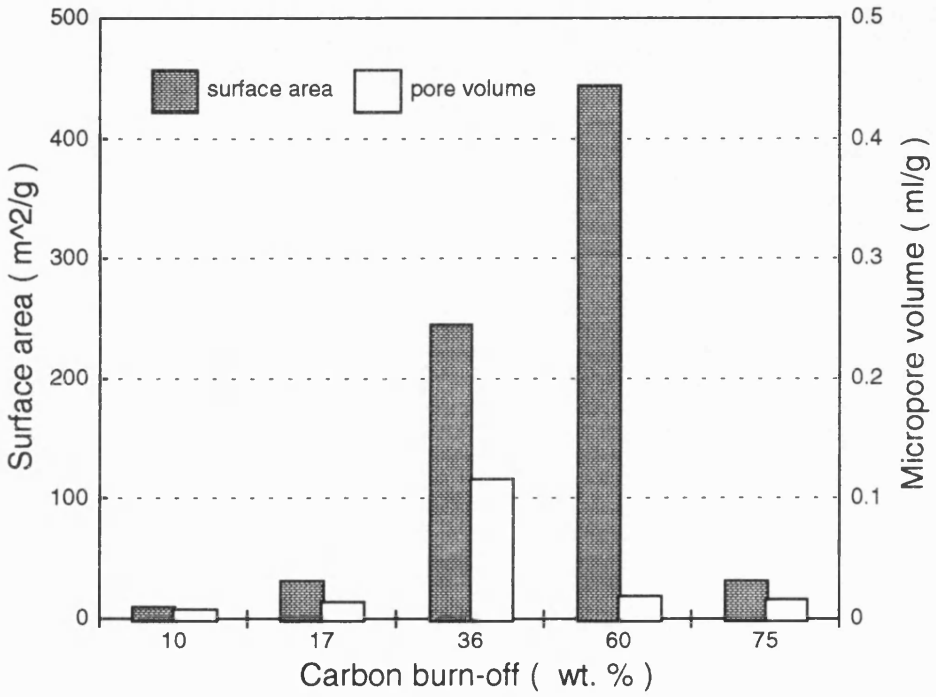

Figure 8.28 The BET surface areas and D-A micropore volumes of CO_2-activated meso-carbon microbeads with different burn-off values.

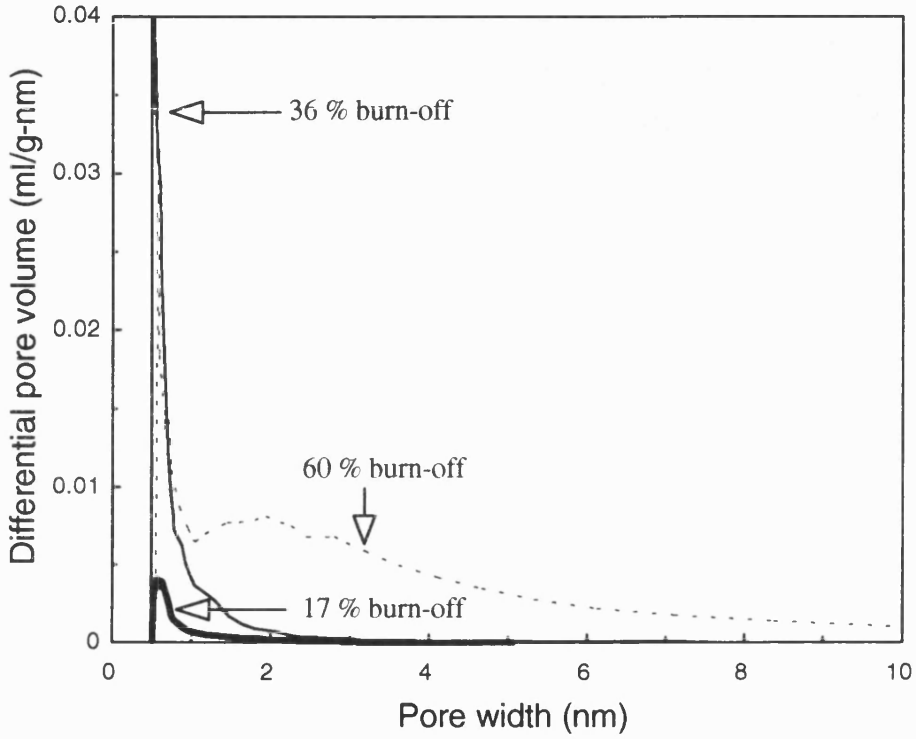

Figure 8.29 The pore size distribution (Horvath - Kawazoe method) of CO_2 activated meso-carbon microbeads with 17 %, 36 % and 60 % burn-off.

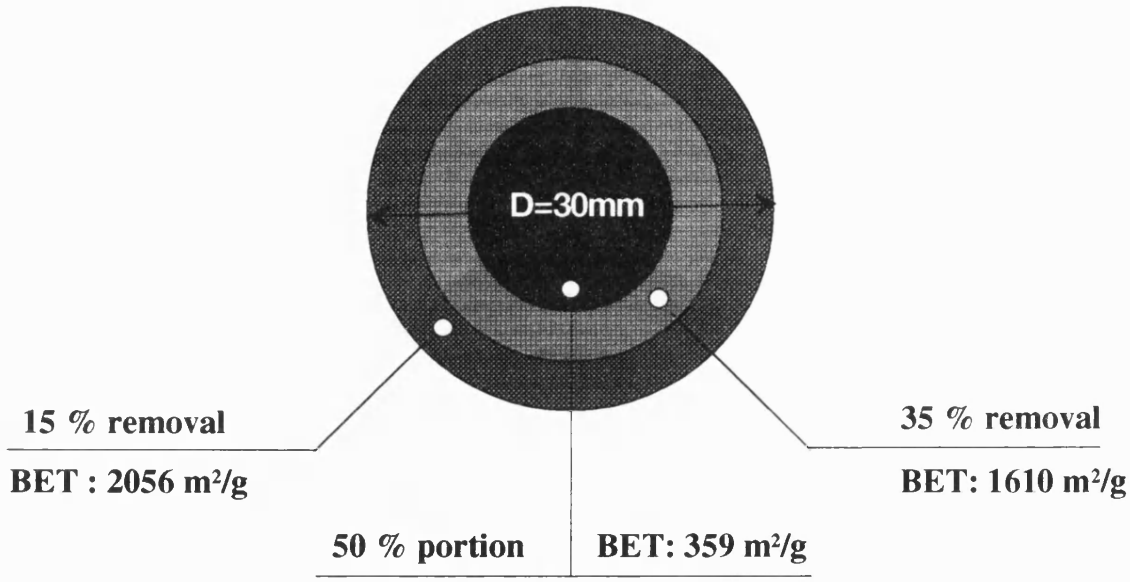

Figure 8.30 A schematic illustration of non-uniform pore network of CO_2 activated phenolic resin bar (Ø 30 x 30 mm) with 60 % overall burn-off.

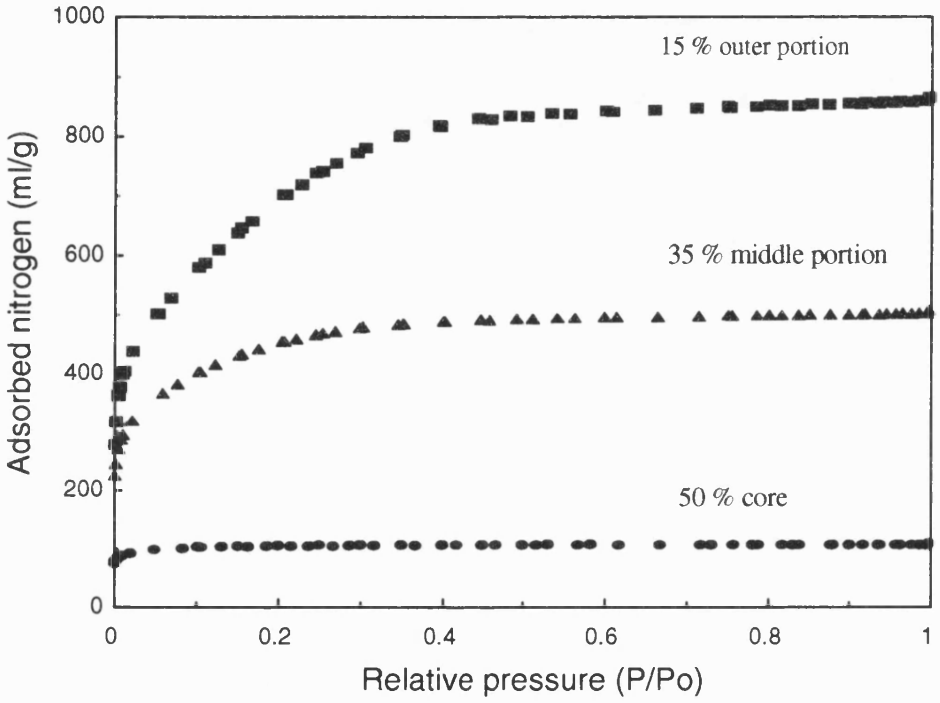

Figure 8.31 The nitrogen adsorption isotherms of different fractions of CO_2 activated phenolic resin bar with a total burn-off of 60 % at 950 °C for 12 hours.

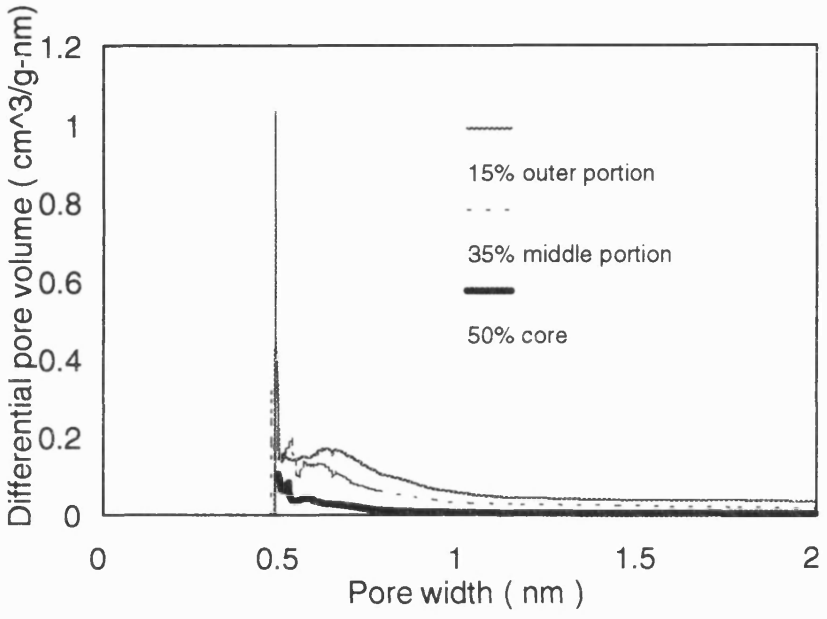

Figure 8.32 The pore size distribution (H-K method) of the differential fractions of CO_2 activated phenolic resin bar. The average pore widths of 15, 35 and 50 wt.% portions are 1.20, 0.85 and 0.61 nm, respectively.

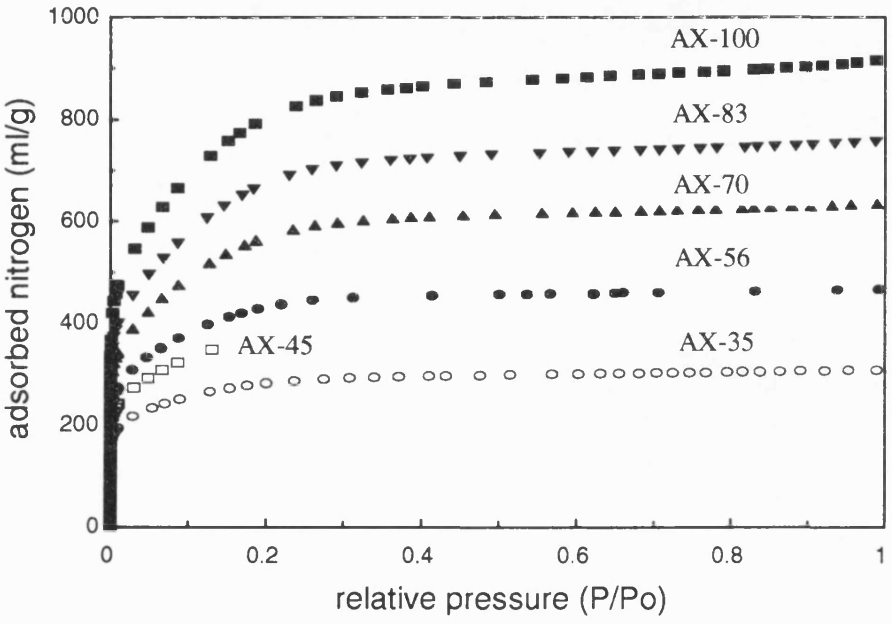

Figure 8.33 The nitrogen adsorption isotherms of the monolith made from AX-21 carbon powder with different ratios of phenolic resin beads. The discs (∅ 25 mm in diameter and 5 to 10 mm in thickness) were formed at 150 °C and 400 Kg cm^{-2}.

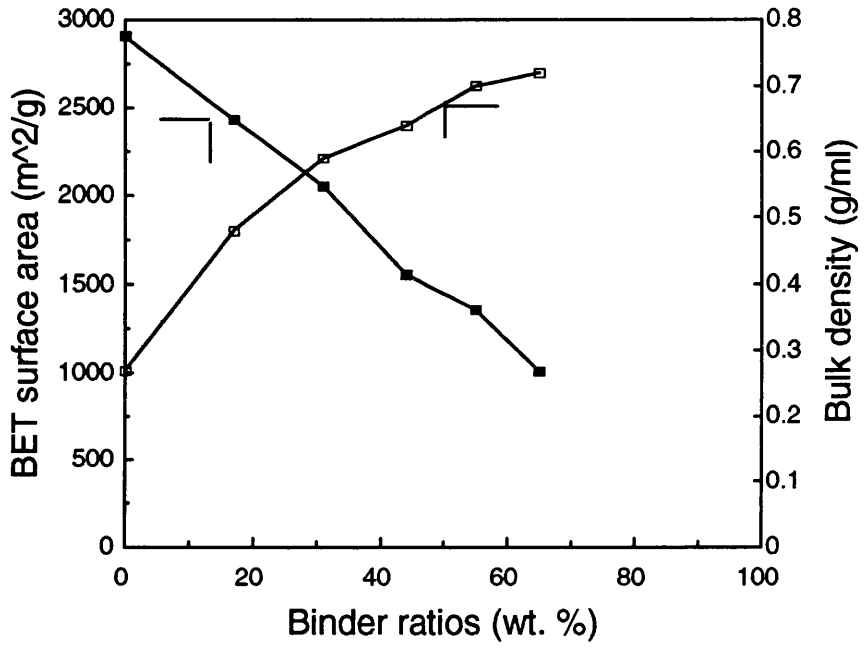

Figure 8.34 The BET surface areas and bulk densities of AX-21 carbon discs with different phenolic resin binders. The AX-21 carbon discs were formed at 150 °C and 400 kg cm^{-2}. The BET surface areas were derived from the nitrogen adsorption isotherms at 77 K and the bulk densities of the discs were calculated from the disc weight and the physical dimensions of the discs measured by a micrometer.

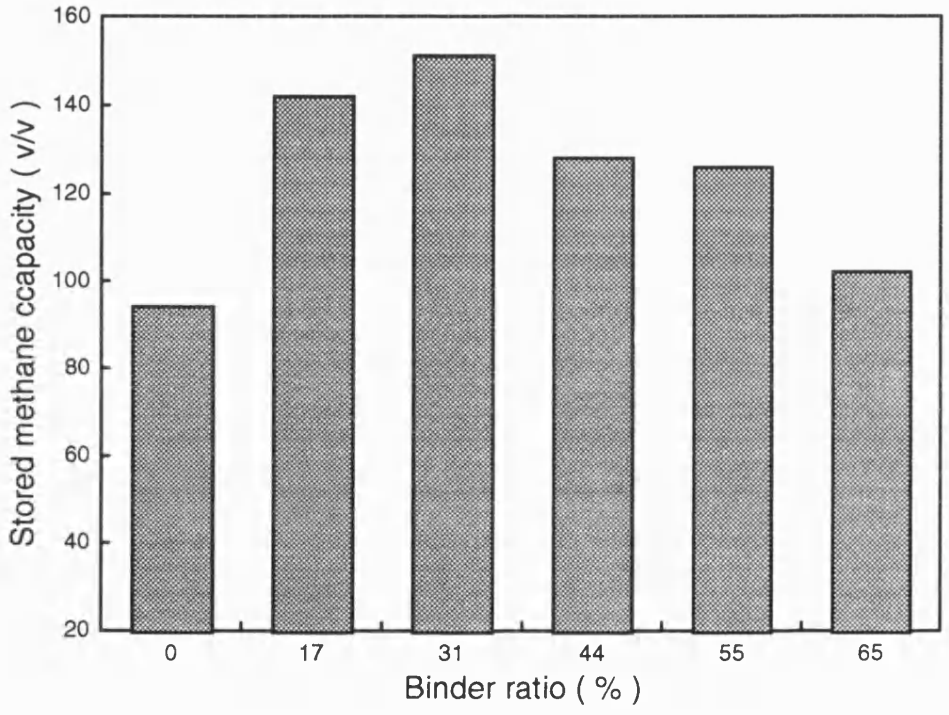

Figure 8.35 The estimated volumetric methane capacity (at 3.4 MPa and 298 K) of the AX-21 carbon monoliths with different binder ratios using the Mullhaupt empirical expression : volumetric methane capacity (v/v) = (1.31 + 0.0044 BET surface area) times bulk density.

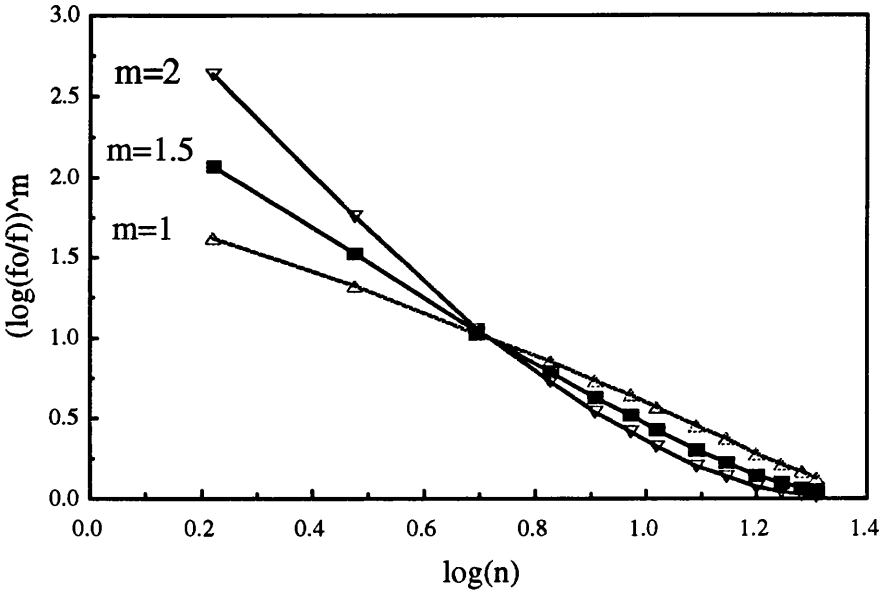

Figure 8.36. The Dubinin-Astakhov transformed isotherms of CO_2 adsorption on AMCB-48 activated carbon monolith at 298 K, m is the third variable in D-A equation, n is the total amount (mmol g^{-1}) of CO_2, f is the fugacity CO_2 at 298 K and f_o is saturation fugacity.

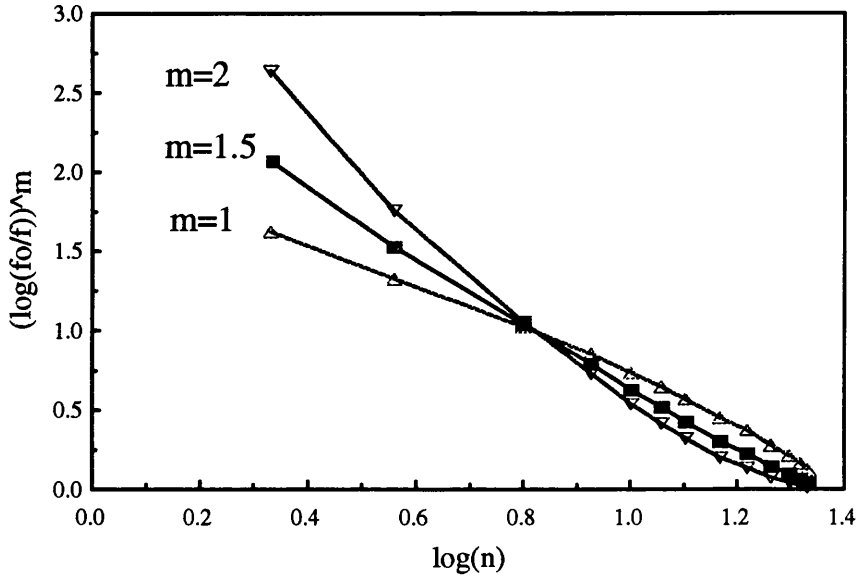

Figure 8.37. The Dubinin-Astakhov transformed isotherms of CO_2 adsorption on AX-83 activated carbon monolith at 298 K, m is the third variable in D-A equation, n is the total amount (mmol g^{-1}) of CO_2, f is the fugacity CO_2 at 298 K and f_o is saturation fugacity.

CHAPTER 9 MEASURED AND ESTIMATED METHANE CAPACITIES ON ACTIVATED CARBONS

9.1 DEFINITIONS OF METHANE CAPACITIES

Volumetric methane capacities are the key criteria to evaluate the suitability of activated carbons for adsorbed natural gas storage as a fuel for natural gas driven vehicles. Different concepts and units were used to report the methane capacities on activated carbons in the literature: methane uptakes in units of g g^{-1} or g cm^{-3} (Quinn and MacDonald, 1992), methane storage capacity in unit of mmol g^{-1} (Chahine and Bose, 1991) (Lewis, *et al*, 1991) (Mullhaupt, *et al*, 1992) (Alcaniz-Monge, *et al*, 1995), and methane stored and delivered capacities in volume of methane per volume of carbon at 273 K and 0.1MPa (Matranga, *et al*, 1992) and at 298 K and 0.1 MPa (Parkyns and Quinn, 1995). It is difficult to compare the results with each other and sometimes the concepts are not clearly defined. In this thesis, three methane capacities: the adsorbed, the stored and the delivered capacities in units of volume of methane at 298 K and 0.1 MPa per volume of activated carbon (including inter-particle voids) were defined as follows.

The adsorbed methane capacity, V_a (v/v) is defined as the volume of the excess methane adsorbed in micropores per volume of activated carbon. The methane uptake, G, (in units of mmol g^{-1}) measured gravimetrically on an electronic microbalance is an excess isotherm. Therefore, V_a is obtained from G by

$$V_a = 24.465\ G\rho \qquad \text{(for 298 K, 0.1 MPa)} \text{ ---------- (9.1)}$$

where ρ (g cm^{-3}) is the packing density of activated carbons, the factor 24.465 (cm^3 $mmol^{-1}$) is the molar volume of methane at 298 K and 0.1 MPa, assuming that methane at 298 K and 0.1 MPa behaves like an ideal gas (the compressibility of methane at 298 K and 0.1 MPa is 0.9977).

The stored methane capacity, V_s (v/v), is defined as the methane stored both in the adsorbed phase (V_a) and in the gas phase (V_g). Therefore, V_s is given by

$$V_s = V_a + V_g \quad \text{----------} \quad (9.2)$$

where V_g was calculated from

$$V_g = \frac{P\, v_t}{ZP_o}\rho \quad \text{----------} \quad (9.3)$$

in which P is the adsorption pressure (MPa), Z is the methane compressibility at P and 298 K, P_o is a reference pressure 0.1 MPa, v_t ($cm^3\ g^{-1}$) is the total pore volume including micropores, mesopores, macropores and interparticle voids per gram of activated carbon, and ρ ($g\ cm^{-3}$) is the packing density of activated carbon.

There is an uncertainty on whether or not micropores should be included in the calculation of the compressed methane in gas phase. For ultra-micropores (equal or less than one methane molecule size) where the potentials of opposite pore walls overlap, there might be no space for free gas molecules once the pore is filled with adsorbed molecules. Therefore, V_g might be over-estimated by including micropores in v_t. On the other hand, V_g might be under-estimated by excluding micropores from v_t, as Parkyns and Quinn (1995) did in their reports, because molecular simulations, Figure 7.6, show that in the middle of the micropores wider than 1.12 nm, the local methane density is mainly attributed to compression because the interaction between gas molecules and the pore walls fades away quickly with their separation distance. In reality, the stored methane capacity V_s should be somewhere between the two extreme values converted by equation 9.2 using values of v_t including and excluding micropore volumes.

The value of v_t excluding and including micropores can be expressed by

$$v_t = 1/\rho - V_o - 1/\rho_c \quad \text{(excluding micropores)----------} \quad (9.4a)$$

$$v_t = 1/\rho - 1/\rho_c \quad \text{(including micropores)----------} \quad (9.4b)$$

where the micropore volume V_o is derived from the Dubinin-Astakhov equation from nitrogen adsorption isotherms, the packing density ρ is calculated from physically measured dimensions and weight of the carbon monolith, and ρ_c is the skeletal carbon density which is taken as 2.0 g cm^{-3} in this study since the densities of KOH-activated meso-carbon microbeads monoliths measured by a helium pycnometry are around 2.0 ± 0.2 g cm^{-3} (Table 9.5). Parkyns and Quinn (1995) used an arbitrary value of ρ_c = 2.2 g cm^{-3} in their expression which is probably too high, considering the disordered carbon structure and the possibility of closed pores not accessible to adsorptive molecules in activated carbons.

The methane compressibility (Z) at 3.4 MPa and 298 K is 0.93 which is calculated by the Peng-Robinson equation of state. Substituting the values of ρ_c = 2.0 g cm^{-3}, Z = 0.93, P = 3.4 MPa, P_o = 0.1 MPa and equation 9.4(a) and 9.4(b) into equation 9.3, the methane stored in gas phase at a filling pressure 3.4 MPa and temperature 298 K is given by

$$V_g = 36 (1 - \rho V_o - 0.5\rho) \quad \text{(excluding micropores)} \quad (9.5a)$$

$$V_g = 36 (1 - 0.5\rho) \quad \text{(including micropores)} \quad (9.5b)$$

Therefore, equation 9.2 becomes:

$$V_s = V_a + 36 (1 - \rho V_o - 0.5\rho) \quad \text{(excluding micropores)} \quad (9.6a)$$

$$V_s = V_a + 36 (1 - 0.5\rho) \quad \text{(including micropores).} \quad (9.6b)$$

The delivered methane capacity, V_d (v/v) is defined as the volume (at 298 K and 0.1 MPa) of methane released at 0.1 MPa after the carbon is loaded and equilibrated with methane at 3.4 MPa and 298 K. So the delivered methane capacity can be calculated from

$$V_d = V_{s2} - V_{s1} \quad \text{----------} \quad (9.7)$$

in which V_{s2} and V_{s1} are the stored methane capacity at pressure 3.4 MPa and 0.1 MPa, respectively.

Based upon the above definitions, the adsorbed, the stored and the delivered methane capacities on activated carbons at adsorption pressure 3.4 MPa, desorption pressure 0.1 MPa and temperature 298 K are discussed in Section 9.2 based upon estimations from BET surface areas and micropore volumes and in Section 9.3 based upon the measured excess methane isotherms.

9.2 ESTIMATION OF STORED METHANE CAPACITY

Certainly the stored methane capacity can be directly obtained from the measurement of methane adsorption on carbons on a high pressure balance. However, a high pressure adsorption facility was not available at the time when this study was commenced and so BET surface areas and micropore volumes were used as preliminary parameters to compare the activated carbons prepared in this study. A number of works (Quinn (1990), Parkyns (1995), Mullhaupt (1992) and Heal (1990)) have shown that there is a linear relationship between methane capacity and BET surfaces or micropore volumes of activated carbons.

BET surface area is a most commonly used parameter both in research and in manufacture of activated carbons, even though the method faces a lot of criticism when applied to microporous carbons. This is because micropore filling occurs instead of multi-layer adsorption as assumed in the BET equation. Also some activated carbons like AX-21 carbon and Maxsorb (Otawa, *et al*, 1992), have BET surface areas near to or over 3000 m^2 g^{-1}; these values are higher than the maximum theoretical value of ca. 2660 m^2 g^{-1} which assumes that both sides of a single graphite sheet are contributing to surface area. In these cases BET surface area does not have a physical meaning, but nevertheless it still reflects the adsorption capability of a activated carbon and, strangely enough, it is found that there is a very good linear correlation between BET surface area and methane uptake for a variety of activated carbons.

The stored methane capacities on the microporous powders and on the monoliths are estimated by using the empirical expressions established by Mullhaupt, *et al* (1992) (using BET surface area) and by Parkyns and Quinn (1995) (using micropore volumes); the

predicted results are listed in Table 9.1. Mullhaupt, *et al* established the relationship between the stored methane, L_{max} (mmol g^{-1}), and the BET surface area, S_{BET} (m^2 g^{-1}) after testing more than 35 commercial carbon adsorbents as follows:

$$L_{max} = 1.31 + 0.00444\ S_{BET} \text{ ---------- (9.8)}$$

L_{max} is converted into the volumetric stored methane capacity, V_s (v/v), by

$$V_s = 24.465\ (\ 1.31 + 0.00444\ S_{BET}\ )\ \rho \text{ ---------- (9.9)}$$

Parkyns and Quinn obtained a correlation between the stored methane, L_{max} (mmol g^{-1}), and the micropore volume, V_o (cm^3 g^{-1}), after testing 43 commercial activated carbons as follows:

$$L_{max} = (9.69V_o + 0.38) + 1.47(\rho^{-1} - V_o - 0.45) \text{ -------- (9.10)}$$

Similarly L_{max} is converted into the volumetric stored methane capacity by

$$V_s = (237\ V_o + 9.2\ )\rho + 36(1 - \rho V_o - 0.45\rho\ ) \text{ -------- (9.11)}$$

The values of L_{max} and V_s for the microporous powders and the carbon monoliths used in this study are estimated by the equations 9.8 to 9.11 and the results are listed in Table 9.1.

The following points can be made from the results. The two empirical expressions (9.8 and 9.10) give a good agreement in the predicted methane storage (L_{max}) on the same activated carbon, which suggests that when a high pressure adsorption facility is not available, the BET surface area or micropore volume (D-A method) deduced from nitrogen adsorption data can be used to estimate the methane storage at a high pressure. Therefore, the suitability of an activated carbon for ANG application can be quickly decided by using the empirical expressions.

The monoliths made from AX-21 carbon or KOH activated meso-carbon microbeads are predicted to have higher stored methane capacities than the reference monolith BG-5R, a coconut shell derived carbon. The monolith made from AX-21 carbon

with 30 % phenolic resin gave the highest stored methane capacity among the AX-21 carbon monoliths with different binder ratios. The monolith made from KOH activated meso-carbon microbeads with 48 % burn-off gave the highest stored methane capacities among all the activated carbons tested.

The stored methane capacities of the powders, AX-21 carbon and KOH activated meso-carbon microbeads with 48 % burn-off (AMCB-48P), are much higher than those of monoliths, in units of mass, but much lower in units of volume because they have a low packing density, i.e. 0.27 g cm^{-3}. The volumetric stored methane capacities of AX-21 carbon and AMCB-48P powders are expected to be enhanced from 94 and 95 v/v to 151 and 154 v/v respectively according to the Mullhaupt's expression after they are consolidated into the monoliths (AX-69 and AMCB-48) with 30 % phenolic resin binder. The enhancement is simply due to the reduction of interparticle voids within the monolith. This improvement in stored methane capacity after the consolidation were verified afterwards by the direct measurement of methane adsorption isotherms (Section 9.3).

Table 9.1 The estimated methane storage (adsorbed at 3.4 MPa and 298 K) on the activated carbons and carbon monoliths from surface areas, pore volumes and bulk densities.

carbons	surface area	pore volume	bulk density	(Mullhaupt, *et al,* 1992)		(Parkyns and Quinn, 1995)	
	(S_{BET}) ($m^2\ g^{-1}$)	(V_o) ($cm^3\ g^{-1}$)	(ρ) ($g\ cm^{-3}$)	L_{max} ($mmol\ g^{-1}$)	V_s (v/v)	L_{max} ($mmol\ g^{-1}$)	V_s (v/v)
AX-100	2909	1.22	0.27	14.2	94	15.2	101
AX-83	2432	1.08	0.48	12.1	142	11.7	137
AX-69	2056	0.91	0.59	10.4	151	9.7	140
AX-56	1553	0.68	0.64	8.2	128	7.6	119
AX-45	1357	0.62	0.70	7.3	126	6.9	118
AMCB-40	1687	0.73	0.67	8.8	144	7.9	130
AMCB-48P	2931	1.35	0.27	14.3	95	16.3	107
AMCB-48	2145	0.96	0.58	10.8	154	10.1	144
AMCB-66	1775	0.85	0.59	9.2	133	9.2	133
BG-5R	847	0.41	0.77	5.1	96	5.0	94

Notes: AMCB-40, -48 and -66 are the monoliths made from KOH activated meso-carbon microbeads with 30 % phenolic resin as binder and the number following AMCB representing the burn-off of meso-carbon microbeads after KOH activation. AMCB-48P and AX-100 are the KOH activated meso-carbon microbeads with 48 % burn-off and the AX-21 carbon powder. The numbers following AX- are the weight percentages of AX-21 carbon powder in the monolith.

9.3 MEASURED METHANE CAPACITIES

The methane uptakes at 298 K on carbon monoliths made from AX-21 carbon, KOH-activated meso-carbon microbeads and coconut shells were measured on a high pressure electronic microbalance in a pressure range from 1 to 40 bar. It should be pointed that the methane uptakes measured gravimetrically on the balance represent the excess methane adsorbed in micropores, which excludes the methane stored in the gas phase. It is important to understand this implication when comparing with the corresponding results obtained by volumetric measurement and molecular simulation which give methane adsorption isotherms including contributions from the gas phase. The adsorbed, the stored and the delivered methane capacities are discussed separately in the following headings.

9.3.1 Adsorbed Methane Capacity

The methane uptakes at 298 K and under the pressure from 1 to 40 bar on the monoliths made from AX-21 carbon powder and from KOH-activated meso-carbon microbeads as well as from coconut shells (a reference material provided by British Gas plc. and made by Sutcliffe Speakman Carbon Limited, UK) are presented graphically in Figure 9.1 and 9.2 and in tabular form in Tables 9.2 and 9.3. The blank test (Table 9.2) shows there is no weight change in the pressure range from 1 to 40 bars, which suggests that the buoyancy effect on such a small sample size (less than 150 mg) is not significant. The calculation in Section 6.1.3 indicates that the buoyancy effect is negligible as long as the carbon sample is less than 150 mg at which the buoyancy is about 0.6 mg at 3.4 MPa and 298 K.

The excess methane adsorption isotherms were obtained by the following expression:

$$I_i = \frac{1000\,(w_i - w_o)}{16\,w_o} \qquad \text{(9.12)}$$

where w_i (mg) is the sample weight recorded at pressure P_i (bar), w_o (mg) is the initial weight of activated carbon, 16 (g mol^{-1}) is the molecular weight of methane and I_i (mmol g^{-1}) is the adsorbed methane per gram of carbon at the pressure P_i.

Table 9.2 The measured methane uptakes at 298 K on the carbon monoliths

Pressure	Blank run	AX-83	AX-69	AX-56	AX-45
(Bar)	(mg)	(mg)	(mg)	(mg)	(mg)
vacuum	106.1	147.9	138.9	132.6	81.5
1	106.1	151.1	142.4	134.5	83.1
2	106.1	153.2	143.4	136.1	84.0
4	106.1	156.3	146.1	138.2	
6	106.1	158.2	148.1	139.8	86.1
8	106.1	160.6	149.7	141.1	
10	106.1	162.2	151.1	142.1	87.3
12	106.1	163.6	152.3	143.0	
16	106.1	165.8	154.0	144.3	88.3
20	106.1	167.5	155.3	145.4	88.8
25	106.1	168.9	156.6	146.6	89.2
30	106.1	170.2	157.6	147.1	89.6
35	106.1	171.2	158.3	147.5	89.8
40	106.1	171.8	158.5	148.1	89.9

Notes: The monoliths of AX-83, -69, -56 and -45 are made from AX-21 carbon powder with different phenolic resin ratios. The number following AX is the weight percentages of AX-21 carbon powder in the monolith.

Table 9.3 The measured methane uptakes at 298 K on microporous carbon powders and monoliths.

Pressure	BG-5R	AMCB-40	AMCB-48P	AMCB-48	AMCB-48	AMCB-66
(bar)	(mg)	(mg)	(mg)	(mg)	(mg) @	(mg)
vacuum	104.7	98.6	66.6	110.1		77.0
1	106.6	100.9	68.0	112.2	112.4	78.2
2	107.9	101.9	69.4	113.8		79.1
4	109.4	103.4	71.0	116.1	116.3	80.3
6	110.3	104.6	73.1	117.9		81.2
8	111.1	105.5	74.5	119.2		82.0
10	111.7	106.2	75.5	120.4	120.6	82.6
12	112.1	106.7	76.6	121.4		83.1
16	112.8	107.7	78.1	123.0		84.0
20	113.3	108.5	79.4	124.2	124.3	84.6
25	113.7	109.2	80.7	125.4	125.5	85.2
30	113.9	109.6	81.7	126.4	126.5	85.7
35	114.1	110.0	82.5	127.1	127.2	86.0
40	114.1	110.3	83.1	127.7		86.4

Note: @ — desorption data; BG-5R is a monolithic carbon made from steam-activated coconut shells; AMCB-40, -48, and -66 are the monolithic carbon made from KOH-activated meso-carbon microbeads with 30 wt.% phenolic resin beads. The number following AMCB is the burn-off of meso-carbon microbeads after KOH-activation.

From the measured excess methane adsorption isotherms (Figures 9.1 and 9.2), the adsorbed methane capacities V_a, are calculated according equation 9.1 and the results are given in Table 9.4. The results in Table 9.4 show that the measured methane uptakes are lower than those estimated from surface area or pore volume by the empirical expressions (refer to Table 9.1). But the linear correlation between the methane uptakes and the BET surface areas of the monolithic carbons still exists as illustrated in Figure 9.3. The regression on the measured G (mmol g^{-1}) against S_{BET} (m^2 g^{-1}) gave the following correlation:

$$G = 2.6 + 0.003\ S_{BET} \quad \text{---------- (9.13)}$$

The constant and the slope in the above expression are of the same order of magnitude as in the empirical expression obtained by Mullhaupt *et al* (1992) but the absolute values are different. This is perhaps due to the similarity in morphology of the activated carbons tested in these study, while the commercial carbons tested by Mullhaupt *et al* are made from different materials in various forms.

Table 9.4 The methane uptake, the adsorbed, the stored and the delivered methane capacities on activated carbons at adsorption pressure 3.4 MPa, desorption pressure 0.1 MPa and temperature 298 K

activated carbons	bulk density ρ ($g\ cm^{-3}$)	methane uptake G ($mmol\ g^{-1}$)	adsorbed capacity ① V_a (v/v)	stored capacity ② V_s (v/v)	delivered capacity ② V_d (v/v)
AX-83	0.48	9.8	115	127~142	111~125
AX-69	0.59	8.7	126	134~151	111~127
AX-56	0.64	7.0	110	120~134	106~119
AX-45	0.70	6.4	110	119~133	98~112
AMCB-40	0.67	7.2	118	126~142	101~117
AMCB-48P	0.27	14.9	98	117~129	108~120
AMCB-48	0.58	9.7	138	145~164	128~146
AMCB-66	0.59	7.3	105	113~130	96~109
BG-5R	0.77	5.6	105	117~127	96~106
A20-15 ③	1.14			120 ⑤	
CHEN-1 ④	1.05			125 ⑤	

Notes: ① the value of V_a is calculated from equation 9.1; ② the low values of V_s and V_d are calculated using equation 9.6.a (excluding micropores) and the high values of V_s and V_d are calculated using equation 9.6.b (including micropores); ③ A20-15 is the carbon cylinder made from coconut shell by air cycle oxidation 20 times to 15 wt.% burn-off; ④ CHEN-1 is made by consolidating commercial coconut carbon NV5M235 with phenolic resin; and ⑤ stored methane capacity is directly measured by weighing the carbon container equilibrated with natural gas (95% methane at) 298 K and 3.4 MPa in Chemisar Laboratories Inc, Canada.

The results in Table 9.4 also show that the methane uptake (G) of AX-21 monoliths decreased with the increase of phenolic resin binder ratio but the volumetric adsorbed

methane capacity on the monolith (AX-69) 31 wt.% phenolic resin binder was higher than those with phenolic resin ratios of 17, 54 and 55 wt.%. This verified the conclusion (Table 9.1) from the estimation that the phenolic resin ratio of 30 wt.% in the consolidated monoliths from microporous powders was optimal in terms of volumetric methane capacities including the adsorbed, the stored and the delivered capacities (Table 9.4). The monolith made from KOH-activated meso-carbon microbeads with 48 wt.% burn-off (AMCB-48) is the best of all the monoliths fabricated.

9.3.2 Stored Methane Capacity

The gravimetrically observed methane uptake on the high pressure electronic microbalance represents the excess number of methane molecules adsorbed in micropores, and it does not include the methane molecules that occupy the same volume in the absence of potential enhancement from the carbon pore walls. Therefore, the total methane isotherm, I_{total}, on an activated carbon can be given by the measured excess methane isotherm (I_{excess}) and the micropore volume, V_o, by the following expression:

$$I_{total} = I_{excess} + \frac{P_i V_o}{Z_i RT} \quad \text{---------- (9.14)}$$

where I_{excess} and I_{total} are in unit of mmol g^{-1}; V_o (cm^3 g^{-1}) is the micropore volume derived from the nitrogen adsorption isotherm by the Dubinin-Astakhov equation; Z_i is the methane compressibility at pressure P_i (atm) and temperature T (298 K); and R (atm m^3 $kmol^{-1}$ K^{-1}) is the gas constant.

The molecular simulation of methane adsorption in a model pore gives the total number of methane molecules, ρ^*_{CH4}, per reduced volume. So the total methane adsorption isotherm, I_{total}, on the void-free model carbon composed of parallel carbon layers separated from each other at a distance of H (between the nucleus centres of adjacent carbon layers) can be obtained from the simulation output, the reduced methane molecule number (ρ^*_{CH4}), by the following equation:

$$I_{total} = \frac{\rho^*_{CH4} H}{\sigma^3_{CH4} M_c A_c} \times 10^3 \quad \text{---------- (9.15)}$$

where I_{total} is in units of mmol g^{-1}; $(\rho^*_{CH4} / \sigma^3_{CH4})$ is in units of methane molecules per cubic nanometer; A_c is the carbon atom number density in units of carbon atoms per square nanometer; H (nm) is the slit width; and M_c is carbon atomic weight.

The measured total methane isotherms of the monolith AX-69, AMCB-48 and BG-5R and a methane isotherm predicted from the molecular simulation are illustrated in Figure 9.4 (a) and (b). Figure 9.4 (a) shows that the predicted isotherm in the high pressure region is higher than those measured on the carbon monoliths. This is expected if the model carbon used in the molecular simulation has an optimal pore structure. However, Figure 9.4 (b) shows that at low pressures the predicted isotherm is lower than the measured value. The problem probably relates to equation 9.14 by which the total isotherm is obtained from the excess experimental isotherm. In ultra-micropores (less than 0.5 nm) the adsorbed methane molecules, as suggested by molecular simulation results (Matranga, *et al,* 1992), are so closely packed that space is no longer available for free gas molecules. So the methane in the ultra-micropores might be double-counted in equation 9.14, which will make the converted total isotherm in the low pressure region higher than the predicted isotherm. The micropore volume (V_o) used in equation 9.14 is deduced from nitrogen adsorption isotherms by Dubinin-Astakhov equation which includes both super-micropores and ultra-micropores. What kind of pore volume should be used in the conversion of an excess isotherm to a total isotherm is a controversial issue. So the measured excess isotherm is more reliable than the converted total isotherm.

The stored methane capacity, V_s, on microporous powders and monoliths is calculated from the measured methane uptake, G, by the equations 9.1 and 9.6, and the results are shown in Table 9.4. As estimated from BET surface area or micropore volume (see Table 9.1), the monolith AMCB-48 is the best among the activated carbons tested in terms of the stored methane capacities. Comparing the measured V_s values (Table 9.6) with the predicted values (Table 9.1), the measured V_s which excludes micropores in the calculation of V_g is lower than those estimated from BET surface areas and micropore volumes, while the measured V_s which includes micropores is close to the predicted values.

The difference between V_a and V_s for carbon monoliths seems not to vary much from one to another. This is because the difference between V_a and V_s is V_g and V_g depends on both micropore volume and bulk density. For AMCB-48P powder, V_g is 19 v/v which is much higher that the values of V_g (10 ± 2 v/v) for the monoliths. This is because the interparticle voids within packed powders are much higher than those of monoliths. The space within a methane storage cylinder can be divided into three fractions: micropores (θ_{micro}), non-micropores ($\theta_{non\text{-}micro}$) including mesopores, macropores and interparticle voids, and solid carbon (θ_{carbon}). Each fraction can be roughly estimated from the packing density (ρ), the carbon density measured by a helium pycnometry (ρ_{He}) and the carbon density measured by a mercury porosimetry (ρ_{Hg}) at the intrusion pressure of 414 MPa by the following formulae:

$$\theta_{non-micro} = \rho\left(\frac{1}{\rho} - \frac{1}{\rho_{Hg}}\right) \quad \text{---------- (9.16)}$$

$$\theta_{micro} = \rho\left(\frac{1}{\rho_{Hg}} - \frac{1}{\rho_{He}}\right) \quad \text{---------- (9.17)}$$

$$\theta_{carbon} = \frac{\rho}{\rho_{He}} \quad \text{---------- (9.18)}$$

The measured densities ρ, ρ_{Hg} and ρ_{He} of microporous powder AMCB-48P, the carbon monolith AMCB-48 and the reference monolith BG-5R are listed in Table 9.5.

Table 9.5 The packing density and the densities measured by helium pycnometry and the mercury porosimetry of the activated carbon powders and monoliths

activated carbon	ρ ($g\ cm^{-3}$)	ρ_{Hg} ($g\ cm^{-3}$)	ρ_{He} ($g\ cm^{-3}$)
AMCB-48P	0.27	0.5869	2.2524
AMCB-48	0.58	0.7971	2.0296
BG-5R	0.77	1.1956	2.1990

The calculated fractions of micropores, non-micropores and solid carbons of BG-5R, AMCB-48 and AMCB-48P are illustrated in Figure 9.5. The comparison in micropore volume fractions in Figure 9.5 indicates that AMCB-48 should give a higher volumetric methane capacity than BG-5R and AMCB-48P because AMCB-48 has a larger micropore proportion and only micropores play a major role in the enhancement of methane density as the molecular simulation results suggest. The experimental results in Table 9.4 proved that AMCB-48 monolith did have a higher volumetric methane capacity at 3.4 MPa and 298 K than the others. The micropore volume fraction in the cylinder filled with AMCB-48P powders was increased from 34 % to 44 % after the powders were consolidated into a monolith AMCB-48 while the non-micropore volume fraction was reduced from 54 % to 27 %. This is the main reason that the volumetric methane capacities of microporous powders such as AX-21 carbon and KOH-activated meso-carbon microbeads are improved after they are formed into monoliths. The reduction in non-microporous volume fraction from powders to monoliths mainly comes from diminishing interparticle voids due to the compacting pressure and the binding energy from phenolic resin. It should be pointed out that the interparticle voids in the monolith made from very fine powders are very likely to be over-estimated by the hexagonal close-packed spheres (HCPS) model in which the particles are assumed to be hard balls equal in diameter. In a real situation, there is a particle size distribution in powders and the smaller particles can fill the voids among bigger particles. The particles are not perfect spheres, so the contact between particles might be partially face to face instead of the complete point contact between hard balls. These effects may minimise interparticle voids. From this point of view, the predicted volumetric methane capacity on the monolith made from powders by HCPS model may be under-estimated.

The volume fractions of micropores, non-micropores and solid carbon can also be estimated from packing density, ρ, and micropore volume, V_o, derived from nitrogen adsorption isotherm by the following formulae:

$$\theta_{non-micro} = 1 - \rho V_o - \frac{\rho}{\rho_{He}} \quad \text{---------- (9.19)}$$

$$\theta_{micro} = \rho V_o \quad \text{---------- (9.20)}$$

The values of θ_{micro} for BG-5R, AMCB-48 and AMCB-48P are 32, 55 and 36 % and $\theta_{non\text{-}micro}$ are 33, 16 and 52 %, respectively. The micropore volume fractions calculated from V_o are always higher than those obtained from ρ_{Hg}. The results obtained by the two methods should not be compared with each other because the division between micropores and non-micropores is ambiguous and different in nitrogen adsorption and mercury intrusion.

The solid carbon fraction of the reference monolith BG-5R is 35 %; this is higher than that of AMCB-48 (29 %), which means that AMCB-48 has more space for methane storage than BG-5R. The higher non-micropore volume fraction of AMCB-48P make its stored methane capacity much higher than its adsorbed methane capacity because the methane stored in bulk phase is significant in the powder packed cylinder. The stored methane capacity at 298 K and 3.4 MPa on the carbon monoliths AX-69 and AMCB-48 are 134 ~ 151 v/v and 145 ~ 164 v/v, much higher than those of commercially available activated carbons. Chahine and Bose reported (1991) the disc (∅ 25 x 5 mm) compacted at 100 ~ 300 MPa from AX-21 carbon powder with 2 % thermoplastic binder gave a stored methane capacity of 144 v/v at 3.5 MPa and 298 K. The stored methane capacity of coconut carbon monoliths (A20-15 and CHEN-1) fabricated in this study is similar to that of BG-5 which is provided as a reference by British Gas.

9.3.3 Delivered Methane Capacity

In most cases the stored methane capacity is sufficient to reflect the capability of an activated carbon for natural gas storage. But sometimes there is a big difference between the adsorbed and the delivered methane capacity. As suggested by the simulation results in Figure 7.14 (Section 7.2.3), 75 % of the adsorbed methane at 3.4 MPa and 298 K in pores of width 0.74 nm can not be delivered at 0.1 MPa and 298 K. The experimental results by Atlanta Gas Light Adsorbent Research Group have shown that about 30 % of the adsorbed methane at 3.4 MPa on the PVDC based carbon monoliths is irretrievable at 0.1 MPa without heating, which suggests that a significant proportion of micropores in PVDC carbons are ultra-micropores. Although the stored methane capacity on PVDC carbons is

very high, around 180 v/v at 3.4 MPa and 298 K, the delivered methane capacity is just around 130 v/v at 0.1 MPa and 298 K, which is still less than the defined target of 150 v/v.

9.3.3.1 The Monoliths With Binders

The delivered methane capacity (V_d) of the monoliths produced in this study were calculated according equation 9.7 and the results are listed in Table 9.4. The difference between the adsorbed and the delivered methane capacity of these activated carbons tested is in a range of 8 to 20 %, which is much less than the difference of 30 % found in the case of PVDC carbon. The highest delivered methane capacity is achieved on the monolith AMCB-48 which can delivery 128 ~146 cubic meters (298 K and 0.1 MPa) of methane per cubic meter of carbon.

The volumetric methane capacities, including the adsorbed, the stored and the delivered capacities, of AX-21 carbon powder were improved after consolidation with phenolic resin binder. The improvement is the result of a compromise between the positive effect of increasing packing density increase and the negative effect in decreasing adsorption capacity due to the addition of phenolic resin binder. The binder does not generate much pore structure without activation. An attempt was made to activate the phenolic resin carbon bond in AX-21 carbon monoliths by reaction with CO_2 at 800 °C for 1 hour. The consequence of the CO_2 activation is that the adsorption capability is improved but the bulk density is reduced as shown in Table 9.6.

Table 9.6 The property of AX-21 carbon monoliths with and without CO_2 activation

monolithic carbons	bulk density ρ ($g\ cm^{-3}$)	surface area S_{BET} ($m^2\ g^{-1}$)	adsorbed capacity, V_a (v/v)	stored capacity, V_s (v/v)	delivered capacity, V_d (v/v)
AX-69	0.59	2056	126	134	111
AX-56	0.64	1553	110	120	106
CO_2-AX-69	0.41	2594	104	118	105
CO_2-AX-56	0.47	1928	114	127	114

Note: CO_2-AX-69 and CO_2-AX-56 are CO_2 activated AX-69 and AX-56; V_s and V_d are obtained from V_a without counting the compressed methane in micropores.

The BET surface area of AX-69 monolith increased from 2056 to 2594 m^2 g^{-1} but the bulk density decreased from 0.59 to 0.41 g cm^{-3} after the CO_2 activation. The net effect is that the adsorbed, the stored and the delivered methane capacities were reduced from 126, 134 and 111 v/v to 104, 118 and 105 v/v, respectively. There is only a little improvement in the volumetric methane capacities on AX-56 after the CO_2 activation.

What occurs during the CO_2 activation is that more of the gasification reactions takes place on AX-21 carbon particles than on the phenolic resin carbon binder because the microporous particles of AX-21 carbon adsorb more CO_2 molecules and have more active sites for reaction. So the pore structure development within phenolic resin binder by CO_2 activation will not happen to the expected extent as intended. Instead the unnecessary further pore widening on microporous particles is inevitable during the CO_2 activation. For the monolith with a high binder ratio like AX-56, CO_2 activation might provide some benefit in opening some binder-blocked pores. The scanning electronic microscope pictures of the AX-21 carbon monoliths with different binder ratios in Figure 9.6 shows that the join between particles is tight and continuous, especially in the monolith with a high binder ratio. Perhaps this is why the methane capacity of the monolith AX-56 has been slightly improved after the CO_2 activation.

Figure 9.7 illustrates the variation in the measured BET surface area versus the binder ratio, comparing with the BET surface area, S_{mono}, expected by the ideal mixing rule assuming that there is no contribution to surface area from binder and no pore blocking of AX-21 carbon by the binder:

$$S_{mono} = \varepsilon S_{AX\text{-}21} \quad \text{----------} \quad (9.21)$$

where ε is the fraction of filler in the monolith and the $S_{AX\text{-}21}$ is the surface area of the AX-21 carbon powder. It seems there is a very good agreement between the measured and the expected surface areas. But it is hard to believe that there is no pore blocking in the monolith with a binder ratio as high as 65 wt.%. It might be another complex case where pore blocking and pore creation (the monoliths were heat-treated at 800 °C in nitrogen) compensate each other.

9.3.3.2 The AX-21 Carbon Powder Packed Under High Pressures

In this study AX-21 carbon powder was packed into a specially designed cylinder (see Figure 6.4) under an elevated pressure without applying any binder. The volume of methane delivered per volume of storage space was measured on the high pressure methane adsorption-desorption test rig (see Figure 6.3). Two packing pressures, 15 and 20 MPa, two loading and unloading times, 5 and 30 minutes (at 3.4 MPa), and two temperatures, 298 and 273 K, were tested and the results of delivered methane capacities are given in Table 9.7.

Table 9.7 The delivered methane capacities of packed AX-21 carbon powder

Pack pressure (MPa)	packing density (g cm^{-3})	void fraction	temperature (K)	loading time (minute)	delivered methane (v/v)
0	0.28	0.86	298	30	83
0	0.28	0.86	298	5	71
15	0.40	0.80	298	30	112
20	0.44	0.62	298	30	128
20	0.44	0.62	298	5	99
20	0.44	0.62	273	30	150

Notes: The void fraction includes all pores within particles and the interparticle voids; The filling pressure is 3.4 MPa and the discharging pressure is 0.1 MPa; the unloading time is 15 minutes.

Packing Pressure

Comparing with compressed methane (34 v/v at 3.4 MPa and 298 K) in the empty cylinder, the delivered methane capacity was enhanced by a factor of 2.44 after the cylinder was filled with AX-21 carbon powder without applying any packing pressure. The capacity was further increased by 3.3 and 3.8 times as the cylinder was packed with AX-21 carbon powder under the pressures of 15 and 20 MPa, respectively. The enhancement in the delivered methane capacity comes from the increase in bulk density of AX-21 carbon

powder after the compacting, or in other words due to the reduction of the interparticle voids within the AX-21 carbon filled cylinder. The bulk density of the AX-21 carbon powder in the cylinder is 0.28, 0.40 and 0.44 g cm^{-3} at the packing pressure of 0.0, 15.0 and 20.0 MPa. The void fraction θ, which is defined as the ratio of total volume V_t, including both interparticle voids and intraparticle pores, to packing volume V_c. V_t is obtained by equation 6.22 from V_t' by charging and discharging the AX-21 carbon-packed cylinder with helium. The slopes of the straight lines in Figure 9.8 correspond to the values of V_t' for packing pressures 0.0, 15.0 and 20.0 MPa. From the values of V_t and V_c the void fractions of the AX-21 carbon-packed bed at pressures 0, 15 and 20 MPa are calculated to be 0.83, 0.79 and 0.60 respectively. The reduction in the void fraction with increase of packing pressure is believed to be the reduction of interparticle voids because the nitrogen adsorption measurement of the compressed AX-21 carbon gives the same surface area and pore volume as the non-compressed AX-21 carbon. This suggests that there is no significant change in the micropore structure of the AX-21 carbon following compression.

In this study, the packing pressure only goes up to 20 MPa due to the pressure limit of the compressor. The bulk density might be further increased by applying an even higher packing pressure. But the residual stress within the packed powders builds up with packing pressure and too high elastic recovery will require a thick and heavy cylinder, which will make the adsorbed methane lose its advantage over the compressed methane in this respect. For the packed pressure of 20 MPa AX-21 carbon powder give a delivered methane capacity of 128 v/v at 298 K.

Loading And Unloading Time And Temperature

Except for the delivered methane capacity, the methane loading and unloading rates are also very important for the application of adsorbed natural gas as a vehicle fuel. The gas filling time should not be too long if the adsorbed natural gas technology is to be commercialised. The methane charging and discharging time also affect the methane capacity because of the heat transferred during loading and unloading the cylinder. The temperature of the carbon bed will go up during methane loading, which will make the adsorption capacity decline, and the temperature will go down during unloading, which will

reduce the methane recovery rate. This is a practical problem in adsorbed natural gas applications. In the experiment, the cylinder was submerged in a thermostatic water bath in order to maintain a constant temperature. Even so, the results in Table 9.7 shows that by reducing the loading and unloading time from 30 minutes to 5 minutes, the delivered methane capacity was reduced significantly. To what degree the temperature will affect the methane capacity was not investigated in detail in this study. The delivered methane capacity of AX-21 carbon power at 273 K is 150 STP v/v, which is 22 STP v/v more than is delivered at 298 K. Sircar, *et al* (1996) reported that the temperature change during adiabatic filling (at 35 bars) and releasing (at 1.35 bars) of methane at 300 K on AX-21 carbon is about 70 K. The temperature variation within the activated carbon vessel during methane or natural gas loading and unloading processes depends on the thermal conductivity of the carbon bed and the vessel, the gas charging discharging rate and the adsorbed capacity of methane or natural gas on carbons.

9.4 SUMMARY

The stored and delivered volumetric methane capacities of microporous powders (AX-21 carbon and KOH activated meso-carbon microbeads) were significantly improved after being consolidated into the monoliths with 30 wt.% phenolic resin beads as binder. The main reason for the enhancement is believed to be the reduction of interparticle voids within the monoliths. An improvement in delivered methane capacity is also achieved by compacting microporous powders into a cylinder under a high pressure. The delivered methane capacities at 298 K, 3.4 MPa filling pressure and 0.1 MPa discharging pressure on the carbon monoliths AX-69 and AMCB-48 are much higher than those on commercially available activated carbons (Quinn and Parkyns, 1995). The upper limit of delivered methane capacity, 146 v/v, of AMCB-48 monolith is close to the defined target of 150 v/v.

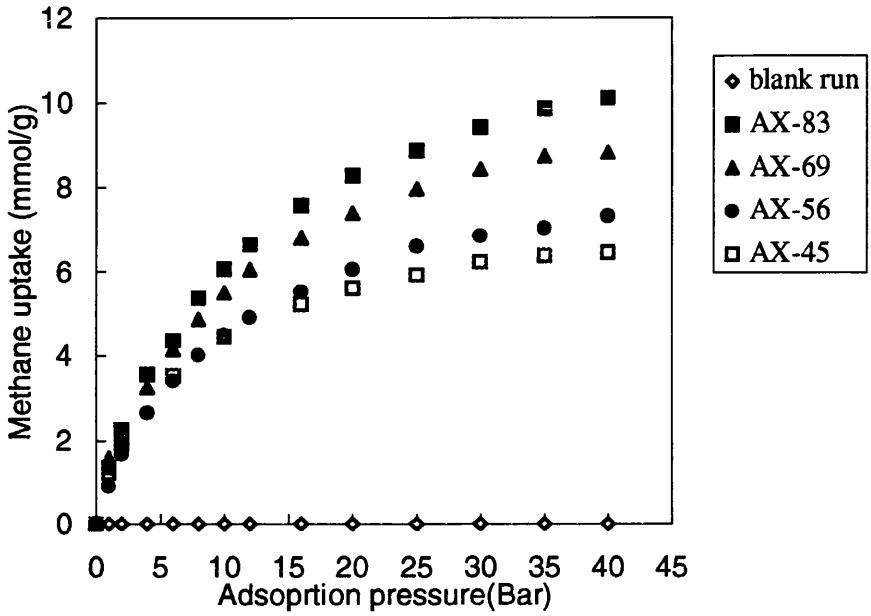

Figure 9.1 The excess methane adsorption isotherms (at 298 K) of a series of monoliths made from AX-21 carbon with different percentages of phenolic resin binder.

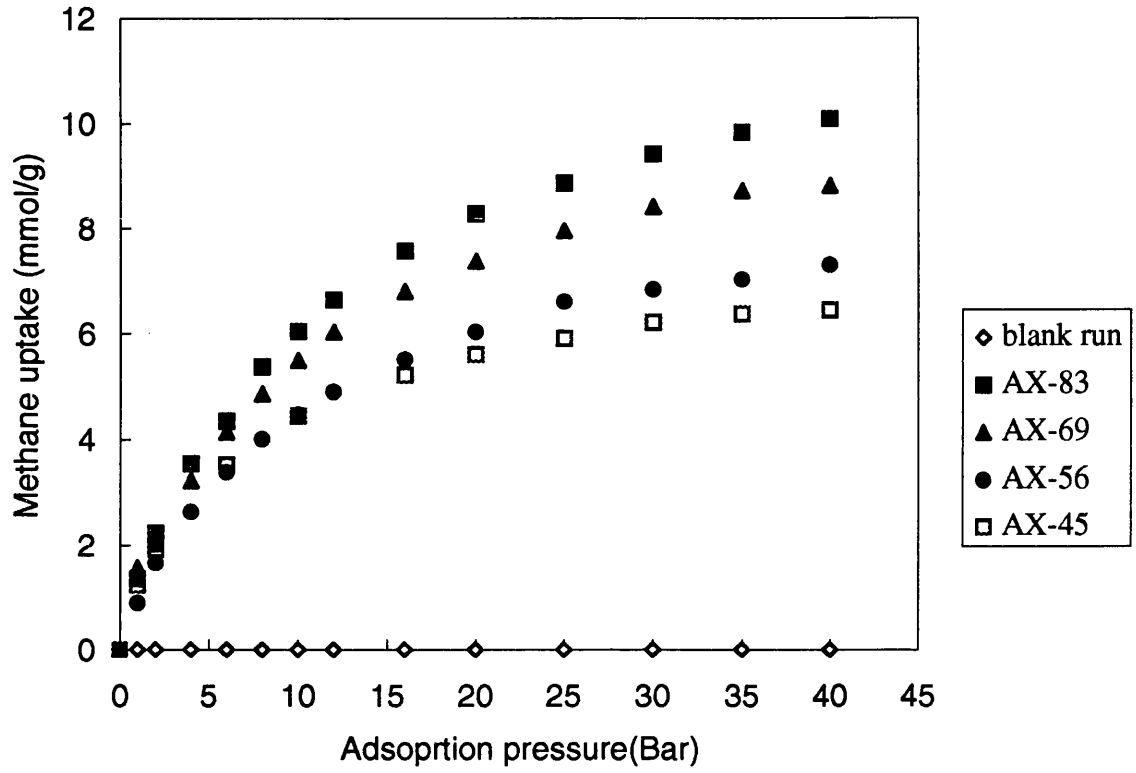

Figure 9.2 The excess methane adsorption isotherms (at 298 K) of the monoliths AMCB-40, AMCB-48 and AMCB-66 which are made from KOH-activated meso-carbon microbeads with different burn-off (the monoliths were made with 30 wt.% phenolic resin compacted at 40 MPa and 150 °C). AMCB-48P is KOH activated meso-carbon microbeads with 48 % burn-off. BG-5R is a reference monolith made from coconut shells by Sutcliffe Speakman plc.

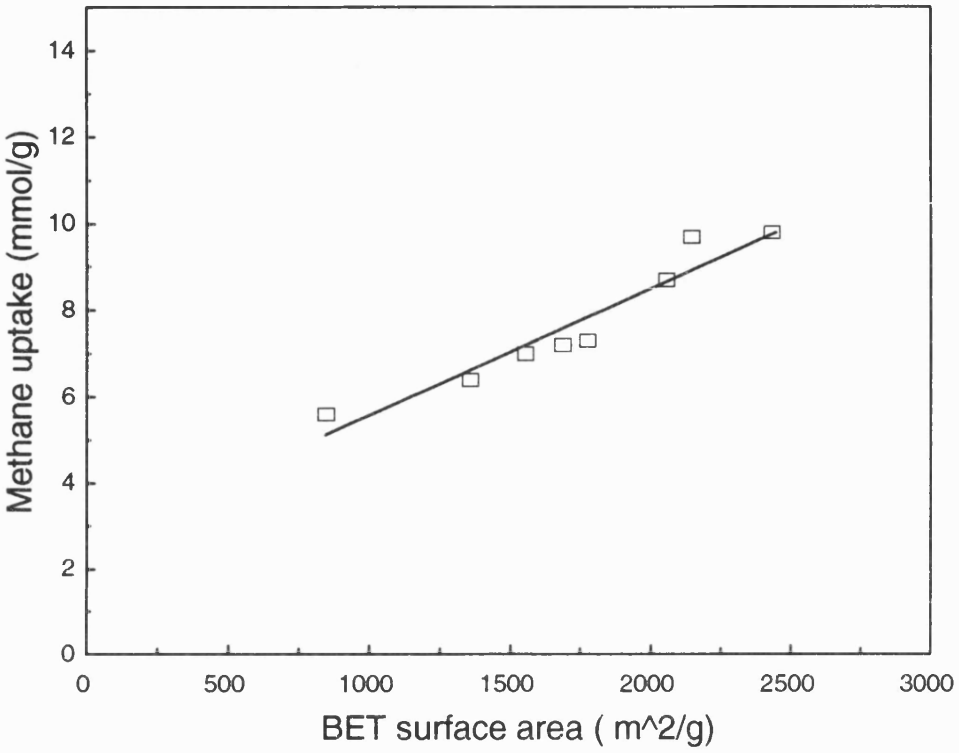

Figure 9.3 The correlation between the methane uptake at 3.4 MPa and 298 K and the BET surface area of monolithic carbons. The rectangles are the measured data and the straight line is the regression.

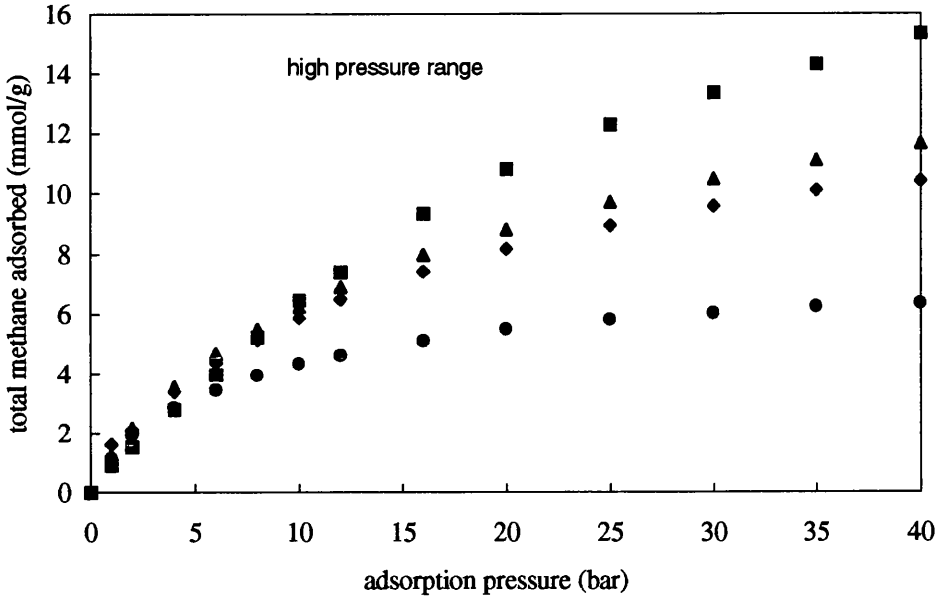

(a)

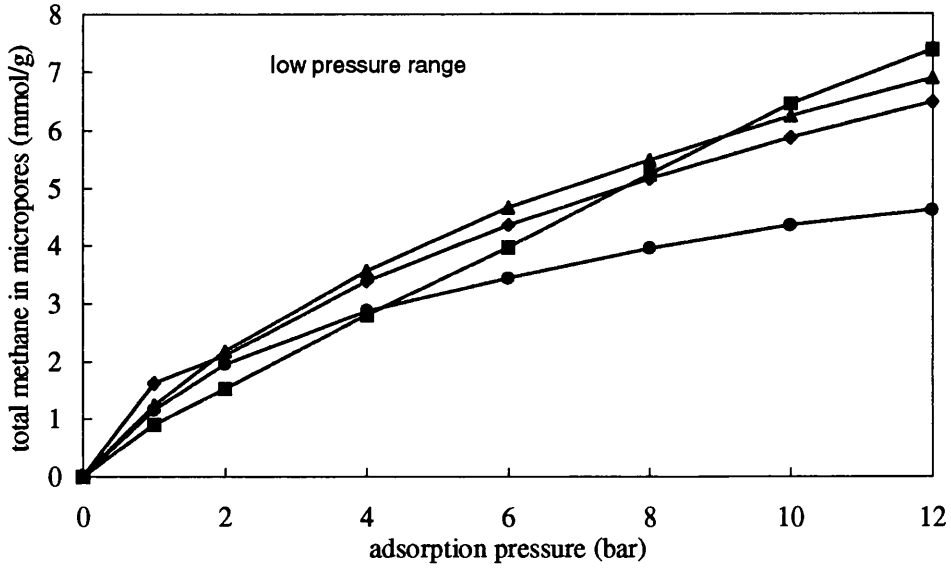

(b)

Figure 9.4 The total methane adsorption isotherms at 298 K on monolithic carbons: (a) in high pressure range and (b) in low pressure range. The circle symbols represent BG-5R, the diamonds AX-69 and the triangles AMCB-48. The rectangles are the total methane isotherm estimated by molecular simulation (model pore parameter: the number of carbon layer in the pore wall is one; the carbon atom density is 33.67 nm^{-2}; the interlayer spacing is 0.3354 nm and the pore width is 1.12 nm. model monolith: void-free and composed of non-interacting parallel slits).

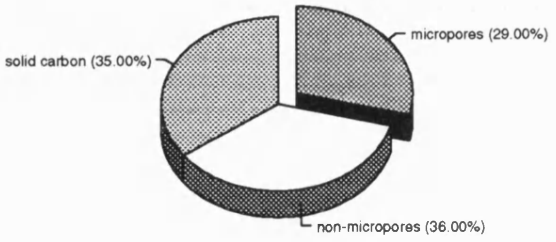

(a)

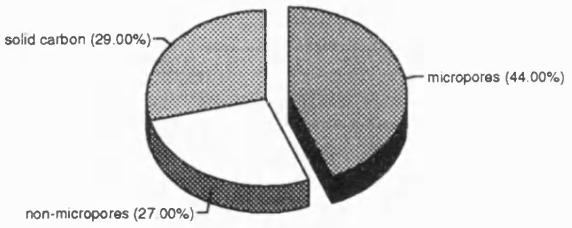

(b)

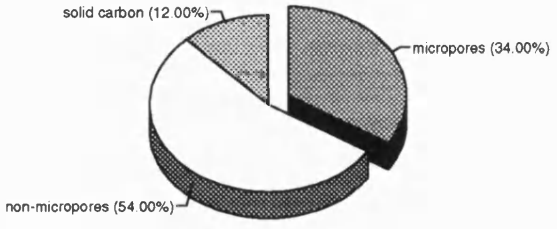

(c)

Figure 9.5 The volume fraction of micropores, non-micropores and solid carbon of (a) carbon monolith (BG-5R) made from coconut shell carbon, (b) carbon monolith (AMCB-48) made from KOH-activated meso-carbon microbeads with 48 % burn-off, and (c) KOH-activated meso-carbon microbeads powder with 48 % burn-off.

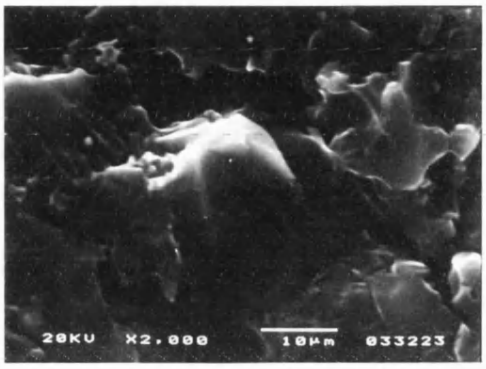

a

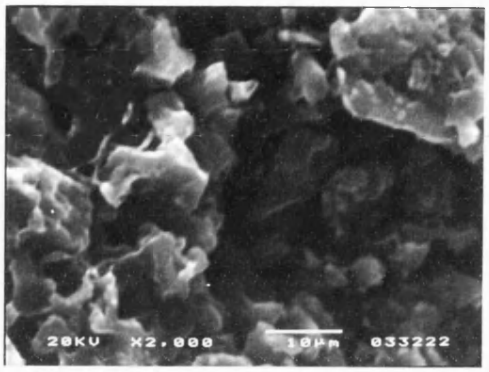

b

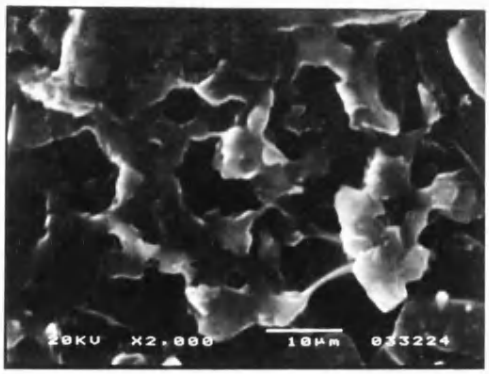

c

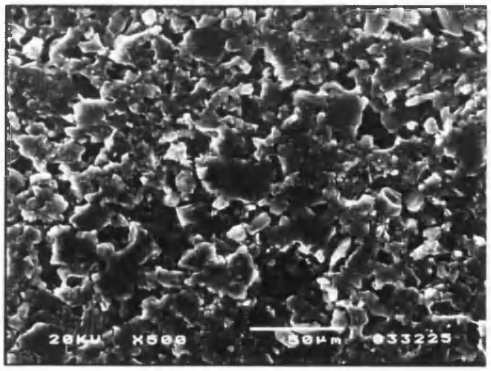

d

Figure 9.6 The scanning electronic microscope image of the monolith made from AX-21 carbon powder with different binder ratios: (a) 35 wt.% phenolic resin; (b) 45 wt.% phenolic resin; (c) 56 wt.% phenolic resin and (d) 69 wt.% phenolic resin.

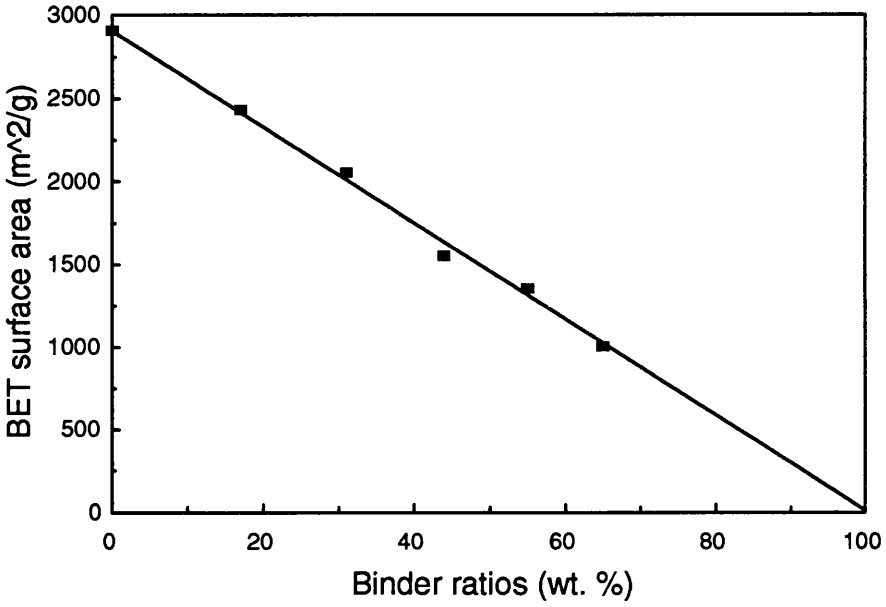

Figure 9.7 The variation in surface area versus the phenolic resin ratio in the monolith made from AX-21 carbon powder. The rectangles are the measured and the straight line corresponds to what is expected assuming that is no contribution in surface area from the phenolic resin binder and no pore block.

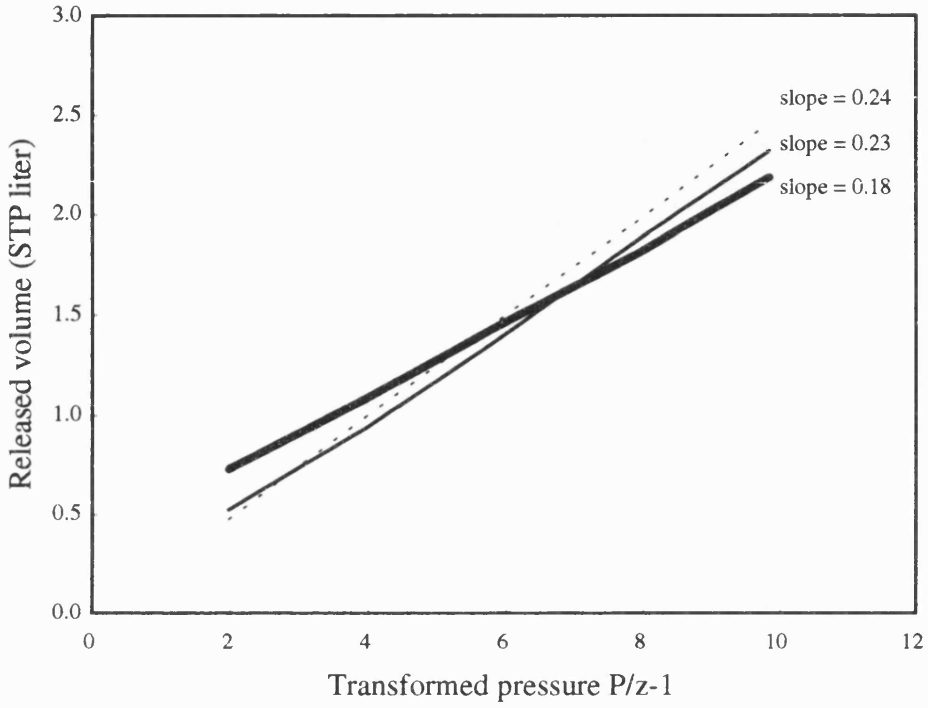

Figure 9.8 The void fraction of the AX-21 carbon filled cylinder at the packing pressures of 0.0 MPa (dot line), 15.0 MPa (thin solid line) and 20.0 MPa (thick solid line). The definition of transformed pressure (P/z-1) was given in Section 6.1.4 and equation 6.21.

CHAPTER 10 CONCLUSIONS AND RECOMMENDATIONS FOR FUTURE WORK

10.1 CONCLUSIONS

The main purpose of this study is to produce and evaluate microporous activated carbons for adsorbed natural gas storage. The research started with a fundamental study on modelling by grand canonical ensemble molecular simulation of methane adsorption in a carbon slit in order to understand the influence of carbon microstructure on the adsorbed methane densities in pores as well as the volumetric methane capacities of carbon monoliths. An optimal pore size of 1.12 nm for methane or natural gas storage at 3.4 MPa and 298 K, was indicated after the simulations.

Efforts have been made to generate microporous carbons with pore sizes around the optimal value by activating graphitizible precursors like meso-carbon microbeads (derived from coal tar pitch) and petroleum coke and non-graphitizible precursors like lignite and phenolic resin through either physical activation (using CO_2) or chemical activation(using KOH, K_2CO_3 and H_3PO_4). It was concluded that KOH is the most effective activating agent to create micropore structure from graphitizible carbon materials but not from non-graphitizible carbon precursors. On the other hand, thermal gasification of carbon by CO_2 was shown to be a very effective process to develop pore structure from non-graphitizible carbons, but the pore size distribution is wider than those of chemically activated carbons.

Carbon monoliths have been made from microporous carbons such as AX-21 carbon powder (a commercial product) and KOH activated meso-carbon microbeads (fabricated in this study). The experimental results and the predicted values have shown that the volumetric methane capacities of the powders are significantly enhanced after being consolidated into monoliths with ca. 30 wt.% of phenolic resin as binder. It was also demonstrated by a study of CO_2 activation of a phenolic resin bar that it is very difficult to generate a uniform micropore network within a large size carbon monolith by direct physical activation of a pre-formed carbon block due to gas diffusion limitations. Instead a compacting process of microporous powders with or without a binder is recommended to

reduce interparticle voids so as to improve their volumetric methane capacities. The simulation and the experimental results as well as the conclusions are summarised more in detail in the following sections.

10.1.1 Molecular Simulations

Grand canonical ensemble Monte Carlo molecular simulations of methane adsorption at 298 K were conducted by varying the carbon pore microstructure such as pore wall thickness (the number of carbon layer within each pore wall, n); carbon atom density of a carbon layer plane, A_c; the interlayer spacing between carbon layers, Δ, and pore width, H. In the simulation the values of n, Δ and A_c were varied within a reasonable range as suggested by experimental measurements of carbon microstructure using high resolution transmission electron microscopy (relating to n), X-Ray diffraction (giving Δ) and helium pycnometry (referring to A_c). The molecular simulations gave the following results.

1. The variation of carbon atom density in the pore wall has a significant influence on adsorbed methane density in model slit-shaped carbon pores, although variations in interlayer spacing and the number ($n > 2$) of carbon layers in the pore wall have little effect.
2. The highest adsorbed methane density at 3.4 MPa and 298 K was achieved in the slit-shaped pore of width 0.74 nm, which is just wide enough to accommodate one layer of methane molecules, where the interaction potential between methane molecules and the opposite pore walls are completely over-lapped and strengthened.
3. The highest volumetric methane capacity at 3.4 MPa and 298 K was achieved in model pores of width 1.12 nm, which can accommodate two layers of methane molecules.
4. The optimal pore size of activated carbons for the adsorbed natural gas as on-board fuel of gas-driven vehicles is around 1.12 nm. Mesopores, macropores and voids play little role in the enhancement of the natural gas storage capacity and ultra-micropores are also not desirable because methane molecules adsorbed in such pores cannot be recovered at the discharging pressure of 0.1 MPa at 298 K.

5. The defined industrial target of the delivered methane capacity on activated carbons, i.e. 150 v/v at 3.4 MPa and 298 K was shown to be theoretically feasible based upon the simulation results on a void-free model carbon. Two configurations, hexagonal close-packed spheres (HCPS) and close-packed parallel cylinders (CPPC), were proposed to model the carbon monoliths made from powders and from fibres. The stored and the delivered methane capacities estimated on the HCPS model with skeletal carbon density of 2.0 g cm^{-3}, pore width of 1.12 nm, interlayer spacing of 0.3354 nm and two carbon layers in each pore wall are in good agreement with the measured values for carbon monolith made from KOH-activated meso-carbon microbeads (48 % burn-off) with 30 % phenolic resin.

10.1.2 Microporous Carbon Production

Graphitizible meso-carbon microbeads and petroleum coke and non-graphitizible lignite have been activated by KOH and K_2CO_3. The reaction temperature, the reaction time and the ratio of the activating chemicals to carbon as well as the reaction atmosphere have been investigated. The experimental measurement gave the following results.

6. Microporous carbon powders can be produced by controlling the burn-off of meso-carbon microbeads to around 50 wt.% through varying reaction time for a given temperature (800 °C) and a ratio (4:1) of KOH to meso-carbon microbeads. The BET surface area and micropore volume of the KOH activated meso-carbon microbeads with 48 % burn-off are 2931 $m^2 g^{-1}$ and 1.35 $cm^3 g^{-1}$ respectively and the average pore size is around 1.0 nm.
7. KOH is more effective than K_2CO_3 in creating micropore structure from graphitizible carbon materials.
8. The reaction atmosphere in KOH activation process is also very important in the development of pore structure besides the temperature, the time and the ratio of reactants. The presence of carbon dioxide in the gas phase prevents the pore development due to the formation of potassium carbonate. A high flow rate of inert protection gas (nitrogen) can minimise the negative influence of carbon dioxide.

A non-graphitizible phenolic resin carbon block and a graphitizible meso-carbon microbeads disk were activated by CO_2. The experimental measurements gave the following results.

9. Thermal gasification of meso-carbon microbeads by CO_2 did not give a very high surface area and a large porosity due to the lack of internal reactive sites within meso-carbon microbeads.
10. The sectioning analysis of the CO_2-activated phenolic resin carbon block proved that the outer layer of the block had been over-activated while the inner core was under-activated due to the gas diffusion limitation within the carbon monolith. This problem is inevitable in the physical activation of a large size monolith. This result suggests that it is very difficult to create uniform micropore structure by directly activating a large piece of carbon block with oxidising gases.

10.1.3 Microporous Carbon Monoliths

Microporous carbon monoliths have been successfully fabricated in this study by compacting mixtures of AX-21 carbon powder or KOH-activated meso-carbon microbeads with phenolic resin beads. The nitrogen adsorption measurement on the monoliths leads to the following conclusions.

11. The surface area and the pore volume of the monoliths made from AX-21 carbon powder decrease linearly with the increase of phenolic resin binder, but the bulk density of the monoliths was enhanced with the addition of binder.
12. 30 wt.% phenolic resin in the mixture with microporous powders was found to be the optimal ratio balancing the porosity and the bulk density of the monolith. The monolith with 30 wt.% binder gave the highest volumetric methane capacity at 298 K and 3.4 MPa.

10.1.4 Methane Capacity On Carbon Monoliths And Packed AX-21 Carbon Powder

The high pressure methane adsorption and desorption tests on the monoliths and on the AX-21 carbon powder gave the following results.

13. The adsorbed, the stored and the delivered volumetric methane capacities of microporous AX-21 carbon powder and the KOH activated meso-carbon microbeads have been significantly improved after being consolidated into monoliths with 30% phenolic resin beads. The best monolith (AMCB-48) produced from the KOH-activated meso-carbon microbeads with 48 % burn-off can adsorb, store and deliver 138, 164 and 146 cubic meters of methane per cubic meter of activated carbon at 298 K, 3.4 MPa charging pressure and 0.1 MPa discharging pressure.
14. The delivered methane capacity of AX-21 carbon powder has been also enhanced from 83 to 128 v/v (loading methane at 3.4 MPa for 30 minutes and unloading methane at 0.1 MPa at 298 K) after AX-21 carbon powder was packed into a cylinder under 20 MPa pressure.
15. The delivered methane capacities on the monoliths or on the packed AX-21 carbon powder are much higher that those of commercially available activated carbons but still lower than the defined target of 150 v/v.

10.2 PROPOSALS FOR FUTURE WORK

Monte Carlo molecular simulation is a very useful method to provide insights into the influence of carbon microstructure on the methane adsorption in micropores. It can also be used to estimate the maximum methane adsorption capacity for a given temperature and pressure based upon the idealised pore model and the simplified carbon morphology. Molecular simulations can not be used to predict precisely the methane isotherms on carbons because the carbon pore structure and surface are much more complex than has been assumed in the models. In this study, attempts have been made to develop model pores that are more realistic than the simple graphite pore models used previously by using the skeletal carbon density measured by helium pycnometry and the pore wall thickness of two carbon layers suggested by high resolution transmission electron microscopy. There are other factors which have been neglected, for example, pore walls were assumed to be smooth and a single pore size is assumed. The simulations would be improved if the following factors can be considered:

i. incorporate some oxygen containing functional groups which normally exist on activated carbon surface to see the influence on methane adsorption.

ii. pore size distribution and particle size distribution should be considered when estimating the methane adsorption capacity on bulk activated carbons.

iii. other types of pore shapes than a slit, such as cones and wedges should be studied.

Carbon monoliths have been successfully made from microporous powders AX-21 carbon or KOH activated meso-carbon microbeads with phenolic resin binder. The best monolith produced can deliver 128~146 cubic meters of methane per cubic meter of carbon at 298 K, which is still lower than the defined industrial target 150 v/v. The delivered methane capacity of the monolith can be further enhanced if:

iv. the bulk density of the monolith can be further increased by using higher compacting pressure. The compacting pressure is only 40 MPa due to the limitation of the press used in this study.

v. the pore size distribution can be further narrowed to be around 1.12 nm by controlling the process parameters.

vi. microporous fibres can be arrayed parallel and bonded into a monolith because the close-packed parallel cylinders have less interparticle voids than the close-packed powders.

Pure methane was used in this study to represent natural gas because natural gas is composed of around 90 % methane. But the small amount of heavy hydrocarbons in the natural gas might block the entrance of micropores. Real natural gas or a gas mixture simulating a natural gas should be used to test the performance of activated carbons for adsorbed natural gas application.

In final conclusions, this thesis has reported a theoretical and experimental study of activated carbons for adsorbed natural gas as an alternative vehicle fuel. Molecular simulations demonstrate for the first time that carbon microstructure has a significant influence on adsorbed methane density and capacity. KOH activation of meso-carbon microbeads and coke is recommended as a best technique to produce microporous carbon after a systematic, experimental study on the development of activated carbons from meso-carbon microbeads, petroleum coke, phenolic resin, lignite, coconut shell and wastepaper by

either physical activation (CO_2 or air) or chemical activation (KOH, K_2CO_3, H_3PO_4). For the first time the influence of CO_2 on KOH activation of meso-carbon microbeads is approved and the mechanism of KOH activation is studied in detail. Microporous carbon monoliths are successfully made from KOH activated meso-carbon microbeads and AX-21 carbon. The best carbon monolith can deliver 146 cubic meter of methane per cubic meter of carbon, which is much higher than all commercial activated carbons.

BIBLIOGRAPHY

Alcaniz-Monge J., Cazola-Amoros D. and Linares-Solano A. and Oya A., (1995). *Extended Abstracts and Program of 22nd Biennial Conference on Carbon*, American Carbon Society, San Diego, USA, pp516-517.

Allen M.P. and Tildesley D.J., (1987). *Computer Simulation of Liquids*. Oxford: Clarendon Press, pp24-25.

Alson J.A., Adler J.M. and Baines T.M., (1989). *Alternative Transportation Fuels*. Westport, CN: Greenwood Press, pp109-143.

Atlanta Gas Light Adsorbent Research Group, (1995). *A Final Report on Adsorbed Natural Gas Research*, GRI-95/0068, p33-74.

Auguie D., Oberlin M., Oberlin A. and Hyvernat P., (1980). *Carbon*, **18**, p337.

Aukett P.N., Quirke N., Riddiford S. and Tennison S.R., (1992). *Carbon*, **30**, p913.

Bansal R.C., Donnet J. and Stoeckli F., (1988). *Active Carbon*. New York: Marcel Dekker Inc., pp8-9.

Brooks J.D. and Taylor G.H., (1968). *Chem. and Phys. of Carbons* (Walker Lr P.L, ed.). New York: Marcel Dekker, **4**, p243.

Brunauer S., Deming L.S., Deming W.S. and Teller E., (1940). *J. Amer. Chem. Soc.*, **62**, p1732.

Byrne J.F. and Marsh H., (1995). *Porosity in Carbons* (J.W. Patrick, ed.). London: Edward Arnold, pp1-48.

Cazorla-Amoros D., Alcaniz-Monge J. and Linares-Solano A., (1996). *Langmuir*, **12**, p2820.

Chahine R. and Bose T.K., (1991). *Extended Abstracts and Program of 20th Biennial Conference on Carbon*, American Carbon Society, pp638-639.

Cracknell R.F, Gordon P. and Gubbins K.E. (1993). *J. Phys. Chem.*, **97**, p494.

Davis R.T., De Witt T.W. and Emmett P.H., (1947). *J. Phys Chem*, **51**, p1232.

DeGance A.E., (1992). *Fluid Phase Equilibria*, **78**, p99.

Derbyshire F, Jagtoyen M. and Thwaites M., (1995). *Porosity in Carbons* (J.W. Patrick, ed.). London: Edward Arnold. pp227-252.

Dollimore D. and Shingles T., (1969). *J. Appl. Chem.*, **19**, p218.

DubininM.M., (1960). *Chem. Rev.*, **60**, p235.

Ehrburger P., Addoun A., Addoun F and Donnet J.B., (1986). *Fuel*, **65**, p1448.

Everett D.H. and Powl J.C., (1976). *J. Chem. Soc., Faraday Trans.* I., **72**, p619.

Fei Y.Q., Yamada Y., Meada T., Shiraishi M. and Derbyshire F., (1994). *Extended Abstracts and Programme of Carbon'94*, July 3-8, 1994, Granada, Spain, Spanish Carbon Group and The University of Granada, p202-203.

Fritz K. J. and Hüttinger K. J., (1992). *Proceeding of Carbon'92*, Doutshes Keramische Gesellschaft, Essen, Germany, D10, p431-432.

Greene D. L., (1989). *Gaseous Fuels: Technology, Performance and Emissions, SP-798, Proceedings of International Fuels and Lubricants Meeting and Exposition*, Baltimore, Maryland, September 25-28, 1989. Society of Automotive Engineers, Inc. pp25-34.

Gregg S. J. and Sing K. S. W., (1982). *Adsorption, Surface Area and Porosity*, sec. ed.. London, New York, Paris, Tokyo, Toronto: Academic Press, pp45-121.

Gregg S. J. and Stock R., (1957). *Trnas. Faraday Soc.*, **53**, p1355.

Greinke R.A., (1994). *Chem. and Phys. of Carbon*, **24,** p4.

Hassler J.W., (1963). *Activated Carbon.* New York N.Y.: Chemical Publishing Company, Inc., pp1-14.

Heal G. R., (1990). Enhanced Methane Adsorption by Activated Carbons, in *Gas Utilization Research Forum* in London, July 11-13th. London: British Gas, London Research Station, 7 pages.

Honda H. and Yamada Y., Oi S and Fukuda K., (1973). *Tanso,* **72**, p3.

Horvath G. and Kawazoe K., (1983). *J. Chem. Eng. Japan*, **16**, p470.

Ingersoll J.G., 1996. *Natural Gas Vehicles.* New York: The Fairmont Press, Inc., p165-209.

International Energy Agency, (1982). *Natural Gas — Prospects to 2000.* France: OECD Publications, p122.

Kasuh T. and Scott D.A. and Mori M., (1988). *Extended Abstracts of Carbon'88*, p146.

Khan A.R. (1986). in "*Proceedings of the Oxford Energy Seminar 1982-1985*", (Mabro R, ed.),. Oxford: Oxford University Press, pp59-60.

Klug H.P. and Alexander L.E., (1974). *X-ray diffraction procedures* — For Polycrystalline and Amorphous Materials, 2nd. ed. Wiley-Interscience Publication, pp667-689.

Knowles D., (1984). *Alternate Automotive Fuels.*. Verginia: Reston Publishing Company Inc., p139-148.

Kodama M., Fujiura T. Esumi K., Meguro K., and Honda H., (1992). *J. Materials Science*, **27**, p6079.

Laine J., Calafat A. and Labody M., 1989. *Carbon*, **27**, p191.

Lecloux A. and Pirard J.P., (1979). *J. Colloid Interface Sci.*, **70**, p265.

Lewis I. C., Greinke R. A. and Strong S. L., (1991). *Extended Abstracts and Program of 20th Biennial Conference on Carbon*, American Carbon Society, pp490-491.

Lippens B.C., Linsen B.G. and Boer J.H., (1964). *J. Catalysis*, **3**, p32.

Margaret K.S., (1989). *Gaseous Fuel: Technology, Performance And Emissions, Proceedings of International Fuels and Lubricants Meeting and Exposition*, Baltimore, Maryland, September 25-28, 1989. Warrendale, PA: Society of Automotive Engineers , Inc., pp1-10.

Marsh H. and Kuo K., (1989). In "*Introduction to Carbon Science*", Edited by H Marsh. London: Butterworths, pp108-145.

Marsh H., Yan D.S`, O'Grady T.M. and Wennerberg A., (1984). *Carbon*, **22**, p603.

Marsh H., Crawford D. O'Grady T.M. and Wennerberg A, (1982). *Carbon*, **20**, p419.

Marsh H, Murdie N and Edwards I.A.S., (1987). *Chem. and Phys. of Carbon*, **22**, p216.

Marsh H. and Walker P.L. Jr., (1979). *Fuel Processing Technology*, **2**, p61.

Matranga K.R., Myers A.L. and Glandt E.D., (1992). *Eng. Sci.*, **47**, p1569.

Mays T.J., (1996). *Fundamentals of Adsorption* (LeVan M.D., ed.). Boston: Kluwer Academic Publishers, pp603-611.

Mays T. J., Seaton N.A. and McEnaney B., (1994). *Extended Abstracts and Programme of Carbon'94*, July 3-8, 1994, Granada, Spain, Spanish Carbon Group and The University of Granada, pp244-245.

McEnaney B and Mays T.J., (1989). in "*Introduction to Carbon Science*", (H. Marsh, ed.). London: Butterworths, pp187-189.

McEnaney B., (1988). *Carbon*, **26**, p267.

Medici M. and Mime D, (1974). *The Natural Gas Industry*. London: Newnes-Butterworths. p66.

Meldrum B.J. and Rochester C.H., (1990). *Fuel*, **70**, p57.

Mikhail R. Sh., Brunauer S. and Bodor, E.E., (1968). *J. Colloid Interface Sci.*, **26**, p45.

Molina-Sabio M., Gonzalez M.T., Rodriguez-Reinoso F. and Sepulveda-Escribano A., (1995). *Carbon*, **34**, p505.

Mochida I., Korai Y., Azuma A., Kakuta M. and Kitajima E., (1991). *J. Materials Science*, **26**, p4836.

Mullhaupt J.T., Bevier W.E., McMahon K.C., Van Slooten R.A., Lewis I.C., Greinke R.A., Strong S.L., Ball D.R. and Steele W.E., (1992). *Proceedings of Carbon'92*, Doutshes Keramische Gesellschaft, Essen, Germany, pp367-369.

Murdie N., Marsh H. and Lin M.F., (1985). *Extended Abstract and Program of 17th Biennial Conference on Carbon*, American Carbon Society, pp55-56.

Nakagawa Y., Fujita K. and Mori M., (1985). *Extended Abstract and Program of 17th Biennial Carbon Conference*, American Carbon Society, pp409-410.

Nicolaon G.A. and Teichner S.J., (1969). *J. Chem. Phys.*, **66**, p1816.

Nitta T., Nozawa M. and Kida S., (1992). *J. Chem. Eng. Japan*, **25**, p177.

O'Callaghan P.W., (1993). in "*Energy Management*". New York: Mcgraw-Hill Book Co., pp2-3.

Ostrejko R., (1901). British Patents 14224 (1900); 18040 (1900); German Patent 136,792.

Otowa T., Nojima Y. and Itoh M., (1996). In "*Fundamental of Adsorption*", (M.D. LeVan, ed.). Boston: Kluwer Academic Publishers, pp709-716.

Otowa T., Nojima Y. and Itoh M., (1994). *Extended Abstracts and Programme of Carbon'94*, July 3-8, 1994, Granada, Spain, Spanish Carbon Group and The University of Granada, Mo: O-5.

Otawa T., Shiraishi M., Tanibata R. and Tanaka N., (1992). *Proceedings of Carbon'92*, Doutshes Keramische Gesellschaft, Essen, Germany, pp944-946.

Ouchi K., (1966). *Carbon*, **4**, p59.

Ouchi K. and Honda H., (1959). *Fuel*, **38**, p429.

Parkyns N.D. and Quinn D.F., (1995). in "*Porosity in Carbons*", (J.W. Patrick, ed.). London: Edward Arnold, pp290-324.

Peng D.Y. and Robinson D.B., (1976). *Ind. Eng. Chem. Fundamental*, **15**, p59.

Platzer N., (1960). *Ann. Chem. Paris*, **51**, p805.

Quinn D.F., (1990). in "*Gas Utilization Research Forum*" in London, July 11-13, 1990. London: British Gas London Research Station.

Quinn D. F. and MacDonald J.A., (1992). *Carbon*, **30**, p1097.

Quirke N. and Tennison S., (1996), *Carbon*, **34**, p1281.

Rao Y.K., Adjorlolo A. and Haberman J.H., (1982). *Carbon*, **20**, p207.

Reid R.C., Prausnitz J.M. and Sherwood T.K., (1977). in *The Properties of Gases and Liquids*, 3rd ed., (Carberry J.J. *et al*, Eds.). New York:McGraw-Hill.

Ricca F., Pisani C. and Garrone E, (1971). in "*Adsorption-Desorption Phenomena*", (Ricca F., ed.). London and New York: Academic Press, pp111-125.

Rodriguez-Reinoso F., Molina-Sabio M., Gonzalez M.T., (1995). *Carbon*, **33**, p15.

Rodriguez-Reinoso F., Garrido J, Martin-Martizez J.M. Molina-Sabio M. and Torregrosa R., 1989. *Carbon*, **27**, p23.

Shadman F. and Sams D. A., (1985). *Extended Abstracts of 17th Biennial Conference on Carbon*, American Carbon Society, p182.

Sing K.S.W., (1967). *Chem. Ind.*, p829.

Sing K.S.W., Everett D.H., Haul R.A.W., Moscou L., Pierotti R.A., Rouquerol J. and Siemieniewska T., (1985). *Pure and Appl. and Chem.*, **57**, p603.

Sircar S., Golden T. C. and Rao M. B., (1996). *Carbon*, **34**, p1.

Steele W.A., (1974). in "*The Interaction of Gases with Solid Surfaces*". Oxford, New York, Toronto and Sydney: Pergamon Press. pp13-68.

Stoeckli H. F., (1977). *J. of Colloid Interface Science*, **59**, p184.

Tan Z. and Gubbins K.E., (1993). *J. Phys. Chem.*, **94**, p6061.

Tateishi D, Esumi K. Honda H. and Oda H., (1992). *Carbon*, **30**, p942.

Tiratsoo E. N., (1967). in "*Natural Gas*". London: Scientific Press Ltd. pp305-330.

Walker P.L Jr., Rusinko F. Jr. and Austin L. G., (1959). *Advan. Catal.*, **11**, p133.

Walton J.P.R.B. and Quirk N., (1989). *Molecular Simulation*, **2**, p378.

Washburn E.W., (1921). *Phys. Review*, **17**, p273.

Weaver C.S., (1989). *Natural Gas Vehicles* — A Review of the State of the Art. in Gaseous Fuel: Technology, Performance And Emissions. Proceedings of International Fuels and Lubricants Meeting and Exposition, Baltimore, Maryland, September 25-28, 1989. pp35-55.

Wennerberg A. N., (1971). US Patent No.3624004.

Wennerberg, *et al*, (1978). US Patent 4082694.

Wigmans T., (1989). *Carbon*, **27**, p13.

Yamada Y., Imamura T., Kakitama H., Honda H., Oi S. and Fukuda K., (1974). *Carbon*, **12**, p307.

Yoshizawa N., Yamada Y. and Shiraishi M., (1994). *Extended Abstracts and Programme of Carbon'94*, July 3-8, 1994, Granada, Spain, Spanish Carbon Group and The University of Granada, pp28-29.

Zander M., (1987). *Fuel*, **66**, p1536.